FUNCTIONALIZED GRAPHENE FOR ENERGY STORAGE AND CONVERSION

A Thesis
Presented to
The Academic Faculty

by

Ziyin Lin

In Partial Fulfillment
of the Requirements for the Degree
Philosophy in the
School of Chemistry and Biochemistry

Georgia Institute of Technology
May 2014

COPYRIGHT 2014 BY ZIYIN LIN

FUNCTIONALIZED GRAPHENE FOR ENERGY STORAGE AND CONVERSION

Approved by:

Dr. C.P. Wong, Advisor
School of Materials Science and Engineering
Georgia Institute of Technology

Dr. David Collard
School of Chemistry and Biochemistry
Georgia Institute of Technology

Dr. Z. John Zhang
School of Chemistry and Biochemistry
Georgia Institute of Technology

Dr. Meilin Liu
School of Materials Science and Engineering
Georgia Institute of Technology

Dr. Thomas Orlando
School of Chemistry and Biochemistry
Georgia Institute of Technology

Date Approved: March 31, 2014

To my wife Yan Liu, my daughter Elaine Y. Lin, my parents, and my parents-in-law for their endless love, support, and encouragement.

ACKNOWLEDGEMENTS

I would like to express my sincere gratitude to my advisor Prof. C. P. Wong for his guidance, support, and encouragement during my PhD study. His dedications to research and insights greatly inspire me. I would like to extend my gratitude to my thesis committee members, Prof. John Zhang, Prof. Thomas Orlando, Prof. David Collard, and Prof. Meilin Liu, for their invaluable discussion and advice.

I would like to thank my collaborators, Dr. Min-kyu Song and Mr. Gordon Waller for the rotating disc measurements, Mr. Sathya Raghavan and Dr. Suresh Sitaraman for finite-element analysis, Dr. Andrew McNamara for the infrared thermal imaging measurements, Dr. Yunnan Fang and Ms. Taoran Le for inkjet printing and gas sensor work, and Dr. Yong Ding for the HRTEM measurement.

I would like to acknowledge the help and discussion from my co-workers: Dr. Kyoung-Sik Moon, Dr. Yaogang Yao, Dr. Wei Lin, Dr. Rongwei Zhang, Dr. Qizhen Liang, Dr. Owen Hildreth, Dr. Yan Liu, Ms. Zhuo Li, Mr. Liyi Li, Mr. Zhenkun Wu, Mr. Wentian Gu, Ms. Chia-Chi Tuan, Mr. Bo Song, Dr. Yanqing Ma, and Mr. Joshua Agar. I also want to thank the undergraduate students who worked hard with me, Mr. Zhou Li, Ms. Chris Lau, Mr. Andrew Bulecza IV and Ms. Brooke Maryniak.

This work is financially supported by defense advanced research projects agency, advanced research projects agency-energy, national science foundation, and semiconductor research corporation.

TABLE OF CONTENTS

LIST OF TABLES

Page

LIST OF FIGURES

Page

SUMMARY

Graphene has great potential for energy storage and conversion applications due to its outstanding electrical conductivity, large surface area and chemical stability. However, the pristine graphene offers unsatisfactory performance as a result of several intrinsic limitations such as aggregation and inertness. The functionalization of graphene is considered as a powerful way to modify the physical and chemical properties of graphene, and improve the material performance, which unfortunately still being preliminary and need further knowledge on controllable functionalization methods and the structure-property relationships. This thesis aims to provide in-depth understanding on these aspects.

We firstly explored oxygen-functionalized graphene for supercapacitor electrodes. A mild solvothermal method was developed for graphene preparation from the reduction of graphene oxide; the solvent-dependent reduction kinetics is an interesting finding in this method that could be attributed to the solvent-graphene oxide interactions. Using the solvothermal method, oxygen-functionalized graphene with controlled density of oxygen functional groups was prepared by tuning the reduction time. The oxygen-containing groups, primarily phenols and quinones, reduce the graphene aggregation, improve the wetting properties and introduce the pseudocapacitance. Consequently, excellent supercapacitive performance was achieved.

Nitrogen-doped graphene was synthesized by the pyrolysis of graphene oxide with nitrogen-containing molecules and used as an electrocatalyst for oxygen reduction reactions. We achieved structural control of the nitrogen-doped graphene, mainly the

content of graphitic nitrogen, by manipulating the pyrolysis temperature and the structure of nitrogen-containing molecules; these experiments help understand the evolution of the bonding configuration of nitrogen dopants during pyrolysis. Superior catalytic activity of the prepared nitrogen-doped graphene was found, due to the enriched content of graphitic nitrogen dopant that is most active for the oxygen reduction reaction.

Moreover, we demonstrated a facile strategy of producing superhydrophobic octadecylamine-functionalized graphite oxide films. The long hydrocarbon chain in octadecylamine reduces the surface energy of the graphene oxide film, resulting in a high water contact angle and low hysteresis. The reaction mechanism and the effect of hydrocarbon chain length were systematically investigated.

In addition to the researches on graphene-based materials, some results on advanced carbon nanomaterials and polymer composites for electronic packaging will also be discussed as appendix to the thesis. These include carbon nanotube-based capacitive deionizer and gas sensor, and hexagonal boron nitride-epoxy composites for high thermal conductivity underfill.

CHAPTER 1

INTRODUCTION

1.1 Structure and Properties of Graphene

Graphene is a single layer of carbon atoms covalently bonded into a two-dimensional honeycomb lattice, whose structure is shown in Figure 1. The carbon atoms are sp^2 hybridized in graphene with a carbon-carbon bond length of 0.142 nm. Graphene can be seen as a basic structural building block for several carbon allotropes: the stacking of graphene forms graphite with a constant interlayer spacing of 0.335 nm; the rolling of graphene into 1D tube and 0D ball forms the carbon nanotubes and fullerene respectively. Since the re-discovery of graphene at 2004,[1] lots of researches have been focused on the exciting material, due to the outstanding properties and a wide range of promising applications.

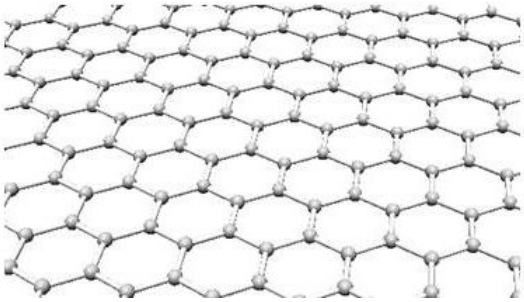

Figure 1. The structure of graphene.

The free standing graphene has high electrical charge carrier mobility up to ~ 200, 000 $cm^2V^{-1}s^{-1}$,[2] and the corresponding conductivity could be in the level of 10^{-6} Ω·cm, comparable to the silver metal. Therefore, graphene could be an excellent electronic conductor.

The thermal conductivity of suspended graphene could be as high as ~5,000 W $m^{-1}K^{-1}$, measured by the non-contact micro-Raman method.[3] Such thermal conductivity is two times higher than that of graphite, which could be attributed to the reduced interlayer phonon scattering. As a result, graphene is a potential material for thermal management in microelectronics, either as a micro heat spreader [4] or thermal interface material.[5] In addition, graphene was used as an ultrahigh thermal conductivity filler that results in significantly enhanced the thermal conductivity of polymer composites.[6]

The optical transparency of graphene (2.3% absorption of white light),[7] coupled with high electrical conductivity, renders its promising application as transparent conducting electrode to replace the expensive indium tin oxide electrode currently used in solar cells, displays and touch panels.[8] The mechanical flexibility of graphene adds another advantage over the conventional rigid electrodes, and extends its application to flexible, wearable electronics.

The mechanical strength of graphene is also very attractive (Young's modulus, ~1100 GPa),[9] which can be used to improve the mechanical properties of graphene-based composites. Graphene has a theoretical surface area of 2630 m^2/g. The high surface area is highly desirable for its application in gas/ion capture and storage, water purification, conductive support for active materials in catalysis and electroanalysis, etc.

1.2 Preparation of Graphene

Graphene does not occur naturally, and its preparation relies on either bottom-up synthesis or physical separation of graphite layers by forcing conditions. Prior works show that the performance of graphene in the aforementioned applications strongly

depends on the preparation method, which has been a major topic of interest nowadays. Many approaches have been successful in producing graphene.

1.2.1 Mechanical exfoliation

The mechanical exfoliation was developed by researchers in university of Manchester to produce graphene, and reported in their prominent papers in Science that is generally considered as the "discovery" of graphene.[1] In this method, the scotch tape is used to attach and peel off graphene from highly ordered prolytic graphite; therefore, it is also called "scotch tape" method. Mechanical exfoliation produces high quality graphene, and has been used for fundamental studies on the structure and properties of graphene, e. g. the measurements of charge carrier mobility,[2] thermal conductivity,[3] and mechanical properties, [9] etc. However, the yield of this method is extremely low, limiting its practical applications.

1.2.2 Epitaxial growth

Graphene can be produced by epitaxial growth from a silicon carbide substrate.[10] Under temperature above 1100 °C, the silicon atoms sublime, leaving the carbon atom layers that form graphene. The crystallinity of graphene from epitaxial growth could be close to that from mechanical exfoliation, and the crystalline size up to hundreds of μm.[11] Although the graphene from epitaxial growth usually stacks together, the interaction between adjacent graphene layers are very weak so that the physical properties of single layer graphene can be preserved. Graphene-based high frequency transistors have been directly fabricated on silicon carbide substrate.[12] The epitaxial growth graphene can be also transferred to arbitrary substrates by various

methods.[13-15] However, the high cost of the substrate, small wafer size, and high processing temperature, limit the application of epitaxial grown graphene.

1.2.3 Chemical vapor deposition

Chemical vapor deposition (CVD) of graphene on various metallic substrates has been a very active research area for producing high quality graphene. During the CVD process, the carbon source, such as methane, decomposes at an elevated temperature and forms graphene on a metal surface; the metal substrate serves as a catalyst for graphene growth. Various metals have been studied, such as nickel, copper, platinum, ruthenium, some alloys, etc.[16] The growth mechanism depends significantly on the nature of metal substrate: two well accepted ones are the precipitation process and surface direct process. The former is through the dissolution of carbon in metals at high temperature and the subsequent precipitation at lower temperature, while the latter is through the surface nucleation and growth of atomic carbon. The focus of most researches in this area is to control of the number of layers and the crystalline size of graphene, and to reduce the overall cost. Single-layer, bi-layer or multi-layer graphene can be controllably grown under many different conditions as a result of the increasing understanding on the growth mechanism. The growth of wafer-level single crystalline graphene was realized recently on copper surface by controlling the number of nucleation sites.[17, 18] People used liquid and solid carbon source to reduce the material cost,[19, 20] and alloy catalyst or plasma-enhanced CVD to reduce the growth temperature.[21-23] Various doped graphene can be produced with the heteroatom-containing precursor added during the CVD process.[24-26] It was found recently that non-metallic substrate can also be used to grow graphene in a CVD environment, which greatly enriches the applicability of CVD

methods; however, the overall quality of graphene is much inferior to that grown on metal substrate.[27, 28] In terms of the application, one of the most promising features for the CVD grown graphene is that it can be transferred to arbitrary substrates via a well-developed method, which coats the graphene first with a polymer, such as poly methyl methacrylate, and then etches the metal substrate out. The easy transfer of CVD graphene enables its application in electronics and transparent conductor. For example, large area roll-to-roll graphene has been fabricated as a transparent electrode.[8] However, the CVD method is still costly, and the growth temperature needs to be further reduced to be compatible with CMOS process.

1.2.4 Liquid exfoliation

The graphene production from graphite by sonication in a liquid solution is called liquid exfoliation method. The mechanical forces during sonication peel graphene layers off from the graphite precursor. The solvent or surfactant used in liquid exfoliation plays a critical role that determines the yield, quality of graphene and processing conditions. The capability of exfoliating the graphite for a certain solvent can be roughly predicated by Hansen solubility parameters.[29] N-Methyl-2-pyrrolidone (NMP) and dimethylformamide (DMF) are among the best known solvents so far. Moreover, graphene can also be produced by sonicating graphite in the aqueous solution of a surfactant, such as sodium dodecylbenzenesulfonate and sodium cholate. The surfactant-coated graphene is stabilized by the electrostatic repulsive force. Generally speaking, liquid exfoliation methods produce high quality graphene with minimal amount of defects and contaminates. The biggest challenge is the low yield, which prevents it from industrial applications. Typical concentration of graphene solutions after liquid

exfoliation is ≤ 1 mg/mL, which means that liters of solvent is required to produce gram-scale graphene; this makes the process costly unless there is a good way to recycle the solvent. Moreover, longtime sonication is always needed that can break the graphene into small pieces, resulting a wide size distribution and small lateral size of less than 1μm. It is nevertheless possible to sort the graphene according to the number of layers and lateral size by centrifuging at different speeds.[29]

1.2.5 Reduction of graphene oxide

The reduction of graphene oxide (GO) is the most promising method for mass production of graphene. GO is a non-stoichiometric material prepared by the oxidation of natural graphite. The most widely used oxidation methods include Hummers' method,[30] Bordie' method[31] and Staudenmaier method;[32] these methods could introduce various oxygen-containing groups on the surface of graphene. The improved synthesis of GO also attracts some research effects recently.[33-35] The structure of GO is of considerable debate, because of the amorphous nature and strong dependence on the specific synthetic process. The Lerf-Klinowski model is the most widely accepted one, and is shown in Figure 2.[36] Oxygen-containing functional groups are dispersed on the graphene sheet, including carboxyls, carbonyls, epoxides and hydroxyls.

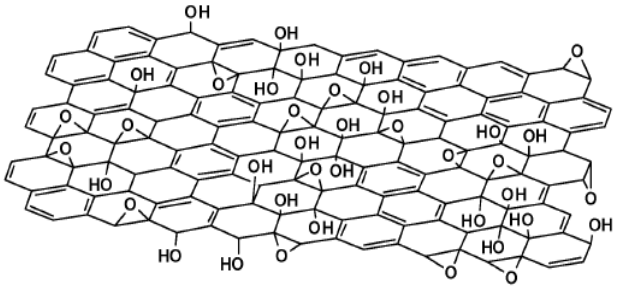

Figure 2. Structure of GO (Lerf-Klinowski model). Reprinted with permission from [36].Copyright 1998 American Chemical Society.

The reduction of GO restores the conjugated system and the increases the electrical conductivity, which is a major research topic in this area. Hydrazine is the most common reducing agent, which has good reduction efficiency but is highly toxic.[37] People have find several lower toxicity reducing agents, such as vitamin C,[38] sodium borohydride,[39] hydroquinone,[40], hydroiodic acid,[41] and metals.[42] In addition to chemical reduction, GO can also be thermally reduced at elevated temperatures; [43, 44] it was found that the thermal reduction of GO starts at a temperature as low as 80 °C.[45] Higher reduction temperature usually leads to lower oxygen content and better electrical conductivity. The concept of thermal reduction can be extended to microwave reduction that utilizes the capability of rapid heating, making the reduction process more efficient.[46, 47] Another variation of thermal reduction is the solvothermal reduction that employs the solvent-GO interaction to control either the reduction kinetics or the functionalization. [48-50] Some other GO reduction methods include laser reduction,[51, 52] and electrochemical reduction.[53, 54] It is also possible to carry out several reduction methods sequentially in order to achieve better reduction.[55]

Despite of such a wide variety of reduction methods, it is very difficult to completely recover the sp^2 conjugated structure and the reduced GO is highly defective; this can be partially mitigated by the healing of defects on reduced GO.[56-58] Nevertheless, in most cases the charge carrier mobility of reduced GO is several orders of magnitude lower than that of pristine graphene. As a result, graphene prepared from the reduction of GO is unlikely to be used for electronics because of the defective nature, but is very promising for energy storage, electrocatalysis, composites etc. where large quantity of material is needed.

1.2.6 Other methods

Bottom-up synthesis of graphene was developed using the condensation of polyaromatic monomers, which achieves highly precise structural control, including crystalline size, edge structure and terminal groups.[59, 60] However, the synthesized graphene has limited lateral size because it becomes insoluble in solutions, making further condensation impossible. The yield of this method is also a challenging issue. Nevertheless, the structural precision of synthesized graphene enables its applications in fundamental studies of the electronic and photoluminescence properties.

Graphene nanoribbons can be produced by unzipping carbon nanotubes either by chemical oxidation[61] or oxgygen plasma treatment.[62]

The intercalation of graphite can be combined with either liquid exfoliation or GO approach to improve the yield and quality of graphene.[63] Typical intercalatants include alkali metals and inorganic acid etc.[64-66] These intercalatants can reduce the interlayer attraction between graphene layers, and produce volatile species upon heating or adding reactive solvents to build up high pressure for efficient exfoliation.

1.3 Functionalized Graphene

With the outstanding intrinsic material properties and a wide range of promising applications, the pristine graphene, however, does not deliver the expected performance in most of cases. For example, graphene has a zero electrical band gap that prohibits its use as field-effect transistors; the low charge carrier density limits the overall electrical conductivity; the poor thermal interface conductance between graphene and most of mating substrate hinders the effective thermal transport. As a filler material, the chemical inertness of graphene causes weak interaction with the matrix and limits the

reinforcement of the mechanical and thermal properties of the composite. As a result, researchers are looking to the functionalization of graphene, which could be a powerful strategy to modify the electrical, chemical, thermal, and interfacial properties of graphene for improved performance.

There are many optional functional groups, which can be generally categorized into three groups:

1) Heteroatom dopants, such as nitrogen, oxygen, boron, phosphorous, etc.
2) Defective sites, which include grain boundaries, in-plane holes, zig-zag/armchair edges, etc.
3) Chemically or physically bonded species such as nanoparticles, small molecules or biomaterials, etc.

Functionalized graphene has found many promising applications with much improved material performance. The in-plane holes are introduced by soft-lithograph in order to open up an electrical band gap for field-effect transistor application.[67]. These defective sites in graphene can also increase the capability of storing charges in supercapacitor applications. For example, graphene was treated by KOH activation in order to create large amount of defects; the activated graphene showed a superior specific capacitance.[68] For the graphene-based polymer composite, functional groups were introduced to the surface of graphene in order to improve the interfacial bonding and the load transfer; as a result, the composite showed much improved Young's modulus, glass transition temperature, and thermal stability.[69] For the transparent electrode based on CVD graphene, HNO_3 or $SOCl_2$ was used to slightly oxidize the graphene, introducing p-type dopants and significantly increasing the electrical conductivity.[8] Moreover,

surfactant molecules could bond onto graphene surface by non-covalent interaction, e.g. π-π stacking or hydrophobic interaction, which can improve the dispersion of graphene in other matrix.

1.4 Research objectives

The research object of the thesis is to utilize the functionalization of graphene as a generic approach to improve the performance of graphene-based material in energy storage and conversion, including:

1) The rational design of functionalized graphene for applications in energy storage and conversion devices on the basis of specific working principle;
2) To develop reliable methods to prepare functionalized graphene with controlled type and density of functional groups;
3) To explore the material performance of functionalized graphene as a supercapacitor electrode and fuel cell cathode catalyst;
4) To understand the structure-property relationship of functionalized graphene for these applications.

CHAPTER 2

SOLVOTHERMAL REDUCTION OF GRAPHENE OXIDE

2.1 Introduction

The pursuit of efficient reduction method is a major topic of interest for graphene preparation from GO approach. Recently several paper reported that GO can be reduced without adding typical reducing agents. These include the sonication of GO in an alkaline solution,[70] hydrothermal treatment in supercritical water,[71] and thermal treatment of GO in propylene carbonate at 150 °C.[72] Other works have demonstrated that GO can be reduced in the presence of amine molecules,[73, 74] and intercalated and exfoliated by tetrabutylammonium cations.[63] The common feature in these reduction methods is that GO is dispersed in a solvent and treated at elevated temperature (from 80 °C to 180 °C), which indicates the involvement of the thermal-driven de-oxygen reaction at elevated temperatures.

The controllable partial reduction of GO is essential to engineer GO's physical and chemical properties. Theoretical study predicts that a wide range of band gap of GO can be obtained by changing the degree of oxidation.[75] Ruoff et. al. demonstrated experimentally that the electrical conductivity of individual GO sheet can be tuned by low temperature reduction.[76] The oxidation degree also determines the interaction between GO and nanocrystals ($Ni(OH)_2$, Au) attached on it.[77-79] To tune the degree of oxidation, the reduction of GO, as a reverse process of oxidation, can be employed. The low temperature thermal reduction described in detail here provides a potential way to control the oxidation degree of GO.

The reduction and functionalization of GO are usually carried out in a liquid phase, by dispersing GO in solvents. The solvent plays an important role because it determines the dispersion and processability of GO and its derivatives. The evolution of surface functionality during reaction usually leads to the change of the dispersion, and in most cases a similar dispersion is desirable for both the precursor GO and the product. The dispersion is affected by the interaction between solvent molecules and GO, which has been studied by Tascon and Ruoff.[80, 81] The polarity of solvents is demonstrated to be a dominating factor for GO dispersion.[80] Since the reduction process is a surface mediated reaction, the solvent-GO interaction also affects the reactivity of GO. However, the reactivity-solvent relation has not been experimentally demonstrated.

We studied the effect of solvent in regulating the reduction of GO. Structural characterizations show that the reduction of GO at low temperatures was due to the decomposition of carboxylic and carbonyl groups. This is promising for the selective reduction of GO. The reduction rate is highly solvent-dependent, suggesting an underlying reactivity-solvent relation. A proposed mechanism is discussed in terms of dipole interaction and hydrogen bonding between the dispersed GO sheets and the solvent molecules. By getting a better understanding of the reduction mechanism at low temperature, our results will help design new chemical methods to achieve either an efficient or a controlled reduction of GO.

2.2 Experimental

2.2.1. Preparation and Thermal Reduction of GO.

GO was prepared by a modified hummer's method.[30] 1g graphite flake (230U from Asbury) was put into a $NaNO_3$ (1 g)/concentrated H_2SO_4 (100 mL) solution in an

ice bath. 6 g $KMnO_4$ was slowly added to the solution, while maintaining the temperature below 20 °C. The mixture was stirred in the ice bath for 2 hours, and for another 0.5 hour in a 35 °C water bath. 46 mL 70 °C water was added dropwise into the flask. The generated heat raised the solution temperature up to 98 °C. 140 mL 70 °C water was then added, followed by 20 mL 30 wt % hydrogen peroxide solution to terminate the reaction. The mixture was filtrated and washed with water to remove the excessive acid and inorganic salts. The resulting GO was dried overnight at 55 °C to produce the GO powder.

The GO powder was re-dispersed in solvent upon sonication. The solvents used in our study were H_2O, DMF, ethylene glycol (EG), and dimethylsulphoxide (DMSO). The suspension was heated in an oil bath at either 100 °C or 150 °C for thermal treatment. The sample for UV characterization was obtained by taking 100 μL suspension from the flask, which was diluted with equal amount of H_2O. After termination of the thermal treatment, the remaining suspensions were filtrated, washed by ethanol and dried in air. In this study, the samples were named by the thermal treatment conditions, GO-Solvent (or Air)-Temperature-Treatment Time.

2.2.2 Characterization

UV spectra were measured by UV-2450 (Shimadzu Co.). Raman characterization was carried out using LabRAM ARAMIS, Horiba Jobin Yvon with a 532-nm-wavelength laser. Fourier transform infrared spectroscopy (FTIR) characterizations were performed at ambient temperature with a spectrometer (Nicolet, Magna IR 560), which is equipped with diffuse reflectance accessories. Powder X-ray diffraction (XRD) analysis was carried out with a X'Pert PRO Alpha-1 system, using Cu Kα radiation (45 kV and 40

mA). Thermogravimetric analysis (TGA) was carried out on a thermogravimetric analyzer (TGA-2050, TA Instruments Co.). Samples were heated at a rate of 20 °C/min in an ambient atmosphere. Contact angle measurements with water droplet were performed with a Rame-Hart goniometer with a charge-coupled device camera equipped for image capture.

2.3 Results and Discussion

2.3.1 Thermal reduction of GO in solvent

The Hummer's method is widely used to prepare GO, which introduces oxygen-containing functional groups into the graphite sheets. As a non-stoichiometric compound, the chemical structure of GO strongly depends on the specific synthetic process. It is generally believed that carboxylic group, epoxy group, carbonyl group and hydroxide group are contained in GO sheets.[82] The π-conjugated system in graphite is disrupted by these oxygen-containing functional groups, producing separated nanocrystalline graphite. These functionalities also change graphite sheet from hydrophobic into hydrophilic. As a result, GO is well dispersed upon sonication in polar solvents such as H_2O, DMF, EG, and NMP. To study the thermal behavior of GO in solvent, we selected H_2O as the solvent for the thermal treatment at 100 °C, which is regarded as a green solvent. DMF, another commonly used solvent, for the reaction at 150 °C. GO-H_2O-100C-24hr and GO-DMF-150C-1hr are discussed in details to demonstrate the reduction of GO in the solvent thermal treatment.

At low concentration (0.2 mg/mL) solution, the GO suspension exhibits a color of light yellow (Figure 3a). In the solvent thermal treatment process, the color gradually

changes to black within the time scale of the experiment, which is usually considered as a sign of GO reduction (Figure 3a). The color change results from the increase of GO absorbance. As shown in Figure 3b, the absorbance of GO suspension in water increases continuously from the starting solution. The increase of background absorption is due to the exfoliation of GO by the intercalation of solvent and increased amount of nanocrystalling graphite.[63] The peak absorption at ~ 230 nm could be attributed to the π-π* transition of C=C bond.[83] A red shift of this peak is usually observed when GO is reduced by reducing agent, such as hydrazine, arising from restoration of conjugated system.[84] However, during the thermal treatment in H_2O, no red shift was observed, indicating that the nanocrystalline graphite does not increase in size. Moreover, there is a shoulder peak at ~ 300 nm, which could be attributed to the n-π* transition of C=O bond.[83] The intensity of this peak decreases, as a result of the eliminating of carbonyl groups in GO.

The structure of reduced GO is characterized by Raman, as shown in Figure 3c. The I_D/I_G ratios are 1.03, 1.14, 1.06 for GO, GO-H_2O-100C-24hr and GO-DMF-150C-1hr, respectively. The I_D/I_G ratio is often used to evaluate the structure of reduced GO. According to the empirical Tuinstra–Koenig relation, the I_D/I_G ratio is inversely proportional to the size of nanocrystalline graphite.[85, 86] However, interpretation of Raman data here is complicated. As Ruoff et al. pointed out, Tuinstra–Koenig relation is not applicable to the early stage of GO structural change upon reduction.[76] The low temperature reduction in their work converts the GO from “amorphous state” to nanocrystalline graphite, where the I_D/I_G ratio is proportional to the square of the nanocrystalline graphite size.[87] The increase of I_D/I_G ratio sometime indicates the

decrease of the topological disorder in graphite layer and the increase the size of nanocrystalline graphite.[87] In our study, the I_D/I_G ratio change is not significant which indicates that the thermal treatment does not affect the nanocrystalline graphite size.

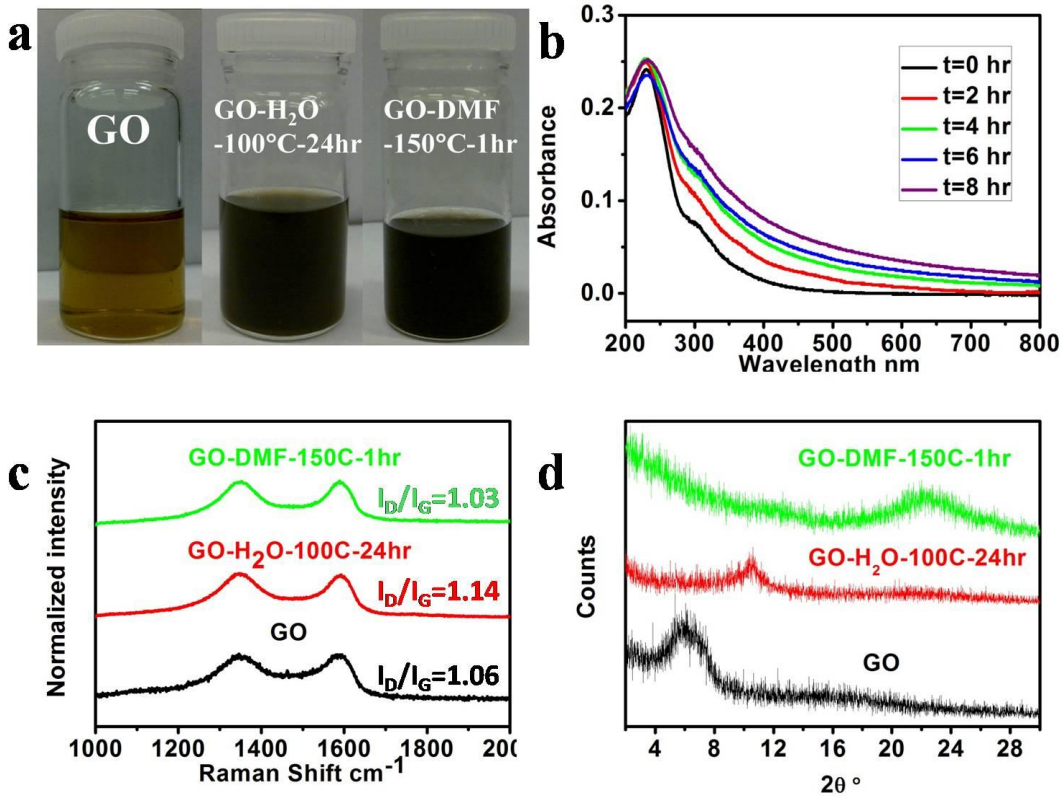

Figure 3. (a) The photographies of GO suspensions before and after thermal treatment (the left image shows GO in water, and GO in DMF has a very similar color); (b) UV (GO-water-150C, treated time is indicated in the inset), (c) Raman and (d) XRD results for GO before and after thermal treatment. Reprinted with permission from [48]. Copyright 2010 American Chemical Society.

The electrical property of GO is closely related to the conjugated structure of graphite layer. The GO and reduced GO were filtrated to produce thin films. The resistances of these films were measured with a Keithley 2000 multimeter. The untreated GO film, which is completely insulating, showed no measurable resistance. After the thermal reduction, the resistance dramatically decreased to 6 MΩ and 6 KΩ for GO-H_2O-100C-24hr and GO-DMF-150C-1hr respectively, corresponding to at least a 3 and 6

orders of magnitude increase of electrical conductivity. It has been demonstrated that the conductivity boost can be achieved by a modest increase of non-oxygenated carbon in GO.[88] The increased conductivity is in line with our conclusion that GO is reduced in the thermal treatment process.

In GO structure, some of the functional groups (epoxy, carbonyl) disperse in the basal plane of GO,[82] which enlarge the gap between adjacent GO sheets. For pristine graphite, the (002) diffraction peak is at ~ 26°, and the inter-plane distance is 0.34 nm. For the GO sample after oxidation, the diffraction peak shifts to ~ 6°, corresponding to an inter-plane gap of 1.5 nm (Figure 3d). This indicates that the GO sheets have been fully exfoliated and are hydrated. We would like to point out that this inter-plane gap is larger than the literature value of ~ 0.7 nm for dry GO.[43] This discrepancy is due to the temperature-sensitive nature of GO reduction. The GO films are thus dried at room temperature instead of at an elevated temperature. H_2O molecules trapped between GO layers enlarge the inter-layer gap. After the thermal treatment, the diffraction peak shift to 10° and 22° for GO-H_2O-100C-24hr and GO-DMF-150C-1hr, corresponding to a distance of 9 nm and 4 nm, respectively (Figure 3d). The decreased inter-plane distance indicates that some of the functional groups decompose during thermal treatment. Furthermore, less H_2O molecules are trapped as the GO sheets becomes less hydrophilic after the thermal treatment. However, the remaining functionalities prevent GO sheets from aggregating back to graphite.

In order to gain insights into chemical structure of GO and treated GO, drift mode FTIR was employed to analyze the existence of functional groups, and their changes after the thermal treatment. In Figure 4a, the pristine graphite only shows three peaks with

absorptions at ~ 3420 cm^{-1}, ~1630 cm^{-1}, and ~1080 cm^{-1}, corresponding to the –OH, C=C, and C-O bonds, respectively. The Hummer's method introduces large quantities of oxygen-containing groups. The peaks at ~ 3420 cm^{-1}, ~ 1720 cm^{-1}, ~1250 cm^{-1}, and ~1060 cm^{-1} signify the presence of –OH, C=O (carboxylic and ketone), C-O (carboxylic), and C-O (epoxy) functional groups, respectively. After the thermal treatment, the absorption at ~ 1710 cm^{-1} greatly decreases in intensity for each sample, as a result of decomposition of carbonyl group (Figure 4b-c). Other peaks from hydroxyl and epoxy groups are still present in the spectra after treatment, as they are stable in this condition.

The introduction of oxygen-containing functional groups decreases the thermal stability of GO. TGA was used to analyze the thermal stabilities of GO and treated GO, as seen in Figure 4d-f. The slight weight loss near 100 °C results from the evaporation of water. The pristine graphite is thermally stable before the completely decomposition after 860 °C in air. For GO, there is a dramatic weight loss (~ 60%) at ~ 200 °C. The decomposition of GO in this stage has been studied by Aksay and Ruoff, who proved that CO_2, H_2O and CO release upon the decomposition of carboxylic group and ketone group.[43, 89] The GO continuously lose weight as temperature increases, and completely decompose after 550 °C. The GO after thermal treatment shows decreased weight loss at ~ 200 °C, indicating a higher thermal stability. For GO-H_2O-100C-24hr, the weight loss is 26 % at ~ 200 °C (Figure 4e). For GO-DMF-150C-1hr, no rapid weight loss is observed at ~ 200 °C (Figure 4f). Furthermore, the temperature where decomposition completed for GO-DMF-150C-1hr is 620 °C, 70 °C higher than GO. `

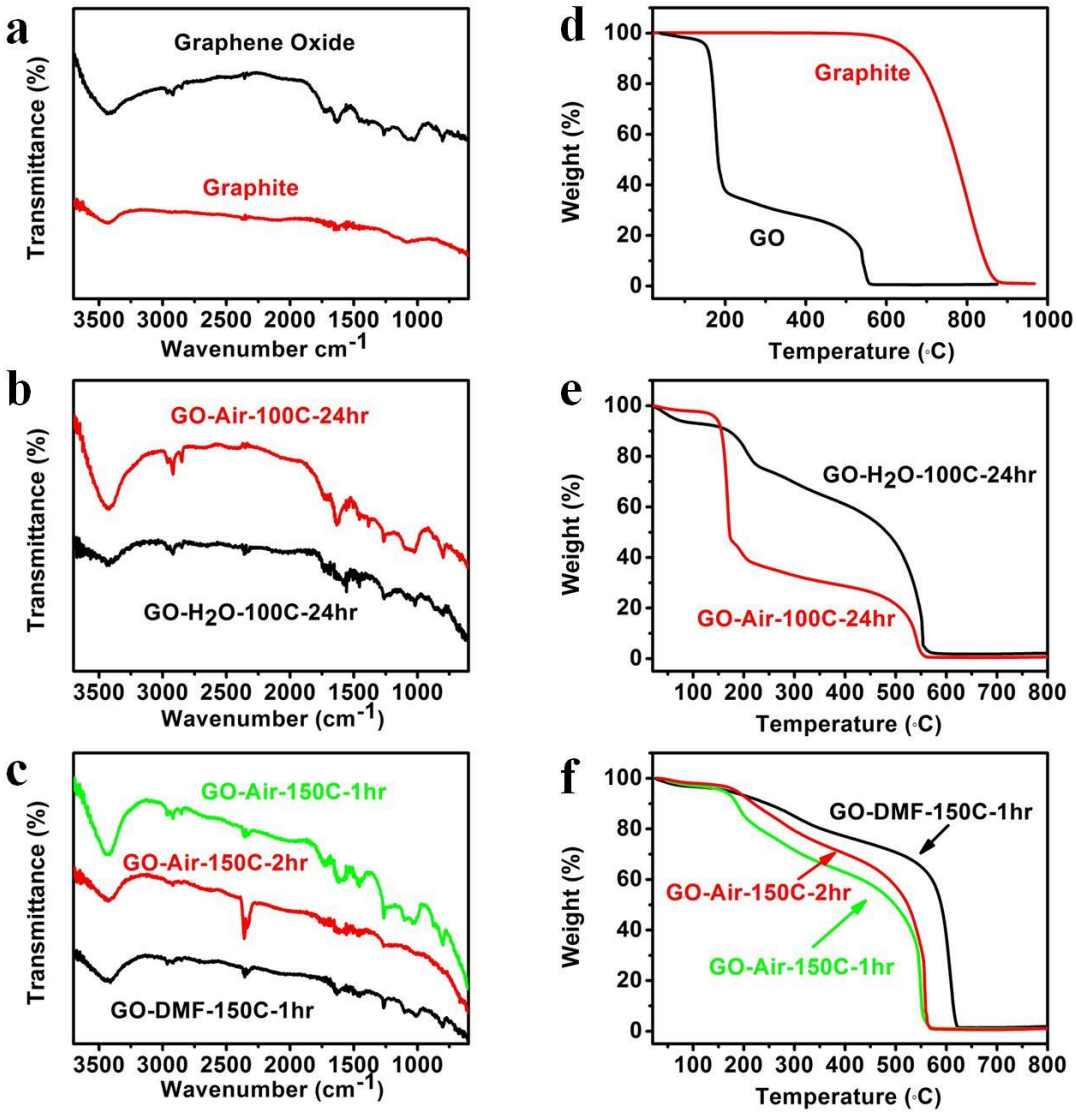

Figure 4. The FTIR results of (a) graphite and GO, (b) GO samples treated at 100 °C, (c) GO samples treated at 150 °C. TGA results of (a) graphite and GO, (b) GO samples treated at 100 °C, (c) GO samples treated at 150 °C. The thermal treatment conditions are indicated by the notation. Reprinted with permission from [48]. Copyright 2010 American Chemical Society.

The high-resolution C1s XPS spectra further confirm the reduction of GO and the chemical structure change during thermal treatment. As shown in Figure 5, the curve fitting yields three components at ~284.9, ~286.7 eV and ~288.5 eV, corresponding to binding energies of carbon in C=C, C-O (hydroxyl and epoxy) and C=O (carboxyl and

ketone) groups respectively.[90] The contribution of C=C band increases from 43.5 % for untreated GO, to 47.5 % for GO-H_2O-100C-24hr, and 66.5 % for GO-DMF-150C-1hr. An obvious narrowing of C=C band is also observed, indicating a more ordered structure for thermal-treated GO. The increase of C=C contribution for GO-H_2O-100C-24hr mainly results from the decreased amount of C=O, while the contribution of C-O is nearly unchanged. This result is in line with our conclusion from FTIR that the carbonyl groups are less stable than hydroxyl and epoxy groups during the thermal treatment. For GO-DMF-150C-1hr, both contributions of C-O and C=O are reduced, evidencing a more efficient reduction of GO. However, there are still significant amount of oxygen-containing groups remaining which are dominated by C-O groups.

To demonstrate the tunability of the degree of oxidation, the wetting property change in this process was characterized by contact angle measurements. The wetting property is a measure of the surface energy, which is directly influenced by the surface functionalities. The GO and treated GO film were obtained by filtration method. As shown in Figure 6, the GO shows a contact angle of 53.8 ± 2.3°, while the GO-H_2O-100C-24hr and GO-DMF-150C-1hr show contact angles of 105.0 ± 2.2° and 121.0 ± 1.7°, respectively. These are close to the reported values for GO and graphene films.[91] The increase in contact angle indicates that GO turns from hydrophilic to hydrophobic, due to the loss of organic hydrophilic functional groups.

The characterizations above suggest that the GO can be partially reduced in H_2O and DMF by the mild thermal treatment. This is probably due to the decomposition of carboxylic groups and carbonyl groups, as well as the structural changes related to epoxy groups. Therefore, the nature of GO solvothermal reduction is a disproportionate reaction,

and the reduced product was collected and analyzed. However, GO is not fully reduced though this method, since most of other functional groups are stable at the temperature range investigated.

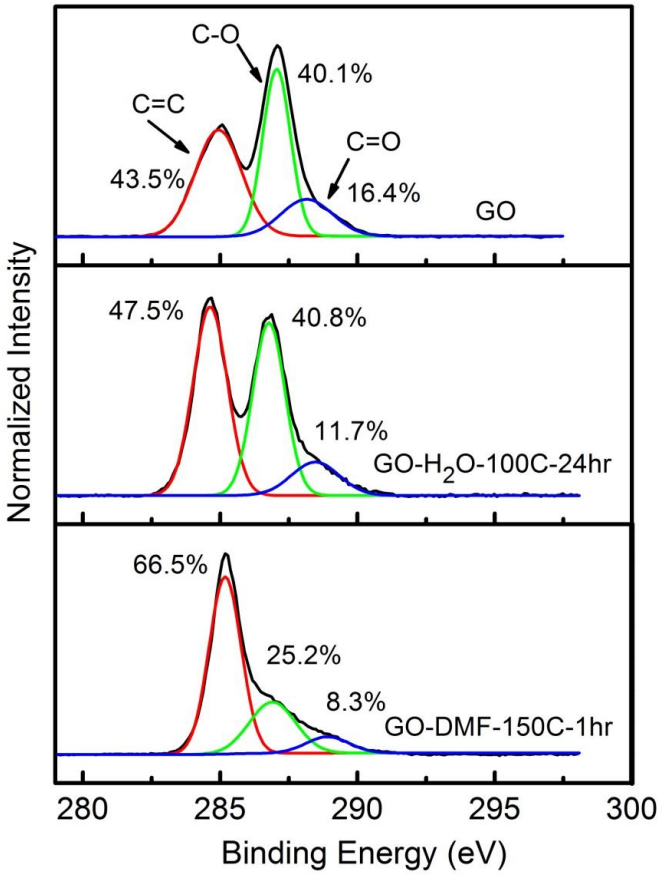

Figure 5. High resolution C1s XPS spectra of GO, GO-H_2O-100C-24hr, and GO-DMF-150C-1hr. Reprinted with permission from [48]. Copyright 2010 American Chemical Society.

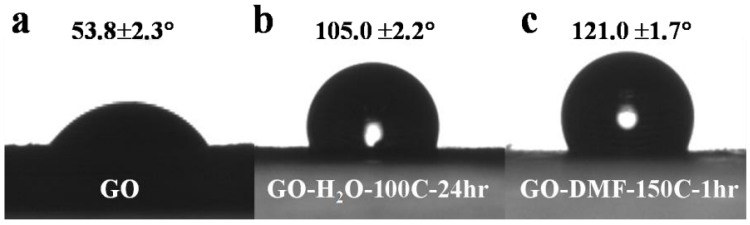

Figure 6. Contact angle measurements of GO and thermal treated GO films. Reprinted with permission from [48]. Copyright 2010 American Chemical Society.

2.3.2 The role of solvent in promoting the thermal reduction of GO

To demonstrate the role of solvent in promoting thermal reduction, GO treated in air instead of in solvent is used for comparison. The color of GO treated in air changed from brown to black after each treatment, indicating the thermal reduction also occurs without the solvent. The efficiencies of GO decomposition in different media could be compared through the TGA and FTIR results.

Figure 4d-f show the TGA results for both GO treated in solvent and in air at 100 °C. The labile functional groups that do not completely decompose during the thermal treatment lead to a weight loss at ~ 200 °C. The amount of weight loss at ~ 200 °C can be used to evaluate the completeness of reduction reaction. The GO-Air-100C-24hr exhibits a weight loss of 50%, which starts from ~ 140 °C, and ends at ~ 170 °C. This is related to the decomposition of carboxylic groups. For GO-H_2O-100C-24hr, no significant weight loss is observed in this region, indicating that the carboxylic group was completely decomposed within 24 hrs. Moreover, the weight loss curves for both samples show a different slope between 180 °C and 220 °C, indicating that there is another decomposition reaction with lower reaction rate in this region. This may be due to the decomposition of carbonyl groups in ketone. The FTIR in Figure 4b shows that there is a strong absorption at ~ 1720 cm^{-1} for GO-Air-100C-24hr, representing carbonyl groups which do not completely decompose within 24 hr treatment in air. In the FTIR spectrum of GO-H_2O-100C-24hr, the peak at 1710 cm^{-1} is weak, suggesting a higher efficiency in removing the carboxylic group. The residual peak may result from the carbonyl groups in ketone, which is more stable than carboxylic group, and do not completely decompose at 100 °C within 24 hr.

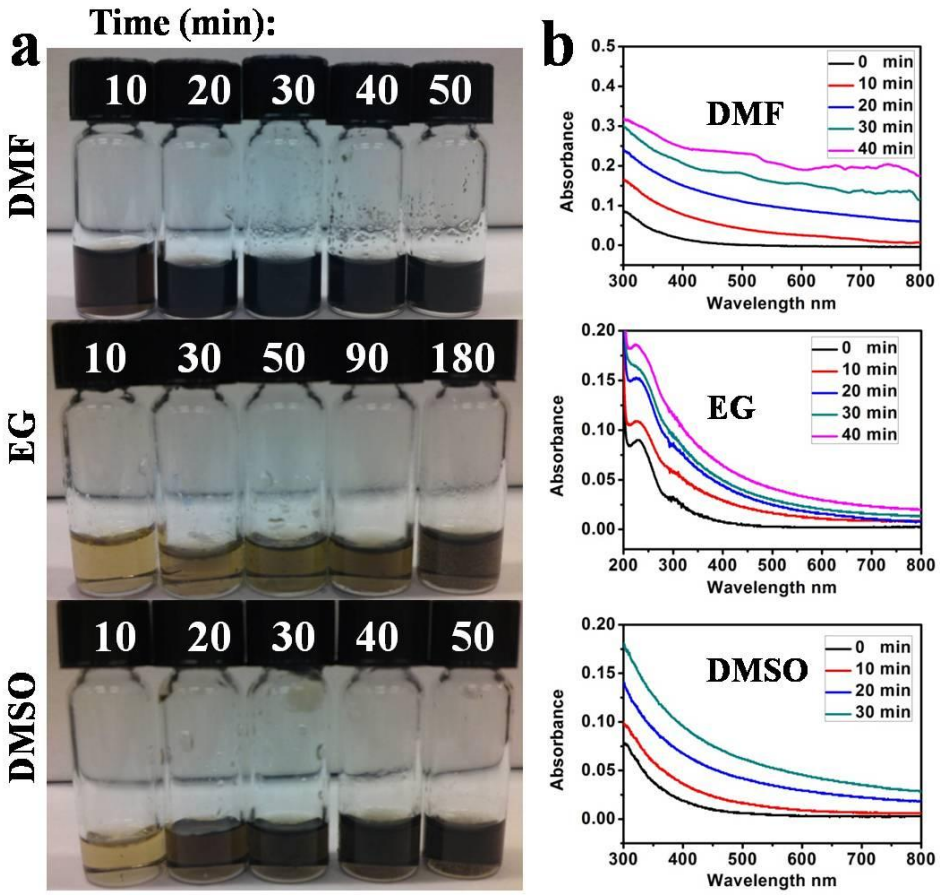

Figure 7.(a) Images of GO in different solvents (DMF, EG, DMSO from top to bottom), which was held at 150 °C for a period of time as indicated; (b) the evolution of UV spectra of GO in different solvents (DMF, EG, DMSO from top to bottom). Reprinted with permission from [48]. Copyright 2010 American Chemical Society.

The GO treated at 150 °C shows a higher stability than that treated at 100 °C, as shown in Figure 4f. All samples treated at 150 °C show nearly no weight loss below 170 °C, due to the complete decomposition of carboxylic groups within 1hr. It is obvious that GO-DMF-150C-1hr exhibits higher stability at higher temperature compared with those treated in air. Between 180 °C and 220 °C, GO-DMF-150C-1hr show a weight loss of 2 %, while the GO-Air-150C-1hr and GO-Air-150-2hr samples have weights losses of 13 % and 6 %, respectively. The decomposition reaction, which can be assigned to the

decomposition of residual carbonyl groups, occurs at the same temperature regions as in 100 °C treated GO. Moreover, GO treated in air decomposes completely at the temperature of 560 °C, while the GO treated in DMF can withstand higher temperature up to 620 °C. FTIR shows a weak adsorption at ~ 1720 cm^{-1} for GO-Air-150C-1hr (Figure 4f), whose intensity continues to decrease when the time increases to 2hr. However, there is no peak from carbonyl group for GO-DMF-150C-1hr.

2.3.3 The solvent-dependence of GO reduction

It is interesting to investigate whether different solvents have different abilities in prompting the GO reduction. The acceleration effect of solvent relates to how it interacts with GO. To study the solvent effect, DMF, EG, and DMSO are selected to investigate solvent effect on the reducing efficiency at 150 °C. All these solvents need to be chemically inert, and with high boiling points and good dispersions for GO. Although EG may get slightly oxidized, this would not affect the analysis. Other good solvents for GO, such as THF, NMP are excluded, because the boiling point of THF is too low; NMP is oxidized and polymerized under our experimental condition. It is found that the type of solvents used to disperse GO and perform the thermal treatment is directly related to the reducing rate. Figure 7a shows clearly that the DMF is a better solvent for GO thermal treatment than EG and DMSO. The color of GO suspension in DMF changed to black after 20 min. However, much longer time is necessary for GO suspension in EG and DMSO to turn to black. Moreover, the dispersion of GO became significantly worse after reduction in DMF, EG and DMSO. This is due to the decomposition of oxygen-containing groups in the reaction, reducing the affinity between GO and the solvent molecules. Thus, reduced GO tends to aggregate.

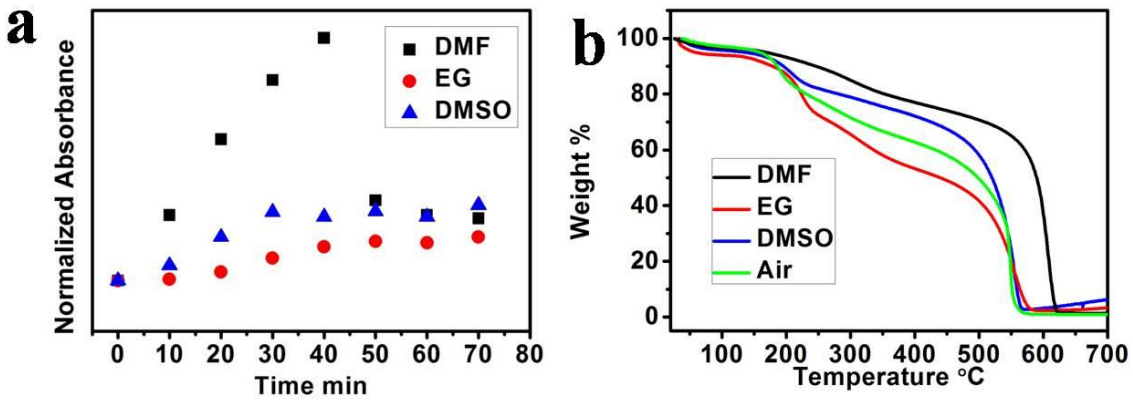

Figure 8. (a) The normalized absorbance at 400 nm for thermal treated GO, which is plotted against the reaction time. All absorbance was normalized to that at t = 0 min. (b) TGA results of GO treated in different solvents at 150 °C for 1 hour. Reprinted with permission from [48]. Copyright 2010 American Chemical Society.

UV spectra collected during the thermal treatment are shown in Figure 7b. The absorbance of all three samples increases with reacting time in the initial stage. This trend is consistent with the color change shown in Figure 7a. To extract kinetics information from the UV data, the absorbance of different GO suspensions was normalized using the initial absorbance value at 400 nm. The plot is shown in Figure 8a. The DMF shows an increased ability to facilitate reduction, while the EG and DMSO have less of an effect. Moreover, for all three solvents used, the absorbance decreases after reaching a maximum value, due to the aggregation of reduced GO. However, it should be mentioned that there is no established relationship between the reduction degree of GO and the absorbance. Thus the UV results can only give a qualitative analysis of the reaction, and are not comparable with other systems or characterization methods.

The TGA results for GO treated in different solvents are plotted in Figure 8b. From TGA curves, it can be concluded that, among three solvents under investigation, the DMF is most effective in accelerating the GO reduction, which is consistent with the UV

results. DMSO shows less accelerating effect. However, GO treated in EG exhibited more weight loss below 250 °C. This indicates that the EG reduces the rate of thermal reduction. These results suggests that oxygen functional groups in GO shows solvent-dependent decomposition rate.

2.3.4 Mechanisms for solvent-dependent reduction

From the results and discussion above, we can conclude that the solvents H_2O and DMF can accelerate the reduction of GO, and there is a strong solvent dependence for the GO reduction kinetics in the solvothermal method. This accelerated GO reduction kinetics is possibly due to the interaction between the solvent molecules and the oxygen-containing groups. Previous study shows that the decomposition of GO is a second-order reaction,[43, 89] in which the reaction rate is proportional to the square of oxygen content.[43] It could be conceptually understood that the GO reduction by releasing of CO_2, H_2O or CO gas occurs upon the "collision" of oxygen-containing functional groups within the basal plane of GO. Compared with solid state GO thermal reduction, the solvent molecules provide a polar environment, which promotes the diffusion of these functional groups at elevated temperature. Therefore, the reduction rate increases in a solvent environment.

We further analyze various types of interacting forces between solvent molecules and GO in order to understand the distinct effects of solvents in GO reduction. A major part of GO-solvent interaction is dipole-dipole interaction. There are large quantities of polar functional groups on the surface, which interact strongly with a polar solvent. From basic organic chemistry, the dipole-dipole interaction between solvent molecules and functional groups can polarize the oxygen-carbon bond and stabilize the intermediate

species. Thus the activation energy of epoxy migration is reduced. Larger dipole moment of solvent leads to the stronger interaction and thus lower activation energy. The dipole moment of DMF, EG, and DMSO is 3.24D, 2.31D, and 4.09D, respectively.[92] Therefore, DMF and DMSO, which have large dipole moments, can accelerate the reduction reaction. The hydrogen bonding is another important interaction between GO and solvents, which can stabilize the epoxy groups and lower its migration rate.[93] Among three solvents, EG is the only protic solvent that can form strong hydrogen bond with epoxy groups in GO. Thus, EG is the least efficient solvent for GO thermal reduction, which reduces the reduction rate. The weak hydrogen bonding between DMF and DMSO, and functionalities on GO may help to explain that DMSO, although with large dipole moment, is less effective than DMF. However, it is not clear why the H_2O, which form strong hydrogen bonding with GO, still accelerates the reduction.

The experimental investigation of solvent-GO interaction and its impact to the GO reduction kinetics is very challenging, due to the lack of tools to probe the interaction and the complexity of GO structure. However, recent theoretical studies could give more insights into this matter beyond the well-known chemistry discussed above. There are several possible structural and chemical changes occur during the thermal reduction of GO, which has be schematically shown in Figure 9. The epoxy group can react with a hydrogen atom in C-H bond to produce a water molecule and recover the sp^2 conjugated structure (Figure 9a);[94] the epoxy groups, when forms a 1 D epoxy line, will cause the break of C-C bond to release the bond stain, resulting to the cutting of graphitic lattice (Figure 9b);[95] various oxygen-containing functional groups, when under certain configurations, could release different species, such as CO_2, CO and O_2 (Figure 9c).[96]

For all these reaction pathways, the migration of epoxy group is a critical and the rate determining step. The energy barrier for epoxy migration is calculated to be ~ 1.52 eV.[97] The presence of water or DMF could effectively reduce the epoxy migration barrier by ~ 0.35 eV so that migration of isolated epoxy can be facilitated.[97] As a result, the overall reduction rate in these solvent increases; this explains our experimental observation that the solvent assist the thermal reduction of GO.

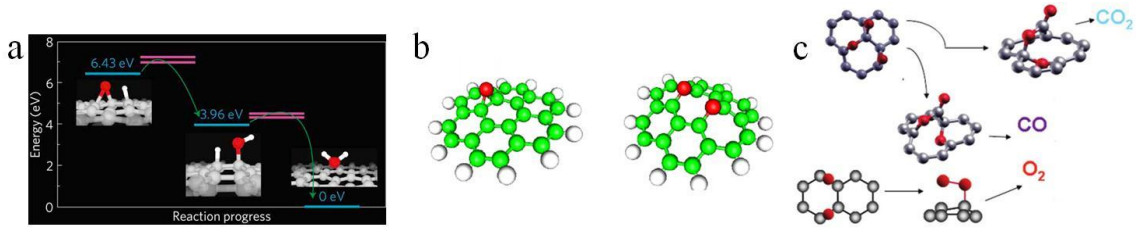

Figure 9. Schematics of proposed structural and chemical changes during GO thermal reduction: (a) An epoxy group reacts with a hydrogen atom to release a water molecule; (b) the formation of 1 D line of epoxy groups leads to the break of carbon-carbon bond; (c) different species (CO_2, CO or O_2) are released when oxygen-containing groups form certain configurations. Reprinted with permissions form [94-96]. Copyrights 2012 Macmillan Publishers Ltd, 2006 American Physical Society, 2011 American Chemical Society.

2.4 Conclusions

The thermal behavior of GO dispersed in solvents at the temperatures of 100 °C and 150 °C was studied. The reduction reaction was characterized by UV, Raman, TGA, FTIR, XRD and XPS. It is found that carboxylic groups and carbonyl groups are decomposed between the temperatures of 100 °C and 150 °C. Therefore, the nature of the solvothermal reduction is a disproportional reaction. The solvent used to disperse GO can assist the decomposition reaction. The interaction between solvent molecules and functional groups promotes the diffusion rate of epoxy groups and plays an important role in the reaction. Different solvents show different abilities to assisting this reaction.

However, the catalytic mechanism is still not clear, because of the limitation of the solvents that can be used in our study. The present results lead to the conclusion that the dipole-dipole interaction promotes the functional groups migration by polarizing the carbon-oxygen bond, and thus accelerates the reduction rate of GO.

CHAPTER 3

OXYGEN FUNCTIONALIZED GRAPHENE FOR SUPERCAPACITOR ELECTRODE

3.1 Introduction

A supercapacitor, also called electrical double layer capacitor (EDLC), is an energy storage component applicable to electric vehicles, consumer electronics, and other devices. Compared to conventional batteries, supercapacitors have advantages of high power density, long cycle life and low maintenance, etc.[98] Remarkably, supercapacitors show highly advantageous power performance over conventional fuel cells and batteries (Figure 10a). However, people still consider the current supercapacitor an immature technology in spite of these attracting characteristics, due to the limited energy density, which is becoming a major hurdle for its implementation in practical applications. For example, to power electric vehicles with supercapacitors, an energy density of at least ~ 30-40 Wh/kg (comparable to lead-acid batteries) is needed. However, the current commercial supercapacitor has an unsatisfactory energy density of 2-10 Wh/kg. Therefore, the improvement of energy density, without compromising the power density, cycling capability and cost effectiveness, is a primary focus in the development of supercapacitors.

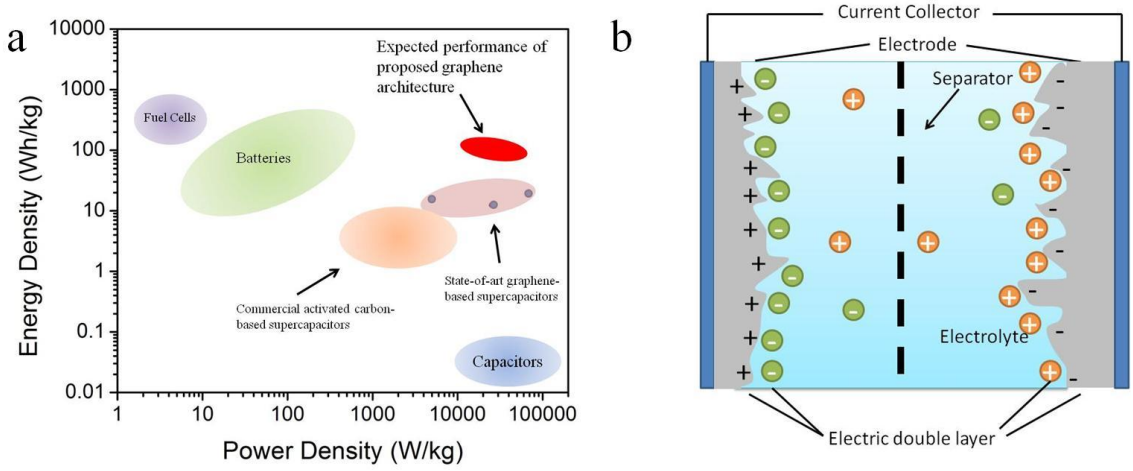

Figure 10. (a) Ragone plot of various energy storage devices, the state-of-art graphene-based supercapacitors, and the expected performance characteristics of proposed graphene architecture. To calculate the power density and energy density of reported graphene materials, the loading of active electrode material in a packaged supercapacitor is assumed to be 30 wt%.[68, 99, 100] (b) The energy storage mechanism of supercapacitor.

The performance characteristics of supercapacitors result from the special energy storage mechanism. As seen in Figure 10b, during the charge of a supercapacitor, ions in the electrolyte are electrostatically adsorbed at the interfaces of porous electrode and electrolyte, forming an electrical double layer. The stored charged ions can be quickly released during discharge, leading to the current passes through the outside circuit. The surface physical adsorption/desorption process enables rapid charge/discharge capability, however causes low energy density compared to chemical reaction-based fuel cells and batteries. The energy stored in a supercapacitor can be calculated by $E = \frac{1}{2}CV^2$, where C is the capacitance mainly related to the electrode material, and V is the operation voltage determined by the electrochemical window of electrolyte. While high energy density can be achieved via either increasing the electrode capacitance or using larger operation voltage, major research efforts nowadays have been focused on novel electrode materials

for higher capacitance because there is little room to push the operation voltage above the electrochemical window of organic electrolyte (2-3 V) and ionic liquids (3-4 V).

The industrial standard electrode material for supercapacitors is activated carbon. However, their issues of large portion of micropores, poor electrical conductivity, poor wetting with polar electrolyte etc, limit the specific capacitance to ~ 100 - 120 F/g. Recently, graphene, a single layer of sp^2 carbon atoms covalently bonded to a hexagonal lattice, attracts lots of research interests due to its outstanding properties including high theoretical surface area (2630 m^2/g), good electrical conductivity and open porous structure. Remarkable achievement has been made in this area that some prototype graphene-based supercapacitors with energy densities of 10-30 Wh/kg have been realized in laboratory scale.[68, 99, 100] However, such high energy densities are achieved by using costly room temperature ionic liquids as electrolyte that has an operation voltage of 3.5 V, instead of by improving the specific capacitances. The specific capacitances of graphene in these works are ~ 140 - 200 F/g,[68, 99, 100] which are still far below the theoretical value (~550 F/g).[100] The unsatisfactory performance of graphene is because that EDLC strongly relies on high specific surface area between electrode/electrolyte interface, which is limited by aggregation and poor wetting between graphene and electrolytes. A potential solution for this problem is functionalization of graphene, especially oxygen-decorated graphene (OG). Oxygen-containing functional groups, such as carbonyl and hydroxyl, provide pseudocapacitance as a complement to EDLC.[101] The hydrophilic nature of these groups improves the wetting between graphene and polar electrolytes, and also prevents aggregations of adjacent graphene sheets. However, the

penalty of losing electrical conductivity arising from the disruption of conjugated system should be avoided, and the density of functionalities needs to be carefully controlled.

It is challenging to prepare OG with controlled density of functionalities using simple direct oxidation of graphene. To introduce oxygen-containing groups, harsh conditions are usually employed due to the inert nature of graphite structure. For example, concentrated H_2SO_4 and $KMnO_4$ are used in Hummers method;[30] concentrated HNO_3 and H_2SO_4 as well as KClO3 are used in Staudenmaier method.[32] Under these conditions, it is unlikely to finely control the density of functionalities. As an alternative way, the reduction of the GO, a highly oxidized form of graphene, is more practical in controlling the density of functionalities. However, methods developed for GO reduction, such as chemical reduction,[37] microwave reduction,[46, 47] and thermal annealing,[55] all aim to achieve an efficient and complete reduction. Controllable reduction and its applications have not been explored.

In this chapter, we used the mild solvothermal method discussed in chapter 2 to reduce GO.[102] Our method distinguishes from previous reported solvothermal methods,[49, 71, 72, 103] as no typical reducing agent was added and a relative low temperature (150 °C) was used. The absence of typical reducing agent, such as hydrazine, allows a high retention of oxygen-containing groups as a source of pseudocapacitance. Furthermore, the kinetics of GO reduction is slow at 150 °C so that the density of functionalities can be controlled by changing the reduction time. A specific capacitance up to 276 F/g was achieved in an optimized condition. Surface functionalities on OG are proven to be critical for achieving superior supercapacitive property, which will be

discussed in terms of their influence on electrical conductivity, pseudocapacitance, wetting properties and aggregations.

3.2 Experimental

3.2.1 Synthesis of OG

GO was synthesized using a modified hummer's method[30]. The preparation of OG was carried out using a previously described method.[102] In a typical process, GO was dispersed in DMF by sonication to form a 1 mg/mL solution. This solution was heated to 150 °C in an oil batch for different durations, producing OG with different density of functionalities. After reduction, OG was filtrated, washed with ethanol, and dried in vacuum. The synthesis of benchmark materials, hydrazine reduced GO, was according to the procedure described in Ruoff's work.[104]

3.2.2 Structural Characterization

Raman characterization was carried out using a LabRAM ARAMIS, Horiba Jobin Yvon with a 532-nm-wavelength laser. FTIR characterizations were performed at ambient temperature with a FTIR spectrometer (Nicolet, Magna IR 560). TGA was carried out on a thermogravimetric analyzer (TGA Q5000, TA Instruments Co.). Samples were heated at a rate of 20 °C/min in air. The XPS was carried out with a Thermo K-Alpha XPS.

3.2.3 Electrochemical Characterization

The electrochemical properties of OG were tested in a three-electrode system. The OG was dispersed in NMP containing polyvinylidene fluoride (PVDF) as a binder. The ratio between OG and PVDF was 95:5 by weight, and the concentration of electrode

materials (OG and PVDF) was 10 mg/mL. To prepare the working electrode, 2.00 μL OG dispersion was transferred onto a glassy carbon electrode (3 mm diameter, 0.07065 cm^2 area) and then dried at 85°C. The OG loading was calculated to be 0.27 mg/cm^2. A Pt wire and Ag/AgCl electrode filled with saturated KCl aqueous solution were used as the counter electrode and reference electrode respectively. Prior to the electrochemical test, dissolved oxygen in electrolyte was removed by bubbling N_2 for 10 mins. Cyclic voltammetry (CV) and galvanostatic charge/discharge were measured on a versastat 2-channel system (Princeton Applied Research). The specific capacitance is calculated according to equation: C=It/V, where I is the charge/discharge current density (A/g), t is the discharge time (t), and V is the voltage (0.8 V). The reported specific capacitance and energy density are all normalized to the weight of OG.

3.3 Results and Discussion

In this study, GO is solvothermally treated for different durations to control the density of oxygen functionalities. Thus OG sample is denoted as OG-time, where time indicates the reaction time (h). The best capacitive performance is obtained in the case of OG-3h, which is discussed in detail here.

3.3.1 Structure of OG

We carried out a set of structural characterizations on OG-3h, including XPS, TGA, FTIR and Raman spectroscopy. Figure 11a shows high-resolution C1s XPS spectra of GO and OG-3h. The C-C fraction increases from 44.0% for starting GO to 54.0% for OG-3h. A narrowing of C-C band suggests a more ordered structure of OG-3h. However, the C-O and C=O fractions are still as high as 28.4% and 17.6% in OG-3h respectively, indicating a significant amount of oxygen-containing groups. Surprisingly with many

oxygen-containing groups, OG-3h still exhibits a much enhanced thermal stability, as seen in TGA results (Figure 11b). GO has a 20.5% weight loss at ~ 200 °C, arising from the decomposition of liable functionalities,[43] and completely decompose at ~650 °C. In contrast, OG-3h shows a slow and continuous weight loss before its complete decomposition at ~720 °C. The enhanced thermal stability of OG-3h suggests that the surface functionalities are groups that have relatively high thermal stability. FTIR spectra are used to examine the nature of surface functionalities. As shown in Figure 11c, GO shows distinct peaks ~ 3420 (broad), ~1725, ~1625 cm^{-1}, corresponding to hydroxyls, carbonyls (carboxylic and ketone), and absorbed water respectively.[82] After the solvothermal treatment, the most significant change is that the ~ 3443 cm^{-1} peak becomes sharper and ~ 1725 cm^{-1} peak is diminished, both due to the decomposition of carboxyls. Sharp peaks at ~1582 and ~1380 cm^{-1} could be attributed to unoxidized aromatic region and hydroxyls respectively.[82] Furthermore, the broad peak ~ 1222 cm^{-1} is related to phenolic, epoxy and ketone groups.[82, 105] FTIR results suggest that the reduction of GO is due to the decomposition of carbonyls, mainly carboxylic groups, and the residual functionalities are mainly hydroxyl, ketone and epoxy groups. More information is obtained from Raman spectra. As seen in Figure 11d, the I_D/I_G ratios of GO and OG-3h do not vary significantly, indicating that the size of nanographite domain does not increase after reaction. This is possibly because instead of recovering the conjugated system, thermal reduction in our method generates holes by releasing carbonyl or epoxy groups in the form of CO_2 and CO. The existence of holes in OG-3h is consistent with the theoretical prediction[106] and experimental observations[107, 108] of the atomic structures of GO and reduced GO. Based on these structural

characterizations, we believe that surface functionalities in OG-3h are mainly hydroxyl, epoxy, ketone groups as well as holes. Although there is no direct evidence about the distribution of oxygen-containing groups, they are most likely on the edge of graphene sheet/holes after the solvothermal treatment because previous studies show that basal plane epoxies and hydroxyls are thermally unstable.[93, 106] A possible structure of OG-3h is shown in Figure 12. The presence of holes in OG-3h, as a special type of functionality, is also important because edges have higher specific capacitance than the basal plane.[109]

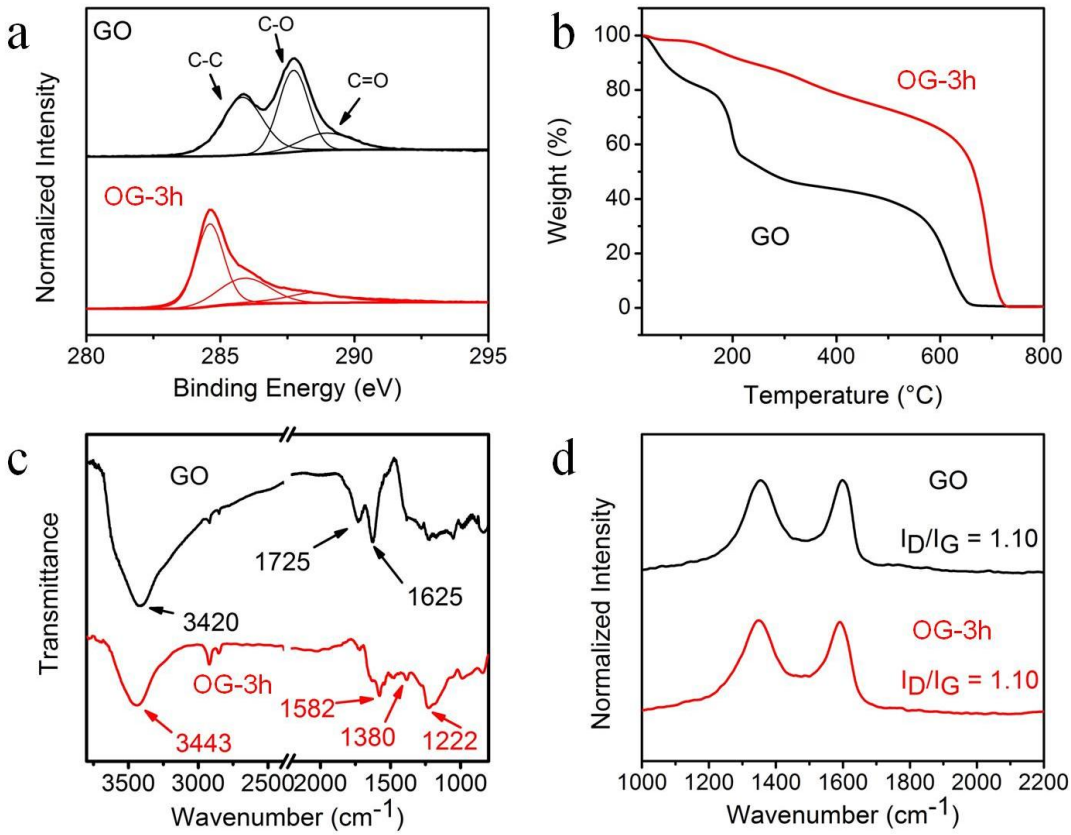

Figure 11. Structural characterizations of GO and OG-3h: (a) high resolution C 1s XPS spectra; (b) TGA curves (ramping rate 20 °C/min, in air); (c) FTIR spectra; (d) Raman spectra. Reprinted with permission from [110].Copyright 2011 American Chemical Society.

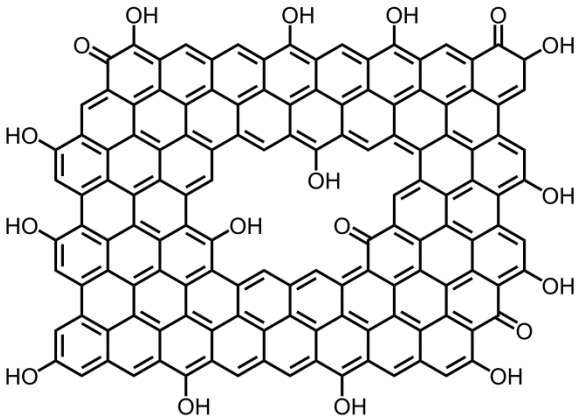

Figure 12. Schematic structure of OG-3h. Reprinted with permission from [110].Copyright 2011 American Chemical Society.

3.3.2 Capacitive performance of OG

The capacitive performance of OG-3h was characterized in a three-electrode system where a 1 M H_2SO_4 was used as the electrolyte. Figure 13a shows the CV curves of OG-3h. At a scan rate of 10 mV/s, OG-3h shows a clear capacitive behavior with a rectangle-like CV curve. Faradic peaks are observed at ~ 0.4 V of anodic scan and ~ 0.35 V of cathodic scan, corresponding to redox reactions of surface functionalities which provide pseudocapacitance. When increasing the scan rate, the CV curve maintains the rectangle shape at 20 mV/s, and is only slightly distorted at 50 mV/s and 100 mV/s, indicating a good wetting and easy access of ions to the OG-3h surface. However, the peaks arising from the redox reactions of surface functionalities are diminished at higher scan rates, due to the relatively slow charge/discharge kinetics compared to EDLC. The specific capacitance of OG-3h is calculated from galvanostatic discharge curves, as seen in Figure 13b. The charge/discharge current density varies from 0.1 A/g to 5 A/g, and the calculated specific capacitances at different current densities are listed in Table 1. OG-3h shows a specific capacitance up to 276 F/g at 0.1 A/g, which is still as high as 205 F/g at 5 A/g. These values are much higher than 238 F/g and 143 F/g measured for hydrazine

reduced GO at 0.1 A/g and 5 A/g respectively (Figure 14). The hydrazine is effective to remove oxygen-containing functional groups. The lower specific capacitance could be attributed to low content of surface functionalities, and severe aggregations and poor wetting properties, which is evidenced by distorted CV curves at 20, 50 and 100 mV/s.

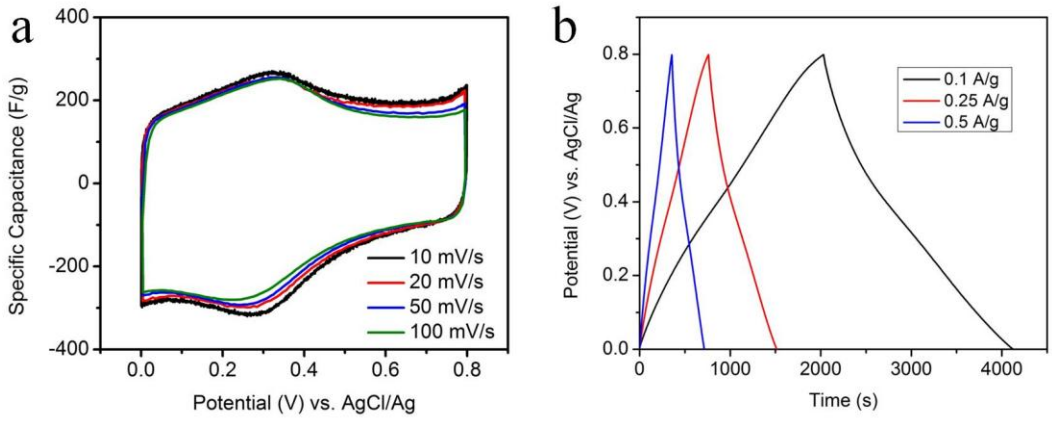

Figure 13.(a) CV curves of OG-3h at different scan rates; (b) galvanostatic charge/discharge curves of fG-3h at charge/discharge currents. Reprinted with permission from [110].Copyright 2011 American Chemical Society.

The Ragone plot in Figure 15 shows that the specific energy of OG-3h is 20.0 and 14.5 Wh/kg respectively at specific powers of 34.5, and 1.69×10^3 W/kg. Moreover, OG-3h shows a high cycling stability in the charge/discharge test (Figure 16a), which is impressive for functionalized carbon materials. It is interesting that the capacitance of OG-3h, instead of decreasing, increases from 236 F/g to ~ 250 F/g. The reason for the increase of capacitance is not clearly at present but it may be because more surface functionalities, especially carbonyl/hydroxyl-type groups, are introduced during the charge/discharge test. This hypothesis is supported by the CV curve in Figure 16b, which shows a larger psedudocapacitance. This interesting phenomenon was also reported by

Ma et al.,[111] and can be used to further functionalize graphene for supercapacitor applications.

Table 1. Capacitances of OG-3h (F/g) at different current densities (A/g) and potential regions.

	0.1	0.25	0.5	1	2.5	5
0- 0.8 V	276	250	236	225	213	205
0 - 0.5 V	335	302	292	280	267	258
0.6 -0.8 V	118	114	106	102	97	95

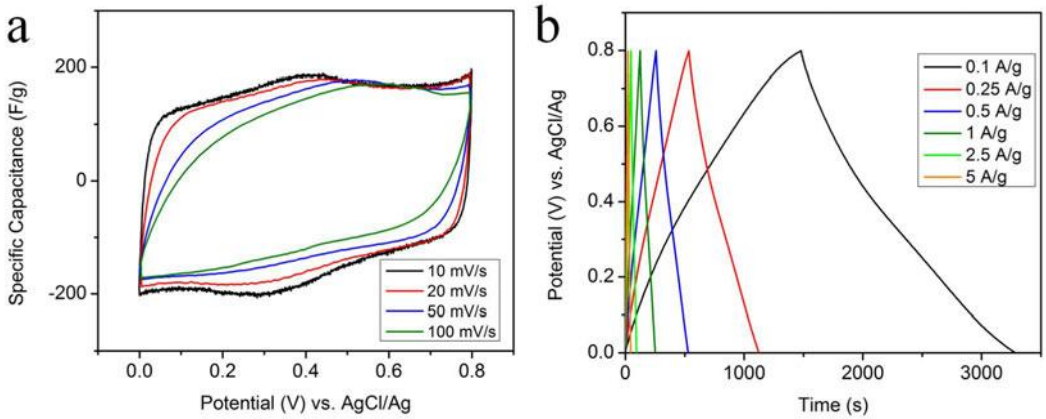

Figure 14. (a) CV curves of hydrazine reduced GO at different scan rates; (b) galvanostatic charge/discharge curves of hydrazine reduced GO at different current density.. The specific capacitance calculated from discharge curves is 238, 195,178, 168, 155, 143 F/g respecitively at 0.1, 0.25, 0.5, 1, 2.5, 5A/g.

A close examination of Figure 13b shows that the discharge curves obviously deviate from the ideal linear shape. Thus OG-3h has different specific capacitances at different potentials, which are listed in Table 1. It is found that the specific capacitance between 0 - 0.5 V is much larger than that between 0.6 - 0.8V. This result together with CV curves suggests that EDLC is responsible for capacitance between 0.6 - 0.8 V and pseudocapacitance becomes dominating at lower potentials. When increasing the discharge current density, the specific capacitance between 0.6 - 0.8 V shows a slower

decrease than that between 0 - 0.5 V, indicating the fast charge/discharge kinetics of EDLC compared to pseudocapacitance.

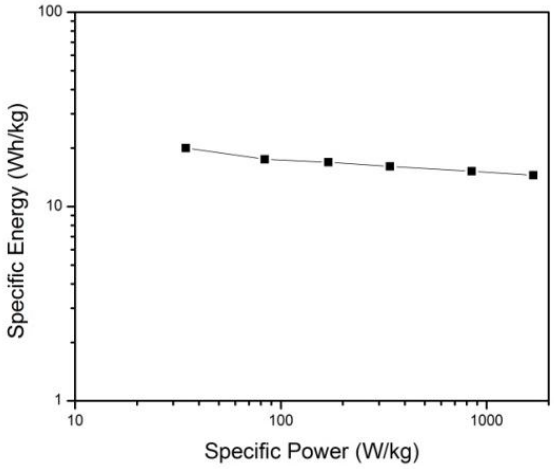

Figure 15. Ragone plot of OG-3h in 1 M H_2SO_4 at a voltage of 0.8 V. The specific power is calculated according to P=V× I and the specific energy is calculated according to E= V× I × t, where V is the averaged voltage over the discharge process, I is the discharge current (A/kg) and t is the dischrage time (h).

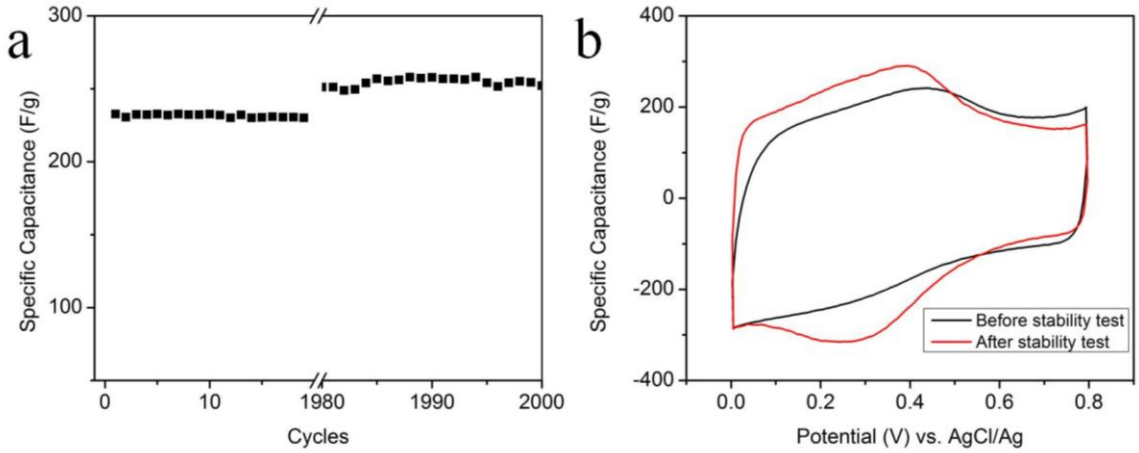

Figure 16. (a) Cycling stability test of OG-3h at a charge/discharge current density of 0.5 A/g and (b) CV curves of fG-2h before and after 2000 cycles at a scan rate of 50 mV/s.

Assuming that the capacitance of OG-3h at 0.6 – 0.8 V are pure EDLC which does not change over the whole voltage range, the dependences of overall capacitance, EDLC and pseudocapacitance on the discharge current density can be plotted, as seen in

Figure 17. The capacitances decrease when increasing the discharge current density. At the largest discharge current density of 5 A/g, the capacitance retention is still as high as 74.3%, 80.5%, 69.6% respectively for overall capacitance, EDLC and pseudocapacitance. Comparing with typical pseudocapacitive materials on graphene/GO, such as conducting polymers,[112, 113] and metal oxides,[114] OG-3h shows a much better rate performance (Figure 17). Thus it can be inferred that the charge/discharge kinetics of pseudocapacitance in OG-3h is faster than typical pseudocapacitive reactions in graphene/GO supported conducting polymers and metal oxides.

A better understanding of the pseudocapacitance in OG-3h can be gained by correlating the structure of OG-3h with previous studies on activated carbon-based supercapacitors. It was found that the pseudocapacitance arises from the reversible redox reactions between oxygen-containing groups and H^+ ions. Thus to achieve a high capacitance, it is preferable to use a H-rich H_2SO_4 solution as the electrolyte. When using a pH-neutral solution, the surface redox reaction is prohibited in the absence of H^+ ions. For example, no faradic reaction is observed between 0.2 - 0.4 V for OG-3h when using a 1 M Na_2SO_4 as the electrolyte (Figure 18). Moreover, mainly carbonyl/hydroxyl-type groups contribute to pseudocapacitance, rather than all oxygen-containing functional groups.[115] For OG-3h, a dominating fraction of surface functionalities are carbonyl and hydroxyl groups, due to their high thermal stability compared to carboxyl groups. The carboxyl groups, which sometimes lead to degradation of carbon materials, are efficiently removed during the solvothermal reaction. Therefore a high pseudocapacitance is obtained without sacrificing the cycling stability. This selectivity is an important advantage of our solvothermal method over other methods for producing

graphene as supercapacitor electrode materials. Furthermore, we would like to mention that the electrochemical behavior of OG are sensitive to dissolved oxygen in the electrolyte. As seen in Figure 19, oxygen molecules may react with OG during discharge process, leading to coulomb efficiencies larger than 100 % and unrealistic high capacitance values. Therefore, to study the capacitive behavior of OG, it is necessary to remove oxygen carefully before electrochemical measurements.

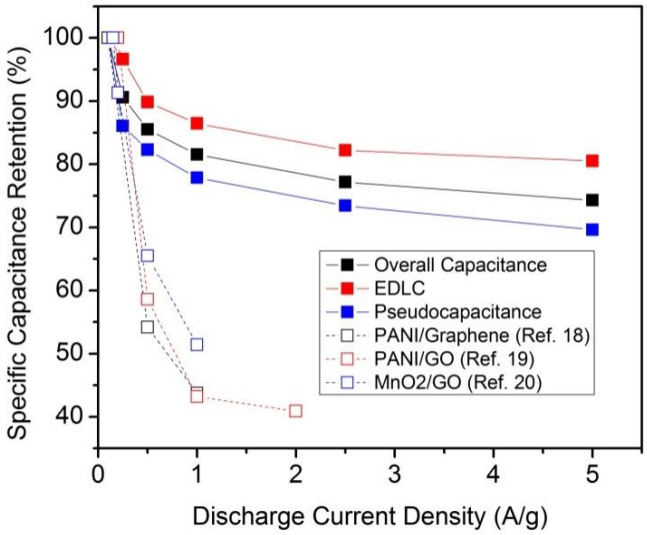

Figure 17. EDLC, pseudocapacitance, and overall capacitance as a function of discharge current density. Results from references are also plotted. The specific capacitance is normalized to the largest capacitance value obtained at the lowest discharge rate. Lines are for visual aids. Reprinted with permission from [110].Copyright 2011 American Chemical Society.

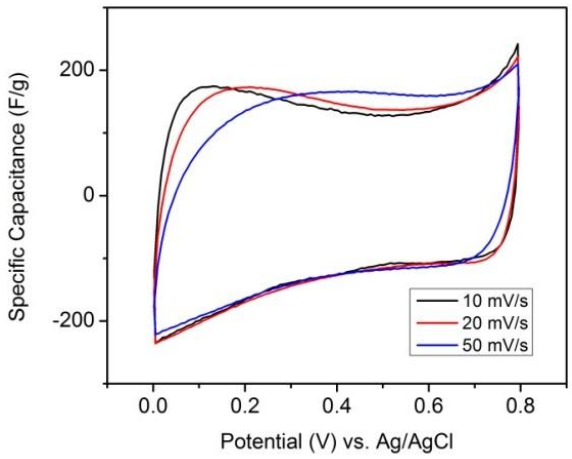

Figure 18. CV curves of OG-3h in 1 M Na_2SO_4 at different scan rates.

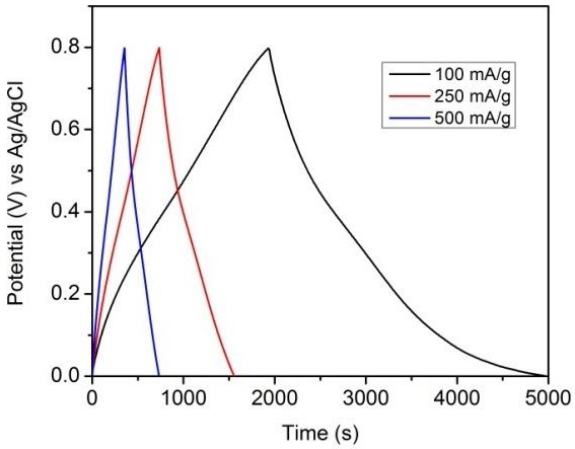

Figure 19. Galvanostatic charge/discharge curves of OG-3h at currents of 100, 250, 500 mA/g. Air saturated 1 M H_2SO_4 was used as electrolyte without bubbling N_2. It is clear the discharge curve are highly distorted at low voltage which leads to a calculated specific capacitance up to 399 /g. Moreover, the coulumb effeciency is higher than 100%, indicating the existence of chemcial reactions between OG and oxygen.

3.3.3 Effect of solvothermal treatment time

XPS, Raman and FTIR were used to study the evolution of OG structure during the solvothermal treatment. The C:O ratio of OGs are calculated from the XPS survey spectra in Figure 20. It can be seen that the C:O ratio increases significantly during the first 2-3 hours, from 1.83 for GO to 5.60 for OG-2h, which however does not change much when further increasing the reaction time. Moreover, the I_D/I_G ratio in the Raman

spectra does not have signifcantly change during the solvothermal reaction, indicating simlar sizes of nanographitic domains (Figure 21). The FTIR spectra of OGs are shown in Figure 22. It can be seen that the peaks of ~3430, ~1725 cm^{-1} becomes diminished in the first 2-3 hours due to the removal of –OH and C=O groups. At longer reaction time, these two peaks do not change much. However, the peak of ~ 1220 cm^{-1} becomes significantly intense, indicating the evolution of funtional groups during solvothermal reaction. The structural changes during solvothermal treatment affect the thermal stability of OGs, as shown in Figure 23. Overall, these structural characterizations show that the solvothermal treatment can effectively remove oxygen-containing functional groups in the first 2 - 3 hours. Longer reactions (>3 hours), instead of further removing surface functionalities, possibly change the atomic structure of OG.

The evolution of the capacitive behavior of OG when increasing the reaction time gives an informative clue on the dependence of capacitance on the density of functionalities. By analyzing the electrochemical test results, a volcano shape relation is found between the specific capacitance of OG and the reaction time, which is shown in Figure 24. As the starting material, GO shows a highly distorted CV curve (Figure 25). The absence of capacitive behavior for GO is due to its poor electrical conductivity which limits the charge migration through the GO sheet. As a result, the EDLC and pseudocapacitance cannot be utilized and the specific capacitance of GO is negligible. At the initial stage of reduction, the specific capacitance of OG increases significantly as a result of increasing electrical conductivity. The specific capacitances of OG-1h and OG-2h are 211 and 250 F/g respectively at 0.1 A/g. However, the low electrical conductivity still limits the utilization of pseudocapacitance, leading to a significant loss of specific

capacitance. For example, the CV curves of OG-1h (Figure 26) show very weak faradic peaks between 0.3 - 0.4 V, although the oxygen content of OG-1h is higher than OG-3h. In the case of OG-2h, the faradic peaks are obvious at low scan rates but become suppressed at higher scan rates, indicating a worse rate performance than OG-3h due to the poor electrical conductivity. The highest capacitance is observed in the case of OG-3h, as we have discussed previously. This "sweet spot" is the spot where the capacitance loss arising from low electrical conductivity is just compensated by the capacitance gained by pseudocapacitance. When further increasing the reduction time, the specific capacitance drops slightly for OG-4h (274 F/g at 0.1 A/g), which becomes obviously smaller for OG-6h (234 F/g at 0.1 A/g). Known that the oxygen content does not differ much for OG-3h, OG-4h, and OG-6h, we believe that the wetting property and aggregations of OG are affected adversely by longer reaction time, which account for the capacitance drop. The evidence is provided by the CV measurement of OG-4h and OG-6h, which are shown in Figure 26. Compared with the CV curves of OG-3h (Figure 13a), the CV curves of OG-4h and OG-6h show more distortions from the ideal rectangle shape at higher scan rates, which could be attributed to poor wetting properties.

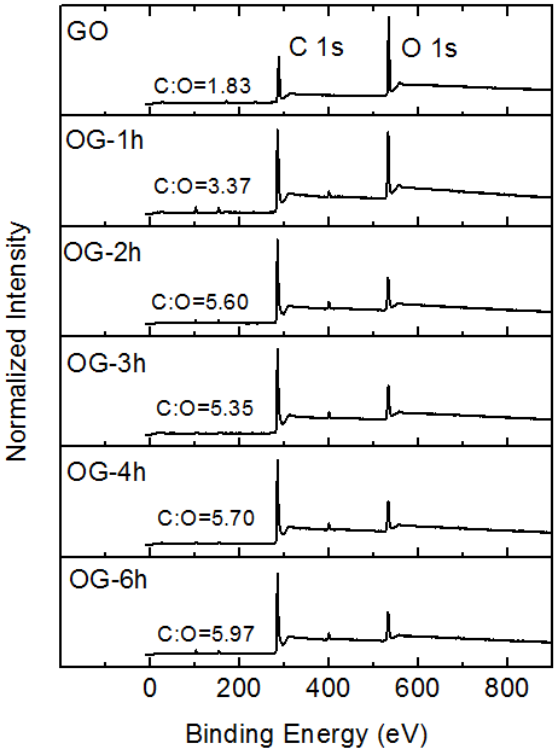

Figure 20. XPS survey of GO and OGs.

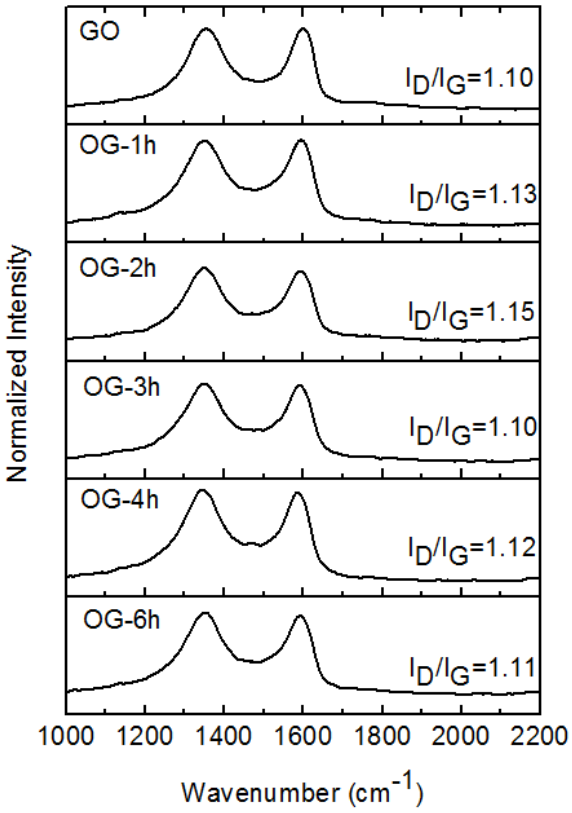

Figure 21. Raman spectra of GO and OGs.

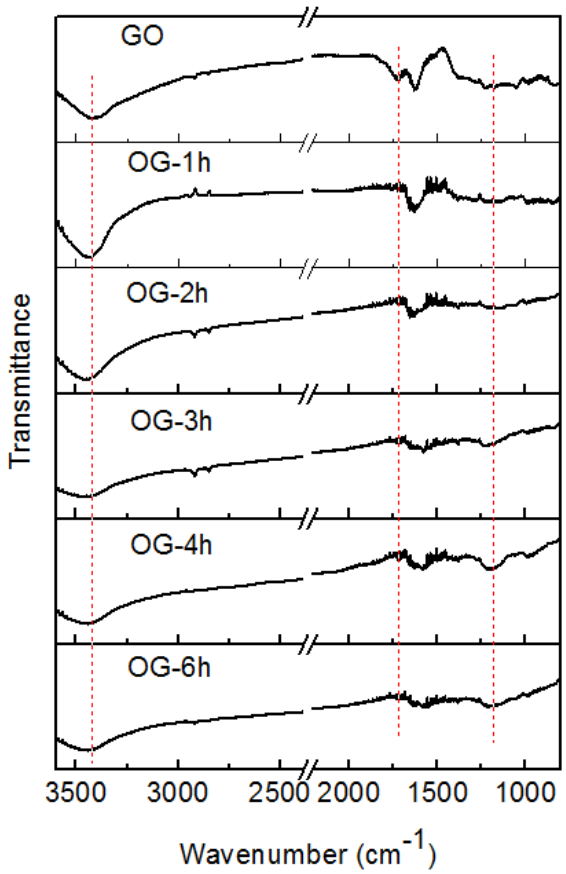

Figure 22. FTIR spectra of GO and OGs.

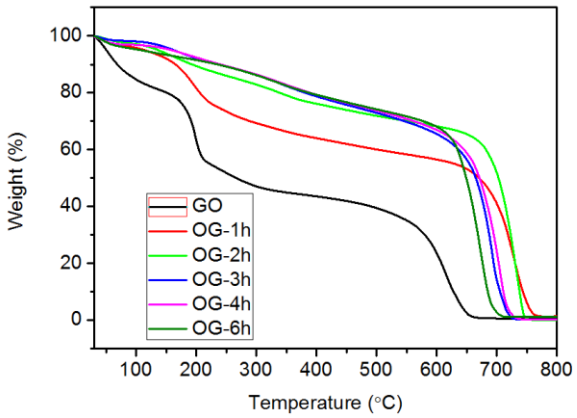

Figure 23. TGA curves of GO and OG. Samples were heated at a rate of 20 °C/min in air.

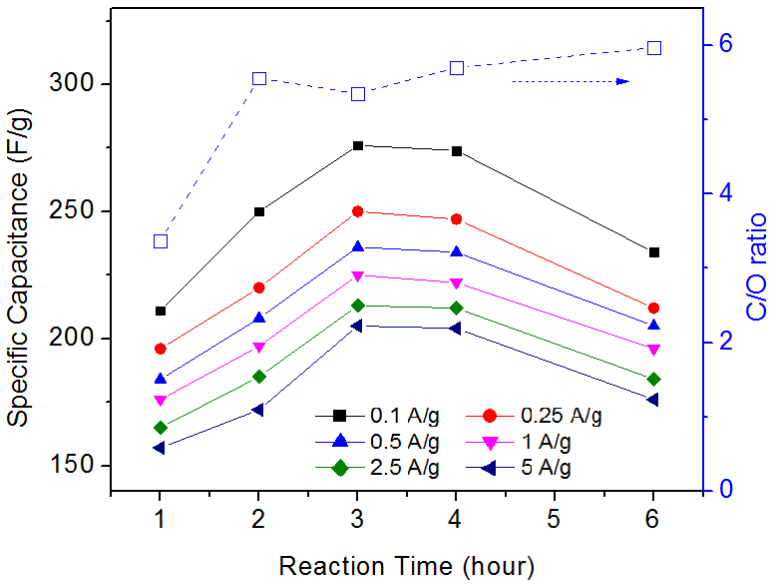

Figure 24. Specific capacitances and C/O ratios of OG with different reaction times.

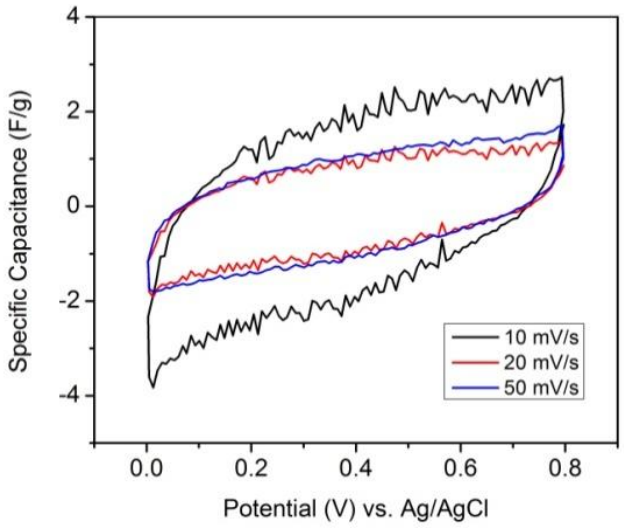

Figure 25. CV curves of GO in 1 M H_2SO_4 at different scan rates.

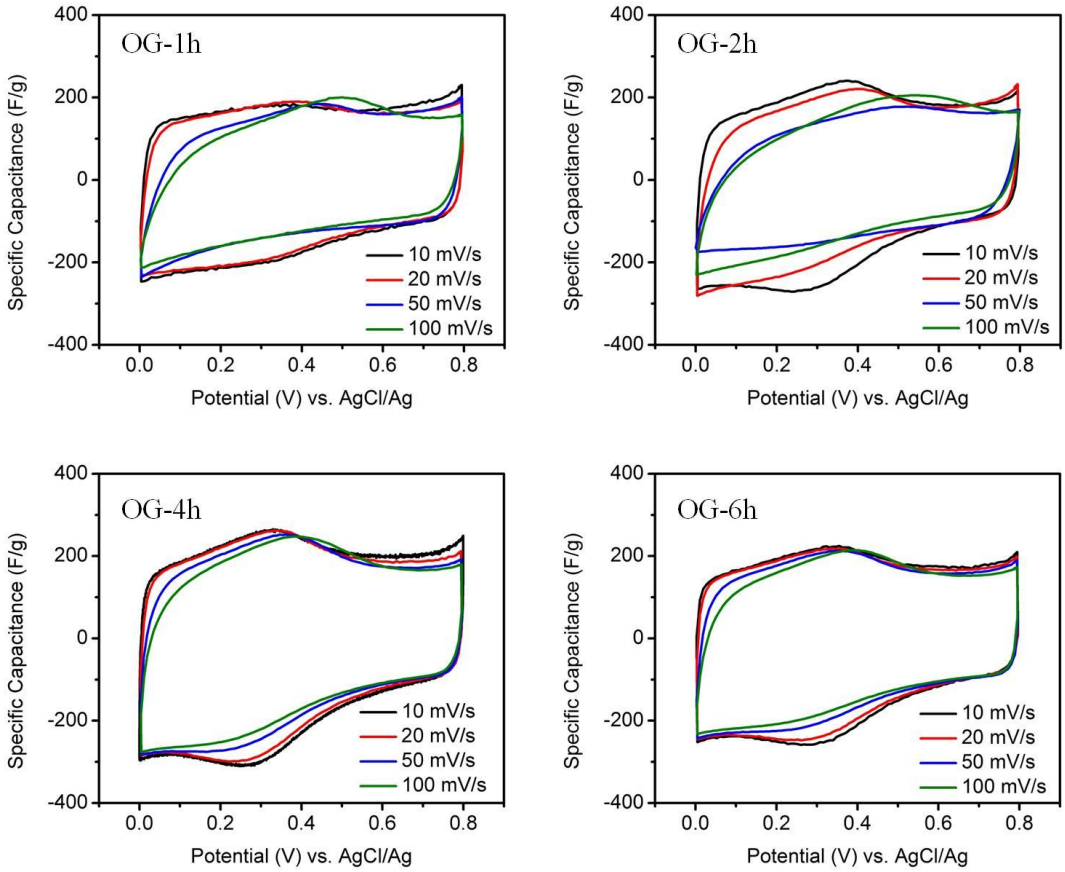

Figure 26. CV curves of OG-1h, OG-2h, OG-4h and OG-6h at different scan rates. 1 M H_2SO_4 was used as electrolyte. Reprinted with permission from [110].Copyright 2011 American Chemical Society.

3.4 Conclusions

The solvothermal method was used to prepare OG-3h, which shows a specific capacitance up to 276 F/g at 0.1 A/g in a 1 M H_2SO_4 electrolyte with good rate performance and cycling stability. The high capacitance is due to the surface oxygen-containing groups, mainly carbonyls and hydroxyls, which lead to large psudeocapacitacne, less aggregation and good wetting properties. The superior capacitive performance of OG-3h demonstrates the importance of controlling the surface chemistry of graphene for supercapacitor applications.

CHAPTER 4

NITROGEN-DOPED GRAPHENE FOR ELECTROCATALYSIS OF OXYGEN REDUCTION REACTIONS

4.1 Introduction

The oxygen reduction reaction (ORR) on the cathode of fuel cells still makes considerable contributions to the energy loss in fuel cells. The traditional Pt-based catalyst, developed for Apollo lunar mission in 1960s, exhibits high catalytic activity, and is being continuously optimized in many ways, including tailoring the size-, shape- and alloy-effect.[116-118] However, the high cost and scarcity of Pt intrinsically limit the large scale production and commercialization of Pt-loaded fuel cells. According to the latest cost analysis, Pt-based catalysts account for ~ 34 % of fuel cell stack cost.[119] In addition, the Pt-based catalyst also suffers from crossover and poisoning effects which compromise the efficiency of fuel cells.[120] The search for alternative ORR catalysts has led to the development of many non-precious metal catalysts, including transition metal-microcycles,[121] nanostructured manganese oxides,[122] and metal-free N-doped carbon materials.[123, 124] Recently, it was reported that the N-doped carbon materials not only have high activity toward ORR, but also long-term durability and tolerance to poisoning. Various forms of N-doped carbon catalysts have been studied, such as carbon nanotube,[123] carbon nanofiber,[125] and graphene.[24] Among them, N-doped graphene (NG) is of particular interest due to the excellent properties of graphene, such as its high the surface area and good electrical conductivity.

Figure 27 shows the schematic structure of NG. The N dopants have several possible bonding configurations, including pyridinic N, pyrrolic N, graphitic N and

oxidized N. Ammonia groups are also possibly in some NGs, but they are unlikely present in NG prepared at high temperatures.

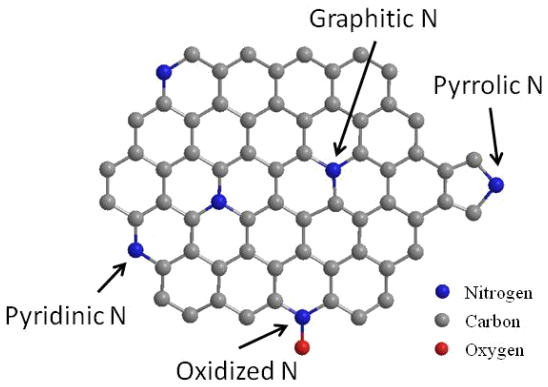

Figure 27. Schematic structure of NG. Reprinted with permission from [126]. Copyright 2013 Elsevier.

Experimentalists are working to identify the active site in NG for ORR catalysis. Conflicting results have been reported: some observed that the content of graphitic N is closely related to the ORR activity,[127, 128] while some claims that the pyridinic N plays a role in the ORR process.[24, 129] Such controversy is largely because of the structural complexity of typical NGs that various N functionalities co-exist, making it nearly impossible to isolate the catalytic activity of individual functionality. In this regard, the mechanistic study by simulations methods may be more insightful. For example, Ikeda et al. found that oxygen molecules are preferentially adsorbed by the C atoms at the zig-zag edge of graphene when a graphitic N is nearby.[130] Zhang et al.'s results suggest that the ORR active site on NG is associated with the C atoms with either high charge density or positive spin density.[131] Ni et al.'s result indicates the graphitic N is the most effective N functionalities in lowering the energy barrier for the dissociation of oxygen molecules.[132] Kim et al. reports that the graphitic N near the edges yields the lowest energy barriers for ORR and hence is the main active sites; however, their

proposed catalytic cycle also involves the transformation between graphitic N and pyridinic N, which explains the controversy whether graphitic N, pyridinic, or both are the active sites.[133] Overall, most of theoretical results and some experimental works suggest that the graphitic N is most responsible for ORR catalytic activity, which serves as an important guideline for material design.

Several methods have been successful in producing NG, which are compared in Figure 28. Chemical vapor deposition (CVD) in the presence of N source is the most common method for the preparation of NG.[25] However, the growth of NG via a CVD method only occurs on the surface of a metal substrate (such as Ni and Cu), and thus is very difficult to scale up. Similarly, segregation growth of graphene, which used pre-dissolved C and N source, also suffers from scalability issue.[134] Cheng and his coworkers developed a solvothermal method to synthesize NG using Li_3N and CCl_4 as the precursors, capable of producing NG in large quantity.[135] Unfortunately, the quality of NG and its catalytic activity is low. Later, people found that GO can be used as a platform, and the N atoms can also be incorporated into the graphene lattice by post treatment, such as thermally annealing with NH_3,[136] arc discharge with pyridine/NH_3,[137] or nitrogen plasma treatment of graphene.[138] The post treatment of GO has good scalability; however, these methods require either toxic gas precursors or special instruments. Moreover, it is difficult to control the type of N functionality in the NG using these methods. It is known that the nature of N functionalities affects the catalytic activity. Accordingly, it is of great importance to develop a facile method to prepare NG with flexibility to control the type of N functionality.

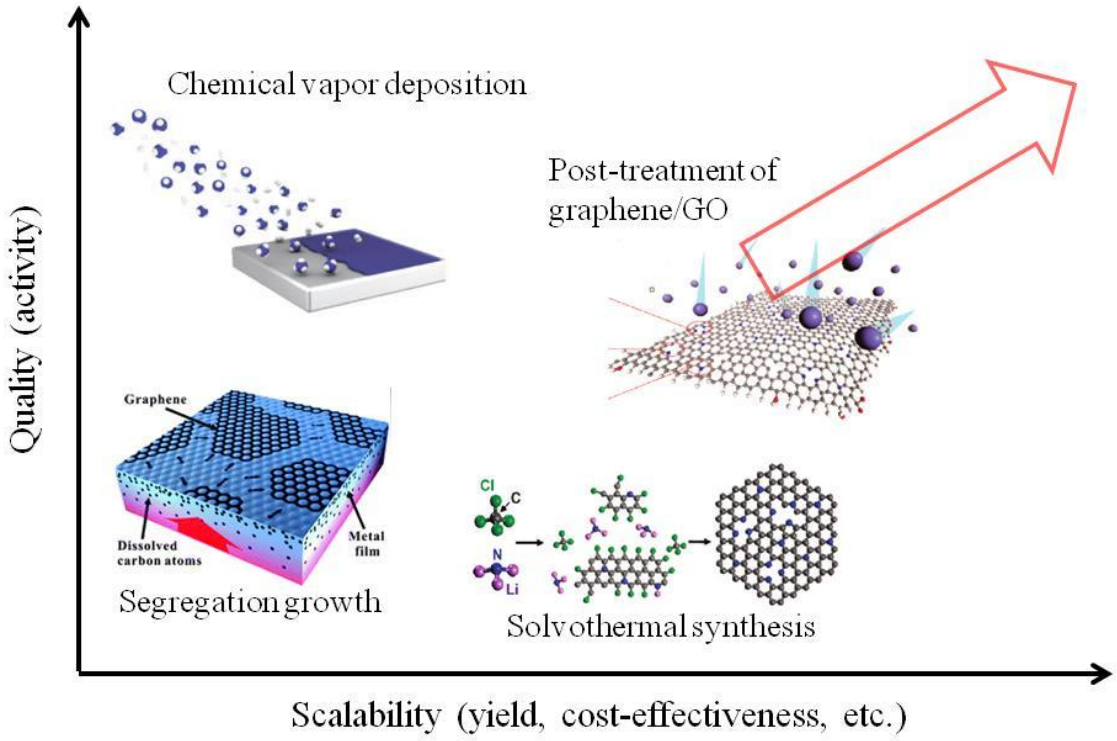

Figure 28. Comparison of various methods to prepare NG in terms of their scalability and NG quality; figures are reprinted with permissions from reference [99, 135, 139, 140]. Copyright 2012 Macmillan Publishers Ltd, 2011 American Chemical Society.

In this chapter, we developed a low cost and scalable method for the preparation of NG by thermally annealing GO with solid N-containing molecules. The basic principle is depicted in Figure 29. GO is used as the starting materials, which is an important derivative of graphene and has lots of oxygen-containing moieties on the graphene sheet, providing reactive sites to interact with other molecules. N-containing molecules are then reacted with GO to incorporate the N atoms into the graphene lattice. After that, pyrolysis at elevated temperature is used for structural re-construction. In this process, the structure of N containing molecules and the pyrolysis temperature are two key parameters to control the bonding configurations of N dopants.

We selected four N-containing molecules for this study, including urea, melamine, polypyrrole (PPy), and polyaniline (PANI); their structures are shown in Figure 30. Urea has a N content of 46.7% and two amino groups for chemical reaction; melamine, a common industrial chemical, is chosen as the N source due to its high N content (66.7% by mass), and bi-functional structure where amino groups can interact with GO and trizine rings can be converted to graphitic N. The favorable formation of graphitic N is expected because of the structural similarity between trizine rings and graphitic N. N-containing polymers PPy and PANI are selected primarily because of their high thermal stability. The GO-N-containing molecule sample were pyrolyzed at elevated temperatures ranging from 400 to 1100 °C to restore the graphene structure with N doping. In this chapter, the NGs are labels as NG-N precursor-pyrolysis temperature. The evolution of NG structure and the catalytic activity are studied to gain insight into the structure-property relation of NG for ORR.

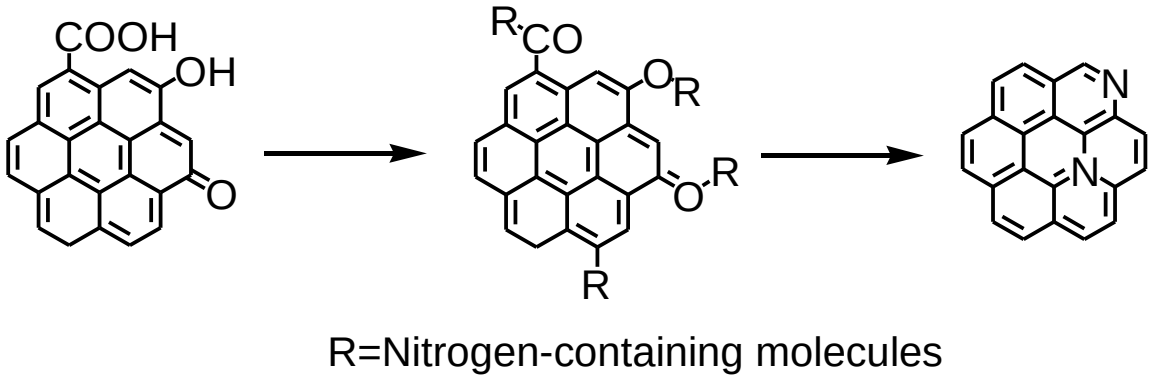

Figure 29. The basic idea of preparing NG by pyrolysis of GO with N-containing molecules.

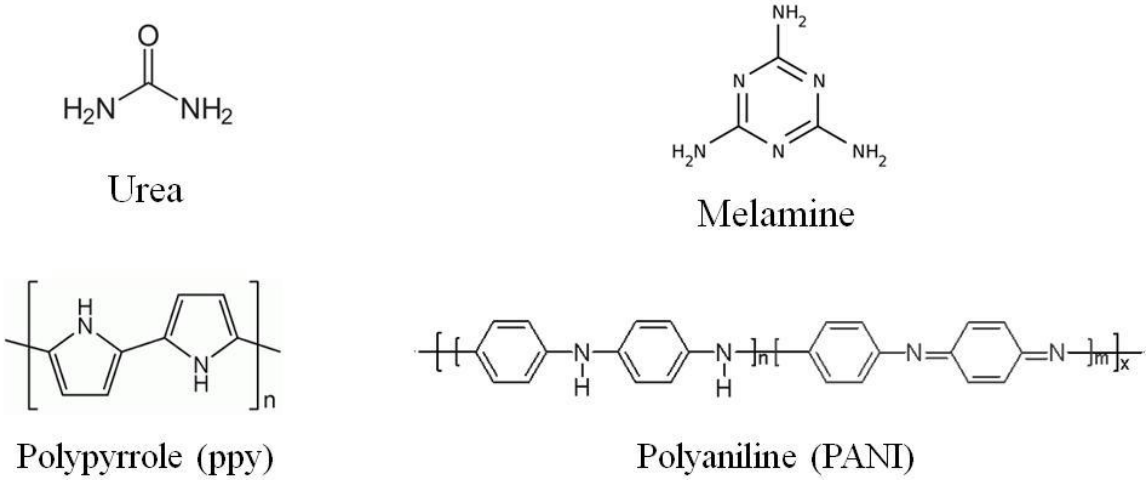

Figure 30. Structures of N-containing molecules used in this study.

4.2 Experimental

4.2.1 Material synthesis

4.2.1.1 GO-urea

GO (50 mg) was dispersed in water (100 mL) by ultrasonication. Then urea (0.25 g) was added into the GO solution which was stirred at 500 rpm until complete dissolution of urea. The solution was dried at 55 °C. The dried GO-urea mixture was pyrolyzed at 800 °C for 30 min in an Ar atmosphere to produce NG. Pure GO was also pyrolyzed at the same condition. The thermally reduced GO is called graphene in the work and used as the control sample.

4.2.1.2 GO-melamine

50 mg GO was dispersed in 100 mL water by sonication. Then 0.25 g melamine was added into the GO solution which was stirred at 500 rpm until significant agglomeration was observed. The solution was dried at 55 °C in an oven. The solid material was collected and homogenized into fine powders using a mortar and pestle. The

GO-melamine powder was pyrolyzed at 900 °C for 30 min in an Ar atmosphere to produce NG.

4.2.1.3 GO-PPy

To prepare GO-PPy composite, 200 mg GO was dispersed in 40 mL water by sonication. Concentrated HCl was added in to the GO suspension to form a 1 M solution. After that, 100 mg pyrrole was added into the GO solution. A catalyst solution of 0.17g $(NH_4)_2S_2O_8$ in 1 M HCl was added. The reaction was carried out at room temperature for 24 hours. Then the GO-PPy composite was collected by vacuum filtration, washed repeatedly with water, and dried at 55 °C over night. The NG was prepared by pyrolyzing the GO-PPy composite at 900 °C for 30 min in an Ar atmosphere. Pure PPy was prepared in the same way without adding GO.

4.2.1.4 GO-PANI

To prepare GO-PANI composite, 200 mg GO was dispersed in 40 mL water by sonication. Concentrated HCl was added in to GO suspension to form a 1 M solution. After that, 100 mg aniline monomer was added into the GO solution. A catalyst solution of 0.17g $(NH_4)_2S_2O_8$ in 1 M HCl was added. The reaction was carried out for 24 hours. Then the GO-PANI composite was collected by vacuum filtration and washed with copious water. The GO-PANI composite was dried at 55 °C over night. The NG was prepared by pyrolyzing GO-PANI composite at 1000 °C for 30 min in an Ar atmosphere. Pure PANI is prepared in the same way without adding GO.

4.2.2 Structural Characterizations:

TGA and differential scanning calorimetry (DSC) were carried out on a simultaneous DSC-TGA analyzer (SDT Q600, TA Instruments Co.). Samples were heated at a rate of 20 °C/min in nitrogen. Scanning electron microscopy (SEM, LEO 1530) and Transmission electron microscopy (TEM, Joel 100 CX) were used to image the morphology of NGs. Electron energy loss spectroscopy (EELS) was acquired on a Tecnai F30 TEM. FTIR characterization was performed at ambient temperature with a FTIR spectrometer (Nicolet, Magna IR 560). Raman characterization was carried out using a LabRAM ARAMIS, Horiba Jobin Yvon with a 532-nm-wavelength laser. The XPS was carried out with a Thermo K-Alpha XPS. The nitrogen adsorption/desorption isotherm was collected at using a Micromeritics TriStar II sorptometer (Micromeritics Instrument Corporation, USA). Powder X-ray diffraction (XRD) analysis was carried out with a Philips X-pert alpha-1diffactometer, using Cu Kα radiation (45 kV and 40 mA).

4.2.3 Electrochemical Characterizations:

The electrochemical properties of NGs were tested in a three-electrode system. A Pt wire and Ag/AgCl electrode filled with saturated KCl aqueous solution were used as the counter electrode and reference electrode respectively. The electrolyte was 0.1 M aqueous KOH solution which was purged by nitrogen or oxygen for 10 min prior to the electrochemical test. To prepare the NG-loaded working electrode, NG was dispersed in the mixture of 5 wt% Nafion solution and water (V: V =1:9) by sonication. 10.00 μL of 1 mg/ml NG dispersion was transferred onto a glassy carbon electrode (GC, 3 mm diameter, 0.07065 cm^2 geometric area) and dried at 80 °C. The NG loading was calculated to be 141 $\mu g/cm^2$. The control sample graphene and Pt/C (20 wt% Pt, Alpha Aesar) on GC were prepared in the same way. CV and linear scan voltammetry (LSV)

were measured on a Versastat 2-channel system (Princeton Applied Research). The electrocatalytic activities toward ORR were also measured using a rotating disk electrode (Pine Instrument, MSR analytical rotator) with a scan rate of 10 mV/s. 28 μL of 1 mg/ml NG dispersion was transferred onto the GC electrode (5mm diameter, 0.196 cm^2 geometric area) embedded in a PTFE holder, and dried in air at 80 °C for 1 hour. A platinum electrode were used a counter electrode. The 0.1 M KOH solution was prepared as electrolyte and saturated with oxygen by bubbling with oxygen gas for 30 minutes before measuring ORR activities. The potential was controlled by a potentiostat (Solartron, SI 1286).

4.3 Results and Discussion

4.3.1 Preparation of NG

4.3.1.1 GO-urea

The morphology of resulting NG-urea-800 is characterized by TEM, as shown in Figure 31a. The highly wrinkled NG has a low contrast under electron beam indicating a small thickness. Raman microscopy offers clear evidence of N-doping in graphene lattice. As seen in Figure 31b, the G peaks of GO, graphene and NG-urea-800 appear at 1600, 1588, and 1580 cm^{-1}, respectively. The downshift of G peak from GO to graphene could be attributed to the restoration of conjugated structure during pyrolysis.[141] The further downshift of G peak in NG concurs with previous reports of NG from other methods, and may be related to the electron donating capability of N heteroatoms.[25, 135, 142] The G peak position is sensitive to the concentration of charge carriers and dopants. For pristine undoped graphene, both n-doping and p-doping will lead to an upshift of D peak

position.[143, 144] The graphene control sample has an upshifted G peak at ~ 1588 cm^{-1} compared to reported value (1580 cm^{-1}) for pristine graphene[145] because of the existence of O-containing residual groups and adsorbed water that lead to a p-doping effect. The downshift of G peak position in NG could be attributed to the fact that the incorporation of N atoms lead to n-doping effect that neutralizes the p-dopant in graphene. This observation is similar to previous reports that the interaction between graphene and electron-donating specifies causes downshifted G peak.[146, 147] Moreover, it is interesting that the electron-donating/withdrawing property of N dopant depends on its bonding configuration. For example, previous studies on N-doped carbon nanotubes showed that graphitic N cause n-type doping, while pyridinic N and pyrrolic N cause p-type doping.[148, 149] Therefore, the downshift of G peak in our observation probably indicates that a relatively high content of graphitic N that leads to an overall n-doping effect.In addition, the I_D/I_G ratio in Raman spectra has been used to evaluate the disorder in graphene materials. It is found that I_D/I_G ratio in GO is 1.10, which increases slightly to 1.13 for graphene and to 1.15 for NG-urea-800. The increased I_D/I_G ratio results probably from the generation of smaller nanocrystalline graphene domains,[37] the loss of carbon atoms by the decomposition of oxygen-containing groups, [48] and the incorporation of N heteroatoms.[25]

The chemical structure of NG-urea-800 was further investigated using FTIR. As shown in Figure 31c, GO shows distinct peaks at ~3420 (broad), ~1725, and~1625 cm^{-1}, which could be attributed to hydroxyls, carbonyls, and absorbed water, respectively.[110] Urea has characteristic peaks at 3320 and 3420 cm^{-1} (amino groups), and 1680 cm^{-1} (carbonyls). In the FTIR spectrum of NG-urea-800, no amino group and carbonyl related

peak can be observed, indicating that these groups completely decomposed during pyrolysis. Moreover, a broad peak at ~ 1100 cm^{-1} appears, due probably to the formation of N-C bonds and the residual C-O groups.

Figure 31d shows the SDT curve, which was used to monitor the physical change and chemical reactions during the pyrolysis of GO-urea mixture. The evaporation of water molecules absorbed on GO results in a slight weight loss below 100 °C, and the melting of urea leads to an endothermic peak at ~ 136 °C. Two dramatic weight losses were observed between ~ 150 - ~ 250 °C and ~ 300 - ~370°C, and were accompanied by large endothermic peaks centered at ~ 240 °C and ~ 360 °C, respectively. The chemical reactions of urea decomposition at these temperatures were found to be very complicated with various reaction intermediates and products, such as cyanuric acid, ammelide and melamine.[150] Moreover, the decomposition of labile oxygen-containing groups on GO occurs at ~ 200 °C. At temperatures between 370 - 560 °C, a gradual weight loss is noted, due to the slow decomposition of GO and urea derivatives. The complete decomposition of GO-urea mixture occurred at ~580-630 °C with an exothermic peak at ~ 610 °C.

XPS was used to characterize the elemental composition of NG-urea-800. As seen in Figure 32, the N content is found to be 7.86 at% from the survey spectrum, which is close to 8.35 at% determined by chemical analysis. The high resolution C1s peak is centered at 284.8 eV with a tail at higher binding energies, indicating the existence of carbon atoms connected to N and O heteroatoms. Peak deconvolution shows that there are 74.3% C=C, 17.5% C=N&C-O, 5.9 % C-N&C=O, and 2.3% O-C=O. The high resolution N 1s could be deconvoluted into four components: 44.4 % pyridinic N, 21.2 % pyrrolic N, 24.0 % graphitic N, and 10.5 % oxidized N. Moreover, the high resolution O

1s spectra could be fitted into two peaks at ~ 532.2 and ~ 536.0 eV, corresponding to hydroxyls and absorbed water, respectively.

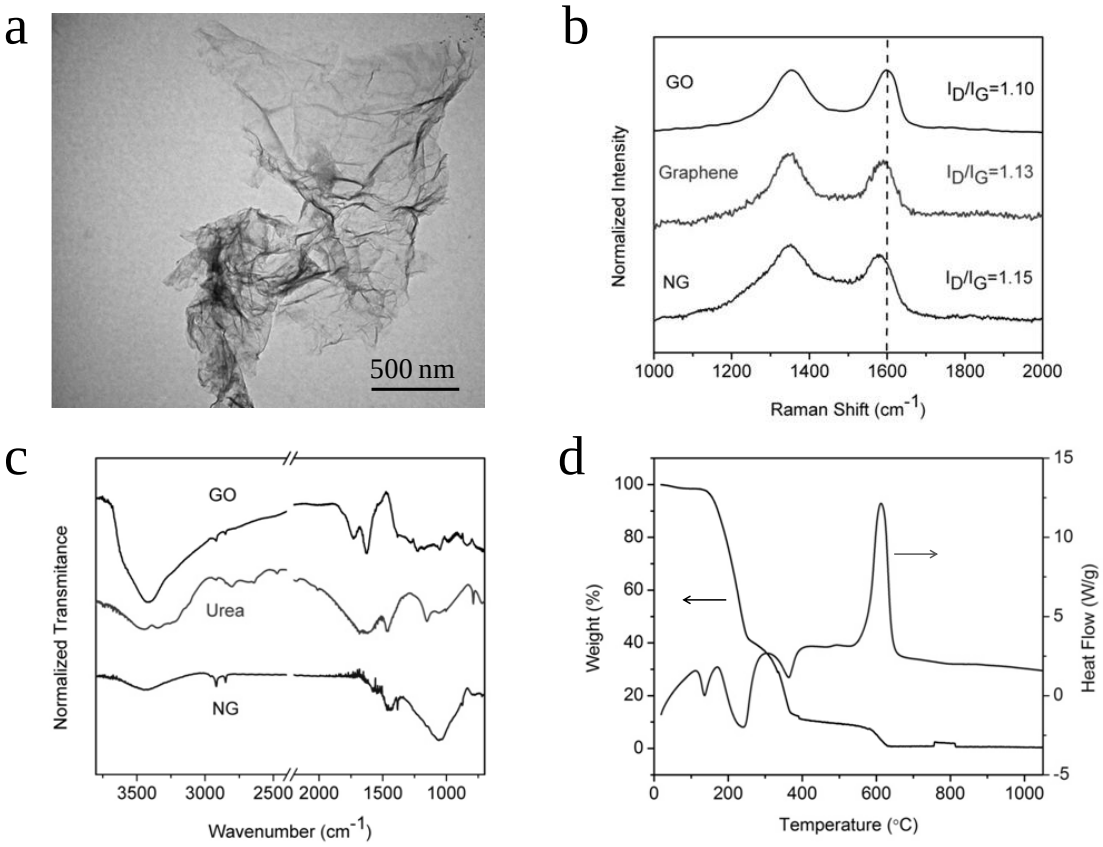

Figure 31. (a) TEM of NG-urea-800; (b) Raman spectra of GO, graphene and NG-urea-800; (d) FTIR spectra of GO, urea and NG-800; (d) SDT curve of GO-urea mixture. Reprinted with permission from [151]. Copyright 2012 Wiley.

The XPS is particularly useful to study the evolution of N functionalities during pyrolysis and gain insight into the pathway of N doping. The N precursor urea has a simple structure and only one type of N in amino groups; however the structure of resulting NG is rather complex with various N functionalities. It is found the graphitic N peak at 401.2 eV becomes increasingly obvious at higher pyrolysis temperatures (Figure 33), as a result of the reconstruction of NG structure and transformations of N functionalities. The favorable formation of graphitic N at high temperatures could be

attributed to its higher thermal stability than pyridinic N and pyrrolic N.[152] Moreover, the change of the shape of N 1s spectrum is accompanied by a gradual decrease of N content, shown in Figure 33 inset. The N content is 13.81 % at 400 °C, and slowly decreases to 10.88 % at 600 °C, 7.86 % at 800 °C and 6.70% at 900 °C.

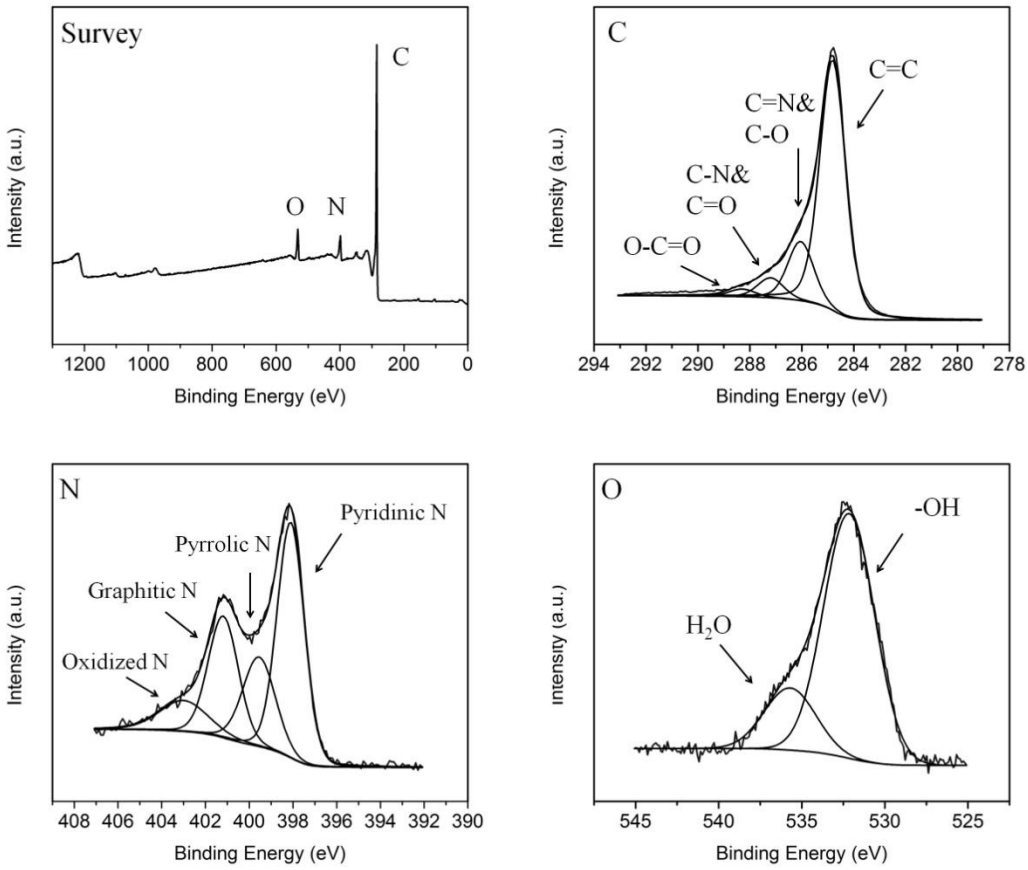

Figure 32. XPS spectra of NG-urea-800: survey spectrum and high resolution C 1s, N 1s and O 1s spectra. Reprinted with permission from [151]. Copyright 2012 Wiley.

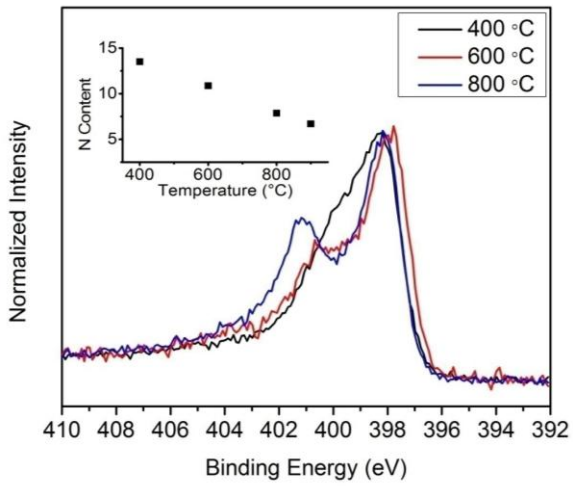

Figure 33. High resolution N 1s spectrum of NG-urea pyrolyzed at different temperatures. Inset, the N contents of NG pyrolyzed at different temperatures determined by XPS survey spectra.

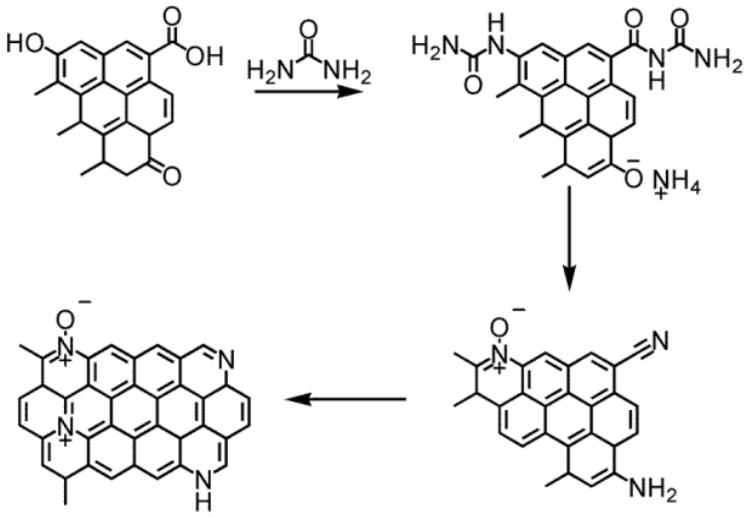

Figure 34. Schematics of GO-urea reaction during mixing and pyrolysis.

There are two possible pathways for N-doping during pyrolysis. The first pathway is via chemical reactions of urea with surface functional groups and subsequent thermal transformations during pyrolysis. For example, oxygen-containing functional group on GO (hydroxyls, carboxyls) can interact with amino groups in urea, contributing to the

incorporation of N into graphene lattice. These N probably exist on the edges in the form of pyridinic N, pyrrolic N at initial stage of pyrolysis, and then transform to graphitic N at higher temperatures.[153] This process is schematically shown in Figure 34. Another possible pathway for N-doping is that carbon nitride, produced by the decomposition of N precursors, acts as an intermediate for the formation of N dopants in NG.[154] Although the preparation of carbon nitride from urea has been reported,[155] this pathway has minor contribution here because: 1) the yield of carbon nitride from urea is very low;[150] 2) the decomposition of carbon nitride (incorporation of N into graphene) occurs below 700 °C, typical leading to a sharp drop of N content at these temperatures.[156] This is contradictory to the gradually decreased N content observed in XPS characterizations. 3) FTIR confirms the absence of signature peak for carbon nitride at ~ 810 cm^{-1}(triazine ring),[156] indicating that it is unlikely that carbon nitride is involved in this process.

4.3.1.2 GO-melamine

GO is a highly oxidized form of graphene with many O-containing moieties on the surface, such as hydroxyls, epoxies, carbonyls and carboxyls. These O-containing groups are hydrophilic and carboxyls bring in negative charges on the GO surface. As a result, GO can be well dispersed in water, as seen in Figure 35. After adding melamine, clear agglomeration occurs, indicating a strong interaction between melamine and GO (Figure 35). The nature of GO-melamine interaction could be hydrogen bonding between amine group in melamine and O-containing groups in GO, ionic bonding between protonated amines and carboxyls, or π-π interaction between unoxidized area in GO and triazine rings.[157, 158] The fact that the colloidal GO dispersion is destabilized by

adding melamine indicates the existence of ionic bonding that compensates the surface negative charge on GO. The strong interaction between GO and melamine allows the formation of a homogenous GO-melamine composite after drying. As a result, a more efficient doping is expected compared to the previously reported mechanical mixing method.[159]

To monitor the chemical reaction during pyrolysis, the thermal profile of pyrolyzing GO-melamine mixture was recorded in SDT in nitrogen atmosphere. As shown in Figure 36, the weight loss at ~ 200 °C is due to the decomposition of labile O-containing groups in GO. There is a significant weight loss between 300-360 °C accompanied by an endothermic peak centered at 348 °C that signifies the sublimation and condensation of melamine. A gradually weight loss is observed between 400-600 °C, possible due to further condensation of melamine and de-oxygenation of GO. No obvious heat flow is seen in this temperature range. The complete decomposition of graphitic structure and carbon nitride was observed at ~ 660 °C with a large exothermic peak. The extensive degradation of carbon nitride is consistent with the previous study on thermal behaviour of melamine.[156]

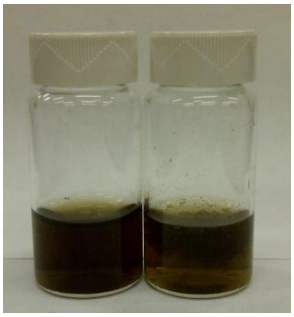

Figure 35. 0.5 mg/mL GO dipersion in water before (left) and after (right) adding 2.5 mg/mL melamine.

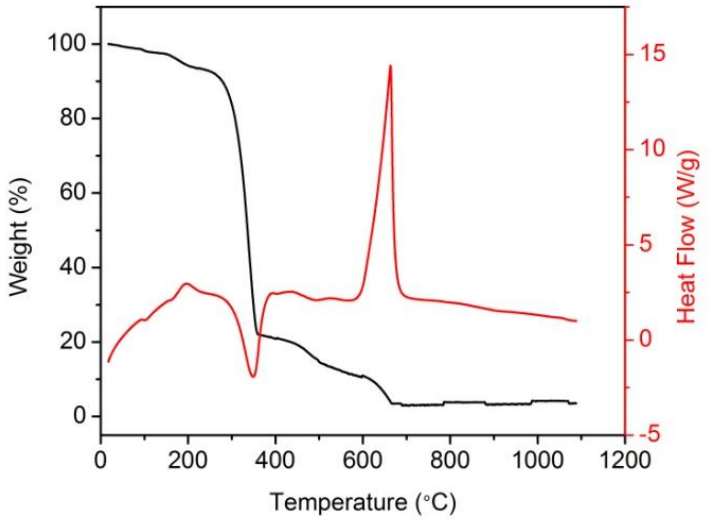

Figure 36. The SDT profile of GO-melamine in nitrogen atmosphere at a ramping rate of 20 °C/min.

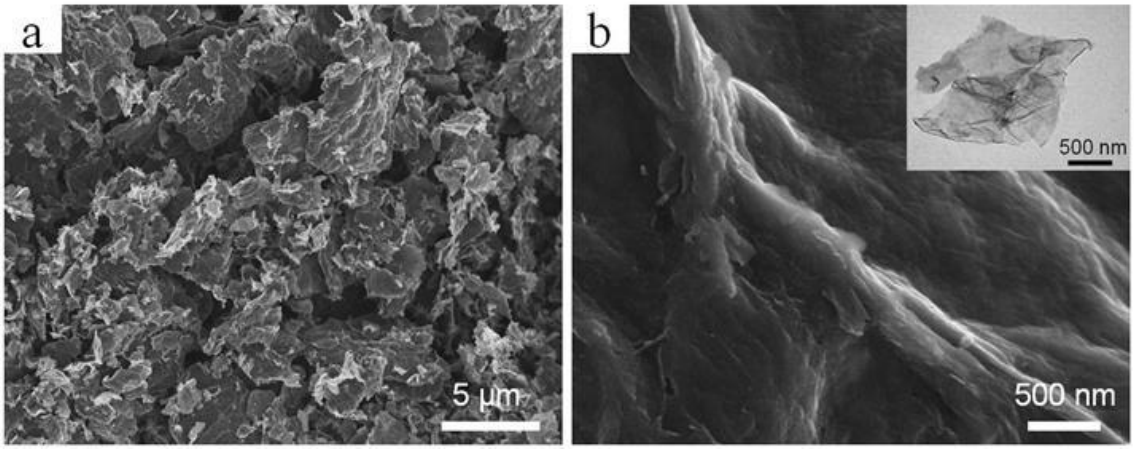

Figure 37. SEM images of NG-melamine-900 at (a) low magnification and (b) high magnification. (Inset, a TEM image of NG-melamine-900). Reproduced from [154] with permission from the PCCP Owner Societies.

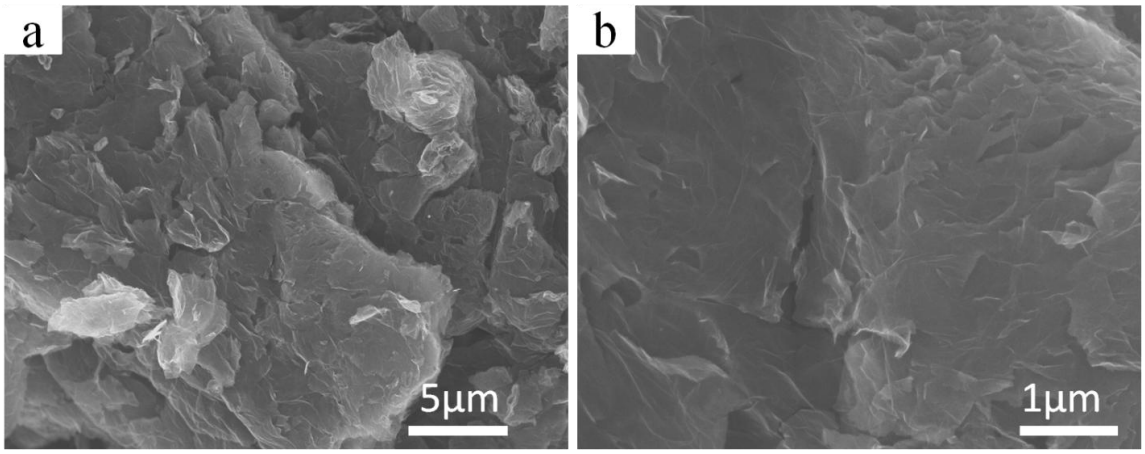

Figure 38. SEM images of graphene at (a) low magnification and (b) high magnification.

Figure 37 shows the morphology of NG-melamine-900. As seen in the SEM image (Figure 37a), the NG-melamine-900 contains high aspect ratio micron-sized flakes, as well as particles with hundreds of nanometers in size. The flake-like NG-melamine-900 is similar to the stacked GO sheets, yet in contrast to pyrolyzed GO which became fully exfoliated at 900 °C (Figure 38). The driving force for GO exfoliation is the high pressure generated by the decomposition of O-containing groups, which produces gaseous molecules faster than their diffusion rate.[43] Exfoliation of GO occurs as soon as this pressure exceeds the van der Waals force between GO sheets.[43] However, after being intercalated by melamine, GO sheets are no longer tightly stacked and thus the high pressure cannot build up. Consequently, no exfoliation is observed for NG-melamine-900. Moreover, the zoom-in image shown in Figure 37b reveals the highly wrinkled nature of NG-melamine-900. The wrinkles on NG-melamine-900 are also observed in TEM (Figure 37b inset).

The N doping in NG-melamine-900 could be directly visualized in energy-filtered TEM images. As seen Figure 39, a uniform distribution of N heteroatom on graphene

lattice is observed. The N content varies between ~ 6-9% among different NG-melamine-900 sheets.

The chemical structure of NG-melamine-900 was investigated using FTIR, as shown in Figure 40a. A complete assignment of peaks is listed in Table 2. In the spectrum of GO, a sharp peak at ~ 1387 cm^{-1}, a signature for -OH groups, is also present in NG-melamine-900, indicating that the hydroxyl is one of the residual O-containing groups in NG-melmaine-900. Four peaks above 3000 cm^{-1} are found in the spectra of melamine, which could be attributed to amino groups. After pyrolysis at 900 °C, these peaks disappear, indicating a complete removal of amino groups. The elimination of ammonia was reported as a pathway for the condensation of melamine.[156] Furthermore, the peaks at ~ 1030 and ~ 810 cm^{-1} are from C-N and triazine rings in melamine and are also seen in the NG-melamine-900, evidencing the existence of melamine-like moieties in NG-melamine-900.

Figure 40b shows the Raman spectra of GO, graphene and NG-melamine-900. After pyrolysis, the I_D/I_G is 1.0 for GO, and increases to 1.12 for both graphene and NG-melamine-900. The increase of I_D/I_G upon GO reduction is normal and could be attributed to the generation of edges and holes. Furthermore, the G peak position shifts from 1599 cm^{-1} for GO to 1589 cm^{-1} for graphene, indicating the restoration of conjugated structure upon pyrolysis. Interestingly, the G peak of NG-melamine-900 further shifts to ~ 1580 cm^{-1}. The downshift of G peak in NG is consistent with the previous report, signifying the successful N doping.[160]

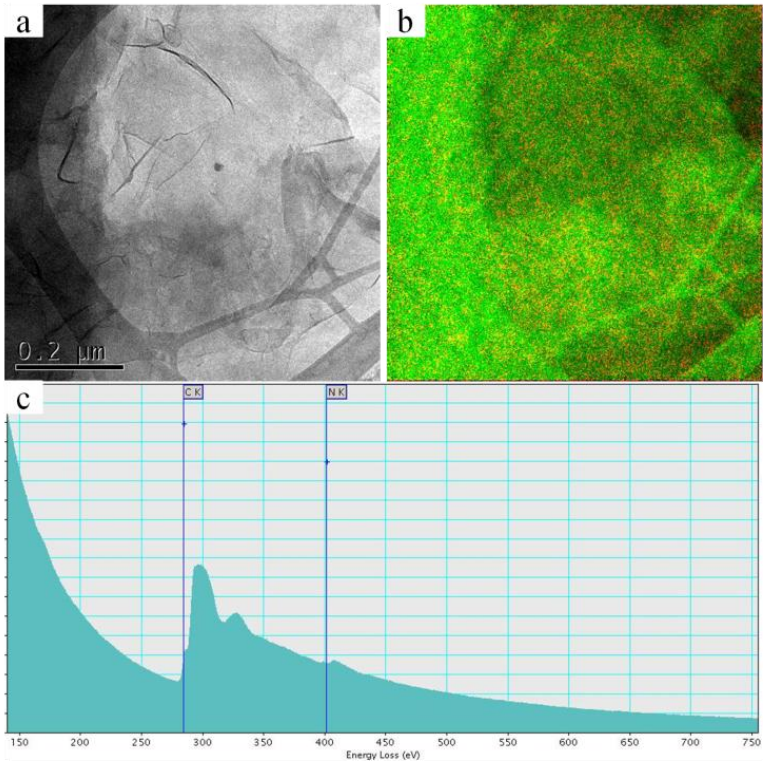

Figure 39. (a) Bright field TEM image and (b) Energy-filtered TEM image of NG-melamine-900. Green background and red dots represent C and N respectively. (c) EELS acquired from the area shown in (a). Reproduced from [154] with permission from the PCCP Owner Societies.

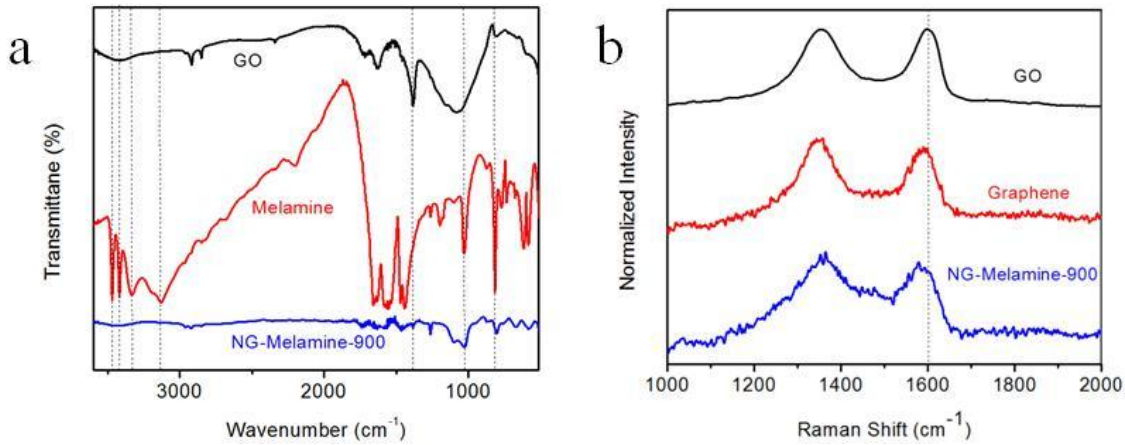

Figure 40. (a) FTIR spectra of GO, melamine and NG-melamine-900 and (b) Raman spectra of GO, graphene and NG-melamine-900. The dash lines indicate the positions of peaks that are specifically discussed. Reproduced from [154] with permission from the PCCP Owner Societies.

Table 2. Peak assignment of FTIR spectra of GO and melamine.[110, 156]

Peak position wavenumber (cm^{-1})	Assignment
GO	
3420 (broad)	O-H , absorbed water
1724	C=O (carboxylic and ketone)
1637	absorbed water
1582	unoxidized aromatic region
1382	O-H
1076 (broad)	C-O (phenolic, epoxy, and ketone groups)
Melamine	
3470, 3426, 3338, 3130, 1650	NH_2
1562, 1468, 1431, 815	1,3,5-s-triazine ring
1030	C-N

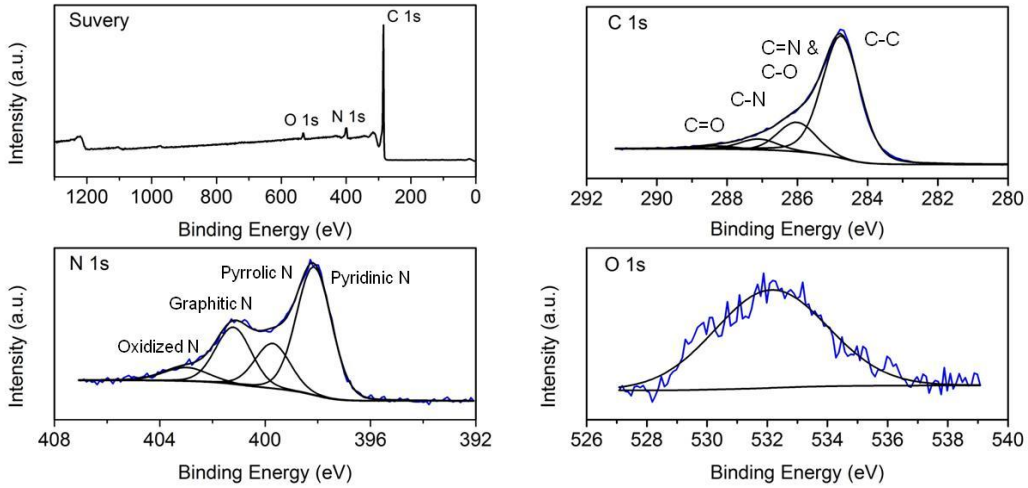

Figure 41. XPS survey and high resolution C 1s, N 1s, O 1s spectra of NG-melamine-900. Reproduced from [154] with permission from the PCCP Owner Societies.

The XPS is used as a primary tool to characterize the chemical composition of NG. Figure 41 shows the XPS spectra of NG-melamine-900. The survey spectrum clearly indicates the existence of N in NG-melamine-900, estimated to be 8.05 %, as well as some residual O-containing groups. The high N content is similar to that determined by EELS. The high resolution C 1s peak is centered at 284.7 eV, typical for the sp^2 graphitic carbon, and has a tail at higher binding energy as a result of carbon atoms bonded to heteroatoms (O and N). Peak deconvolution is carried out to fit the C 1s spectra into four

components, which are sp^2 C (284.7 eV), C-O/C=N (286.0 eV), C-N (287.2 eV) and C=O (288.3 eV).[161] It is found that 74.1 % C is from graphite structure, 17.9 % from C-O/C=N bonds, 6.0 % from C-N and 1.9 % from C=O bonds. The N 1s spectrum of NG-melamine-900 can be deconvoluted into four components at 398.1, 399.6, 401.2, and 403.0 eV, corresponding to pyridinic N, pyrrolic N, graphitic N, and oxidized N respectively.[152] The percentage of graphitic N is up to 24.6 %, which could be attributed to the structural similarity between melamine and graphitic N. The existence of pyrrolic N, which is not present in precursor melamine, is probably a product of the reaction between GO and amino groups in melamine. Furthermore, the O 1s spectrum was reasonably fitted into a single peak at 532.1 eV, indicating that hydroxyls, probably in a phenol form, are major O-containing groups in NG-melamine-900.[90] This is consistence with the FTIR results. The high thermal stability of phenol was also reported recently.[162]

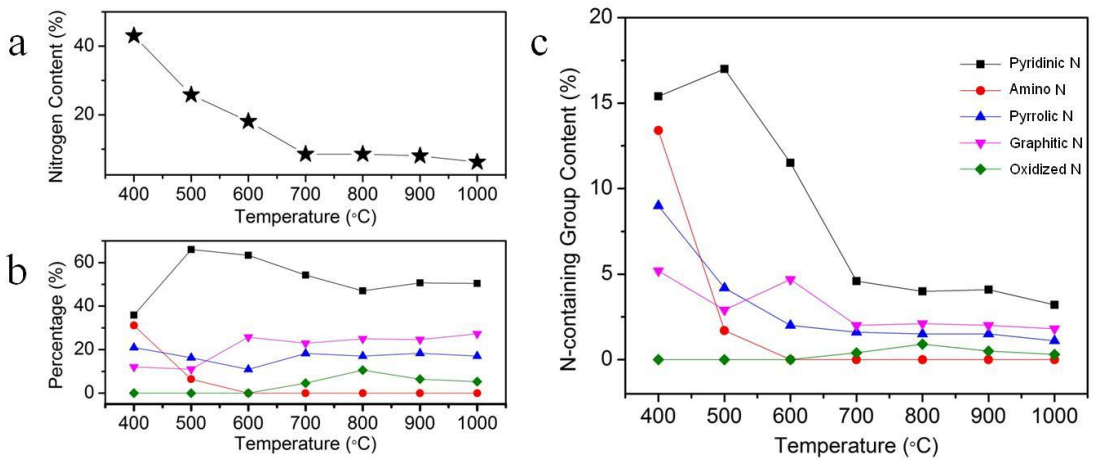

Figure 42. Evolution of N-containing groups in NGs from XPS characterizations: (a) total N content (b) percentage of each N-containing group and (c) N-containing group content as a function of pyrolysis temperature. Lines are for visual aids. Reproduced from [154] with permission from the PCCP Owner Societies.

It is found that the pyrolysis temperature is the primary factor determining the structure of NGs. The evolution of N-containing groups upon pyrolysis is studied by analyzing a series of XPS spectra of NG-melmaine. The total N content is obtained from XPS survey spectrum and plotted in Figure 42a as a function of pyrolysis temperature. A high N content of 43.0% is found in NG-melamine-400, indicating an initial stage of the condensation of melamine and formation of carbon nitride. This is consistent with the SDT profile which gives a temperature of ~348 °C for the sublimation and condensation of melamine. The N content continuously decreases when increasing the temperature to 700 °C, due to further condensation of melamine by deammonation reaction. However, it is found that the N content of NG-melamine-700, NG-melamine-800 and NG-melamine-900 shows similar values of 8.55%, 8.53%, and 8.05%, respectively. The fact that N content does not vary much between 700 - 900 °C likely results from that at temperatures higher than 700 °C, condensed melamine fully incorporates into the graphitic structure and become thermally stable. At a higher temperature of 1000 °C, the N content starts to drop to 6.24 %.

There are two possible pathways for N-doping during pyrolysis. The first pathway is that carbon nitride, produced by decomposition of melamine, acts as an intermediate for the formation of N dopants in NG. Another pathway is via chemical reactions of melamine with surface functional groups and subsequent thermal transformations during pyrolysis. To elucidate the doping mechanism for pyrolysis of GO-melamine, the following controlled experiments were carried out: 1) GO-melamine mixture was washed by copious water before pyrolysis to remove excessive melamine. It was found that the N content in resulting NG is significantly lower (< 3 %), indicating that excessive

melamine, which are critical for the formation of carbon nitride, plays a role in doping process. However, we found that further increase the melamine/GO ratio to 10 does not lead to a higher N content in NG, probably because only carbon nitride adjacent to graphene could be converted to NG. 2) The GO-melamine was pre-reduced before pyrolysis (300 °C in H_2/Ar) to remove oxygen-containing functional groups that can react with melamine. The resulting NG from reduced GO-melamine has a N content of 7.41 %, which is closed to NG reported in main text, indicating the minor role of oxygen-containing functional groups in the doping process. Therefore, we conclude that the conversion of carbon nitride to NG is a dominate pathway for N-doping.

To study the transformation of N-containing groups during pyrolysis, the percentage of different N-containing groups is obtained from XPS N 1s spectra and plotted in Figure 42b. It is found that the percentage of N-containing groups shows dramatic changes at temperatures below 700 °C as a result of transformation reactions between different N functionalities, and becomes relatively stable at higher temperatures. The absolute N-containing group content is calculated and shown in Figure 42c. The following points can be addressed to gain insight into the chemical reactions during pyrolysis: (1) amino N dramatically decreases from 13.4 % in NG-melamine-400 to 1.7 % in NG-melmaine-500 and disappears at 600 °C and higher, which is consistent with the FTIR result that ammonia peaks are only observed in NG-melamine-400 but not in other NG samples (> 400 °C) (Figure 43). The rapid decrease of amino N confirms that condensation of melamine is through elimination of ammonia, which is completed at temperatures below 600 °C. (2) pyridinic N, a major N-containing group in NG, increases slightly between 400-500 °C, from 15.4 % in NG-melamine-400 to 17 % in NG-

melamine-500, and meanwhile, pyrrolic N drops from 9 % in NG-melamine-400 to 1.2 % in NG-melamine-500. Thus, it is possible that some of pyrrolic N becomes pyridinic N (or graphitic N) at 400-500 °C. This is in contrast to previous report that pyrrolic N is stable until 600 °C.[152] (3) The percentage of N functionalities in NG, especially the high content of graphitic N, is significantly different from typical carbon nitride prepared from melamine,[163] confirming that N is effectively doped into the graphitic lattice instead of forming carbon nitride clusters on graphene.

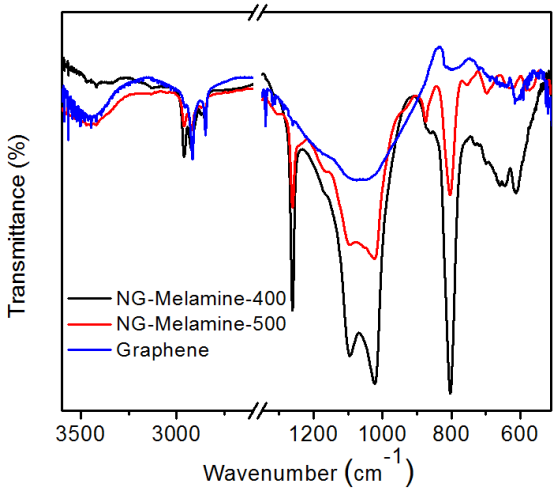

Figure 43. FTIR spectra of NG-melamine-400, NG-melamine-500 and graphene.

4.3.1.3 GO-PPy

GO-PPy was synthesized via an in-situ polymerization of pyrrole in a GO solution. The PPy grow preferentially on the surface of GO sheet due to the electrostatic interaction between positively charged pyrrole and negatively charge GO, and the π-π interaction between pyrrole ring and conjugated segment in GO. As a result of this strong interaction, GO acts as a structuring agent that PPy forms a thin layer on GO (Figure 44a), which is in contrast to the granular-like ppy obtained without adding GO (Figure Figure 45). The incorporation of PPy also changes the stacking of GO sheets, from a 2D

closely stacked layer to a 3D porous structure (Figure 44b). This phenomenon has also been found in the preparation of GO-conducting polymer hydrogel, which was attributed to the increased ratio of bonding/repulsive forces that stabilizes the GO hydrogel network: by adding conducting polymers such as PPy, the negative charges on GO is neutralized that weaken the electrostatic repulsive force, and one polymer chain can interact with multiple GO sheets to strengthen the bonding force.[164, 165]

During the pyrolysis of GO-PPy, the PPy decomposes and re-constructs, forming NG that attaches on reduced GO surface. As a result, clean multi-layer graphene sheet was observed after pyrolysis (Figure 44c). The semi-transparency of NG-PPy-900 sheet under electron beam indicates a very small thickness. Interestingly, the 3D structure was largely preserved after pyrolysis at 900 °C, as seen Figure 44d, which could be attributed to the open porous structure that facilitates the diffusion of gaseous species generated by the decomposition of labile functional groups in GO-PPy. In comparison, the exfoliation of GO occurred when closely packed GO was pyrolyzed at the same temperature (Figure 38). The 3D NG-PPy-900 architecture gives rise to a high portion of meso- and micro-pores, revealed by the nitrogen adsorption/desorption isotherm which shows a type-IV curve with an H2-type of hysteresis loop (Figure 46). Brunauer-Emmett-Teller (BET) surface area of NG-PPy-900 is measured to be ~370 m^2/g and the averaged pore diameter is ~ 5.3 nm (Figure 46 inset). Moreover, the XRD pattern of NG-PPy-900 shown in Figure 47 has a very broad peak centered at ~ 26.0 °, indicating the partially ordered stacking of NG with an interlayer spacing of 0.342 nm that is close to 0.335 nm for graphite.

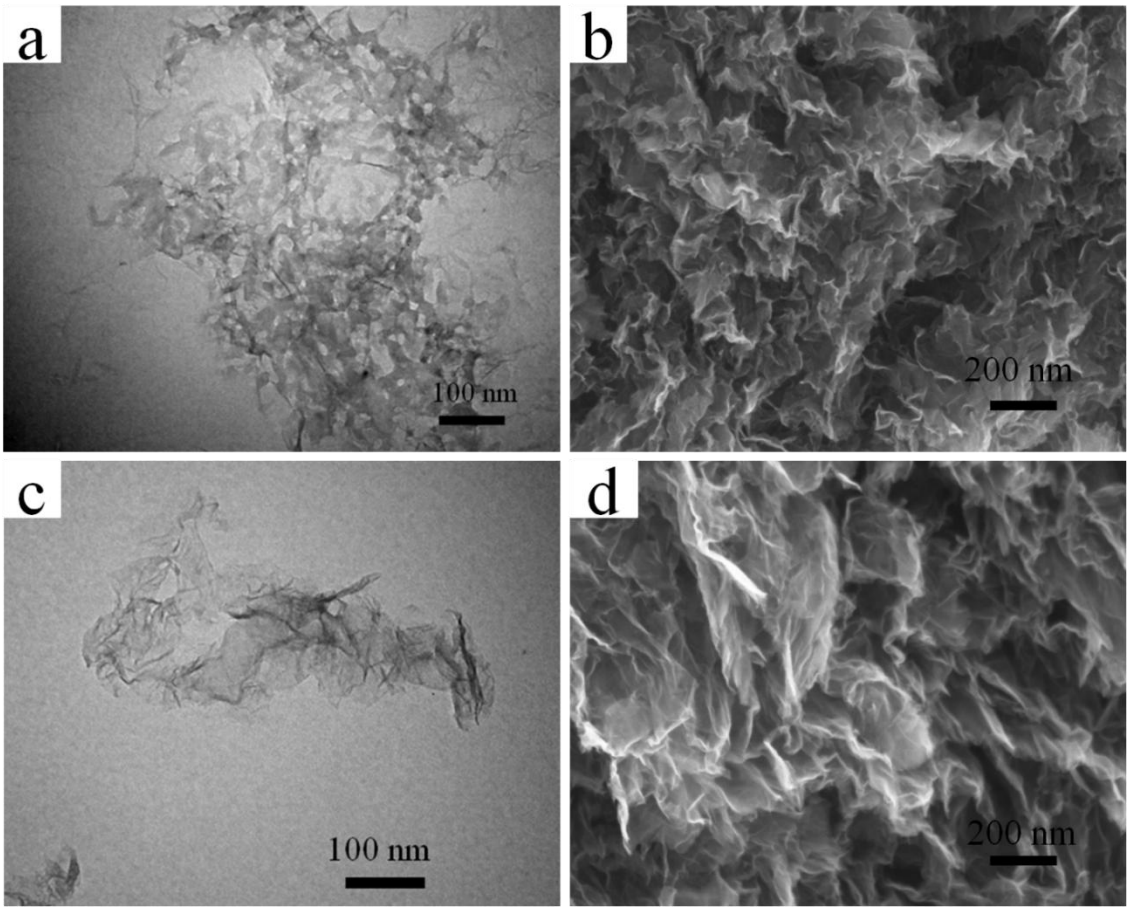

Figure 44. TEM (a) and SEM (b) images of GO-PPy; TEM (c) and SEM (d) images of NG-PPy-900. Reprinted with permission from [126]. Copyright 2013 Elsevier.

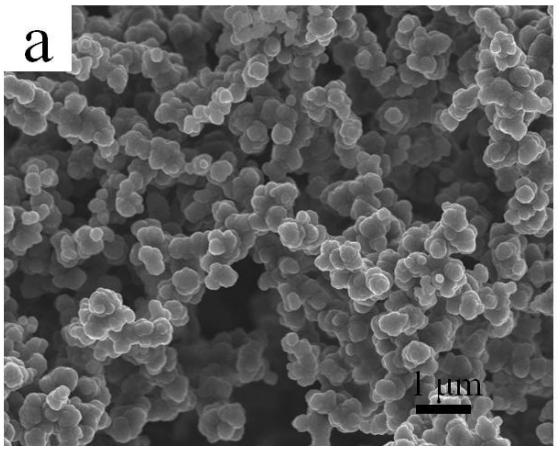

Figure 45. SEM images of the PPy synthesized without adding GO.

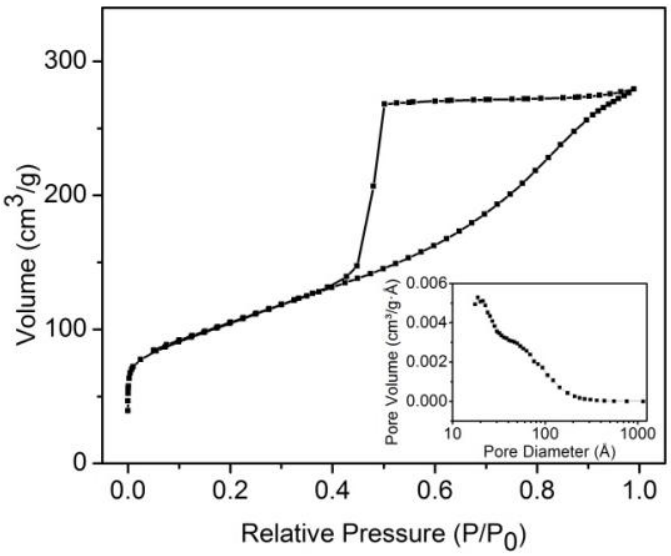

Figure 46. Nitrogen adsorption-desorption isotherm of NG-PPy-900; inset is the pore size distribution calculated from the adsorption branch on the basis of the Barrett-Joyner-Halenda (BJH) model. Reprinted with permission from [126]. Copyright 2013 Elsevier.

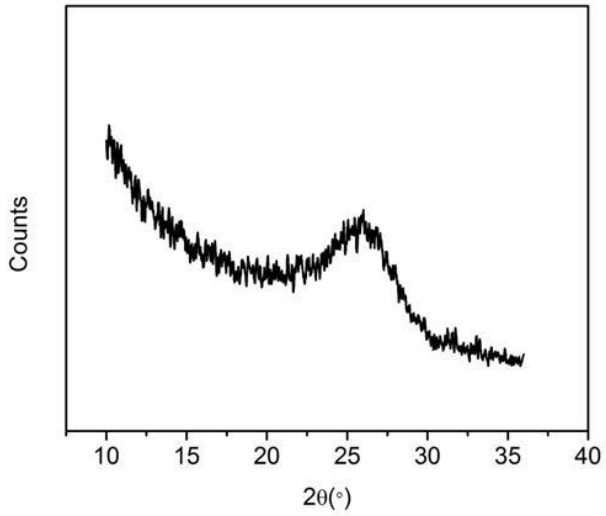

Figure 47. XRD pattern of NG-PPy-900.

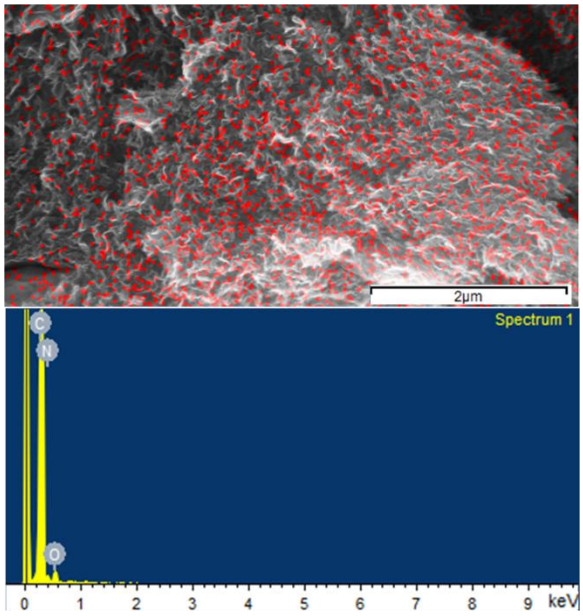

Figure 48. N mapping of NG-PPy-900 and corresponding EDS spectrum; red dotes indicate the N doped sites. Reprinted with permission from [126]. Copyright 2013 Elsevier.

The N doping in NG-PPy-900 could be directly visualized from the N elemental mapping result by energy dispersive spectrum (EDS). As seen in Figure 48, the N heteroatoms distribute uniformly throughout the surfaces of NG-PPy-900. The chemical composition of NG-PPy-900 was further characterized by XPS. As shown in Figure 49a, the survey spectrum of NG-PPy-900 reveals the presence of C, O, and N without any other impurities and the N content is found to be ~ 2-3 at% from the spectra collected at different locations. High resolution XPS was used as a primary tool to investigate the NG structure. The asymmetric high resolution C 1s peak has a tail at high binding energies indicating that a large portion of C atoms are connected with N and O heteroatoms (Figure 49b). Peak decovolution reveals four components at 284.7, 285.8, 287.2, 288.4 eV in the C 1s spectrum of NG-PPy-900. In addition, the high resolution O 1s spectrum indicates that the O atoms exist mainly in the form of C=O and C-OH (Figure 49b).

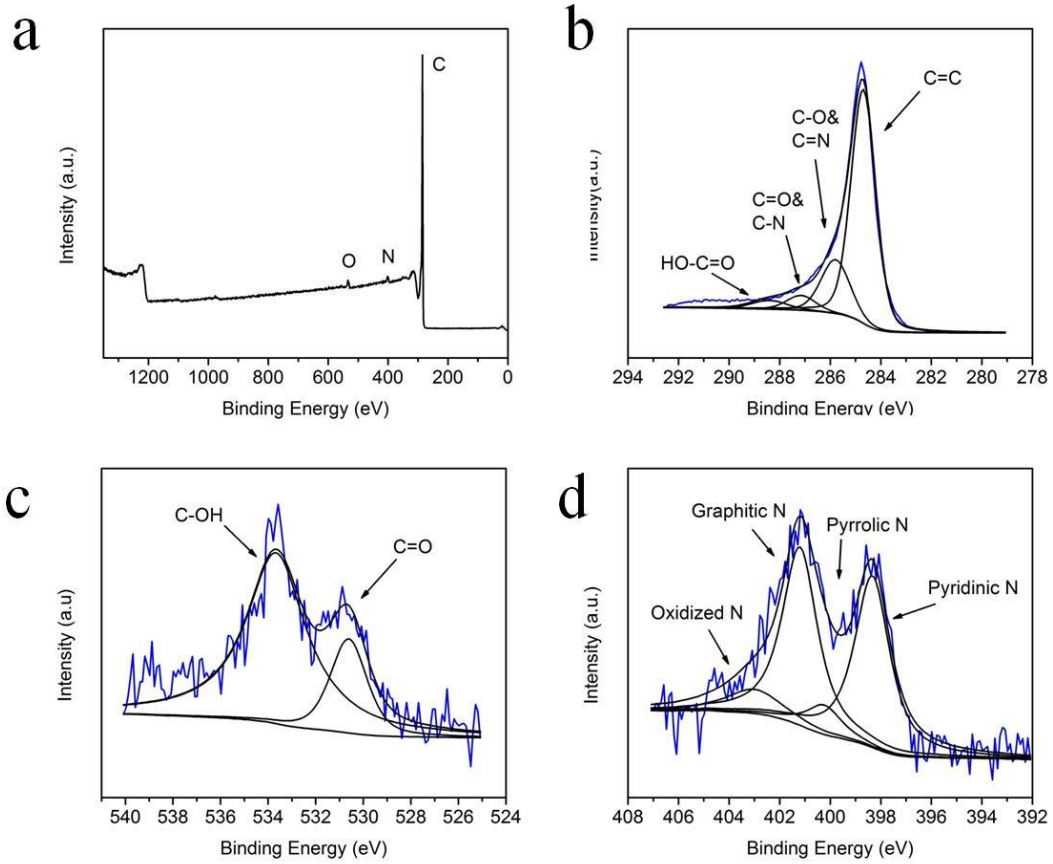

Figure 49. XPS (a) survey spectrum and high resolution (b) C 1s, (c) O 1s (d) N 1s spectra of NG-PPy-900. Reprinted with permission from [126]. Copyright 2013 Elsevier.

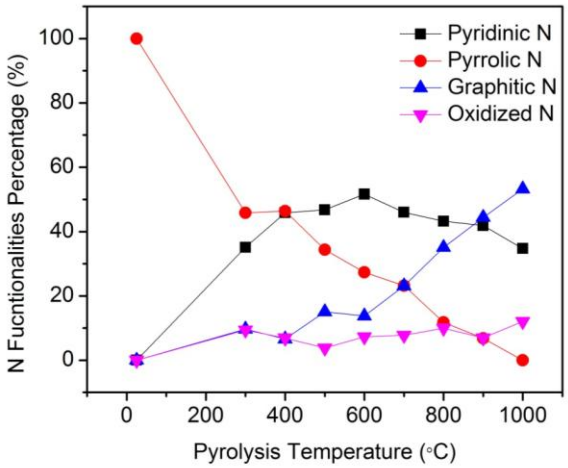

Figure 50. Evolution of N functionalities in NG-PPy with pyrolysis temperature. Reprinted with permission from [126]. Copyright 2013 Elsevier.

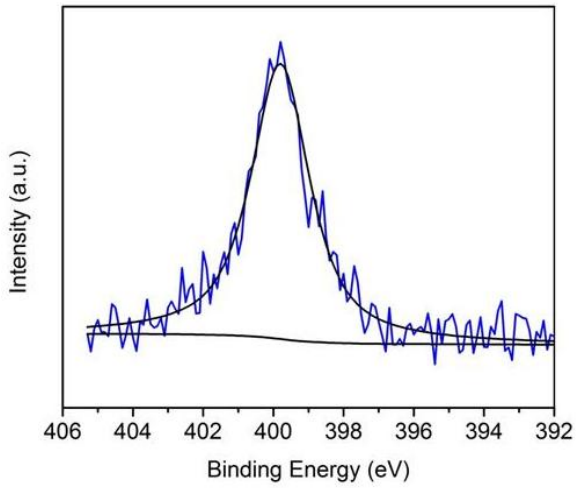

Figure 51. XPS high resolution N 1s spectrum of GO-PPy.

The high resolution N 1s spectrum is very useful to probe the nature of N functionalities in NG. Peak deconvolution shown in Figure 49d suggests four types of N functionalities in NG-PPy-900, which are pyridinic N (298.3 eV), pyrrolic N (400.2 eV), graphitic N (401.2 eV), and oxidized N (403.0 eV). The NG-PPy-900 has ~ 44% graphitic N, which is much higher than those (~20 %) reported in previous works where melamine and urea were used as the N source.[154, 166] This high percentage of graphitic N in NG-PPy-900 may be attributed to the structure of the N source PPy; the N atoms in PPy can be easily converted to graphitic N. To investigate the transformation of N functionalities during pyrolysis, the percentages of N functionalities in NGs prepared at different temperatures are plotted in Figure 50. The entire N in the initial GO-PPy is in the form of pyrrolic N as a result of the structural regularity of PPy monomers (Figure 51). As the GO-PPy being heated to elevated temperatures (>300 °C), the pyrrolic N percentage decreases while the pyridinic N percentage increases monotonically, indicating a transformation from pyrrolic N to pyridinic N. However, the pyridinic N percentage starts to drop at temperatures greater than 600 °C with a simultaneously

increase of graphitic N percentage, implying the transformation of pyridinic N to graphitic N. Moreover, it is also possible that pyrrolic N directly transforms to graphitic N at temperatures above 500 °C. Therefore, the high pyrrolic N content in the starting GO-PPy could be a major reason that such a high graphitic N content was obtained in NG.

The chemical reaction during pyrolysis and the structural evolution of NG were also investigated using SDT, Raman and FTIR spectroscopy. It is found from the SDT curve (Figure 52) that the decomposition of PPy starts at ~ 270 °C, leading to a gradual weight loss and a broad exothermal peak centered at 300 °C. This extensive chemical reaction above 270 °C corresponds well with the evolution of N functionality determined by XPS. The Raman spectrum of graphene has been used to evaluate the structural disorder. As seen in Figure 53a, the I_D/I_G ratio is 1.10 for as prepared GO-PPy, and decreases to ~ 0.94-0.97 for NGs pyrolyzed at 300-600 °C, which is indicative of thermal reduction of GO and the restoration of the conjugated system. However, the I_D/I_G ratio starts to increase at higher temperatures, reaching 1.11 for NG-PPy-900 and 1.17 for NG-PPy-1000, due probably to the decomposition of epoxy and hydroxyl groups that could cause cracking of the in-plane C=C and the generation of more defects. Figure 53b shows the FTIR spectra of GO-PPy and NGs pyrolyzed at different temperatures, which have broad and overlapped peaks suggesting the complexity of their chemical structures. The characteristic peaks of PPy ring at ~1542 and ~ 1466 cm^{-1} are observed in the spectrum of NG-PPy-300, but slowly diminished in those of NGs pyrolyzed at greater temperatures, indicating the break of PPy rings during pyrolysis. Moreover, the peaks at ~ 1580 and ~ 1384 cm^{-1} are resulted from C=C and O-H groups respectively.[82, 110]

The broad peaks at 1300-800 cm^{-1} could be assigned to C-N and C-O groups. [82, 154, 166]

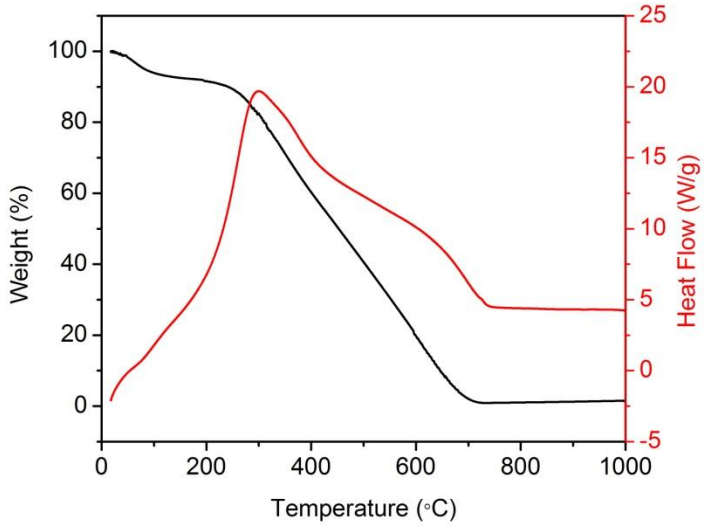

Figure 52. SDT curve of PPy in nitrogen atomsphere with a heat rate of 20 °C/min.

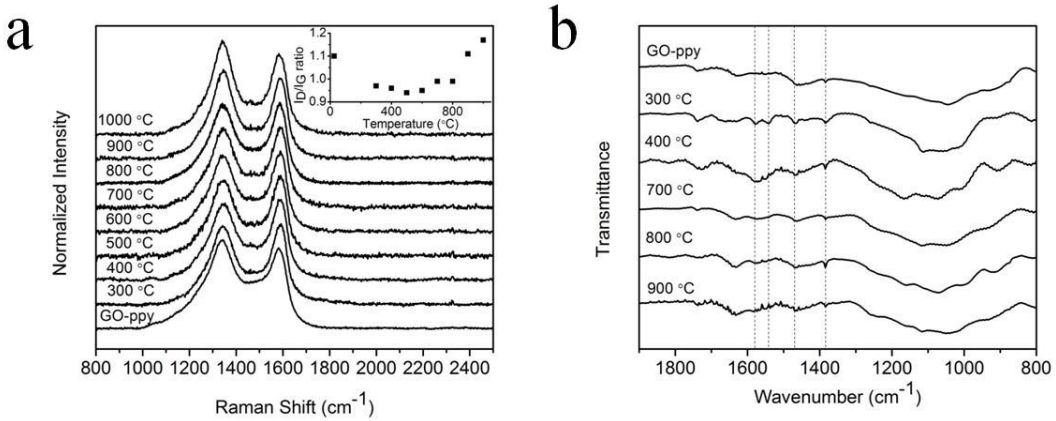

Figure 53. (a) Raman spectra of NG-PPys prepared at different temperatures (inset, I_D/I_G ratio of NGs prepared at different temperatures). (b) FTIR spectra of NG-PPys prepared at different temperatures. The transmittances were normalized to the strongest peak.

4.3.1.4 GO-PANI

GO-PANI was synthesized via an in situ polymerization reaction, where aniline monomer was polymerized in an acidic GO solution using ammonium persulfate as the

catalyst. The GO acts as a structuring agent so that a uniform layer of PANI was coated on GO sheet (Figure 54a). In comparison, PANI nanorods were obtained without adding GO (Figure 55). The GO-PANI sheets stack into a 3D porous structure as a result of the introduction of PANI (Figure 54b), which changes the attractive/repulsive force ratio between GO sheets.[164, 165] This phenomenon has been discussed in previous studies on GO-conducting polymer hydrogels.[164, 165] Clean multi-layer graphene with lots of wrinkles was produced after pyrolysis, as shown in Figure 54c. The semi-transparent nature of NG-PANI-1000 under TEM observation indicates a small thickness. The SEM image shown in Figure 54d reveals that the 3D assembly of NG-PANI-1000 was largely preserved after pyrolysis. The 3D architecture leads to a high portion of meso- and micro-pores. Figure 56 shows the nitrogen adsorption/desorption isotherm of NG-PANI-1000, which has a type-IV curve with an H2-type of hysteresis loop.[167] The BET surface area of NG-PANI-1000 is measured to be ~377 m^2/g with an average pore diameter of ~ 11.5 nm (Figure 56 inset).The XRD pattern of NG-1000 shown in Figure 57 has a broad peak at ~ 26.2 °, corresponding to an inter-layer spacing of 0.340 nm that is close to 0.335 nm for graphite.

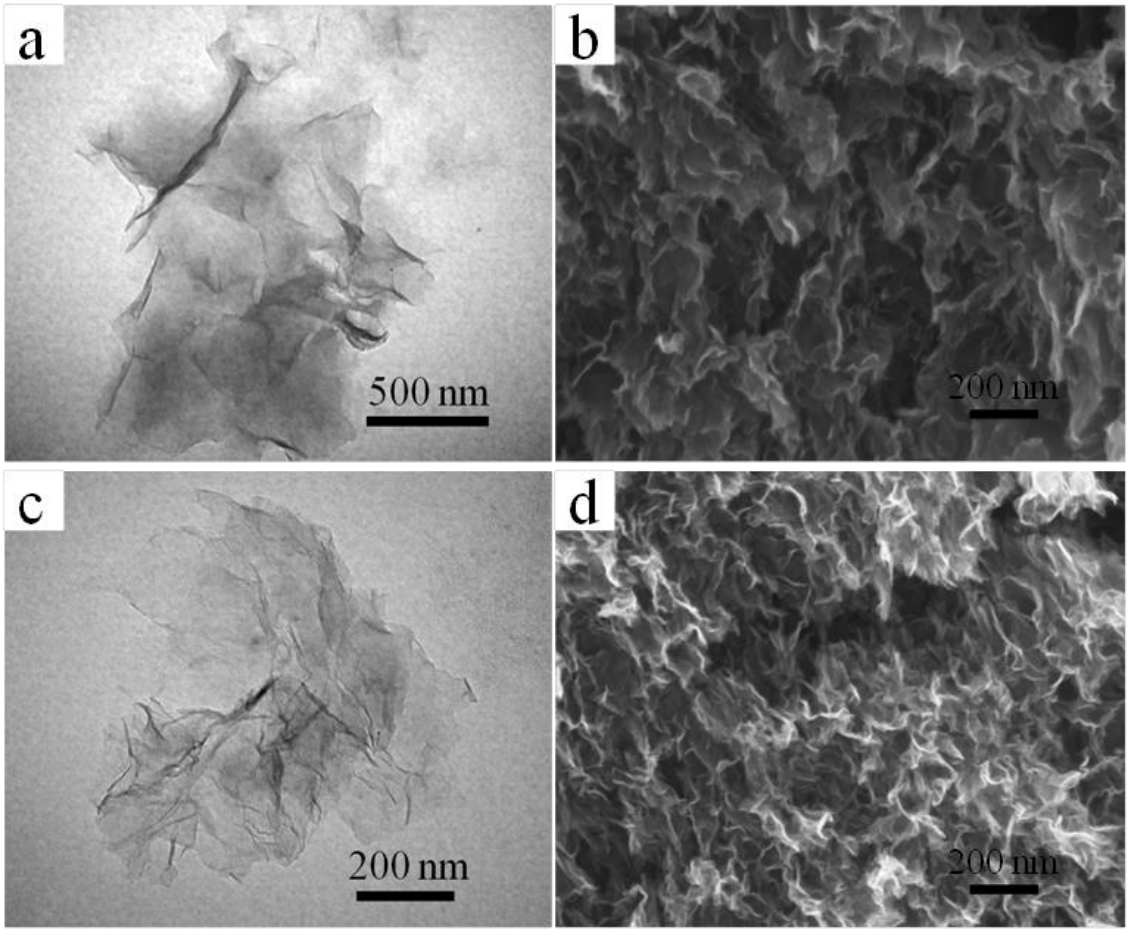

Figure 54. (a) TEM and (b) SEM image of GO-PANI; (c) TEM and (d) SEM image of NG-PANI-1000. Reprinted with permission from[168]. Copyright 2013 Elsevier.

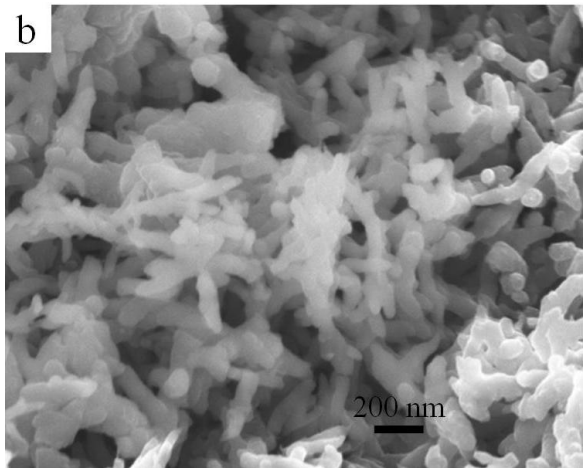

Figure 55. SEM image of PANI synthesized without adding GO.

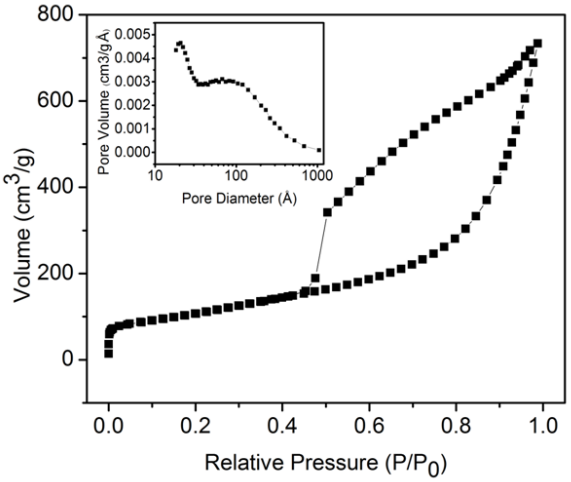

Figure 56. Nitrogen adsorption-desorption isotherm of NG-1000; inset is the pore size distribution calculated from the adsorption branch on the basis of the Barrett-Joyner-Halenda (BJH) model. Reprinted with permission from[168]. Copyright 2013 Elsevier.

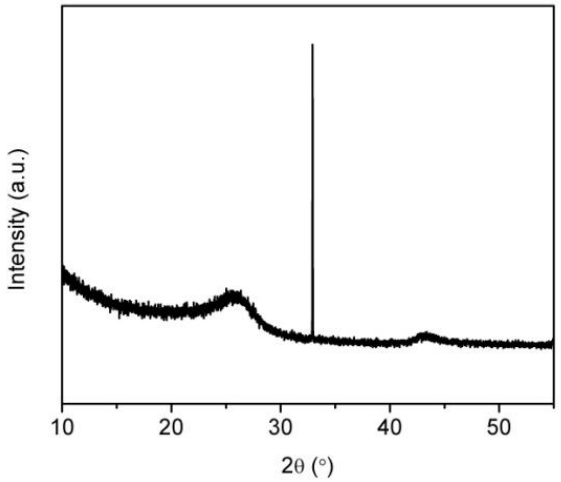

Figure 57. XRD pattern of NG-PANI-1000. The sharp peak at ~ 33 º results from the Si substrate.

XPS is used to probe the chemical composition and structure of NGs. As shown in Figure 58a, the survey spectrum of NG-PANI-1000 reveals the presence of C, N and O without any other impurities. The N content is found to be 2.4 at%. The successful N-doping was also confirmed by elemental mapping using energy dispersive spectroscopy (Figure 59). The high resolution N 1s spectrum was used primarily to determine the

bonding configurations of N atoms in NG. As seen in Figure 58a inset, the peak deconvolution suggests four components in NG-PANI-1000 centered at 398.2, 400.0, 401.0, and 403.0 eV, corresponding to pyridinic N, pyrrolic N, graphitic N and oxidized N, respectively. [169, 170] The graphitic N percentage is as high as 51.1%, which is vital to high catalytic activity. In addition, the high resolution C 1s spectrum shows a peak centered at 284.7 eV, and a tail at higher binding energies that is caused by hetero N and O atoms in NG (Figure 58b). Moreover, the deconvolution of high resolution O 1s spectrum suggests that the O atoms exist in –OH groups and absorbed water molecules (Figure 58c).

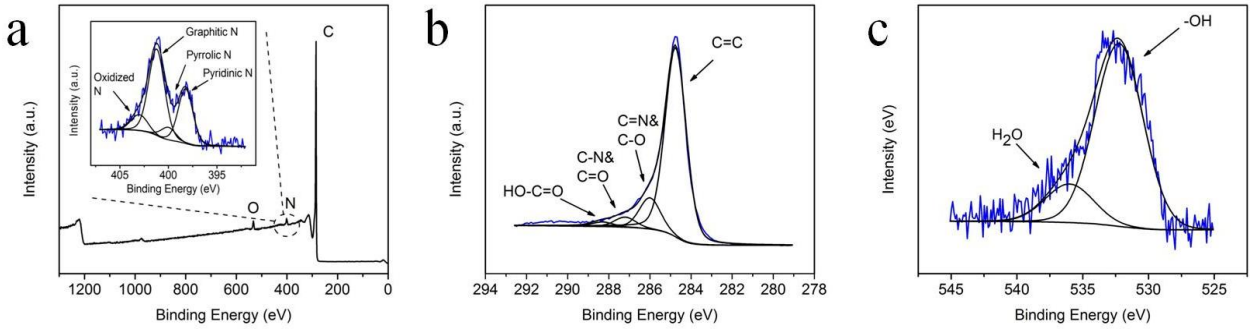

Figure 58. XPS (a) survey spectrum of NG-PANI-1000 and high resolution N 1s spectrum; high resolution (b) C 1s and (c) O1s spectra of NG-PANI-1000. Reprinted with permission from[168]. Copyright 2013 Elsevier.

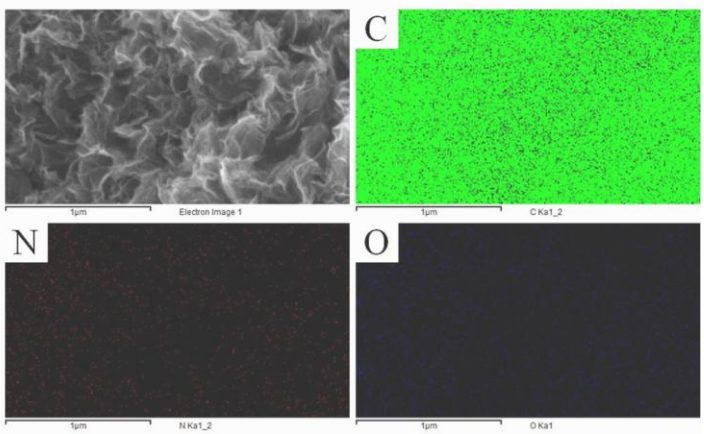

Figure 59. Energy dispersive spectrum of NG-PANI-1000.

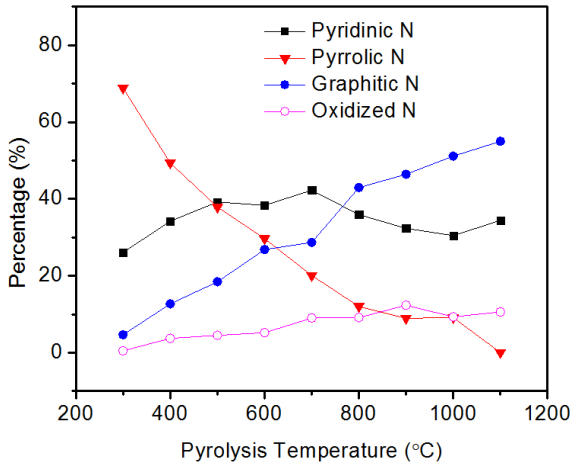

Figure 60. Evolution of N functionalities in NG-PANI with pyrolysis temperature. Reprinted with permission from[168]. Copyright 2013 Elsevier.

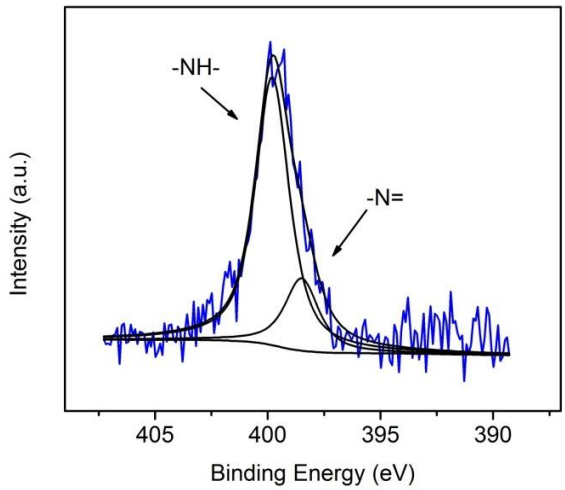

Figure 61. High resolution N 1s spectrum of GO-PANI.

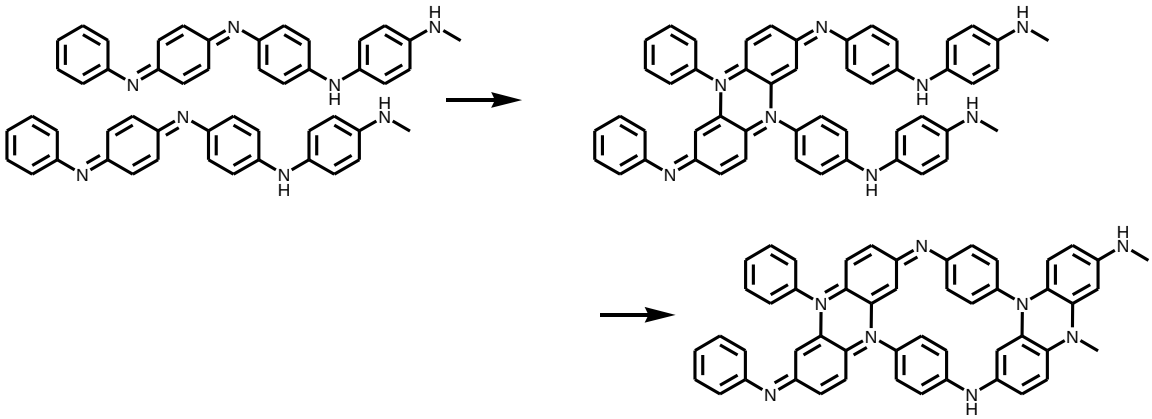

Figure 62. Possible chemical reactions during the pyrolysis of GO-PANI.

The evolution of N functionalities during pyrolysis was investigated by plotting the percentages of N functionalities with respect to the pyrolysis temperature, as shown in Figure 60. The N atoms in as prepared GO-PANI exist in imine and amine groups (Figure 61). After being pyrolyzed, pyridinic N forms as a result of the cross-linking of PANI chains,[171, 172] while pyrrolic N is generated from amines N.[154, 166] When increasing the pyrolysis temperature, the decomposition and re-construction of PANI lead to a monotonic decrease in percentage of the pyrrolic N,[1] and an increase in percentage of the pyridinic N and graphitic N, suggesting a transformation of pyrrolic N to pyridinic N and graphitic N. A possible cross-linking reaction of PANI chains is shown in Figure 62. Moreover, the pyridinic N percentage drops at temperatures greater than 700 °C, due probably to the transformation of pyridinic N to graphitic N. The change in N functionalities during pyrolysis of GO-PANI is generally consistent with our previous findings. [154, 166]

The pyrolysis of PANI was monitored by SDT analysis (Figure 63), which reveals several major physical changes and chemical reactions during the pyrolysis of PANI, including the loss of adsorbed water at ~ 100 °C, desorption of volatile compounds and dopant between 200-300 °C, and structural decomposition of PANI at temperatures greater than ~350 °C. It was also reported that the cross-linking reaction of PANI occurs at temperature above 170 °C.[171, 172] These chemical reactions of PANI are in line with transformations of N functionalities in NG. The structural change of NGs during

[1] It is impractical to distinguish pyrrolic N and amine N because their XPS peaks are very close. Here pyrrolic N represents both pyrrolic N and residual amine N. However, we believe the contribution of amine N is very small due to its thermal unstability.

pyrolysis was further investigated using Raman and FTIR spectroscopies. Raman spectroscopy is useful to measure the structural disorder in graphene materials. Figure 64a shows the Raman spectra of GO-PANI and NG-PANIs pyrolyzed at different temperatures. It is found that the I_D/I_G ratio decreases from 1.17 initially for GO-PANI to 0.95-0.99 for NG-PANI-300 – NG-PANI-600, due to thermal reduction of GO. Then the I_D/I_G ratio starts to increases to ~ 1.1 for NG-PANI-800 – NG-PANI-1100 due to the decomposition of epoxy and hydroxyl groups that leads to the in-plane C=C crack. As shown in Figure 64b, the FTIR spectrum of GO-PANI shows characteristic peaks for both GO and PANI. Peaks at ~3440, 1632, and 1384 cm^{-1} could be attributed to O-H stretching in hydroxyls and physisorbed water, HOH bending in physisorbed water, and C-O bending in phenol groups respectively.[82] The broad peak between 1000-1200 cm^{-1} results from the stretching of C-O and C-C. PANI has characteristic peaks at ~ 1464 cm^{-1} from the benzenoid structure, ~ 1300 $cm^{-1}$from the C-N stretching of a secondary aromatic amine, and ~1237 cm^{-1} from the $C\text{-}N^{\cdot+}$ stretching in the polaron structure.[173] As the GO-PANI being pyrolyzed at 300 °C, the peak at ~1562 cm^{-1}, a shoulder peak in GO-PANI, becomes very obvious, which could be attributed to C=C stretching in reduced GO and the quinonoid structure of PANI.[110, 173] Moreover, the peaks at ~1632, ~1300 and 1237 cm^{-1} disappear, due to the removal of physisorbed water and the decomposition of PANI. In the spectrum of NG-PANI-400, the peak at 1464 $cm^{-1}$are much diminished as a result of the decomposition of benzenoid structure. Finally in NG-PANI-1000, O-H in phenols, C-O and C-N are major residual functional groups.

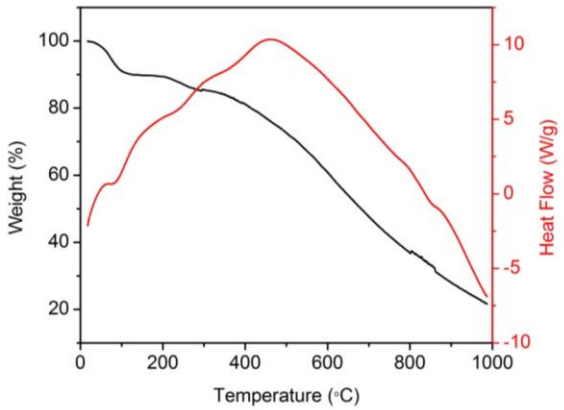

Figure 63. SDT curve of PANI in a nitrogen atmosphere with a ramping rate of 20 °C/min.

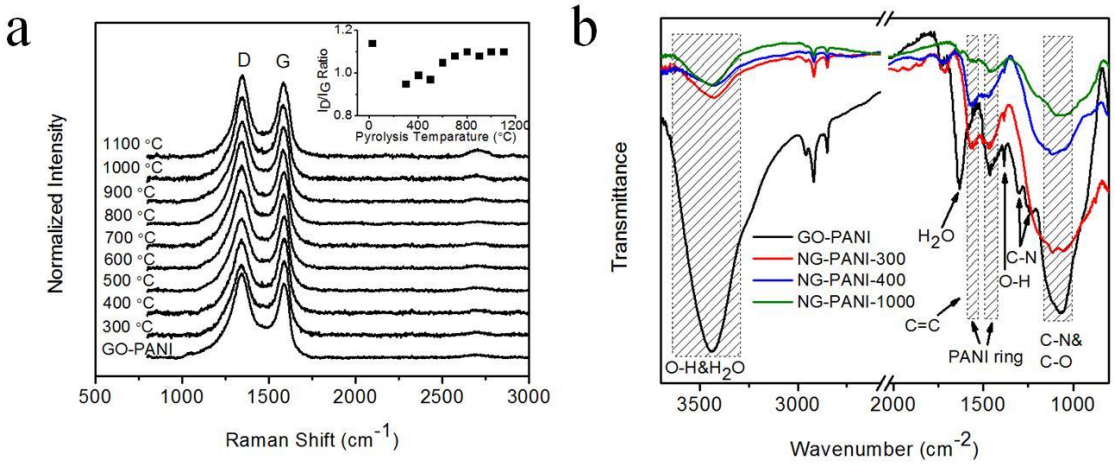

Figure 64. (a) Raman spectra of NG-PANIs prepared at different temperatures and the inset is the corresponding I_D/I_G ratio; (b) FTIR of NG-PANIs prepared at different temperatures. Reprinted with permission from[168]. Copyright 2013 Elsevier.

4.3.1.5 Effect of synthesis conditions on the structure of NG

In the synthesis of NGs, the pyrolysis temperature and the structure of N-containing precursors are two parameters that can be used to control the structure of NG. We have used four N-containing precursors for NG preparation, and for each N-containing precursor, the structure of NGs prepared at different temperatures were studied in detail. On the basis of the aforementioned results, it is possible to discuss the effect of synthesis conditions on the NG structure.

Figure 65 shows the schematic of N functionality evolution during pyrolysis and their corresponding temperature ranges, which is helpful to discuss the effect of pyrolysis temperature. The amino N is the least thermally stability group, being fully converted to either pyridinic N or pyrrolic N at temperature below 400 °C. At temperatures of ~ 300-700 °C, pyrrolic N is converted to either pyridinic N or graphitic, suggested by the simultaneously decrease of pyrrolic N percentage and the increase of pyridinic N and graphitic N percentages. At higher temperatures than 700 °C, graphitic N is the only thermally stable functionalities. Moreover, the conversion of N functionality is accompanied by the loss of N atoms, and as a result, the total N content decreases with the temperature. Overall, high pyrolysis temperature is beneficial for producing NGs with high graphitic N content; intermediate pyrolysis temperature leads to high percentage of pyridinic and pyrrolic N; low pyrolysis temperature is necessary for high percentage of amino N.

Figure 66 compares the XPS N 1s spectra of NGs prepared from different N-containing precursors that have the best ORR catalytic activity in their category (Section 4.3.2). It is evident that the small molecules, urea and melamine, produce NGs with high pyridinic N percentage, while the conjugated polymers, PPy and PANI, produces NGs with high graphitic N percentage. This trend is because that N atoms in PPy and PANI are in conjugated systems that share more structural similarity with the graphitic N, making them easier to be converted to graphitic N.

Overall, high pyrolysis temperature and N-containing conjugated polymers are optimal to prepare NGs with high graphitic N that is critical for ORR catalysis. Further, these discussions also provide important guideline for the preparation of NGs for

applications beyond ORR catalyst. For example, NGs can be used as anode of lithium-ion battery, where the pyridinic N is the most beneficial group; therefore, intermediate pyrolysis temperature and small molecule N-containing precursors may produce NG with larger capacity, better rate and cycling performance.[174-177]

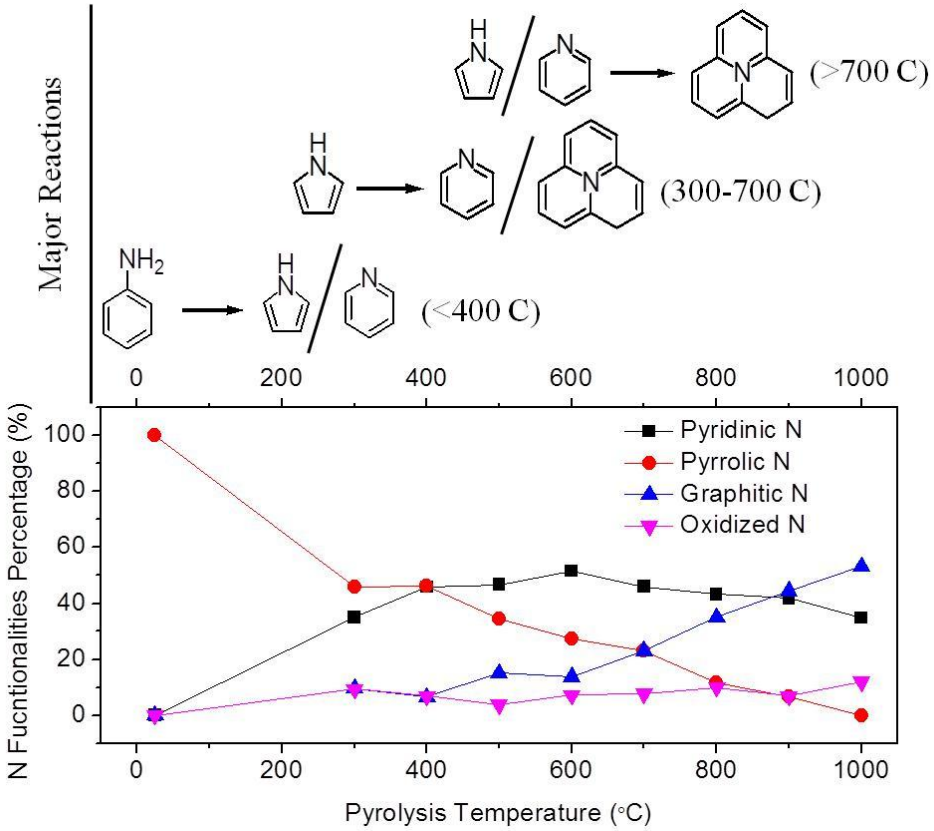

Figure 65. Effect of pyrolysis temperature on the structure of NGs: schematic of chemical reactions at different temperature range and the N evolution of NG-PPy.

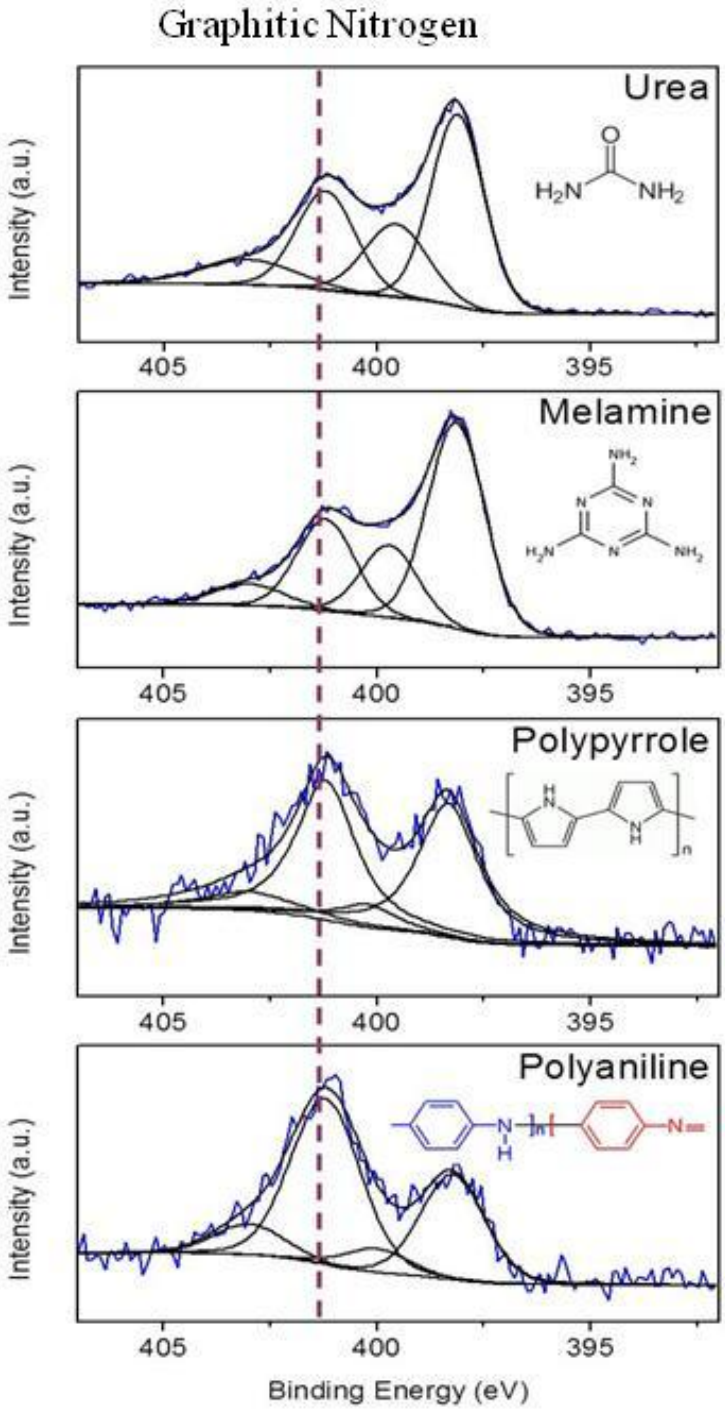

Figure 66. Effect of N-containing precursors on the structure of NG.

4.3.2 Catalytic activity of synthesized NG

4.3.2.1 GO-urea

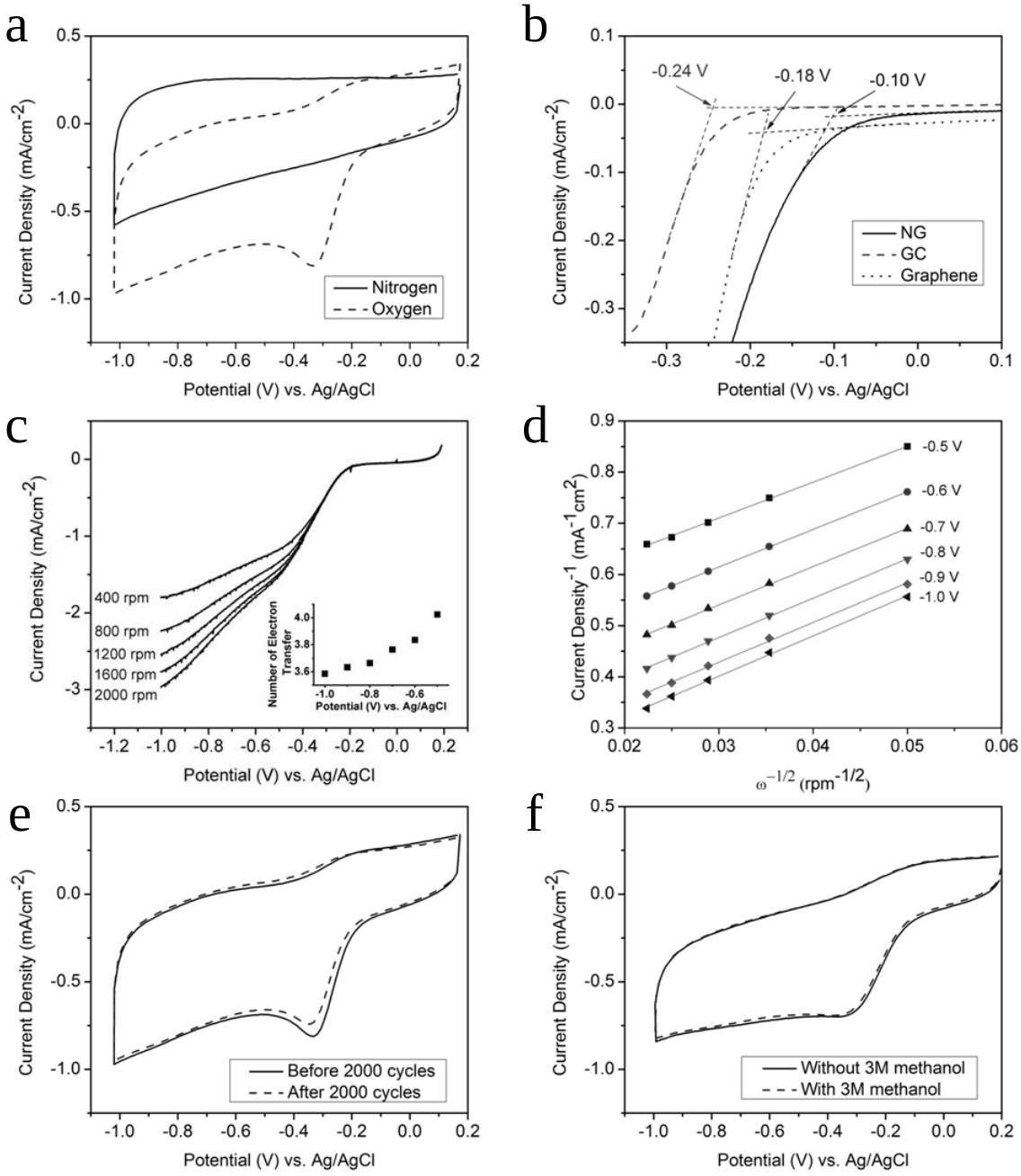

Figure 67. Electrochemical characterizations of NG-urea-800: (a) CVs in 0.1 M KOH at a scan rate of 100 mV/s; (b) LSVs of glassy carbon electrode (GC), graphene, NG-urea-800 in 0.1 M oxygen saturated KOH at a scan rate of 10 mV/s; (c) RDE measurement of NG-urea-800 in 0.1 M oxygen saturated KOH at a scan rate of 10 mV/s (inset: number of electron transfer as a function of potential); (d) Koutecky–Levich plots of NG-urea-800 at different electrode potentials; (e) CVs of NG-urea-800 before and after stability test (2000 cycles in oxygen saturated 0.1 M KOH at a scan rate of 100 mV/s); (f) CVs of NG-urea-800 with and without 3 M methanol (in oxygen saturated 0.1 M KOH at a scan rate of 100 mV/s). Reprinted with permission from [151]. Copyright 2012 Wiley.

Figure 67 shows the electrochemical characterizations of NG-urea-800 as a metal-free catalyst for ORR. In a nitrogen saturated KOH solution, a clean capacitive CV background is seen (Figure 67a). The introduction of oxygen leads to a large cathodic current with a peak at ~ -0.32 V, indicating the ORR catalytic activity. The onset potential for ORR is an important criterion to evaluate the activity of electrocatalyst. As shown in Figure 67b, the graphene control sample shows a positively shifted onset potential at - 0.18 V compared to -0.24 V measured on glassy carbon (GC) and ~ -0.4 V measured on CVD grown graphene,[24] due probably to the existence of large amount of holes and edges which have higher electrochemical activity than basal plane. However, the NG-urea-800 shows a much higher activity, as evidenced by the onset potential of -0.10 V, which could be attributed to the effect of N-doping. The ORR on a catalyst surface could through either a two-electron process producing peroxide or a four-electron process producing water as the product. It is obvious that the four-electron pathway is more efficient and favorable. The number of electron transfer per oxygen molecule on NG was determined from RDE measurements, as seen in Figure 67. The Koutecky–Levich equation was used to analyze the number of electron transfer:[24]

$$\frac{1}{J} = \frac{1}{J_L} + \frac{1}{J_K} = \frac{1}{B\omega^{1/2}} + \frac{1}{J_K},$$

$$B = 0.2nFC_0(D_0)^{2/3}\nu^{-1/6}$$

where J, J_L, J_k are measured current density, diffusion-limiting current densities and kinetic-limiting current density respectively; ω is the rotation speed in rpm, F is the Faraday constant (96485 C/mol), D_0 is the diffusion coefficient of oxygen in 0.1 M KOH (1.9×10^{-5} cm^2/s), υ is the kinetic viscosity (0.01 cm^2/s), and C_0 is the bulk concentration of oxygen (1.2×10^{-6} mol/ cm^3). 0.2 is a constant when the rotation speed is expressed in

rpm. From the fitting result shown in Figure 67d, it is found that ORR on NG-urea-800 is dominated by an efficient four-electron process with water as the product. The number of electron transfer is 4.0 at -0.5 V, which gradually decreases to 3.6 at -1.0 V.

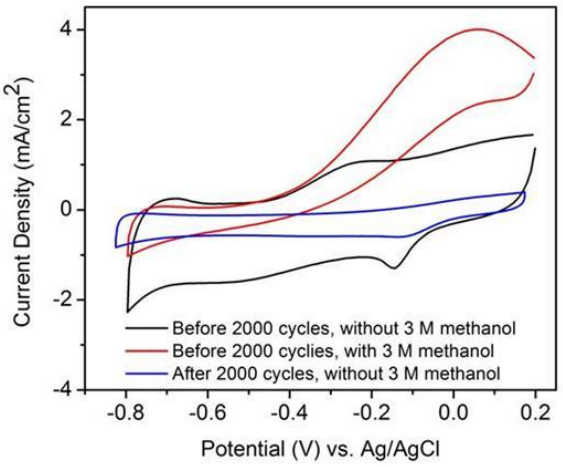

Figure 68. CV curves of Pt before and after 2000 CV cycles in oxygen saturated 0.1 M KOH without 3 M methanol and the CV curve in oxygen saturated 0.1 M KOH with 3 M methanol.

In addition, the reliability tests reveal that NG-urea-800 has high cycling stability and tolerance to crossover effect. As seen in Figure 67e, after 2000 consecutive CV cycles in oxygen saturated KOH, the CV does not show significant change in shape and area. This is in contrast to the loss of the active surface area for Pt/C catalystas a result of possible migration, dissolution or aggregation of Pt nanoparticles (Figure 68). The high stability of NG-urea-800 could be attributed to the strong covalent bonds between the active sites and graphitic lattice. Moreover, methanol, a common fuel for fuel cells, is added to the KOH electrolyte to examine the resistance of NG-urea-800 to crossover effect. As seen in Figure 67f, the CV of NG-urea-800 in the presence of 3 M methanol does not change much, indicating that methanol does not interfere with the ORR reaction on cathode. However, the oxidation of methanol occurs on Pt/C surface which greatly compromise the fuel cell efficiency (Figure 68).

4.3.2.2 GO-melamine

The catalytic activity of NG-melamine-900 was first examined using CV in the nitrogen or oxygen saturated 0.1 M KOH solution. Figure 69a shows a typical CV for NG-melamine-900. In nitrogen saturated KOH, a featureless capacitive current background was observed between -1.0 and 0.2 V. After introducing oxygen, a large cathodic current with a peak at -0.34 V is clearly observed, evidencing the catalytic activity of NG-melamine-900 toward ORR. The onset potential of oxygen reduction was measured by LSV. As seen in Figure 69b, NG-melamine-900 exhibits an onset potential of -0.10 V. In comparison, the graphene control sample has an onset potential of -0.19 V, and the state-of-art Pt/C catalyst shows higher activity by an onset potential of -0.03 V. However, the advantage of NG-melamine-900 over Pt/C is clearly seen in the stability and crossover tests. As seen in Figure 69c, after 2,000 CV cycles, NG-melamine-900 shows a negligible degradation. Moreover, the addition of 3M methanol, a common fuel in fuel cells, does not change the CV of NG-melamine-900 significantly (Figure 69d).

The ORR reaction on NG-melamine-900 is also studied by RDE, as seen in Figure 70. The number of electron transfer per oxygen molecule is calculated by Koutecky–Levich equations, and found to be 3.3-3.7 at potentials ranging from -1 to -0.3 V (Figure 70 inset). This suggests that the ORR catalyzed by NG-melamine-900 is dominated by a one-step four-electron pathway producing water molecules.

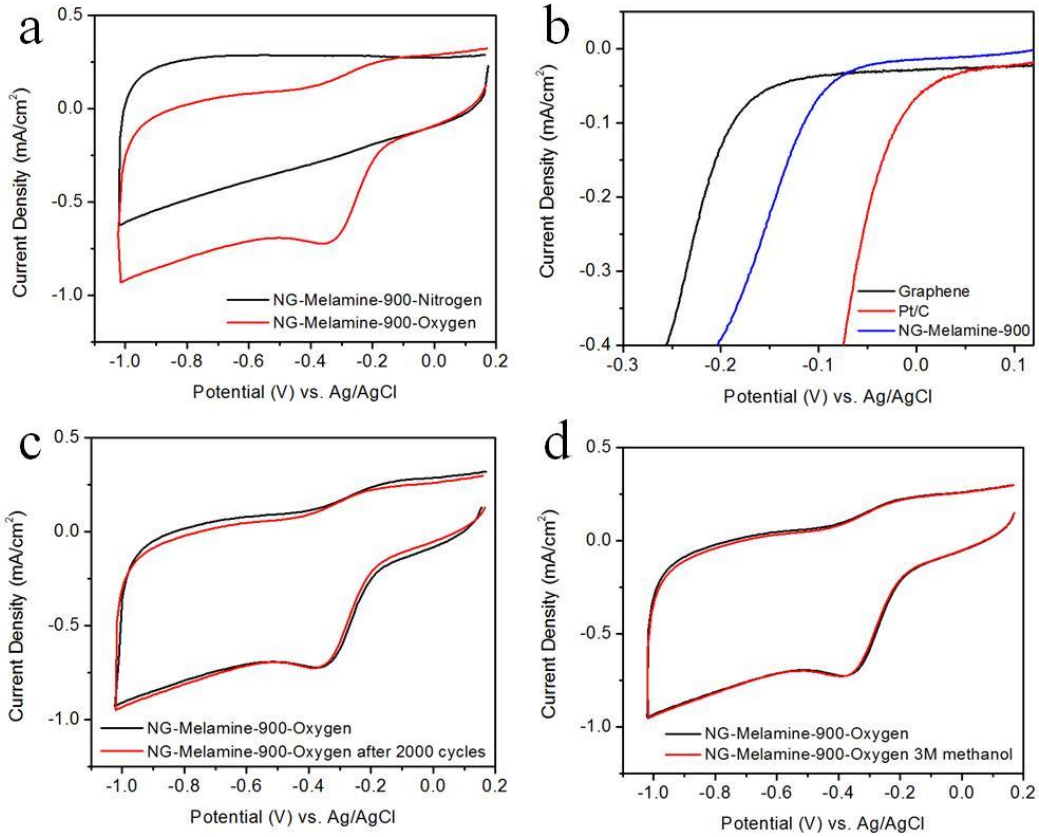

Figure 69. Electrochemical characterizations of NG-melamine-900: (a) CVs in 0.1 M KOH at a scan rate of 100 mV/s; (b) LSVs of graphene, NG-melamine-900and Pt/C in 0.1 M oxygen saturated KOH at a scan rate of 10 mV/s; (c) CVs of NG-melamine-900 before and after stability test (2000 cycles in oxygen saturated 0.1 M KOH at a scan rate of 100 mV/s); (d) CVs of NG-melamine-900 with and without 3 M methanol. Reproduced from [154] with permission from the PCCP Owner Societies.

The catalytic activity of NG-melamine-900 is highly dependent on the pyrolysis temperature, which could be attributed to the competition between N content and electrical conductivity. As seen in Figure 71, NG-melamine-400 and NG-melamine-500 show onset potentials at -0.25 and -0.21 V respectively. Their limited catalytic activities, although with high N content, could be attributed to the existence of a significant amount of electrically insulating carbon nitride. As a result, electrons cannot effective propagate through the carbon nitride/NG structure. The low electrical conductivities of NG-melamine-400 and NG-melamine-500 are revealed by the negligible capacitive

backgrounds in their CVs (Figure 72). The removal of carbon nitride at higher temperature leads to an improved electrical conductivity and thus an enhanced capacitive current background (Figure 72). The onset potentials of NG-melamines (> 600°C) shift positively as a consequence. However, once the pyrolysis temperature is higher than 900 °C, the N content decreases, resulting in a slightly lower activity for NG-Melamine-1000 (Figure 71).

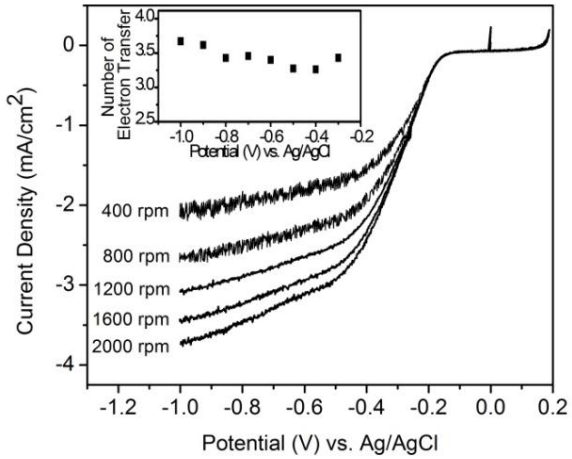

Figure 70. RDE measurement of NG-melamine-900 in 0.1 M oxygen saturated KOH at a scan rate of 10 mV/s; inset: number of electron transfer as a function of potential. Reproduced from [154] with permission from the PCCP Owner Societies.

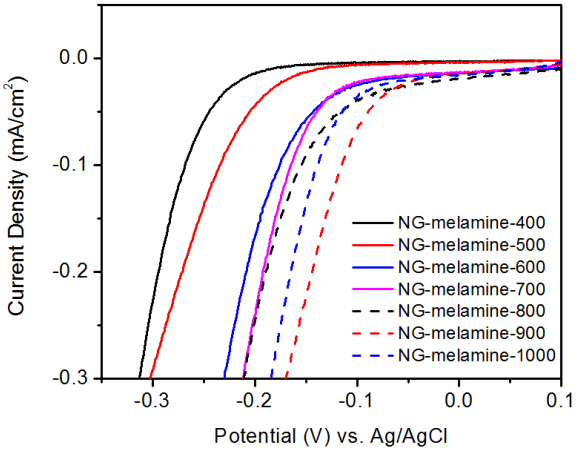

Figure 71. LSV curves of NG-melamines in a 0.1 M oxygen saturated KOH at a scan rate of 10 mV/s.

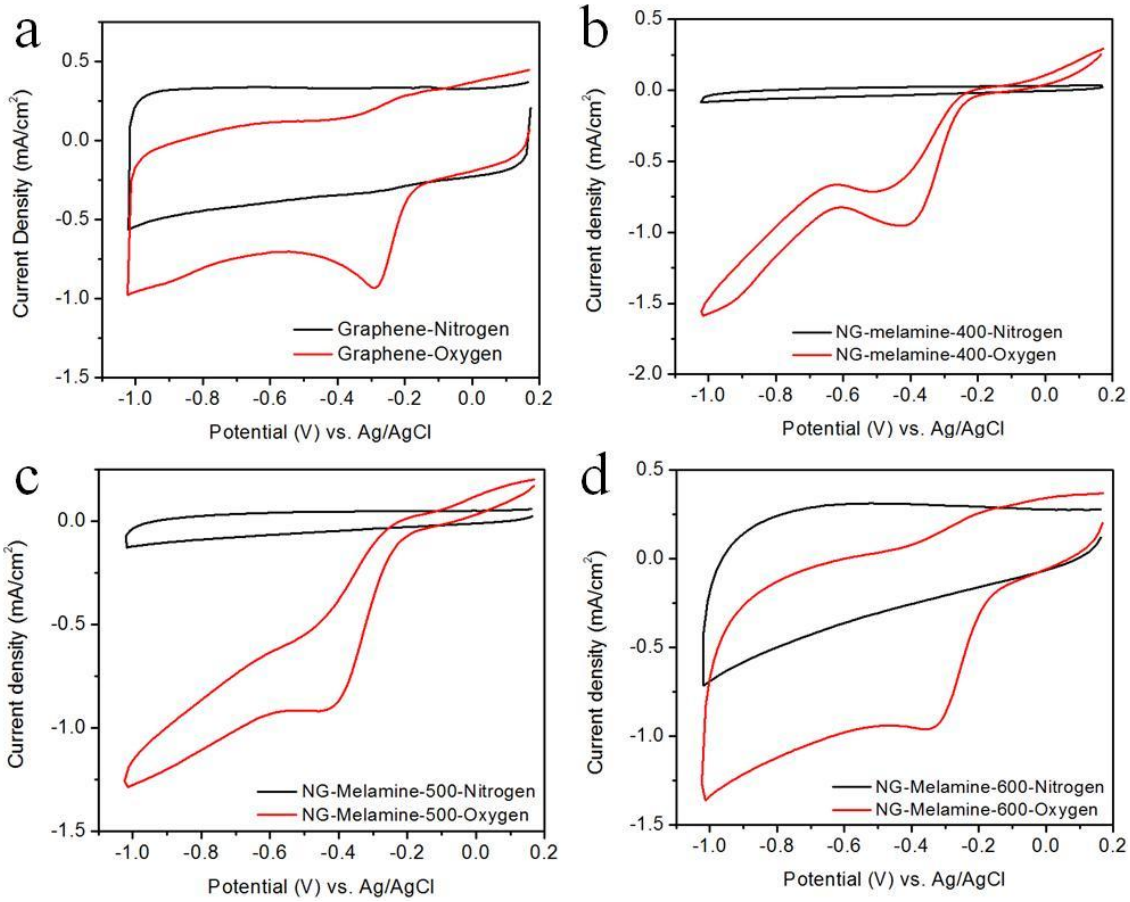

Figure 72. CVs of graphene, NG-Melamine-400, NG-melamine-500, and NG-melamine-600.

4.3.2.3 GO-PPy

The catalytic activity of NG-PPy-900 was examined in a conventional three-electrode system using nitrogen or oxygen saturated 0.1 M KOH as electrolyte. The CV curve of NG-PPy-900 (Figure 73a) shows a clean capacitive current background in the nitrogen saturated electrolyte, whereas an obvious cathodic current appears in the oxygen saturated electrolyte with a peak at - 0.22 V, indicating the occurrence of ORR on the NG-PPy-900 surface. We used RDE measurement to investigate the ORR kinetics of NG-PPy-900 (Figure 73b). The number of electron transfer is calculated to be 3.8-3.9 between -0.3 and -0.6 V from the slope of Koutecky-Levich plots (Figure 5b inset),

suggesting a predominant four-electron ORR catalyzed by NG-PPy-900. The superior stability and tolerance to crossover effect were also seen in NG-PPy-900. For example, after 2000 CV cycles in the oxygen saturated 0.1 M KOH, minimal change was observed in the CV curve of NG-PPy-900 (Figure 74a). Moreover, the presence of 3 M methanol did not hinder the catalytic ORR on NG-PPy-900 (Figure 74b).

The pyrolysis temperature has a profound influence on the catalytic activity of NGs. As seen in Figure 73c and d, 900 °C appears to be an optimal temperature since NG-PPy-900 displays a larger kinetic limiting current (9.0 mA/cm^2 at -0.4 V) with a desired four-electron pathway (3.8 at -0.4 V), compared to samples pyrolyzed at 800 and 1000 °C. It is obvious that the dependence of catalytic activity on the pyrolysis temperature is correlated with the aforementioned evolution of NG-PPy structure during pyrolysis, from which some useful insights can be gained into the structure-property relation of NG-PPy as ORR catalyst. Firstly, the catalytic activity of NG-PPy increases with pyrolysis temperature between 400 – 900 ° C, which can be seen from the positively shifted onset potential (Figure 75). This increase of catalytic activity with pyrolysis temperature is in line with the increase of graphitic N content, but does not agree with the change of pyridinic N content that starts to drop above 600 °C. This result provides additional evidence that graphitic N, instead of pyridinic N, is the N functionality most responsible for ORR catalytic activity. Secondly, pyrolysis at a temperature higher than 900 °C causes the decomposition of some N functionalities and a resulting decrease of catalytic activity. As a result, the highest catalytic activity is obtained at an intermediate temperature of 900 °C. Thirdly, besides the N functionalities, the defects and graphene edges, which can enhance the ORR catalytic activity of N-doped carbon materials,[178]

could also partially account for the catalytic activity and its change with pyrolysis temperature. It has been shown from the Raman spectra (Figure 53a) that more defects are produced at high temperatures (>800 °C). The generation of defects could improve the catalytic activity and mitigate the catalytic activity drop caused by the low N content. Consequently, NG-PPy-1000, though with a smaller number of electron transfer (3.2 at -0.4 V), shows a comparable kinetic-limiting current (8.5 mA/cm^2 at -0.4 V).

In addition to ORR, we also tested the catalytic property of NG-PPy-900 toward oxygen evolution reaction (OER), the reverse reaction of ORR. As seen in Figure 76, when the CV scan was extended to water oxidation regime, large anodic current appeared due to the oxidation of water. Moreover, cathodic current peak in the ORR regime was observed as a result of the reduction of evolved oxygen. It is found that the OER catalytic activity of NG-PPy-900 are superior to undoped graphene, commercial Pt/C and glassy carbon electrode (Figure 76 inset), signifying the potential application of NG as a bifunctional electrocatalyst for both ORR and OER for unitized regenerative fuel cells[179] and rechargeable metal-air batteries.[180]

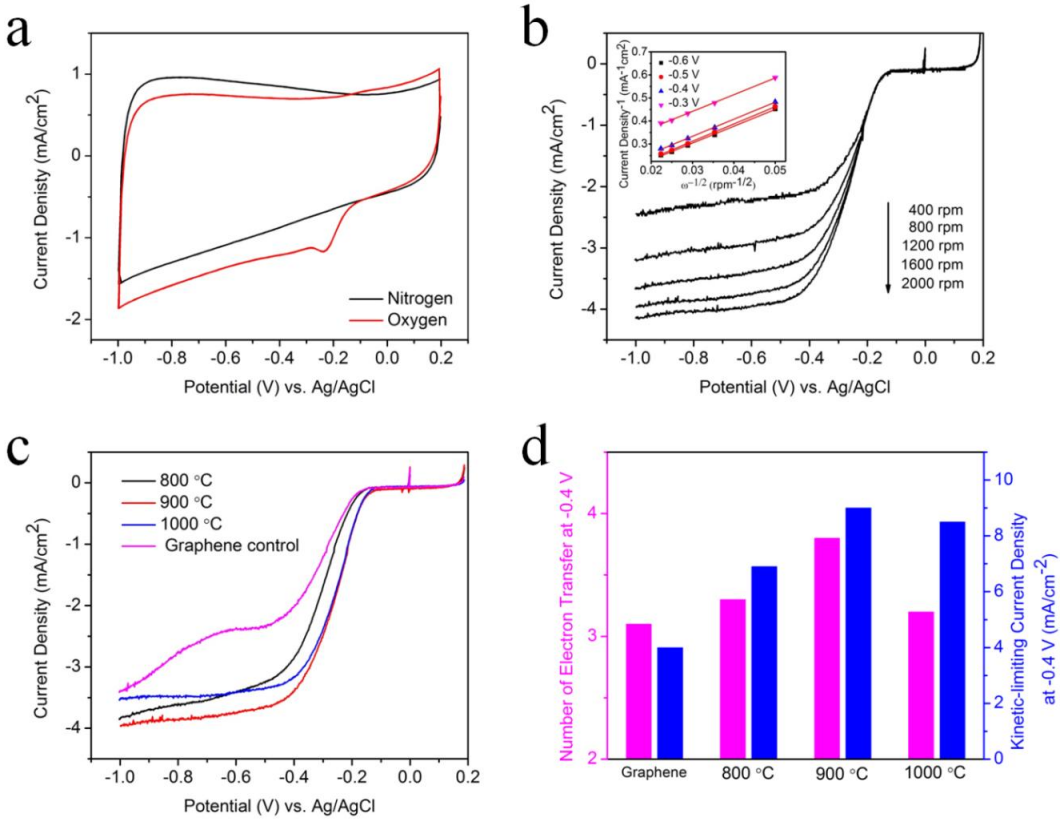

Figure 73. Electrochemical characterizations of NGs for ORR. (a) CV curves of NG-PPy-900 in nitrogen or oxygen saturated 0.1 M KOH with a scan rate of 100 mV/s. (b) RDE measurement of NG-PPy-900 in oxygen saturated 0.1 M KOH with a scan rate of 10 mV/s; the inset shows corresponding Koutecky-Levich plots at different potentials. (c) LSV curves and (d) catalytic activity of graphene, and NGs prepared at different temperatures in oxygen saturated 0.1 M KOH with a scan rate of 10 mV/s and a rotation rate of 1600 rpm. Reprinted with permission from [126]. Copyright 2013 Elsevier.

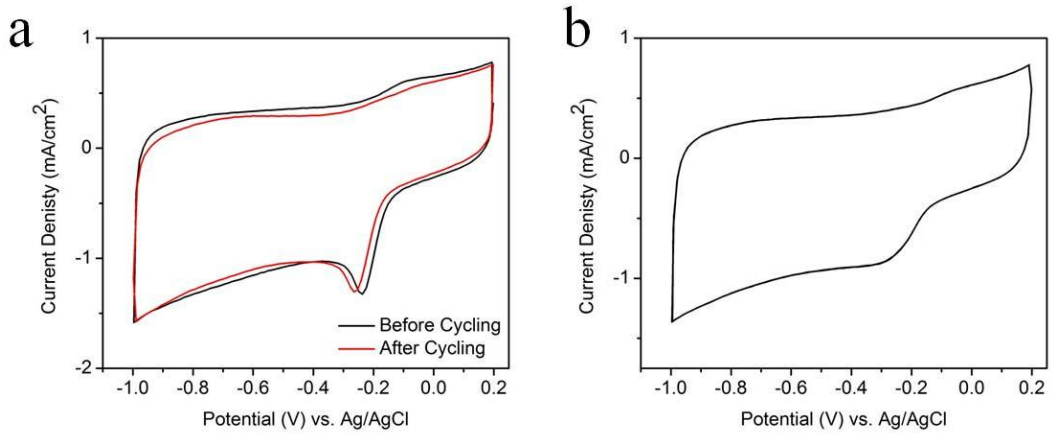

Figure 74. CV curves of NG-PPy-900 (a) before and after 2000 CV cycles in oxygen-saturated 0.1 M KOH, and (b) in oxygen-saturated 0.1 M KOH containing 3 M methanol.

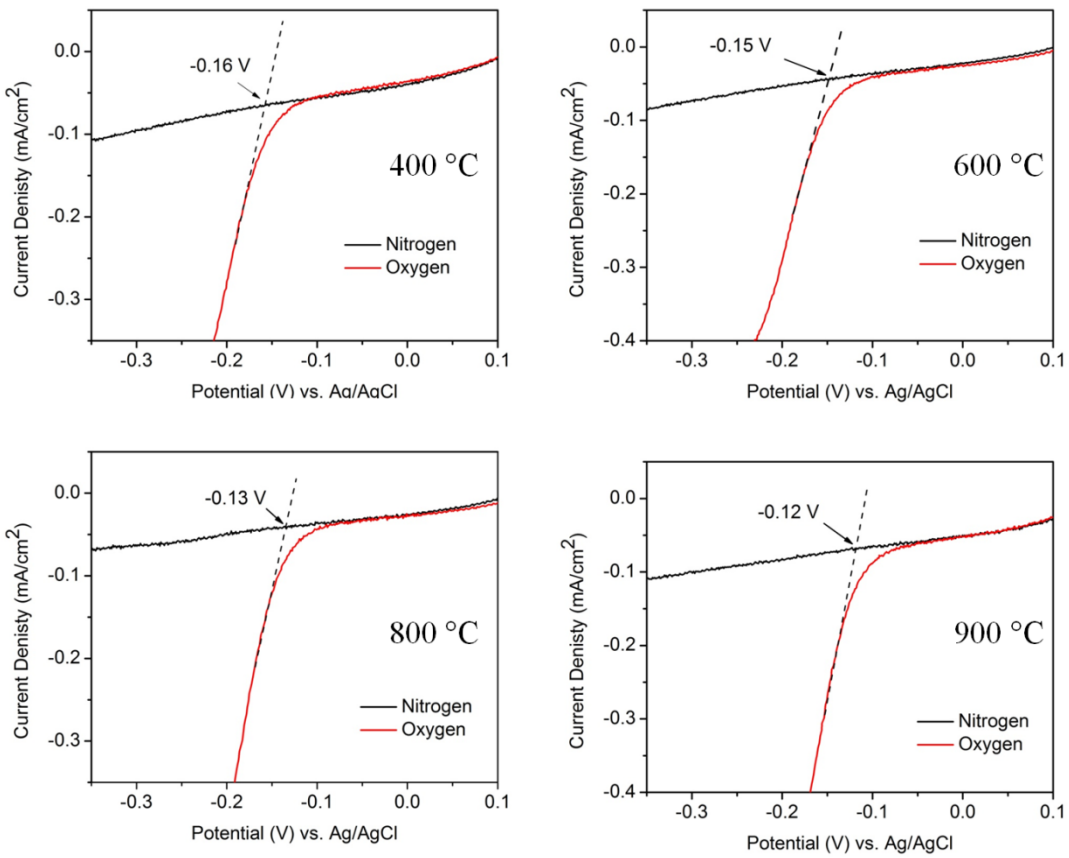

Figure 75. LSV curves of NGs prepared at different temperatures in nitrogen or oxygen saturated 0.1 M KOH with a scan rate of 10 mV/s.

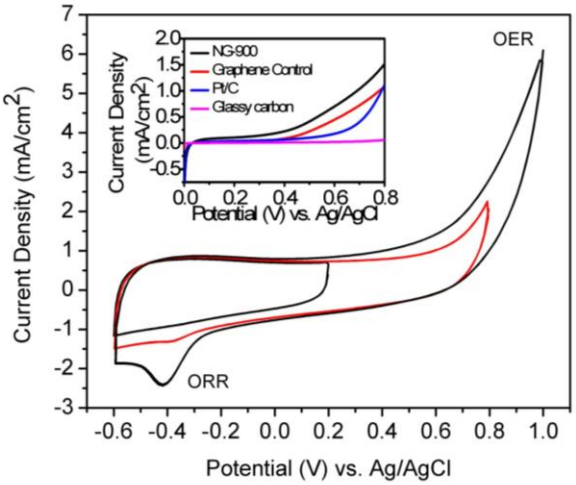

Figure 76. CV curves of NG-PPy-900 in nitrogen saturated 0.1 M KOH with a scanning rate of 100 mV/s. The inset is LSV of NG-900, graphene control, Pt/C and glassy carbon electrode in 0.1 M KOH with a scanning rate of 10 mV/s. Reprinted with permission from [126]. Copyright 2013 Elsevier.

4.3.2.4 GO-PANI

The catalytic properties of NG-PANI-1000 were investigated in a conventional three-electrode system. As seen in Figure 77a, CV of NG-PANI-1000 reveals a pure capacitive current background in nitrogen saturated electrolyte. In oxygen saturated electrolyte, a prominent cathodic current appears with a peak centered at -0.22 V, indicating a high ORR catalytic activity. RDE measurement was used to characterize the kinetics of ORR catalyzed by NG-PANI-1000, as shown in Figure 77b. The number of electron transfer is calculated to 3.8-3.9 between -0.35 and -0.5 V from the Koutecky-Levich plots (Figure 77b inset), suggesting that the ORR on NG-PANI-1000 surface produces water via a desirable four-electron pathway. The kinetic limiting current is 8.9 mA/cm^{-2} at -0.35 V, and up to 11.6 mA/cm^{-2} at -0.40 V. Moreover, the reliability test of NG-PANI-1000 showed superior long-term stability and resistance to methanol crossover to the commercial Pt/C catalyst (Figure 78). After 2000 CV cycles in oxygen saturated electrolyte, the CV curve of NG-PANI-1000 showed minimal changes. Moreover, the addition of 3 M methanol didn't hinder the ORR on NG-PANI-1000.

It was found the ORR catalytic activity of NG-PANI depends strongly on the pyrolysis temperature. The numbers of electron transfer at -0.35 V are 3.21, 3.31, 3.93, and 3.48, respectively, for NG-PANI-800, NG-PANI-900, NG-PANI-1000, and NG-PANI-1100 (Figure 79). This dependence is resulted from the previously mentioned evolution of NG-PANI structure during pyrolysis. As shown in Figure 60, the graphitic N content increased with pyrolysis temperature, leading to a higher catalytic activity. However, at temperature greater than 1000 °C, the decomposition of N functionalities

occurred, which lowers the N content (N content in NG-PANI-1000 is 1.1 at%) and the resulting catalytic activity.

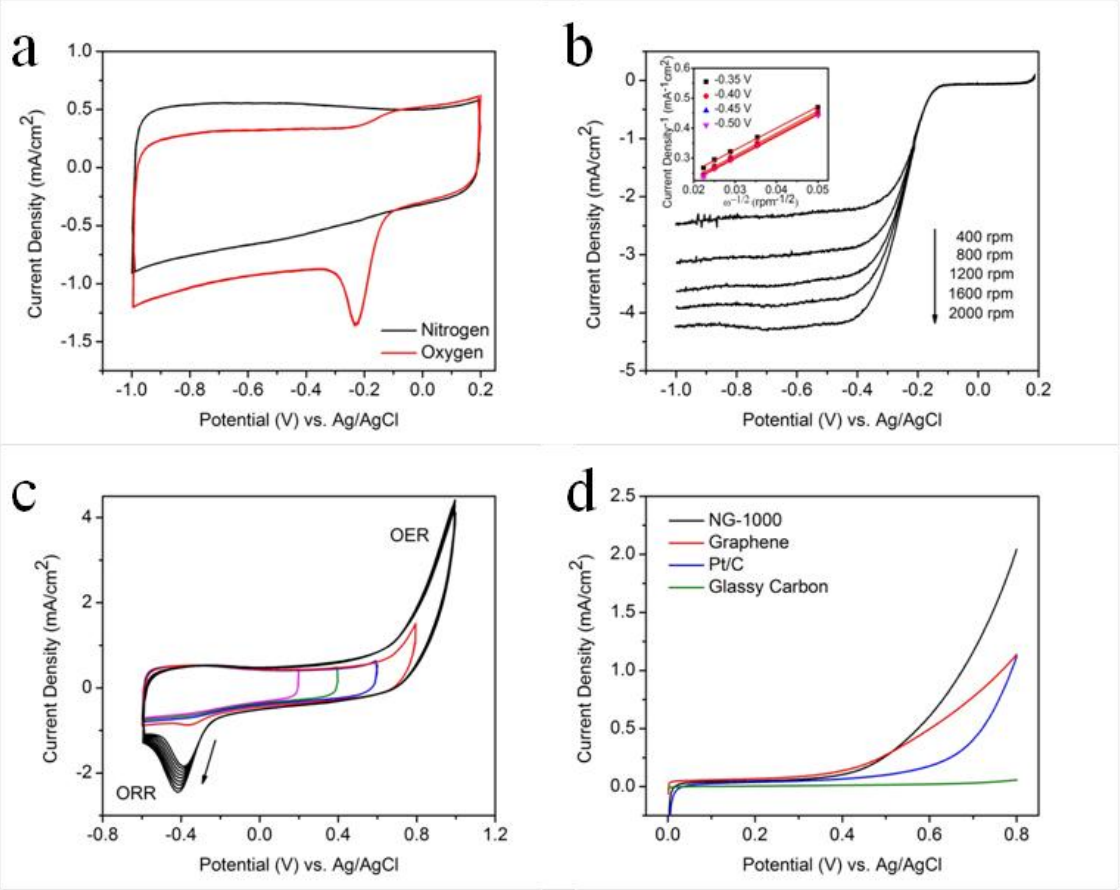

Figure 77. Electrocatalytic activity of NG-PANI-1000 toward ORR and OER. (a) CV curves of NG-PANI-1000 in nitrogen or oxygen saturated 0.1 M KOH with a scanning rate of 100 mV/s. (b) RDE measurement of NGs in oxygen saturated electrolyte with a scanning rate of 10 mV/s. Inset is the Koutecky–Levich plots at different potentials. (c) CV curves of NG-PANI-1000 in nitrogen saturated 0.1 M KOH with a scanning rate of 100 mV/s. (d) LSV of NG-PANI-1000, graphene, Pt/C and glassy carbon electrode in 0.1 M KOH with a scanning rate of 10 mV/s. Reprinted with permission from[168]. Copyright 2013 Elsevier.

We extended the CV potential range step by step to water oxidation regime to study the catalytic activity of NG-1000 toward OER. As seen in Figure 77c, the large anodic current appears when the electrode potential was scanned between -0.6 and 0.8 V, indicating the occurrence of OER on NG-PANI-1000 surface. Moreover, the evolved

oxygen can be reduced, leading to a cathodic current peak in the ORR regime. When the potential was further extended to 1.0 V, the OER current and the resulting ORR current increased dramatically. The ORR current also increased with the number of cycles due probably to the accumulation of evolved oxygen. It was found that OER catalytic activity of NG-PANI-1000 is higher than those of undoped graphene, the commercial Pt/C catalyst, and the glassy carbon electrode, as evidenced by the LSV curves of these materials shown in Figure 77d.

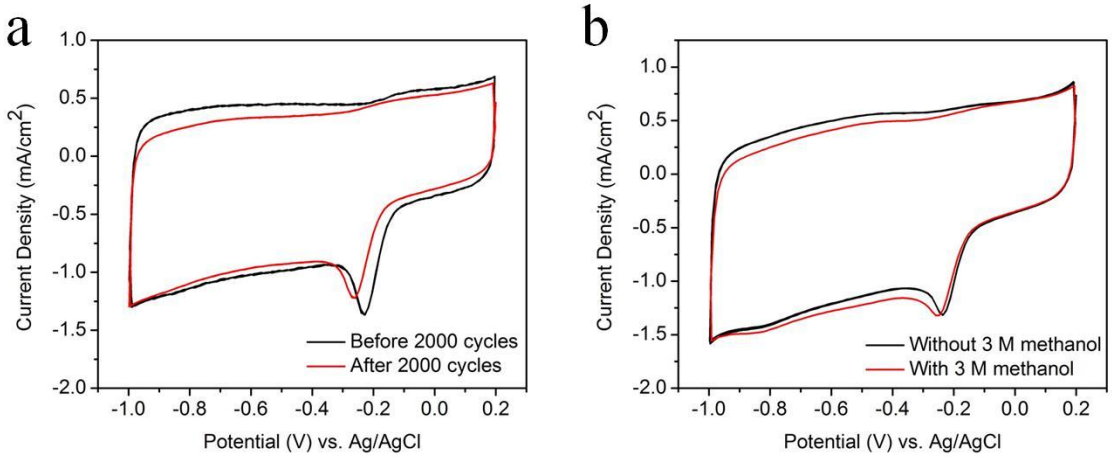

Figure 78. Reliability tests of NG-PANI-1000. (a) CV curves of NG-PANI-1000 before and after 2000 CV cycles in oxygen saturated 0.1 M KOH. (b) CV curves of NG-PANI-1000 in oxygen saturated 0.1 M KOH with and without 3 M methanol.

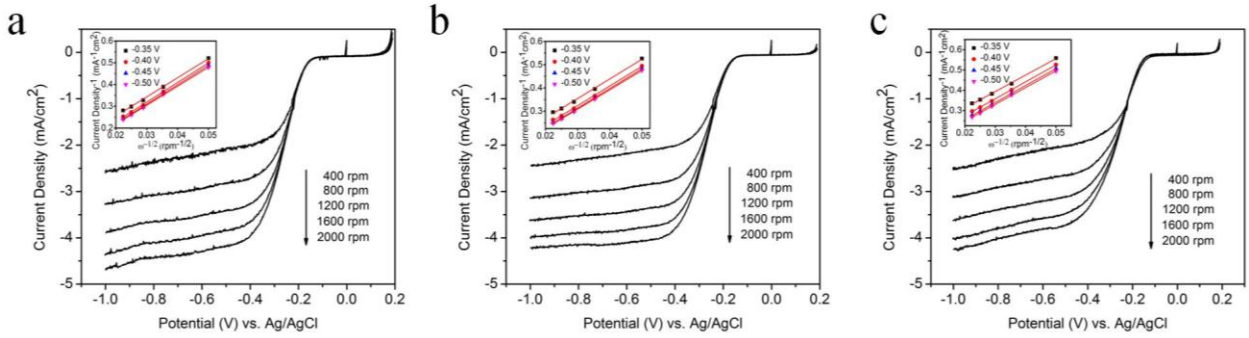

Figure 79. RDE measurements of NG-PANI-800 (a), NG-PANI-900 (b) and NG-PANI-1000 (c) in oxygen saturated electrolyte with a scanning rate of 10 mV/s. Insets are the corresponding Koutecky–Levich plots at different potentials.

4.3.2.5 Structure-property relationship of NG from different synthesis routes

Table 3 summarizes the N content, graphitic N percentage and catalytic performance of our NGs and other materials reported in literatures. Depending on the preparation methods, the typical total N content in NG ranges from ~ 2 to 8 at%, and the percentage of graphitic N is ~ 20 %. It can be seen that all the NGs have numbers of electron transfer larger than 3, suggesting that they catalyze four-electron reduction oxygen to water. Moreover, the kinetic limiting current is positively correlated with the percentage of graphitic N, supporting the argument that graphitic N is most responsible for catalyzing ORR.

Table 3. The catalytic properties of NGs prepared by difference methods.

Preparation method	N content	Graphitic N Percentage	Number of Electron Transfer (Potentials)	Kinetic Limiting current (Potentials)	High Stability	Tolerance to crossover effect
CVD[24]	~ 4 at%	-	3.6-4 (-0.4 to-0.8 V vs. Ag/AgCl)	-	Yes	Yes
NH_3 heat treatment[181]	2.8 at%	13.9%	3.8 (-0.5 V vs. SHE)	-	Yes	Yes
Chemical modification and heat treatment[182]	1.73 at%	-	3.2-3.5 (-0.3 to -0.4 V vs. Ag/AgCl)	-	Yes	-
Pyrolysis of GO and urea	7.86 at%	24.0 %	3.6-4 (-1.0 to -0.5 V vs. Ag/AgCl)	1.4 mA/cm^2 (-0.4 V)	Yes	Yes
Pyrolysis of GO and melamine	8.05 at%	24.6%	3.3–3.7 (-0.3 to -1.0 V vs. Ag/AgCl)	4.6 mA/cm^2 (-0.4 V)	Yes	Yes
Pyrolysis of GO and PPy	2-3 at%	44%	3.8-3.9 (-0.3 to - 0.6 V vs. Ag/AgCl)	9.0 mA/cm^2 (-0.4 V)	Yes	Yes
Pyrolysis of GO and PANI	2.4 at%	51%	3.8-3.9 (-0.3 to -0.6 V vs. Ag/AgCl)	11.6 mA/cm^2 (-0.4 V)	Yes	Yes

4.4 Conclusions

We developed a simple method for large-scale preparation of NG via pyrolysis of GO and N-containing molecules. Two small molecules (urea and melamine) and two polymers (PPy and PANI) were studied, and the structures of resulting NGs were characterized in detail, which gave in-depth understanding on the doping mechanism and

the evolution of N-functionalities with temperature. As expected, the structure of N-containing molecules and pyrolysis temperature play major roles in determining the structure of NG. Higher pyrolysis temperature increases the percentage of graphitic N, due to its high thermal stability. Moreover, structurally similar N functionalities are easier to be converted to graphitic N. As a result, NG-PANI-1000 has a high graphitic N percentage of up to 51% (relative to the total N content). The electrochemical characterizations revealed that NGs prepared from all four precursors can catalyze four-electron ORR for the formation of water, and exhibit superior cycling stability and anti-methanol poisoning effect. Moreover, the RDE study of ORR kinetics on different NGs suggests that high graphitic N is helpful to increase the kinetic limiting current, which is generally in line with previous theoretical and experimental studies that graphitic N is most responsible for ORR catalytic activity. Overall, this chapter depicts a low-cost and scalable method to prepare NG with controlled structure, which is very promising as a catalyst for fuel cells and metal-air batteries.

CHAPTER 5

SUPERHYDROPHOBIC ALKYLAMINE-FUNCTIONALIZED GRAPHITE OXIDE FILM

5.1 Introduction

The lotus effect evokes lots of studies on self-cleaning superhydrophobic surface, which exhibits a static water contact angle larger than 150 º and hysteresis smaller than 10º.[183-189] These surfaces have been widely used for anti-stiction and anti-contamination films in opto-electronics, biochemical sensors, and microelectromechanical systems (MEMS).[190-192] Various methods and materials have been applied to generate superhydrophobic surfaces including carbon based materials such as self-cleaning carbon nanotube (CNT) forests, pillars, films or nanocomposites.[193-197] Unfortunately, the fabrication of CNT-based self-cleaning surfaces is generally limited by its high cost and wafer-sized production.

Recently, graphene, an allotrope of carbon, and related materials have attracted considerable attention due to their high structural strength, excellent electrical properties and so on.[2, 9] Several experimental and simulation studies have been focused on the surface property and wettability of graphene/graphite films.[198, 199] Epitaxial grown graphene exhibits a contact angle of 92.5 º, which is close to 91 º for highly oriented pyrolytic graphite.[91] The graphene film, due to an enhanced surface roughness, has a larger contact angle of 127 º.[200] Koratkar et al. reported that the surface roughness can be tuned by changing the solvent composition, which produce graphene films ranging from superhydrophobic to superhydrophilic.[201]

GO is a derivative of graphene consisting of oxygen functional groups on their basal planes and edges, which can be synthesized by chemical oxidation of graphite. GO is well dispersed in polar solvents, due to the hydrophilic functional groups. The ease of synthesis and the good processiblity make GO a promising precursor for graphene and its derivatives. Understanding the wettability of GO film is very important for the in depth study of graphene-based functional materials. Untreated GO films are hydrophilic with a water contact angle of 67.4 ˚.[200] So far, few studies have been conducted on tuning the wettability of GO films, and have been limited to the functionalization of GO with phenylisocynate to produced enhanced hydrophobic GO films.[73]

In this study, we demonstrate a facile way to synthesize superhydrophobic GO films with water contact angles of 163.2 º ± 1.5 º by functionalizing GO with octadecylamine (ODA). ODA has a long hydrocarbon chain, which will lower the surface energy of ODA functionalized GO (ODA-GO). The ODA-GO films exhibit an enhanced surface roughness, which is essential for its superhydrophobicity. Superhydrophobic surfaces based on ODA-GO can be obtained by various methods, suggesting the potential application in superhydrophobic coating.

5.2 Experimental

5.2.1 Functionalization of GO and preparation of ODA-GO films

100 mg GO was dispersed in 100 mL ethanol containing 400 mg ODA. The suspension was sonicated for 2 hours. The ODA-GO was separated by filtration using a nylon membrane (0.02 μm, Whatman) and finally washed with ethanol to remove the excess ODA. The obtained ODA-GO film was dried in vacuum, and treated at 150 ºC for 1 hour. The thermal-treated ODA-GO was re-dispersed in ethanol and filtrated to form

the superhydrophobic ODA-GO film. The modification of GO with other alkylamines, incluing hexylamine (HA), dodecylamine (DDA), and hexadecylamine (HDA), followed the same experimental procedure.

5.2.2 Characterizations

The FTIR characterizations were performed at ambient temperature with a spectrometer (Nicolet, Magna IR 560), which is equipped with diffuse reflectance accessories. XRD analysis was carried out with a Philips X-pert alpha-1diffactometer, using Cu K_α radiation (45 kV and 40 mA). TGA was measured on a thermogravimetric analyzer (TGA-2050, TA Instruments). Samples were heated at a rate of 20 °C/min in ambient atmosphere. Wyko Optical Profilometer (Veeco Instruments) was used to test the film roughness by both vertical scanning (VSI) and phase shifting interferometry (PSI). The surface roughness was measured in two lateral scales, 0.9 ×1.2 mm^2 and 187.2 × 246.0 μm^2. Contact angle measurements were performed at ambient conditions using a Rame-Hart goniometer with a charge-coupled device camera equipped for image capture. Contact angle was measured right after dropping a 4 uL water droplet on each film. SEM LEO 1550 was used to investigate the surface morphology under an accelerating voltage of 4 kV.

5.3 Results and Discussion

5.3.1 Grafting of ODA on GO surface

GO is a non-stoichiometric material with lots of oxygen-containing functional groups dispersed both in the basal plane and along the edges. The chemical structure of GO has been extensively studied but still controversial. It is generally agreed that the

hydroxyl and epoxy groups are major functionalities that mainly exist in the basal plane with other functional groups located at the edges, including carboxylic and carbonyl groups.[82] These oxygen-containing functional groups make the GO hydrophilic with a surface free energy of 62.1 mJ/m^2.[200] To lower the surface free energy and turn it into hydrophobic, ODA was selected to chemically modify the GO. After functionalization, octadecyl groups are exposed instead of hydrophilic functionalities on GO sheets. The surface energy of octadecane is 29.98 mJ/m^{-2} (Lange's Handbook of Chemistry,13th edition). Therefore, the ODA-GO is expected to have a similar surface energy to octadecane, which is lower than that for graphite, 54.8 mJ/m^2; GO, 62.1 mJ/m^2; and graphene, 46.7 mJ/m^2.[200]

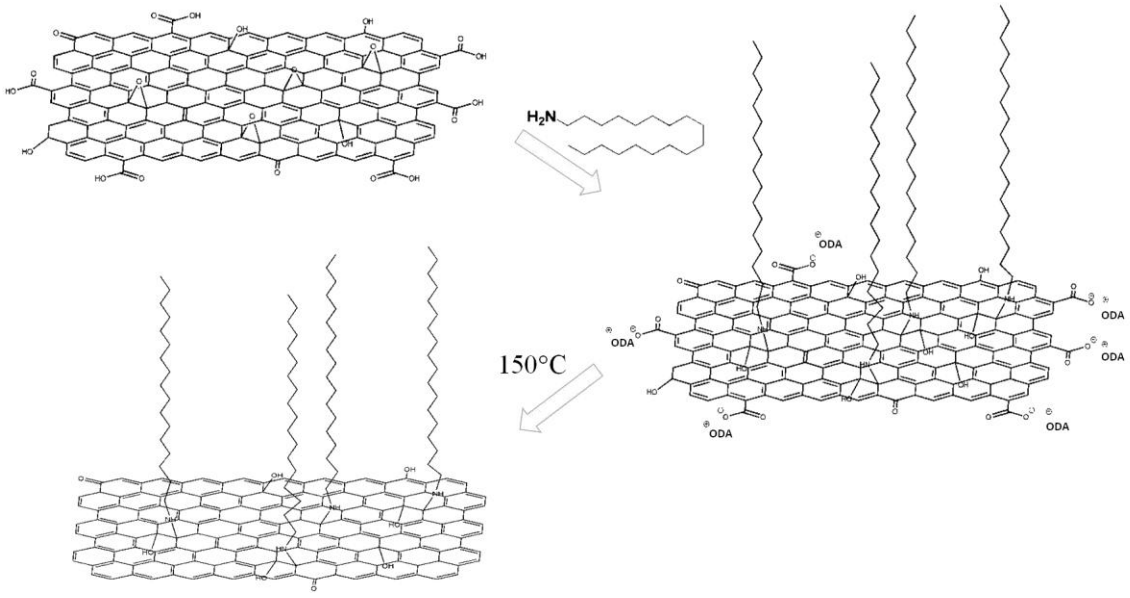

Figure 80. The structure change of GO in the ODA reaction and thermal treatment. Reprinted with permission from [157].Copyright 2011 American Chemical Society.

A schematic description of the process is shown in Figure 80. The interaction between GO and ODA has three possibilities: hydrogen bonding, electrostatic attraction between carboxylic group and protonated amine, and nucleophilic substitution between

epoxy and amine.[202] A previous study shows that the nucleophilic substitution reaction dominates this reaction.[202] The amine group acts as a nucleophile and attacks the carbon atom in epoxy groups, grafting the long hydrocarbon chain of the ODA onto GO sheets. In addition, the hydrogen bonding and electrostatic attraction also exist, due to the presence of hydroxide and carboxylic groups.

The FTIR spectra of GO, ODA and ODA-GO, as shown in

Figure 81, give information of the chemical reactions in the ODA functionalization step. In the spectrum of ODA, there are three strong peaks above 3000 cm^{-1} which disappeared after reacting with GO, indicating a strong interaction between $–NH_2$ groups and GO. For the starting GO, the peaks at ~ 3420 cm^{-1}, ~1630 cm^{-1}, are related to the –OH and C=C bonds, respectively. In the ODA functionalization, these bonds were intact, and thus the corresponding peaks did not change significantly either in intensity or position. The peak at ~1720 cm^{-1} is from carboxylic groups. Its intensity decreased after ODA functionalization, indicating that carboxylic groups interact with ODA molecules. The broad peak at ~960 - ~1160 cm^{-1} can be attributed to C-O bonds in epoxy groups. The epoxy groups are reacting sites with ODA, generating C-OH and C-N bonds. The C-O (epoxy and alcohols) and C-N peaks are overlapped in the same region of wavenumbers, leading to the broader ~ 1100 cm^{-1} peak for ODA-GO. The most significant change in FTIR spectrum of ODA-GO was the large intensity increase for peaks from ~2850 to ~3000 cm^{-1} and at ~1460 cm^{-1}, corresponding to the C-H stretching and deformation. This is due to the introduction of long hydrocarbon chain into GO sheets.

Figure 82 shows the TGA curves for GO, ODA, ODA-GO and thermal-treated ODA-GO. ODA showed a rapid weight loss starting at temperature as low as 120 ºC, and a ~90% weight loss is observed between 120 ºC and 230 ºC. However, GO was thermally stable below 180 ºC, only with a moderate weight loss that results from the removal of adsorbed water. The GO started to decompose and exhibited a ~ 24 % weight loss between 180 ºC and 230 ºC, due to the decomposition of labile oxygen-containing functionalites. At the temperature range of 230 ºC to 500 ºC, GO decomposed at a lower rate. However, when the temperature was higher than 500 ºC, GO decomposed rapidly, and completely decomposed at ~ 540 ºC.

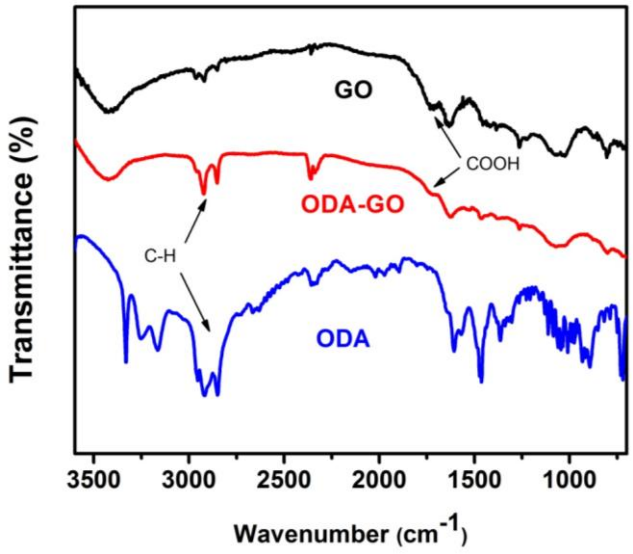

Figure 81. FTIR spectra of GO, ODA-GO, and ODA. Reprinted with permission from [157].Copyright 2011 American Chemical Society.

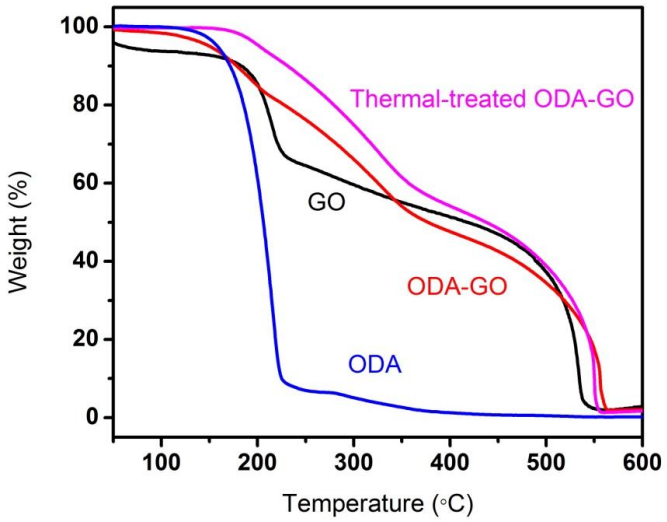

Figure 82. The TGA curves of GO, ODA, ODA-GO and thermal-treated ODA-GO. The TGA was conducted in air at a ramping rate of 20 °C/min. Reprinted with permission from [157].Copyright 2011 American Chemical Society.

The effects of ODA functionalization and 150 ºC thermal treatment on the thermal behavior of GO can be discussed in terms of desorption of water, physically bonded ODA and chemical bonded ODA. Below 100 ºC, ODA-GO and thermal-treated ODA showed nearly zero weight loss, indicating an enhanced hydrophobicity that minimizes the amount of absorbed water. However, ODA-GO, different from GO, showed a gradual weight loss of ~ 10 % from 150 ºC to 180 ºC, which could be attributed to the desorption of physical bonded ODA.[203] These ODA molecular may be positively charged and electrostatically bonded with negatively charged carboxylic groups, which prevents them from being washed away by ethanol. The carboxylic groups are stable during the ODA functionalization but decompose in the thermal treatment at 150 ºC. Thus an enhanced thermal stability was observed for thermal-treated ODA-GO with negligible weight loss below 180 ºC. The removal of hydrophilic carboxylic groups, together with physically bonded ODA molecules, contributes to lowering of the surface

energy of ODA-GO film, which will be discussed later. Between 180 ºC and 230 ºC, ODA-GO showed no rapid weight loss, which is different from both GO and ODA. The reduced weight loss for ODA-GO suggests that 1) some labile oxygen-containing groups on GO were partially decomposed during the reaction with ODA; 2) only small amount of ODA is physically bonded to GO. However, at higher temperature, ODA-GO showed a higher weight loss rates than GO. Previous studies show that the decomposition of chemical bonded amine occurs at the temperature range of 200 ºC to 500 ºC.[204-206] Therefore, the higher weight loss rate for ODA-GO is due to the decomposition of covalent bonded ODA, together with the decomposition of GO. The thermal treated ODA-GO showed a similar curve to ODA-GO between 230 ºC and 500 ºC, suggesting that the covalent bonded ODA is stable during the thermal treatment at 150 ºC.

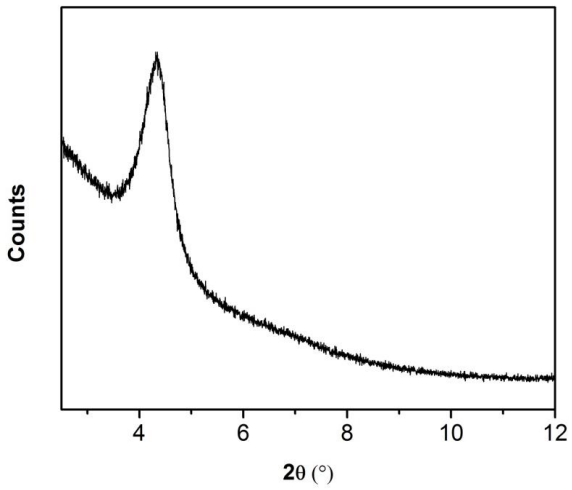

Figure 83. XRD pattern of ODA-GO film. Reprinted with permission from [157].Copyright 2011 American Chemical Society.

The chemical structure change of GO after functionalization also affects its stacking. The XRD pattern of ODA-GO film is shown in Figure 83. The peak at ~4.3 ° can be assigned to the graphite (002) diffraction. According to the Bragg equation, the corresponding distance between two adjacent ODA-GO sheets is ~ 2.1 nm. This value is

comparable to the calculated value of ~2.5 nm using the equation derived by Bourlinos:[202]

$$D_{002}(Å) = 6.1 + I_c \sin\theta$$

where 6.1 is the thickness of GO sheets in Å , I_c is the length of hydrocarbon chain of amine molecule ($I_c = 1.5 + 1.265(n - 1)$, n, number of carbon atoms), and $\theta = 54°$ which describes the orientation of amine molecule relative to the GO sheet. Bourlinos' model is based on the assumption that hydrocarbon chains are tilted toward the basal plane of GO sheet, rather than parallel. This assumption is valid, as presented in their paper, because hydroxide groups exist in the basal plane after functionaliztion, which make the basal plane hydrophilic. The hydrophobic chain is less likely to contact the basal plane. Another sound reason is the "self-support" effect by the high density hydrocarbon chains. The steric effect will prevent long chains from parallel conformation.

5.3.2. Fabrication of superhydrophobobic ODA-GO film

After functionalization and thermal treatment, the resulting ODA-GO was dispersed in ethanol and filtrated to form a film. The surface morphology of starting GO film and ODA-GO film are shown in Figure 84. Compared with the starting GO film (Figure 84a), the ODA-GO film (Figure 84b) exhibited an enhanced surface roughness, which consisted of many separated ODA-GO domains with lateral dimensions range from several to tens of micrometers. The origin of the large surface roughness of ODA-GO can be explained in terms of dispersion behaviors. The unmodified GO is well dispersed in ethanol, a polar solvent, leading to a slow vacuum filtration process. Thus GO sheets form a well-stacked film with a smooth surface, which is thermodynamically stable. However, for ODA-GO and thermal-treated ODA-GO, their hydrophobic nature

leads to poor dispersion in ethanol and the formation of aggregated domains. These large domains tend to be randomly oriented in the resulting film due to a fast filtration process. Thus significant surface roughness can be produced, which is critical for fabricating superhydrophobic surfaces. To determine the average roughness, we used Wyko optical profliometer to measure the thermal-treated ODA-GO film (Table 4). Figure 84c shows a 3D image of the thermal-treated ODA-GO film. The thermal-treated ODA-GO film showed an average mean square roughness (R_a) of ~ 9.24 μm with a peak-to-valley value (R_t) of ~121 μm. This surface roughness is much larger than GO film, which has a R_a of 2.14 μm with a R_t of ~ 53 μm.

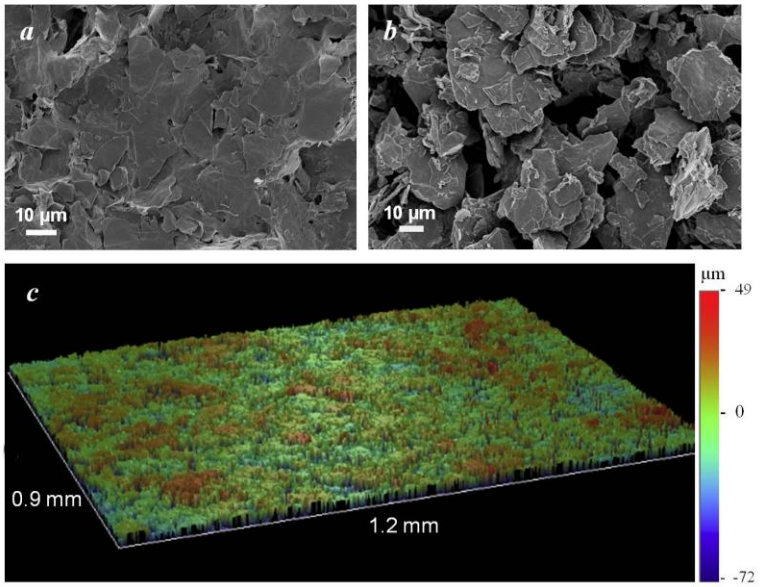

Figure 84.SEM images of (a) starting GO film and (b) ODA-GO film after thermal treatment and (c) the surface roughness measurement result for ODA-GO film. Reprinted with permission from [157].Copyright 2011 American Chemical Society.

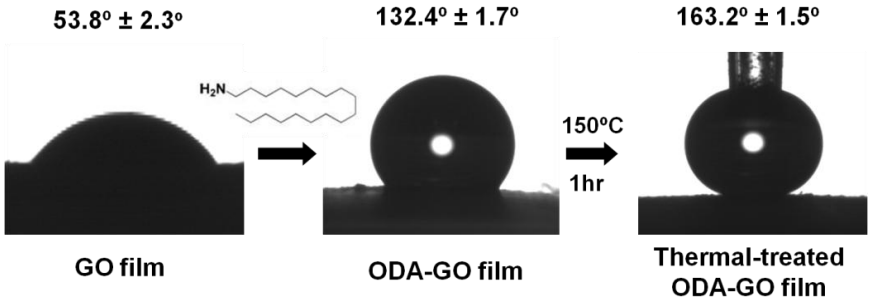

Figure 85. Contact angle results for GO film, ODA-GO film, and thermal-treated ODA-GO film. Reprinted with permission from [157].Copyright 2011 American Chemical Society.

Table 4. Surface roughness measurement of GO, ODA-GO and thermally treated ODA-GO films

	Vertical step interferometry (VSI)		Phase shifting interferometry (PSI)	
	0.9 ×1.2 mm^2	187.2 × 246.0 μm^2	0.9 ×1.2 mm^2	187.2 × 246.0 μm^2
GO	2.14 µm (52.57 µm)*	1.24 µm (21.54 µm)	1.76 µm (12.36 µm)	1.10 µm (9.77 µm)
ODA-GO	5.35 µm (92.70 µm)	5.23 µm (89.19 µm)	2.05 µm (12.38 µm)	2.57 µm (15.17 µm)
Thermal-treated ODA-GO	9.24 µm (121.07 µm)	9.94 µm (126.91 µm)	2.77 µm (16.62 µm)	too rough to be measured

* average mean square roughness (peak-to-valley value)

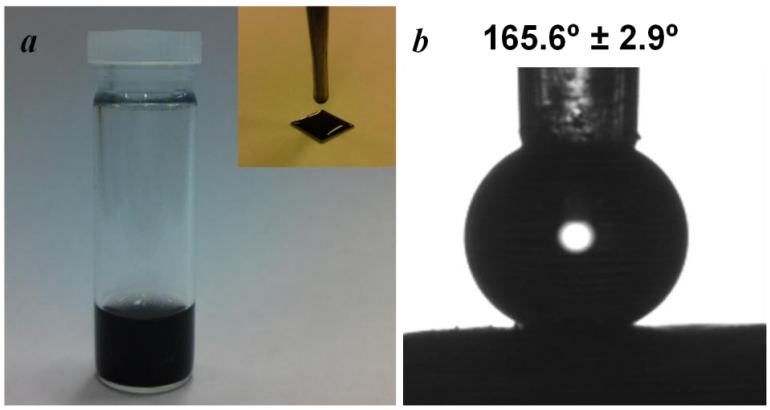

Figure 86. (a) Photograph of ODA-GO suspension in ethanol (~ 1.5 mg/ml), the inset shows drop-coating method to coat ODA-GO on silicon and (b) the measured contact angle. Reprinted with permission from [157].Copyright 2011 American Chemical Society.

The influences of surface energy and surface roughness on the wetting property of GO films are confirmed by the contact angle measurements, which are shown in Figure 85. The starting GO film exhibited a contact angle of 53.8 º, due to the hydrophilic

oxygen-containing groups on surface. After ODA functionalization, attached hydrophobic hydrocarbon chains make the ODA-GO film hydrophobic, and the R_a for ODA-GO is 5.35 μm (Table 4). Thus the contact angle increases to 132.4 º. However, the superhydrophobicity was not achieved until the ODA-GO was treated at 150 °C for 1hr and re-dispersed to fabricate the film. The significance of thermal treatment, as demonstrated before, is to remove the remained labile oxygen-containing groups that are hydrophilic, and physisorbed ODA molecules. Compared to as-prepared ODA-GO, the surface energy of thermal-treated ODA-GO sheet is further reduced by the thermal treatment. As a result, the dispersion of thermal-treated ODA-GO in ethanol becomes worse, which leads to a large R_a of 9.24 μm. Both the low surface energy and enhanced surface roughness make the thermal-treated ODA-GO film superhydrophobic with a high contact angle of 163.2 º and a low hysteresis of 3.1 º.

To demonstrate the potential application of ODA-GO in superhydrophobic coating, ODA-GO was dispersed in ethanol forming ~ 1.5 mg/ml dispersion, as shown in Figure 86a. A thin ODA-GO coating on silicon substrate was achieved using a drop-coating method (Figure 86a, inset). The contact angle on this surface was 165.6 º, which was similar to that on films fabricated by the filtration method. In another experiment, dry solid ODA-GO particles were spray coated on a silicon substrate and it also formed a superhydrophobic surface. We believe that the ODA-GO coated superhydrophobic surfaces can be achieved by various coating methods. Therefore ODA-GO is a practical material for low-cost and large-scale superhydrophobic coating.

5.3.3. Effect of alkyl chain length on the superhydrophobicity

In addition to ODA, other alkylamines with various chain length was used to modified GO, which includes HA, DDA, and HAD. The surface morphologies of functionalized GO films were imaged in SEM, as shown in Figure 87. It can be seen in Figure 87a and b that HA-GO as well as DDA-GO have relatively smooth surface. Some aggregated domains are densely packed and the surface roughness is small. However, for HDA-GO and ODA-GO, there are many large domains with the lateral dimensions of tens of micrometer, which are randomly oriented; this special morphology results in a large surface roughness. The difference in the surface morphology of functionalized GO can be explained by their dispersion behaviors. To fabricate a film, functionalized GO is firstly dispersed in ethanol by sonication, followed by a vacuum-assisted filtration. If the functionalized GO is well-dispersed in ethanol, the filtration process tends to be slow and forming a smooth surface which is thermodynamically stable. However, if the dispersion is poor, the filtration would be very fast, which leads to a very rough surface. The dispersion of functionalized GO is related to the surface energy. Due to the relatively high surface energy of ethanol, a better dispersion is expected for functionalized GO which has a high surface energy. Therefore, we believe that HA-GO and DDA-GO have higher surface energy than HAD-GO and DDA-GO. The water contact angle measurements are shown in Figure 88. The HA-GO, DDA-GO, HDA-GO and ODA-GO exhibit a contact angle of 98.0 ± 2.3 °, 111.7 ± 2.5 °, 154.2 ± 2.6 °, and 163 ± 1.5 °, respectively. It can be seen clearly only HDA-and ODA-GO films achieve superhydrophobic surfaces. This could be explained by differently molecular structure of aliphatic amines. Due to the fact that all functionalization reactions were carried out in the same conditions, a similar density of functionalization is expected. In this case, the

amine molecule with a longer hydrocarbon chain would lead to more decrease of surface energy since it has larger free volume and can cover larger area on GO sheet. Therefore, the surface energies of functionalized GO follow the order of HA-GO > DDA-GO > HDA-GO > ODA-GO. Moreover, the surface roughness increases when using an amines molecule with longer hydrocarbon tail, which has been discussed previously. The combined effect of surface energy and surface roughness lead to different contact angles of functionalized GO films.

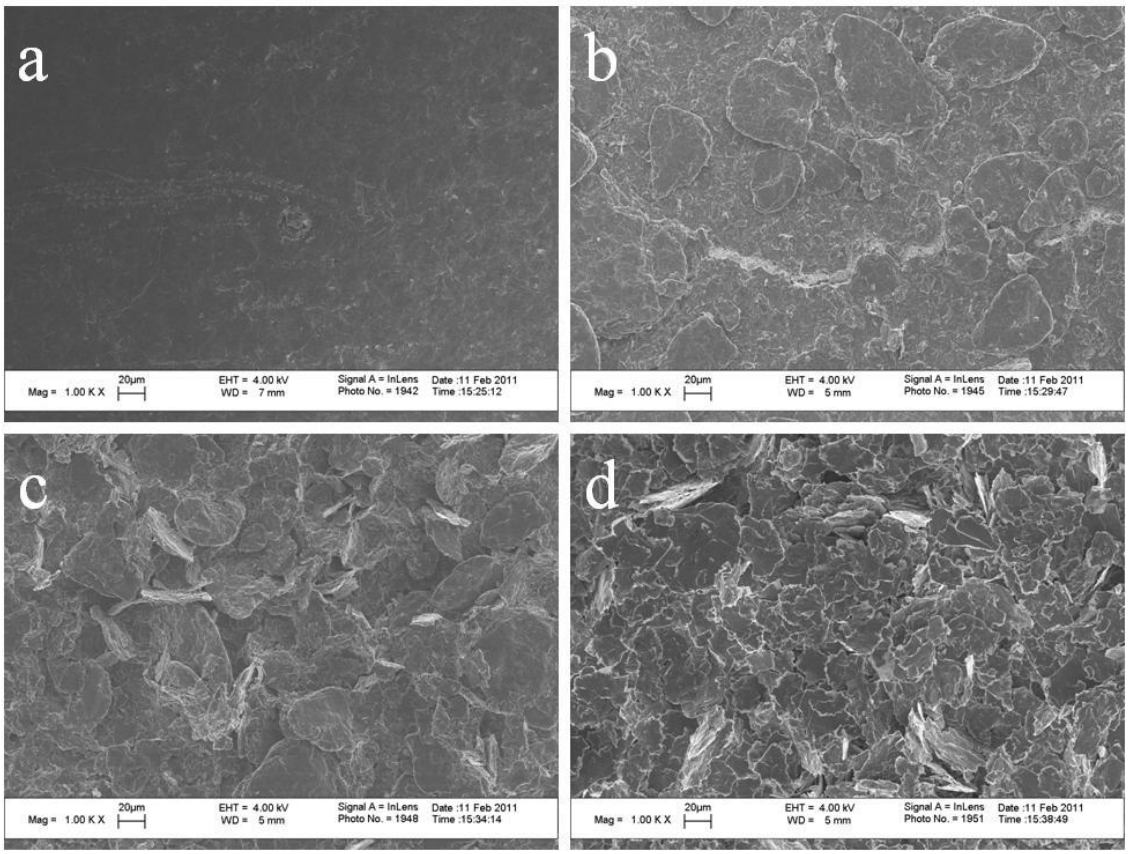

Figure 87. SEM images of (a) HA-GO, (b)DDA-GO,(c) HAD-GO, and (d) ODA-GA films. Reprinted with permission from [207]. Copyright 2011 IEEE.

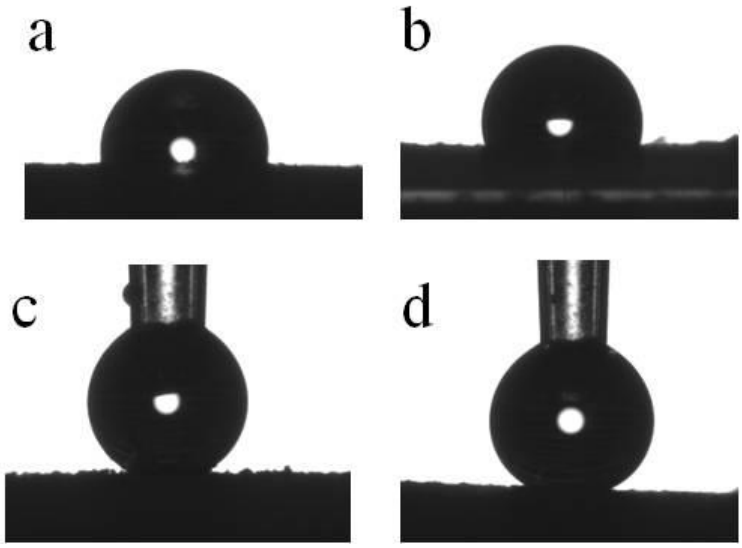

Figure 88. Water contact angle measurement of functionalized GO: (a) HA-GO, (b)DDA-GO,(c) HAD-GO,(d)ODA-GA. Reprinted with permission from [207]. Copyright 2011 IEEE.

5.4 Conclusions

The superhydrophobic functionalized GO film can be easily prepared via reacting GO with ODA, followed by a short thermal treatment process. The long hydrocarbon chain in ODA reduces the surface energy of GO sheet. The functionalized GO film exhibits a high contact angle (163.2 º) and low hysteresis (3.1 º). The self-cleaning GO film shows potential application in low-cost and large-scale superhydrophobic coating. This strategy can help improve our understanding of GO surface functionalization and realize the multi-functional applications of GO films.

CHAPTER 6

CONCLUSIONS AND SUGGESTED WORK

6.1 Conclusions

Although graphene holds many promises for a wide range of applications, the pristine graphene usually shows unsatisfactory performances, due to some intrinsic limitations including the low charge carrier density, tendency to aggregate and poor interaction with matrix, etc . The purpose of this thesis is to explore novel methods for the functionalization of graphene toward improved performance characteristics in the area of energy storage of conversion, primarily focusing on supercapacitors and electrocatalysis of oxygen reduction. Besides the fundamental chemistry, the scalability of functionalized GO production is another important consideration in designing the experimental approaches. In most the thesis work, GO is chosen as the graphene precursors mainly because its low-cost and scalability compared with other graphene preparation methods, making it the most plausible way for industry scale application of graphene. Though it is easy to make GO, the chemistry of GO is often mysterious when people try to utilize it in various areas; this could be attributed to the amorphous nature and structural complexity, resulting in difficulties in characterizing the molecular structure of GO and GO derivatives. Another challenge is the meta-stability of GO that makes it very sensitive to the temperature, storage time, pH values and solvents. As a consequence, most of researches in this area are empirical. Nevertheless, we provide solid evidence in the thesis work that the functionalization of graphene is a very powerful method to modify the chemistry and physics of graphene-based materials.

We first studied the thermal behavior of GO dispersed in solvents at the temperatures of 100 °C and 150 °C, and confirmed the reduction of GO during this process. Structural characterizations show that the nature of the solvothermal reduction is a disproportionate reaction. An interesting observation is that the solvent used to disperse GO greatly affects the rate of reduction reaction, which can be explained by some theoretical findings that the interaction between solvent molecules and functional groups could promote the diffusion rate of epoxy groups and plays an important role in the reaction. As a result, different solvents show different abilities to assisting this reaction: DMF and water speed up the reduction rate, whereas EG slows down the reduction rate. On the basis of the solvothermal reaction, OG was prepared using DMF as the solvent, in which the type and amount of residual functional groups were controlled by adjusting the reduction time. Under the optimal conditions, OG shows superior specific capacitance values up to 276 F/g that was measured in the H_2SO_4 electrolyte using a three-electrode system. Details characterizations and control experiments revealed the important role of oxygen functional groups, which can improve the wetting behavior and introduce the pseudocapacitance.

The second part of research is the controlled synthesis of NG for ORR catalysis. GO was used as the precursor and reacted with N-containing molecules to incorporate the N atoms into the graphitic lattice. After that, high temperature pyrolysis was used to reconstruct the structure of such GO derivatives to obtain NG. In the research, four N-containing molecules were investigated, including urea, melamine, PPy and PANI. The essential parts of this work are the characterizations of the structure of resulting NGs, studies on the evolution of N-containing functional groups during pyrolysis, and

correlations between the NG structure and the electrocatalytic properties. Through extensive experimental work, we found that the structure of N-containing molecules and pyrolysis temperature are two major factors that determine the structure of NG. Structurally similar N functionalities are easier to be converted to graphitic N. For example, the N atoms in conjugated systems in the case of PPy and PANI tend to transform to graphitic N more efficiently. Moreover, higher pyrolysis temperature tends to increase the graphitic N percentage because of its relatively high thermal stability. As a result, NG-PANI-1000 showed the highest graphitic N percentage of up to 51% (relative to total N content). In terms of the electrochemical properties, NGs prepared from all four precursors, though with different graphitic N contents, catalyze four-electron ORR for the formation of water, and exhibit superior cycling stability and anti-methanol poisoning effect. However, as revealed by RDE measurements, the graphitic N content has a direct influence on the kinetic limiting current: high graphitic N percentage increase the kinetic limiting current. This finding is consistent with previous theoretical and experimental studies that graphitic N is most responsible for ORR catalytic activity; high graphitic N percentage may provide more active catalytic sites.

In the third part, we used alkylamine to modify GO in order to engineer its surface energy and the morphology of GO-derivative films. The long hydrocarbon chain in alkyamines could reduce the surface energy of GO sheet, in which the length of hydrogencarbon chain plays a critical role. The superhydrophobic functionalized GO film can be prepared via ODA modification of GO which can achieve high water contact angle (163.2 º) and low hysteresis (3.1 º). The self-cleaning GO film shows potential application in low-cost and large-scale superhydrophobic coating.

Overall, we demonstrated that GO, as one of the most important precursors for graphene production, is a versatile platform for producing functionalized graphene, by either selective removal of oxygen functional groups, or incorporation of other molecules/structures. The superior performances of OG and NG as supercapacitor electrodes and ORR electrocatalysts render the functionalization of graphene a generic and effective strategy for tuning the chemistry and physics of graphene-based materials for various applications.

6.2 Suggested work

6.2.1 Molecular spacer modified graphene architecture for supercapacitors

Current graphene-based electrodes for supercapacitors have limited specific capacitance of 100-200 F/g,[2] far below the theoretical value of ~ 550 F/g. This unsatisfactory performance of graphene results from the fundamental issues of severe aggregation that reduces the usable surface area and the inertness of graphene basal plane in adsorbing ions. It is possible to overcome these limitations by tailoring the structure, the stacking, and chemical reactivity of graphene nanosheets. However, no such a method is available yet. Moreover, the correlation between microscopic chemical structure and the macroscopic properties of graphene-based materials is largely unknown, which is

[2] These values were measured in a two-electrode system and the graphene-based electrodes were prepared with an industry acceptable thickness. When a three-electrode system or a thinner electrode was used, the specific capacitance would be higher, which could be found in many literature; however, those values are not representative of the true material performance.

another hurdle for the rational design of graphene-based materials for supercapacitor applications.

A potential strategy to fundamentally solve these issues is to develop molecular spacer modified graphene architecture for high performance supercapacitor electrodes, which could enable tremendously large usable surface area, excellent electrical conductivity, and pseudocapacitive capability. The proposed approach is schematically shown in Figure 89. The key points include:

1) Molecular spacers of various dimensions will be grafted onto the basal plane of graphene surface to avoid the aggregation of graphene sheets and tune its interlayer spacing for matching the ion size in electrolyte. This approach could address the issue of aggregation for fully utilizing the EDLC to a value of 400-500 F/g.

2) Pseudocapacitive groups will be integrated onto the backbone of the molecule spacer, which offers further increased capacitance, fast charge/discharge rate and good cycling capability. This approach targets at addressing the issue of low EDLC of graphitic structure to achieve additional pseudocapacitance of 400-800 F/g, while maintaining the superior stability and rate performance of supercapacitor electrode.

Therefore, the overall specific capacitance will be 800-1300 F/g for the proposed graphene structure; the energy density per active electrode will be ~ 28 Wh/kg in aqueous electrolyte, ~ 170 Wh/kg in organic electrolyte, and above 400 Wh/kg in ionic liquid. As the active electrode material accounts for 30 wt % of a packaged supercapacitor,[68] the energy density in a device level will be above 8 Wh/kg for aqueous electrolyte, above 50 Wh/kg for organic electrolyte, and above 120 Wh/kg for ionic liquids. Such a high energy density is 2× higher than lead-acid batteries, reaching the lower end of conventional

lithium ion batteries. Moreover, the power density will be in the level of 5,000-100,000 W/kg, two orders of magnitude higher than conventional batteries, and the life time will be >10,000 cycles.

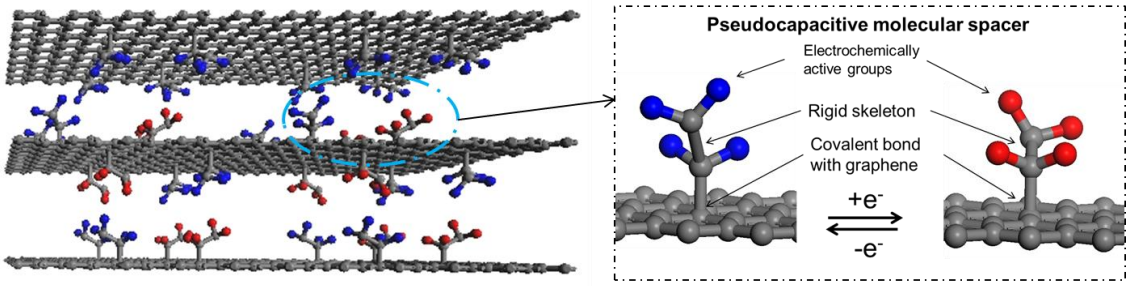

Figure 89. Schematic of proposed pseudocapacitive spacer grafted on graphene.

To fully utilize the surface area of graphene, the most important step is to graft molecular spacers onto the graphene surface, and achieve control over the interlayer spacing via proper choice of molecular spacers. As schematically shown in Figure 90a, the interlayer spacing is directly linked to the dimension and coverage of the molecular spacer. At low spacer coverage, the interlayer spacing will expand unevenly as a result of the flexibility of graphene sheets. With higher and higher spacer coverage, either interdigital or non-penetrating structure can form between adjacent graphene layers, corresponding to a relatively uniform interlayer spacing of 1× and 2× the length of molecular spacer respectively. Therefore, the length and the coverage of the molecular spacer will be two primary parameters for tuning the interlayer spacing of graphene. Other factors affecting the interlayer spacing include the rigidity and width of spacer backbones, and the tilt angle of the long-axis of molecular spacer relative to graphene basal plane. Additionally, the chemical and electrochemical stability and the nature of bonding force to graphene are critical for the cycling life and operation voltage of electrode. To meet these requirements, inert organic molecules with the capability of

forming covalent bonds to graphene are high desirable. Figure 90b shows the structure and lengths of some optional molecular spacers, including flexible alkyl and rigid aromatic spacers. Specifically, the rigid aromatic spacer will be the focus in the part as it can be used as the backbone for pseudocapacitive spacer. It is expected that interlayer spacing can be effectively tuned over a range of 0.6 nm to 5 nm with a step size of ~0.1 nm by changing the molecular spacer and grafting density.[3] By grafting molecular spacer, fully exfoliated graphene can be prepared with a targeting accessible surface area close to 2000 m^2/g.[4] Moreover, interlayer spacing could be optimized with respect to each ion size by measuring the specific capacitance of graphene with gradually changed interlayer spacing. Here a three-electrode system will be preferential to precisely control the electrode potential in positive or negative range to investigate the behaviors of anions and cations respectively, in which the diffusion, adsorption and EDLC formation of ions will be studied using techniques such as CV, constant current charge-discharge, electrical

[3] 0.6 nm could be achieved by grafting a benzene ring at low coverage: (0.2 nm+0.34 nm intrinsic interlayer spacing+ ~ 0.1 nm C-C bond between benzene-graphene). 5 nm could be achieved by grafting octadecylamine high coverage: 2×(2.1nm+0.1 C-N bond)+0.34. The step size of 0.1 nm is derived by the length of C-C bond, which can be achieved by adding an end methyl group.

[4] The difference from the theoretical surface area is caused by the additional weight from the molecular spacer and the loss of surface area for anchoring the spacers. However, in certain cases when aromatic spacers are used, the spacer can also adsorb ions contributing to the EDLC as a result of the similar structure to the graphitic edge. This will be a topic of great interest.

impedance spectroscopy etc. The flexible control over the graphene interlayer spacing will be extremely useful to engineer the electrode separately for the anode and cathode with respect to the specific sizes of cations and anions. Using this approach, we target the EDLC at of 400-500 F/g in typical electrolytes (aqueous and organic electrolyte, ionic liquids).

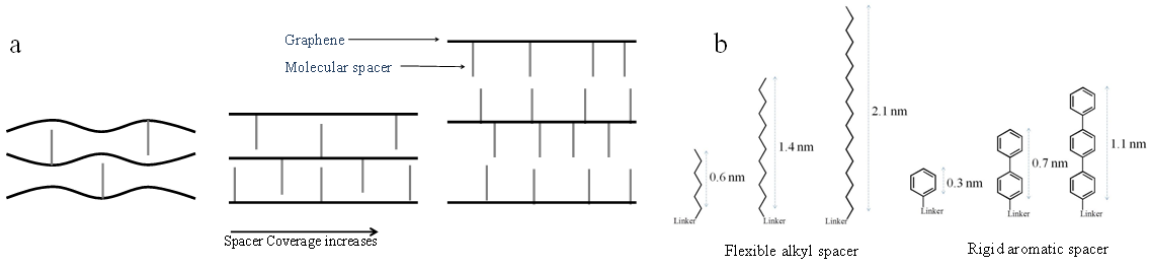

Figure 90. (a) Schematics of graphene with molecular spacer and the evolution of interlayer spacing with the increases of spacer coverage; (B) structures and lengths of optional molecular spacer including flexible alkyl spacer and rigid aromatic spacer. The "linker" refers to the molecular structure used to form covalent bond with graphene.

The second step of this approach is to integrate pseudocapacitive functional groups onto the backbone of the molecular spacer to overcome the restriction of small EDLC and the poor pseudocapacitive performance of conventional metal oxides and conducting polymers. The pseudocapacitive segment locates closely to graphene sheets so that the charge transport will not be affected. Moreover, these pseudocapacitive segments are immobilized on graphene surfaces via covalent bonding, greatly reducing the chance of structural deformation. Therefore, such molecular level integration enables not only large pseudocapacitance but also fast charge transfer and high cycling stability. Figure 91 shows optional molecules and their redox reactions. Phenol/quinone redox couple is one of the fastest redox reactions that can be switched at 10 Hz,[208] and provide a high specific capacitance up to 1800 F/g (Figure 91a). Our research in Chapter 3 demonstrated that functionalized graphene with phenol/quinone modified edges offers

large pseudocapacitance and superior rate performances to conventional pseudocapacitive materials. Simple calculation implies that 10 % coverage of phenol/quinone on graphene (one phenol/quinone group per 10 carbon atoms in graphene) gives rise to a theoretical specific capacitance of 1,150 F/g.[5] Moreover, conducting polymer oligomer is another catalog of pseudocapacitive spacers, which need to be covalently bonded to graphene surface (Figure 91b). The covalent bonding will lead to better charge transfer than physical interactions between conducting polymers and graphene does.

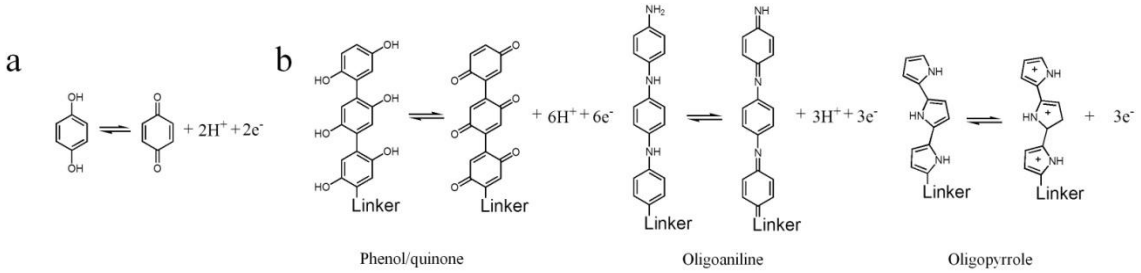

Figure 91. (a) Schematic of the redox reaction using charge/discharge phenol/quinone group and (b) the structure of some optional pseudocapacitive spacers including phenol/quinone groups, oligoaniline and oligopyrrole.

The redox reaction of pseudocapacitive materials occurs at a certain potential, at which a large capacitance is observed. Unfortunately, in most cases, this redox potential lies in the middle of the operation voltages, which means less energy could be stored/extracted during charge/discharge. It is therefore desirable to find a pseudocapacitive reaction that happens at higher potentials. As seen in Figure 92a, the shift of redox potential from V_0 to a high potential of V_1 leads to a much higher energy density, although the specific capacitance does not change. The use of molecular pseudocapacitive spacer in the proposed work offers a highly advantageous flexibility in tuning the redox potential via modifying the pseudocapacitive functional groups. To

[5] At 10% coverage, the loading of phenol/quinone is 48 wt% so that the theoretical specific capacitance is 1800*0.48+550*0.52=1150 F/g.

increase the redox potential, electron-withdrawing groups, such as fluorine, chloride, nitro and trifluoromethyl, can be grafted on the pseudocapacitive spacer by using corresponding precursors, as shown in Figure 92b.[209, 210]

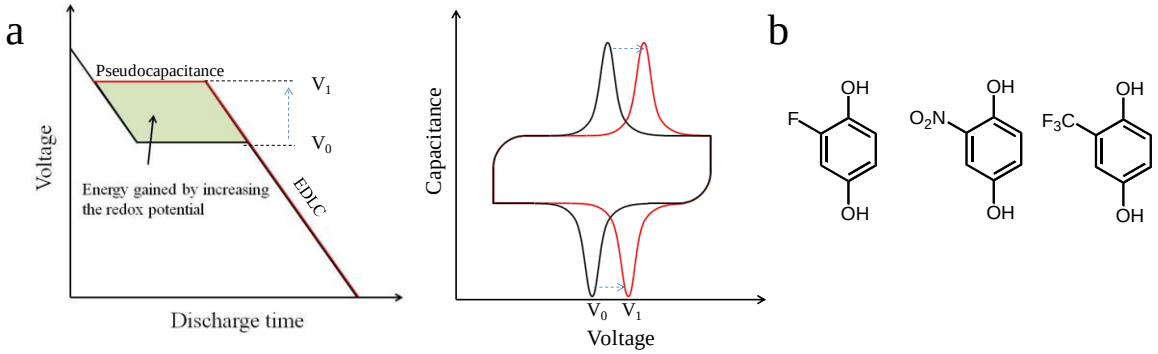

Figure 92. (a) Schematics of the benefit of positively shifted redox potentials in increasing the energy density: discharge curve at constant current density and CV curves showing positively shifted redox potential; (b) electron-withdrawing groups that can be grafted onto phenol/quinone group to shift its redox potential.

The covalent bonding between molecular spacers and graphene is highly desirable. Compared to molecules bonded through non-covalent interactions such as π-π stacking, hydrogen bond or weak Van der Waals forces, covalently bonded molecule spacers have less risk of diffusing out during repeated supercapacitor operation, ensuring a long cycling life. To covalently bond the molecular spacer to graphene, the following chemical reactions (Figure 93) will be worth exploring:

1) *Nucleophilic addition reaction* between the epoxy group and an nucleophile such as amino group is useful when GO is used as the graphene precursor (Figure 93a);

2) *Diazonation and azidation reactions* can graft a conjugated aromatic structure on the sp^2 carbon of graphene and are useful for pseudocapacitive spacers where fast charge transport is needed (Figure 93b and c);

3) *Diels-Alder reaction* is a green reaction that grafts spacers on graphene basal plane (Figure 93d).

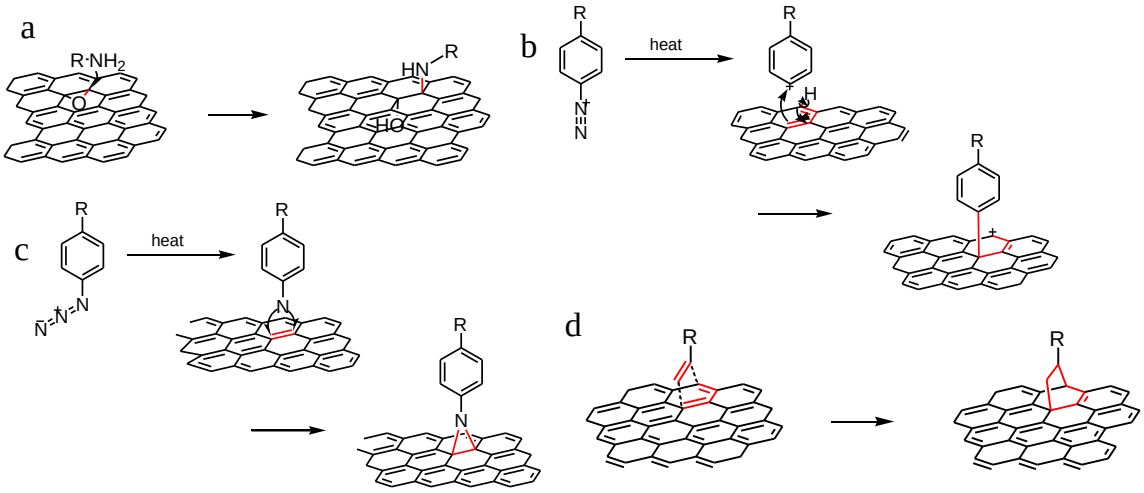

Figure 93. Optional chemical reactions for grafting spacer onto graphene/GO: (a) nucleophilic addition of epoxy group; (b) diazonation reaction; (c)azidation reaction; (d) Diels–Alder reaction.

To integrate the pseudocapacitive capability, spacers with complex structures will be grafted onto the graphene surface. The design of spacer structure and grafting methods is a determining factor for the material performance and cost. There are two generic approaches, "graft from" and "graft to"

a) "Graft from" approach: In this approach (Figure 94a), the first pseudocapacitive segment, after being grafted onto graphene surfaces, will be further chemically modified to generate an active group for reactions with other segments. The synthesis of complex molecular spacer will be carried out on graphene surface. The advantages of this process include high graphene yield, ease to separate and purify graphene from reaction mixture (centrifuge or filtration). However, the control over the structure of molecular spacer will be challenging, and molecular spacers with diverse structures, e.g. different numbers of repeating unit, could be produced. In addition, excessive amount of reagent will be needed to fully modify the spacers on the graphene surface.

b) "Graft to" approach: The second method is "graft to" approach, in which pre-synthesized molecular spacer with complex structures will be one-step grafted onto graphene surface (Figure 94b). This approach will have better control over the uniformity of spacer structure. However, the reaction between molecular spacer and graphene typically has low yield and thus excessive amount of pre-synthesized spacer is needed. Considering that multi-step synthesis of spacer, the cost-effectiveness could be a major issue of this approach.

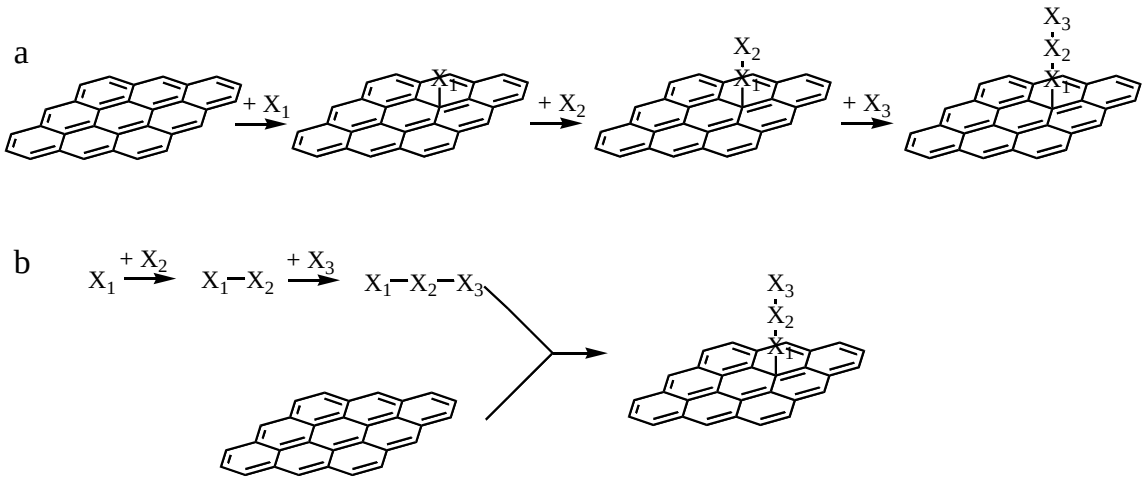

Figure 94. Schematics of grafting pseudocapacitive molecular spacers onto graphene via (a) "graft from" approach and (b) "graft to" approach. X refers the repeating unit in the pseudocapacitive molecular spacer.

The spacer coverage on graphene is a critical parameter in the proposed work, which affects all the materials properties of graphene. The study on these effects will not only benefit the improvement of specific capacitance, but also provide guidelines for tuning the macroscopic properties of graphene-based materials for other applications.

a) Electrical conductivity of graphene: The equivalent series resistances (ESR) and rate capability of supercapacitors are directly affected by the electrical conductivity of electrode materials. Graphene is superior to activated carbon with respect to its high intrinsic electrical conductivity. However, the grafting of molecular spacer will inevitably

introduce defective sp^3 bonds into graphene sp^2 network, producing scattering center and lowering down the charge carrier mobility.[211] On the other hand, the electron/hole doping effect of molecular spacer increases the charge carrier density, compensating decreased the charge carrier mobility.[211] As a result, a complex relationship is expected between the graphene electrical conductivity and spacer coverage. It is expected that at low coverage of molecular spacer, the degradation of electrical conductivity is negligible, while at high coverage the electrical conductivity decrease rapidly, contributing to the internal resistance and lowering the power performance.

b) Interlayer spacing and specific area: the interlayer spacing will increases obviously with the addition of molecular spacer, and reach a value comparable to the length of spacer at intermediate coverage corresponding to the interdigital structure, and a value comparable to 2× of the spacer length at high coverage corresponding to the non-penetrating structure. Accordingly, the specific surface area will increase rapidly with adding molecular spacer until reaching a fully extended stage corresponding to the theoretically surface area. Then it will decrease slightly with coverage due to the additional weight from the spacer.

c) Pseudocapacitance: the pseudocapacitance is expected to increase linearly with coverage at a relatively wide range.

Overall, there will be a "sweet spot" that produces an optimized specific capacitance (Figure 95). In order to find this sweet spot, graphene with gradually changed spacer coverage need to be prepared via tuning a reactant ratio and reaction time.

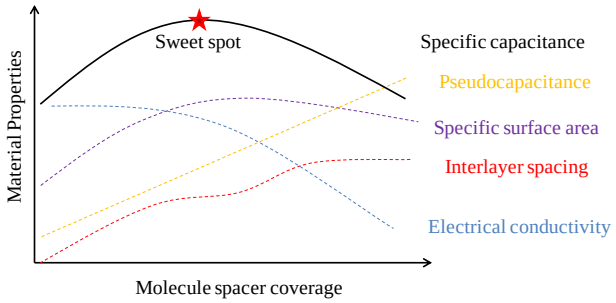

Figure 95. The sweet spot of specific capacitance and different material properties as a function of molecular spacer coverage.

6.2.2 Three-dimensional doped graphene framework-based hybrid catalysts/electrodes

The results depicted in Chapter 4 provide a highly controllable, scalable and flexible method to prepare doped graphene materials for various applications. The knowledge gained through this research could be extended beyond the preparation of NG for ORR to the general areas of electrocatalysis or other electrochemically active electrode. Several promising directions are

- 3D framework to enhance the mass transport

Most of the electrochemical reactions occur at the three-phase boundary, which means that for the reaction to proceed it requires the electron form the electrode, the reactants from the medium, and the catalytic active sites on the electrode materials (Figure 96). As a result, high electrical conductivity, large amount of catalytic sites, and good diffusion of reactants are critical for high catalytic performance. We have been focusing on increasing the number of active sites while maintaining good electrical conductivity, while paid less attention to enhance the mass transport. The findings on 3D assembly of graphene by adding PPy and PANI provide new opportunities to produce 3D graphene structure. Such 3D framework could be preserved after freeze drying or

supercritical drying. Moreover, the 3D structure offers better mechanical robustness, making it possible to direct use it as the electrode without adding binders and the tedious electrode preparation process.

– Boron, phosphorus or sulfur doping or co-doping

There are many options to dope graphene other than N. Several papers have reported B-, P-, and S-doped graphene that also exhibit ORR catalytic activity.[212-216] Therefore, it will be meaningful to utilize our process to formulate B-, P-, and S-doped or co-doped graphene for electrocatalysis applications.

– Synergetic effect between the dopants and other nanomaterials

Instead of as active catalyst, the doped graphene could be used as catalyst support for other nanomaterials (Figure 96b), such as metallic nanoparticles, quantum dots, biomaterials etc.[217-219] The special chemical and electronic property of doped graphene may have synergetic effect with these nanomaterials and bring in more intriguing applications.

– Extended applications in batteries, supercapacitors and electrocatalysis

The NG has other applications in lithium-ion batteries,[174] supercapacitors,[99] carbon dioxide storage[220] and carbocatalysis.[221] It will be very interesting to characterize our NGs for these applications, though the desirable N-functional groups may be different.

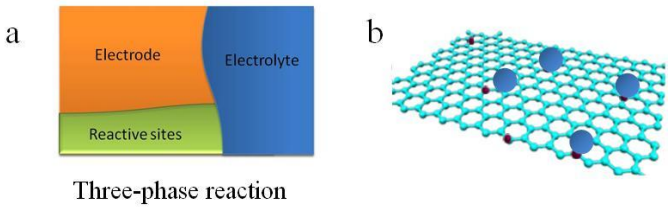

Figure 96. Schematic of (a) three-phase reaction and (b) the hybrid of doped graphene and nanoparticles.

APPENDIX A

ROBUST VERTICALLY ALIGNED CARBON NANOTUBE-CARBON FIBER PAPER HYBRID AS VERSATILE ELECTRODES FOR SUPERCAPACITORS AND CAPACITIVE DEIONIZATIOND

Introduction

The vertically aligned carbon nanotube (VACNT) array is a promising electrode material for supercapacitors,[222-225] batteries,[226-228] sensors[229, 230] and capacitive deionizer because of the outstanding material properties of CNT such as high specific surface area, excellent electrical conductivity and superior chemical stability. The vertical alignment in VACNT is another attracting feature for its application in energy storage and conversion devices. This special architecture leads to much shortened electrolyte diffusion paths compared to the tortuous ones for conventional electrodes. The enhanced mass transport along the alignment direction results in superior rate performance and the possibility of making ultra-thick battery electrodes or 3D batteries. Several research groups have demonstrated that the VACNT-based supercapacitor electrodes offered superior power density to conventional activated carbon and non-aligned CNTs.[222, 223] The VACNT was also used as a 3D platform for the deposition of active materials for high power lithium ion batteries, lithium sulfur batteries, etc.[226-228]

VACNT is usually synthesized using a chemical vapor deposition method. The substrate for VACNT growth typically consists of metal nanoparticles on several insulating layers, such as silicon oxide, alumina oxide etc. These insulating layers help

immobilize the catalyst particles for efficient CNT growth, which however turns out to be a great obstacle for many applications where electrical conductivity is required. Therefore, the hybrid material of VACNT on a conductive substrate is attracting for practical applications. The growth of VACNT directly on conductive substrate was researched and has been realized in several reports.[225, 231, 232] Unfortunately, the overall quality of CNTs and the controllability of growth are not as good as those of CNTs made by conventional growth methods. The transfer of VACNT to conducting substrate is another straightforward solution. Successful transfer of VACNT has been achieved by using low temperature melting solder[233] or through covalent bonding with various self-assembled monolayer.[234, 235] Good electrical conductivity and well-maintained alignment were obtained in those reports; however, the sophisticated process and the use of reactive materials limit the practical applications of VACNT. Dry contact transfer and polymer adhesive transfer technologies are thus developed with a simplified process, which utilizes the strong Van der Waals interaction and polymer adhesion force respectively. [236-240] A potential issue for these methods is the mechanical robustness, which is critical for practical applications but was not studied in those reports.

In this work, we fabricated a hybrid structure of VACNT arrays on carbon fiber paper (CFP) substrate and studied its performance as supercapacitor and deionizer electrodes. The VACNT-CFP is fabricated by transferring VACNT on to CFP substrate with the help of silicone as an adhesive. This process is schematically depicted in Figure 97. Various CNTs can be transferred independent on their height and dimensions. The silicone elastomer is chosen because it is highly chemically stable, resistant to most of solvents, and most importantly, flexible and stretchable that will not alter the mechanical

property of substrate. Though VACANT can be transferred to arbitrary substrate using this approach, the CFP is specially chosen because of its low cost, good electrical conductivity and chemical inertness. With large contact area between VACNT and CFP, surprisingly low interface resistance is found between VACNT-CFP despite the pure Van der Waals interaction. Such all-carbon hybrid with a small amount of silicone adhesives is an attracting material as the electrode for energy storage devices because of the superior chemical stability. Indeed, excellent performance was found when the VACNT-CFP was tested as supercapacitor and deionizer electrodes.

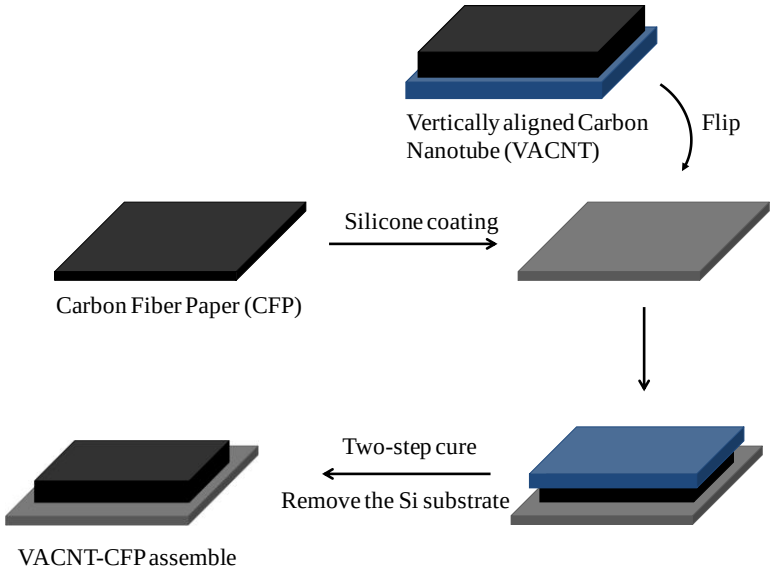

Figure 97. Schematic illustration of the fabrication process of VACNT-CFP assembles. Reprinted with permission from [241]. Copyright 2013 Elsevier.

Experimental

VACNT growth

VACNT arrays were synthesized in a 1.5-inch diameter aluminum tube furnace. The catalysts were prepared by a sequential electron-beam deposition of Al (10 nm) and Fe (2.0 nm) on Si wafers with a 300 nm SiO_2 layer. CNT growth was carried out at 750

°C with 350 sccm Ar, 150 sccm C_2H_4, and 300 sccm H_2. The water vapor was introduced into the furnace by bubbling Ar gas through water.

Preparation of VACNT-CFP assembles

In a typical process, silicone resin (Dow Corning HIPEC Q1-4939, Part A: Part B=1:1) was carefully coated on the as-received carbon fiber paper (CFP, 2050-A from Fuel cell store) at a loading of ~ 20 mg/cm^2. VACNT of 1×1 cm^2 was flipped on the CFP. Then the silicone was cured at 110 °C for 1 hour, during which 20 g weight was applied to improve the contact between VACNT and CFP. After that, the Si substrate was removed and the VACNT was left on CFP. Finally, the silicone resin was fully cured at 150 °C for 1 hour.

Characterizations

SEM LEO 1530 was used to characterize the morphology of samples using an accelerating voltage of 4 kV. Nitrogen-adsorption/desorption measurements were conducted on an Autosorb-1 analyzer (Quantachrome Instruments, Boynton Beach, FL, USA). The electrical resistance of VACNT-CFP was measured using a Keithley 2000 multimeter and a Hewlett-Packard 6553A DC power supply. The electrochemical measurements, including CV, galvanostatic charge/discharge and electrochemical impedance spectroscopy, were measured on a Versastat 2-channel system (Princeton Applied Research). The supercapacitor and deionization tests were tested in a beaker-type cell using a two-electrode configuration. Each VACNT-CFP was clipped to the end of a CFP strip and the other end of the CFP strip was connected to metal clips. The electrolyte was 1 M NaCl aqueous solution. Only the VACNT-CFP and CFP strip was immersed in the electrolyte to avoid the corrosion of metal clips. The distance between VACNT-CFP

electrodes is ~5 mm. Before the electrochemical measurements, VACNT-CFP was treated by UV-ozone at room temperature for 20 minutes in order to improve the wetting of CNTs with aqueous electrolyte.

Results and Discussion

Figure 98a shows the cross-section image of a typical VACNT array with a thickness of 660 um. The vertical alignment of CNTs is evident from Figure 98 b and c. The CNTs are multi-walled with a diameter of ~ 20 nm. The high thickness uniformity ensures good contact between the VACNT surface and CFP, and is a critical factor for the successful transfer of VACNT. Figure 98d shows the morphology of CFP and the diameter of each carbon fiber is ~ 8 um. The porous structure of CFP causes empty space where CNT tips have no direct contact with carbon fibers. This issue is mitigated by the highly entangled VACNT tips (Figure 98b) which increase the contact area at CNT-CNT, enabling the transverse contact and electron transport between adjacent CNTs.

Figure 99 shows the morphology of a VACNT-CFP. After transfer, the vertical alignment of CNTs is well maintained and no buckling of CNT was observed. The top surface of the VACNT-CFP corresponds to the root of VACNT arrays. As seen in Figure 99b and c, the catalyst particles can be observed as bright dots on the top surface. The interface morphology between VACNT and CFP is shown in Figure 99d and e. Both CFP and the bottom of VACNTs are impregnated with silicone, and this provides the adhesion force for CNT transfer. Examinations of different locations find that the bottom 5 to 20 um of VACNT is covered by silicone. This part of VACNT cannot contribute to the adsorption of ions, however it only counts less than 5 % of total surface area when thick VACNTs films are used (>500 um). Therefore, the loss of surface area by using silicone

resin could be negligible. Moreover, the silicone resin is highly flexible and stretchable so that flexible VACNT structure can be made if a flexible substrate is used. We successfully transferred the VACNT on a bulky paper using the same approach. As shown in Figure 99f, the VACNT-bulky paper shows excellent flexibility.

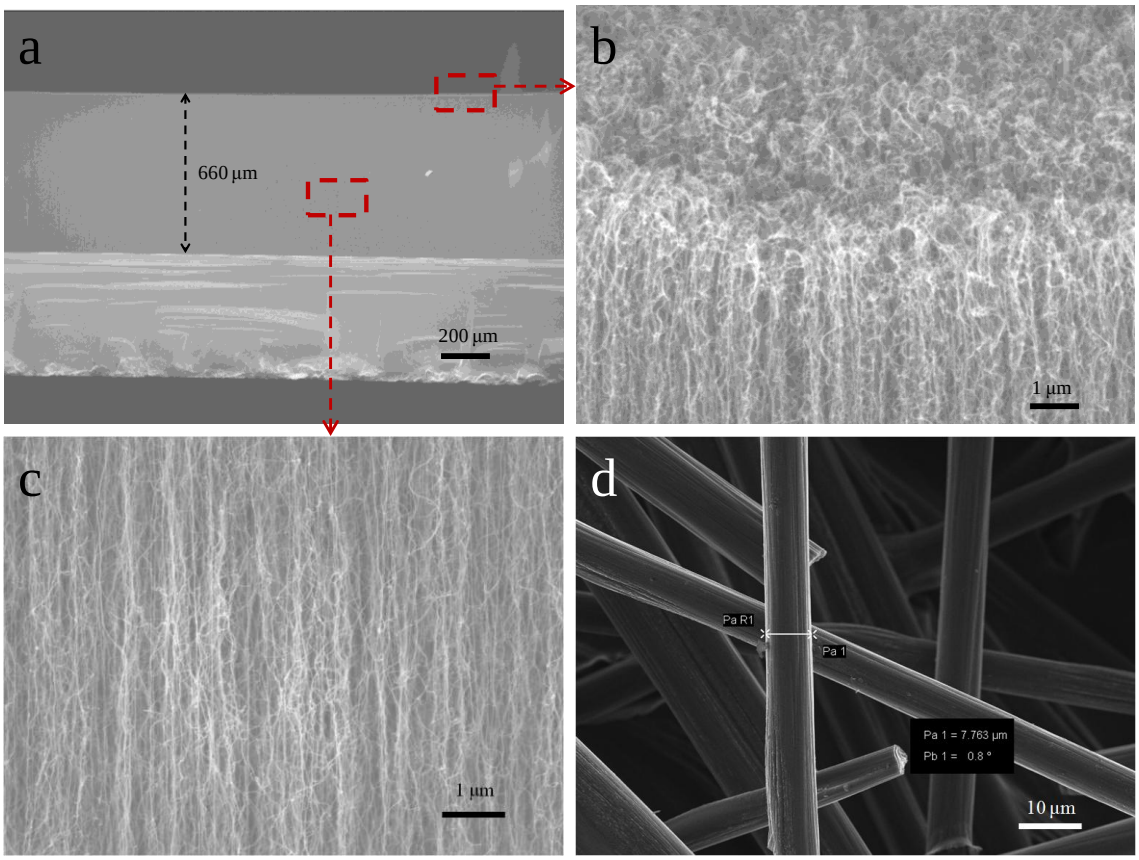

Figure 98. SEM images of (a) the cross-sections of VACNT, (b) bird view of VACNT top surface, (c) high magnification image of VACNT and (d) CFP. Reprinted with permission from [241]. Copyright 2013 Elsevier.

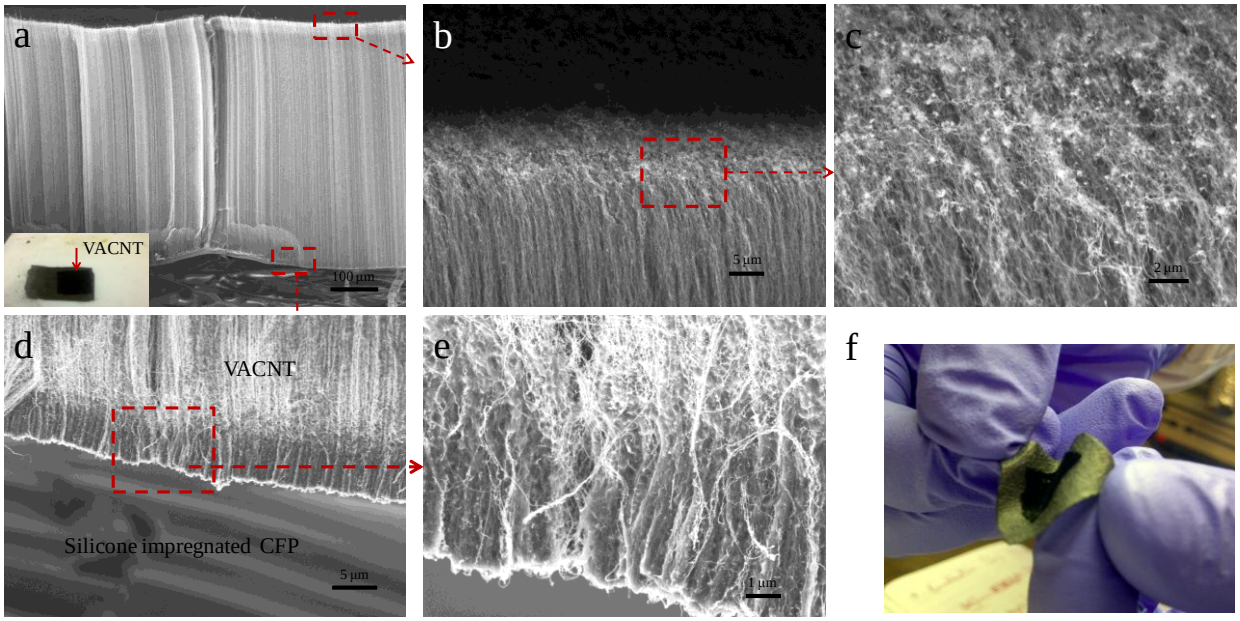

Figure 99. SEM images of (a) VACNT-CFP assemble, (b, c) the top surface of VACNT-CFP assembles, and (d, e) the interface between CFP and VACNT. The CNT covered by silicone resin is darker than uncovered one. (f) Rumpling of flexible VACNT-bulky paper assemble. Reprinted with permission from [241]. Copyright 2013 Elsevier.

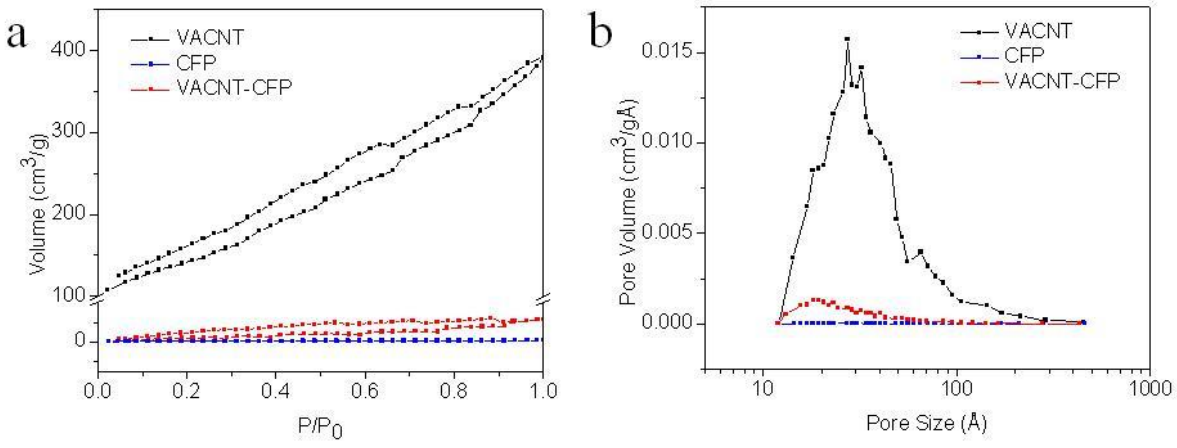

Figure 100. Nitrogen adsorption–desorption isotherm (a) and the pore size distribution (b) of VACNT, CFP, and VACNT-CFP. The pore size distribution was calculated from the adsorption branch on the basis of the Barrett–Joyner–Halenda (BJH) model. Reprinted with permission from [241]. Copyright 2013 Elsevier.

Figure 100 shows the BET and microporosity measurement of VACNT, CFP and VACNT-CFP. The surface area of VACNT is 474.3 m^2/g, which is typical for multi-walled CNTs. The introduction of VACNT onto CFP increases the surface area from 0.9 m^2/g for CPF to 5.8 m^2/g for VACNT-CFP, as shown in Figure 100a. Such increase in surface area is significant, considering the low content of VACNT (< 2 wt%). The pore size distribution results in Figure 100b show the existence high percentage of 2-10 nm mesopores in both VACNT and VACNT-CFP, which could make significant contribution

For the electrical measurement of VACNT-CFP assemble, Ti/Au (30/150 nm) electrodes with a diameter of 500 um were deposited on the top surface of transferred VACNT and the CFP substrate by electron-beam evaporation (Figure 101inset). The electrical resistance of VACNT-CFP was measured using a four-probe method. As shown in Figure 101, typical ohmic contact behaviors in current-voltage are observed for both CFP and VACNT-CFP. The resistance of the CFP substrate is 0.052 Ω, whereas the resistance from VACNT top surface to CFP substrate shows a slightly higher value of 0.058 Ω. The increase of resistance results from the contributions of the VACNT-CFP interface resistance and the resistance of the VACNT, while the latter is largely negligible because of the high electrical conductivity of VACNT. Therefore, the interface resistance can be calculated as 0.058-0.052=0.006 Ω. The excellent electrical transport through VACNT-CFP interface is evident as interface resistance is as low as ~ 0.006 Ω, which is sufficient for most of energy storage and conversion devices. Because no special modification was carried out on VACNT and CFP surfaces, the interaction between VACNT-CFP is pure Van der Waals force. The low interface resistant could be attributed to the large contact area between VACNT-CFP and thin interface thickness. Though the

electrons transport through the Van der Waals interaction is inferior to that through conjugated bonds, the electrical resistivity of graphite in c-axis is still as low as ~ 0.005 Ωcm.[242, 243] The large contact area by entangled CNT tips is equivalent to large cross-sectional area, which lowers the electrical resistance according to the classic ohms' law. Compared with previous works, the resistance of VACNT-CFP in this work is comparable to those of reports using low temperature melting solder[233] and self-assembled monolayer,[234] but significantly lower than those of works using polymeric adhesives.[237, 239, 240]

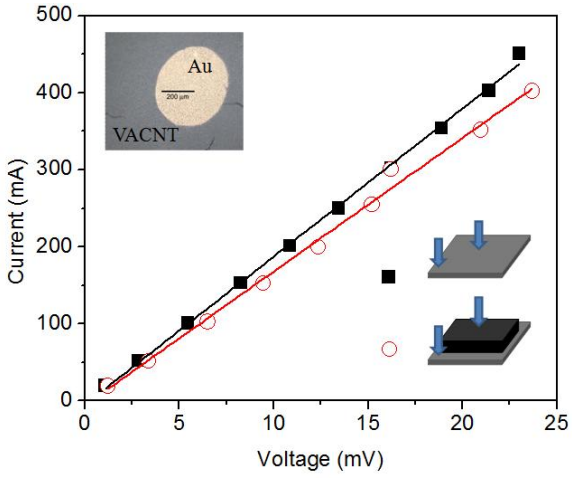

Figure 101. Current-voltage curves of CFP and VACNT-CFP. Inset is the picture of Ti/Au electrode on VACNT surface. Reprinted with permission from [241]. Copyright 2013 Elsevier.

The electrochemical performance of VACNT-CFP was tested in a two-electrode configuration using 1 M NaCl aqueous solution as the electrolyte. Two nearly identically VACNT-CFP were fabricated with ~ 1×1 cm^2×0.1 cm (VACNT height) VACNT arrays. Figure 102a shows the CV curves. The VACNT-CFP shows a typical EDLC behavior with rectangle CVs. The area of CV for VACNT-CFP is considerably larger than CFP alone, due to the large surface area of VACNTs. In order to investigate the high rate

performance of VACNT-CPF, we used fast scanning rates from 100 mV/s to 1 V/s, corresponding to discharge time of 10s to 1s, which is significantly quicker than the operation of typical activated carbon- and randomly packed CNT-based supercapacitors. Remarkably, at a high scanning rate of 1 V/s, the shape of the CV curve of VACNT-CFP is still close to rectangle, indicating the excellent electrical and ionic transport properties. The areal capacitance of VACNT-CFP is calculated from the CV curve using the equation: $C = \frac{\int IdV}{S\Delta Vr}$ where C is the areal capacitance, I is the current, V is the applied voltage, S is the area of one VACNT electrode, ΔV is the range of voltage scan and r is the scanning rate. The areal capacitance is found to be 6.1, 5.2, and 4.5 mF/cm^2 at scanning rates of 100, 500, 1000 mV/s, respectively. Moreover, constant current charge-discharge was carried out using difference current densities (Figure 102b). The linear charge and discharge curves further confirm the pure EDLC behavior of VACNT-CFP. The areal capacitance can be calculated by $C = \frac{It}{S\Delta V}$, where t is the discharge time. The areal capacitances are 6.7, 6.3, and 6.1 mF/cm^2 respectively at current density of 0.1, 0.2 and 0.5 mA/cm^2.

The cycling stability is an important requirement for supercapacitor electrodes. We carried out cycling test using a charge-discharge current density of 0.5 mA/cm^2. Instead of decreasing, the areal capacitance of VACNT-CFP increase slightly at first 2000 cycles (Figure 102c), owing to the improved wetting by applying a potential.[244] The capacitance is very stable and shows no degradation after 10,000 cycles. Moreover, the electrochemical impedance spectroscopy of VACNT-CFP before and after the cycling tests shows negligible changes (Figure 102d), indicating the superior stability of the

interfaces between VACANT and CFP. The equivalent series resistance (ESR) is 7.1 ohm before cycling and 7.6 ohm after cycling. The main source of ESR is the electrical wiring in the test setup as the CFP-only control sample shows a comparable ESR. The EIS curve at low frequency region shows a large phase angle of > 80 °, indicating a nearly ideal EDLC behavior.

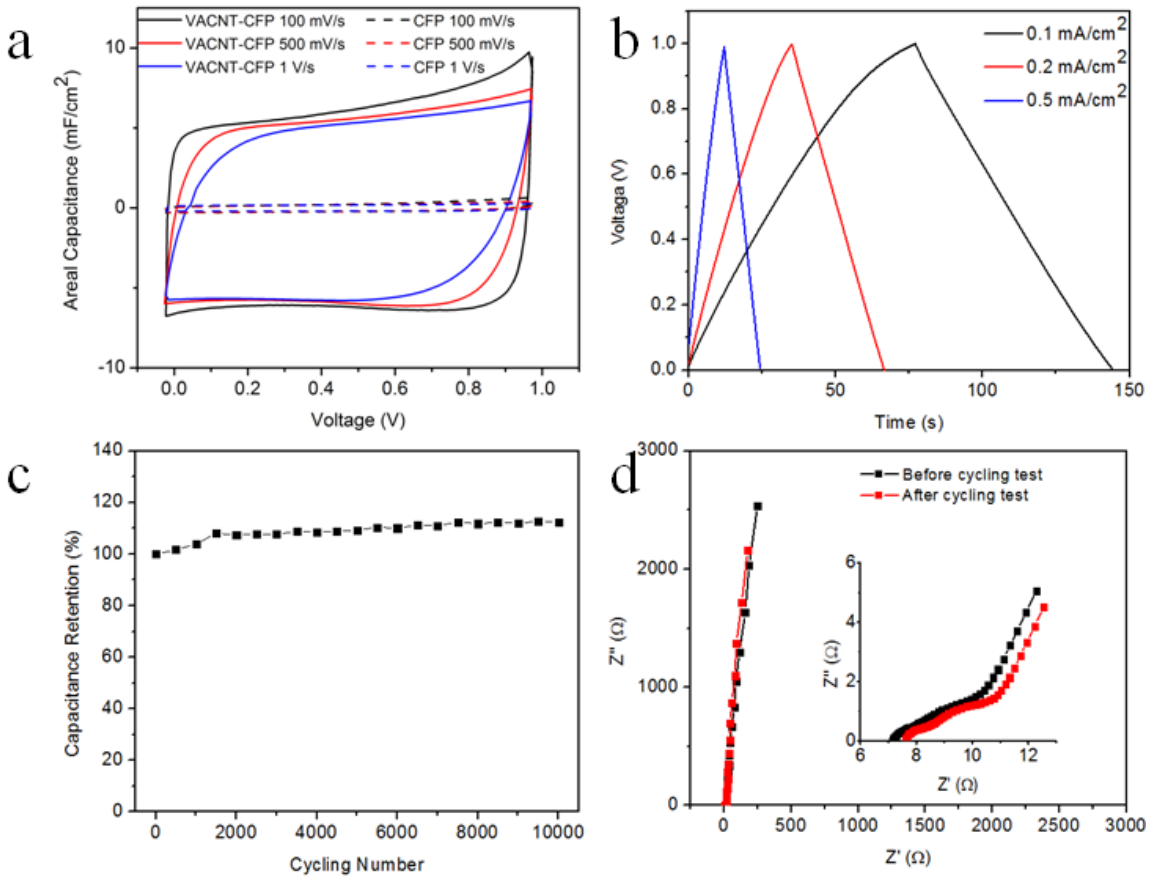

Figure 102. (a) CV curves of the VACNT-CFP assemble and CFP control sample at different scanning rate. Charge-discharge curves (b) and cycling test of VACNT-CFP. (d) The EIS of VACNT-CFP before and after cycling test. Reprinted with permission from [241]. Copyright 2013 Elsevier.

Another important application of VACNT is water deionizer, which has the same working principle with supercapacitors. For this application, the good adhesion of VACNT on substrate is required in addition to electrochemical properties in order for the VACNT to survive from the water flow. The mechanical robustness is becoming more

critical for miniaturized deionization devices in microelectronic cooling loops where the flow rate of water can be up to several lither per minute. In order to evaluate the resistance to the impact of water flow, VACNT-CFP was first put under flowing tap water. No noticeable damage or change of electrical properties was found, suggesting the strong interface bonding. Further, we investigated the performance of VACNT-CPF under flowing electrolyte. A peristaltic pump was used to control the flow rate from 0 up to 2000 mL/min (Figure 103a). The CVs of VACNT-CFP was recorded and shown in Figure 103b. The shape of CV shows little changes with the flowing rates, suggesting the superior mechanical reliability of VACNF-CPF assembles.

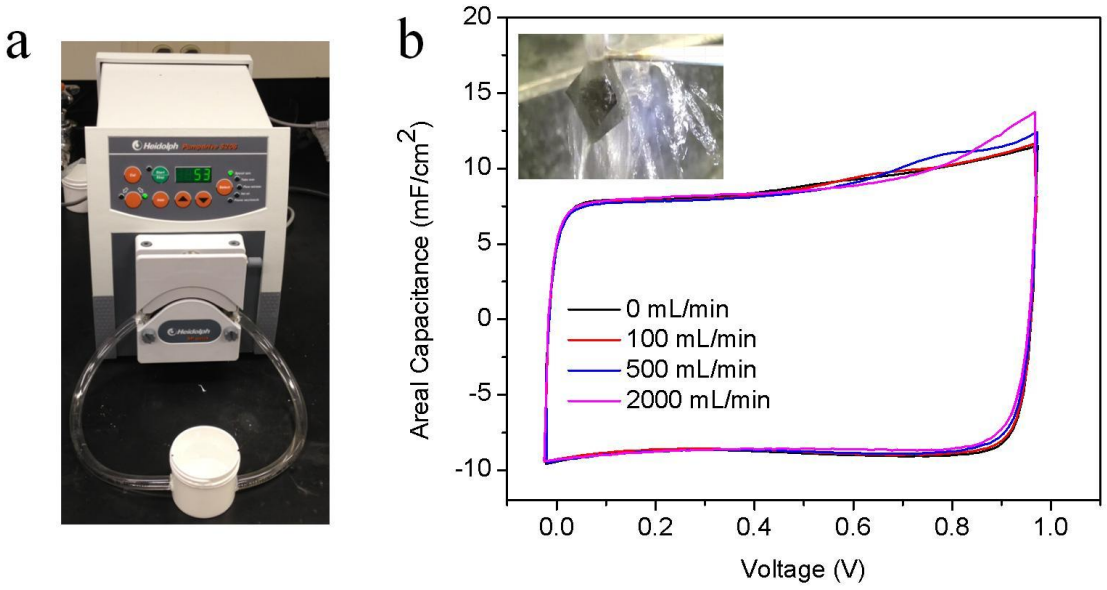

Figure 103. (a) The peristaltic pump and setup for testing the performance of VACNT-CFP in flowing water. (b) CV curves of VACNT-CFP with different flow rate; the scanning rate is 100 mV/s. The inset is a picture shows VACNT-CFP survives from the impact of flowing tap-water. Reprinted with permission from [241]. Copyright 2013 Elsevier.

Summary

In summary, we successfully fabricated a VACNT-CFP hybrid structure by transferring VACNT onto a CFP substrate with the help of a silicone resin adhesive. Surprisingly low interface resistance was observed at the VACNT-CFP interface due to the large contact area despite the pure Van der Waals interaction. We demonstrate that the VACNT-CFP can be used as high performance electrodes for supercapacitors and deionizers with excellent rate performance and mechanical robustness. Such VACNT-CFP can be also used as a current collector for ultra-think battery electrode or 3D battery.

APPENDIX B

PREPARATION OF WATER-BASED CARBON NANOTUBE INKS AND APPLICATION IN THE INKJET PRINTING OF CARBON NANOTUBE GAS SENSORS

Introduction

Carbon nanotubes (CNTs) have been widely studied as a functional component in portable gas sensors operating at ambient temperate and with ultra low/zero power, due to its excellent property including high electrical conductivity, specific surface area and chemical stability etc. Various carbon nanotube-based gas sensors have been demonstrated with high sensitivity for NO_2, NH_3, NO etc.[245] Recently by using single walled CNTs, a part per billion (ppt)-level detection of NO_2 has been achieved.[246] However, most of previous studies on CNT-based sensors, focusing on high sensitivity, require complicated fabrication processes and are very difficult to scale up. This is largely due to the lack of reliable methods to accurately position CNTs between microelectrodes, and the high cost of the photolithography process. Facile and reproducible fabrication processes are needed for integrating CNTs in real sensor devices for practical application.

Inkjet printing is as one of key technologies in emerging printed electronic devices which can achieve precisely and spatially controlled deposition of various materials on arbitrary substrates, and has found wide application in the miniaturization of electronic packaging, optical and medical devices as well as sensors.[247] In particular, inkjet-printed gas sensors have drawn an increasing interest due to its low cost, large-

scale production and the wide application in public safety related areas. Previous research efforts have focused on inkjet printing of conducting polymers, such as polyaniline, and excellent gas sensing capabilities (10 ppb detection of NH_3) has been observed.[248] However, to prepare the ink, sophisticated procedures are often required to control the morphology and dispersion of conducting polymers in solvent. As an alternative material for inkjet-printed gas sensor, CNT is advantageous due to its predefined morphology that simplifies the ink preparation process and the aforementioned gas sensing properties. We have previously studied the fabrication of CNT-based wireless sensors via inkjet printing, using CNT in DMF as the ink.[249] The use of proper organic solvents, such as DMF and NMP, is necessary for the good dispersion of CNTs in these organic solvents. However, most organic solvents are very toxic, and this brings considerable environmental and safety concerns. In this regard, water-based CNT ink is highly desirable for "green" printing technology.

In this study, a water-based CNT ink is developed by direct dispersing functionalized CNTs in water. The functionalized CNT is prepared via an oxidation process, which introduces hydrophilic oxygen-containing functional groups on the surface of CNT. As a result, a good dispersion of CNT in pure water can be obtained without the help of toxic organic solvent or extra surfactant that are necessarily in previous studies. [249, 250] In our experiment, multi-walled CNT are used as the starting material because their outer walls can be used for chemical modification, while the inner walls maintain the structural integration and thus electrical conductivity. The water-based CNT ink was inkjet-printed on paper, a low-cost, flexible and light-weight substrate. The gas sensing property of inkjet-printed CNT is investigated and a higher sensitivity toward

NO_2 is observed. The eco-friendly water-based CNT ink shows a promising application in large scale production of CNT gas sensors.

Experimental

Preparation of water-based CNT ink

The pristine CNT is purchased from Sun Nano (Nanchang, China), which has a diameter of 10-20 nm and a length of 10-15 μm. The functionalization of CNT was carried out via a modified oxidation process in a previous report.[116] In a typical experiment, 0.5 g as-received CNTs was dispersed in a mixture of 80ml H_2SO_4 and 94 ml HNO_3. The solution was then sonicated at 60°C for 2 hours (B2500A-MTH, VWR). The functionalized CNT was separated by vacuum filtration, washed with adequate water to remove residual acids, and dried overnight at 60 °C in an oven. Then, dried CNT powder was collected and dispersed in water at a concentration of 5 mg/mL. Sonication was applied until a uniform dispersion was obtained. Glycerol was added to CNT-water dispersion with a weight ratio of 1:3 (glycerol: water) to meet the viscosity and surface tension requirements for inkjet printing.

Inkjet Printing of CNT

A Dimatix Materials Printer (DMP-2800 Series) was used for inkjet printing of CNT ink onto a Kodak photo paper substrate. A10 pL cartridge was chosen, providing a 2 μm diameter nozzle for accurate deposition while maintaining a good passage of CNT through the printer. The temperature of printer platen was set to 60°C to assist in the evaporation of water and glycerol. Additionally, the print head was set at 40°C, with a voltage on each muzzle which is set independently between 34-40V and calibrated by

observation on the drop watcher. Careful calibration of the printer was necessary to ensure the optimal fluid flow and good printing results. The fabrication procedure was separated into two parts, fabrication of the silver metallic traces and subsequent deposition of CNTs. First, 10 layers of silver ink (CCI-300, Cabot Corporation) were deposited and cured under 120°C for 8 hours. Next, the CNT ink was printed via following procedures: First, 25 layers of CNTs were deposited with periodically cleaning the print head; then the CNT on paper was baked at 150 °C in an oven to remove the solvent and any traces of glycerol. The printing process was repeated to achieve 50, 75, and 100 total layers. The 75 layers CNT samples have been chosen for sensor characterizations.

Characterizations

FTIR characterizations were performed at ambient temperature with a spectrometer (Nicolet, Magna IR 560). Raman characterizations were carried out using LabRAM ARAMIS, Horiba Jobin Yvon with a 532 nm wavelength laser. The microscopic structure of printed CNTs on paper was observed in SEM (LEO 1530) operated at an accelerating voltage of 4 kV. The gas sensing property of printed CNT was examined by a TIN-TEK FlexStream gas generator. A network analyzer (Rohdes and Schwarts ZVA 8) was used to measure the impedance of inkjet-printed CNT sensor from 50MHz to 3GHz. All samples used for frequency sweep were printed using 75 layers of MWCNT and 10 layers of a conductive silver ink. The testing procedure was as follows: (1) the impedance measurement in air; (2) cleaning by purging pure nitrogen for 5 minutes; (3) introducing 10 ppm NO_2 and impedance measurements;(4) purging N_2 for the recovery time measurements.

Results and Discussion

In general, pristine CNT has very poor dispersion in water due to its intrinsic hydrophobicity. Therefore, to prepare water-based CNT ink, hydrophilic groups are introduced into the outside wall via an oxidation process in the acid mixture of H_2SO_4 and HNO_3. Various oxygen containing functional groups on CNT surfaces help achieve a much better dispersion of CNT in water as a result of their polar and ionic nature. As seen in Figure 104, a stable CNT solution in water/glycerol with a concentration up to ~ 5 mg/mL in water can be prepared for inkjet printing, which still maintains a good dispersion after 1 month. These functional groups are investigated by FTIR, as shown in Figure 105a. The peaks at ~3400, ~ 1717, ~ 1633, ~ 1100 cm^{-1} are from the –OH, C=O in carboxyls, unoxidized C=C edges and C-O groups respectively,[48, 110] which confirm a successful functionalization of CNT. Another function of severe oxidation process is to cut the long CNT (> 10 μm) into shorter pieces,[251] which is critical to allow CNTs to pass the small nozzle (2 μm) during printing. The Raman spectra of CNTs before and after oxidation are shown in Figure 105b. The peaks at ~ 1330 cm^{-1} is defect-related D peak, while the peak at ~1565 cm^{-1} is called G peak which results from the graphitic strcuture in CNTs. The intensity ratio of D peak and G peak (I_D/I_G) ratio is an important parameter to study the structure of carbon materials. According to the empirical Tuinstra-Koenig relation, the I_D/I_G ratio is inversely proportional to the size of nanocrystalline graphite.[85] The fact that I_D/I_G ratio increases from 1.25 to 1.41 after oxidation reaction indicates that more defects, probably in the form of oxygan-containing functional groups, are created on the CNT surface, which is consistent with FTIR result.

Figure 104. CNT ink (~5 mg/mL water). Reprinted from [252]. Copyright 2011 ASME.

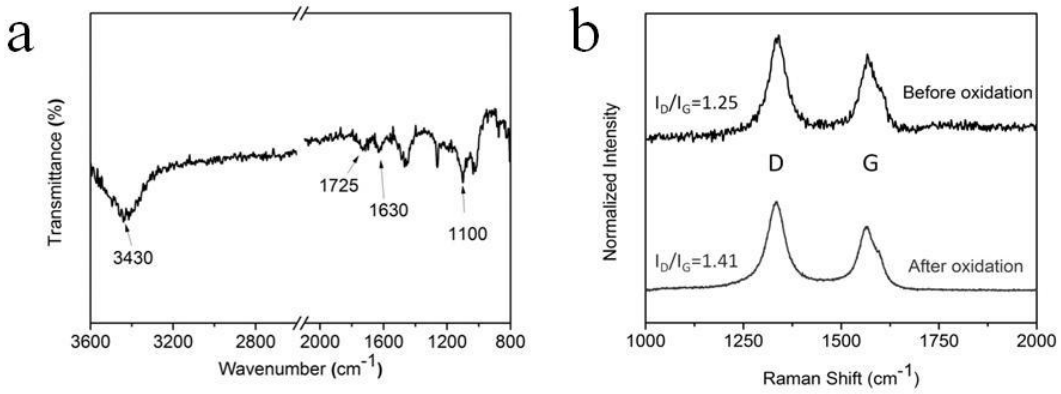

Figure 105. (a) FTIR spectra of functionalized CNTs and (b) Raman spectra of CNTs before and after oxidation. Reprinted from [252]. Copyright 2011 ASME.

The water-based CNT ink was directly printed on a paper substrate after a mild sonication, which is shown in Figure 106. A commercial silver ink was printed before printing CNT to provide electrical conductivity. The CNTs were printed between silver lines in the form of a rectangle. The microscope morphology of printed CNT on the paper substrate was observed by SEM (Figure 107). As seen in Figure 107a, the surface of CNT is relatively smooth, indicating the uniformity of the water-based CNT ink. From the zoomed in image in Figure 107b, it is found that CNTs are highly entangled with polydispersed diameters, ranging from ~ 10 to ~ 50 nm. However, it is very difficult to

estimate the length of CNT from the SEM images. In order to measure the thickness of printed CNT layer, bird-view image was taken, which is shown in Figure 107c. The printed CNT layer on paper substrate is clearly seen. The thickness of 50-layer CNT is estimated to be ~ 1 um. The boundary between CNT and Ag was also imaged where CNT is tightly covered on the nanosized Ag particles, forming the electrical contact (Figure 107d).

The DC conductance of the printed CNT was measured for the various numbers of layers using a standard digital multimeter. Three samples were measured for each number of layers and the average values are shown in Table 5. It is found that the DC conductance increases when more layers of CNTs were printed, due to the larger conducting cross-section. However, the thickness of printed CNT may not be proportional to number of layers so that measured DC conductance does not linearly increase with the number of printed layers.

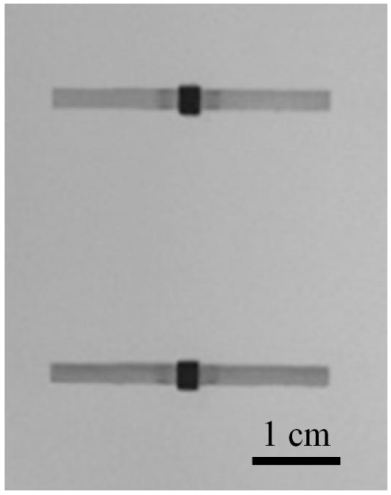

Figure 106. Optical Image of printed CNT sensors: the black rectangle and bright long patterns are printed CNTs and silver ink, respectively. Reprinted from [252]. Copyright 2011 ASME.

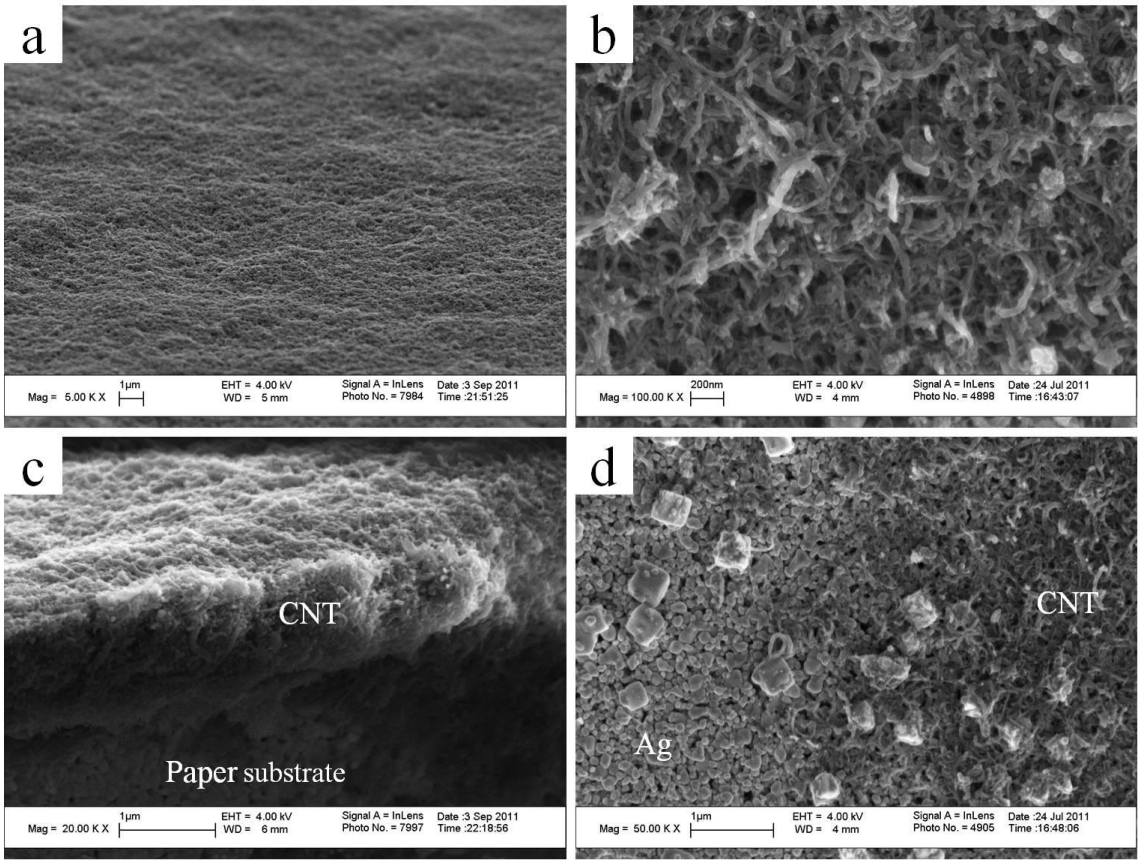

Figure 107. SEM images of printed CNT: (a) bird view of CNT surface at an angle of 30 °; (b) morphology of CNT at high magnification; (c) bird view of CNT-paper interface at an angle of 30 °C; (d) CNT-Ag boundary. Reprinted from [252]. Copyright 2011 ASME.

Table 5. DC Characteristics of printed CNT sensor. Reprinted from [252]. Copyright 2011 ASME.

Number of Layers	25	50	75	100
DC Conductance [mS]	1.514	2.521	3.717	4.228

To demonstrate the gas sensing capability of inkjet-printed CNT, NO_2 was introduced into the CNT surfaces at different concentrations ranging from 10 - 90 ppm. Selected result on a printed 75-layer CNT is given in Figure 108. The particular frequencies were chosen due to their placement in non-licensed spectrum bands, facilitating device development. In particular, 2.4 GHz belongs to the U.S. industrial,

scientific and medical (ISM) radio bands. 10 ppm NO_2 is introduced to the CNT sensor as a minimum concentration. A sharp increase of RF conductivity at 2.4 GHz upon that small concentration of NO_2 exposure was observed, indicating a quick response of the CNT sensor. The response time is in the level of several seconds. After the conductivity reaches the equilibrium, the increase of conductivity is found to be up to ~ 30%, which is typical for CNT-based NO_2 sensors. After NO_2 exposure, N_2 was applied again to study the recovery time of CNT sensor. It is found that the recovery time is very long, which is typical for CNT-based NO_2 sensors. The long recovery time could be attributed to the strong interaction between CNT and NO_2. For example, electron-rich groups on CNTs, such as –OH groups have strong chemical bonding with the electron-withdrawing molecule NO_2. Moreover, the large thickness of the CNT layer also contributes to long recovery time.

The mechanism of the electrical property change of CNT by certain gases has not been clearly understood yet. Among several proposed mechanisms, "charge transfer" has been most discussed. For CNTs functionalized by oxygen-containing groups, a p-type behavior is usually observed where holes are main charge carriers.[253] Meanwhile, the analyte NO_2 molecules act as hole donors when interacting with CNTs, which can transfer ~ 0.1 hole per molecule.[254] Thus in the presence of NO_2 the electrical conductance of CNTs increases as a result of higher charge carrier density. Moreover, it has been reported defects on the outside wall of CNTs enhance the interaction of NO_2 with CNT, which improves the sensitivity.[255] Further researches should be made to elucidate the sensing mechanism, especially the role of defects, and facilitate carbon materials for RF wireless sensor applications.

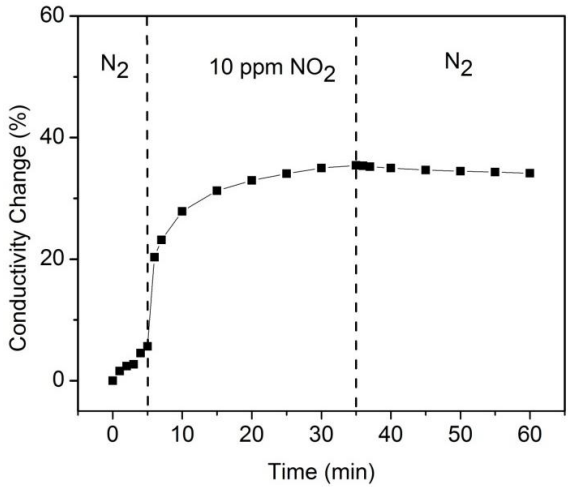

Figure 108. The conductance change of inkjet-printed 75-layer CNT at 2.4GHz as a function of time. 10 ppm NO_2 was introduced between 5 and 35 mins. Reprinted from [252]. Copyright 2011 ASME.

The CNT-based gas sensor can be incorporated into an antenna structure as a passive sensor. The changes in charge transport of CNT would alter the electrical properties of the antenna such as resonant frequency, backscatter radiated amplitude and phase etc. The passive antenna based design, such as radio frequency identification device (RFID), currently finds lots of applications because it readily yields a low or zero powered wireless solution with ability to create planar and flexible devices. In addition, there exists the ability to improve sensitivity of the overall device via careful choices in the antenna design process and nanomaterials. This feasibility study demonstrated a strong potential of inkjet printed MWCNTs for high sensitivity wireless RF sensors.

Conclusions

An oxidization process is developed to functionalize CNT with hydrophilic oxygen-containing groups, which improve the dispersion of CNT in water. A CNT-based gas sensor is fabricated via inkjet printing of the water-based CNT ink, which shows a high sensitivity of the CNT-based sensor toward NO_2. The CNT structure could also be

incorporated into an antenna structure for wireless gas sensing. The water-based CNT ink shows great potential for green and mass production of CNT sensors via inkjet printing.

APPENDIX C

EXFOLIATED HEXAGONAL BORON NITRIDE-BASED POLYMER NANOCOMPOSITE WITH ENHANCED THERMAL CONDUCTIVITY FOR ELECTRONIC ENCAPSULATION

Introduction

Thermal management is one of the most critical challenges in current electronic packaging in order to dissipate the large heat flux from high density/high power ICs and ensure high performance and long lifetime for the electronics.[256-259] In current packaging schemes, the ICs are mostly encapsulated by polymeric materials which provide an important pathway for heat dissipation.[258, 259] However, the thermal conductivity of the typical polymeric encapsulant is far below the practical needs for efficient heat dissipation. The thermal conductivity of highly silica-filled epoxy underfill is < 0.5 W/mK. Therefore, the development of highly thermally conductive encapsulant materials is of great importance for the development of packaging technologies.

The incorporation of high thermal conductivity filler has been widely used to improve the thermal conductivity of polymer matrix. Typical filler materials include metals (Ag, Al etc),[260, 261] carbon-based materials (carbon fiber, graphite, diamond),[262-264] and ceramics (boron nitride and alumina nitride, etc).[265, 266] In order to achieve the high thermal conductivity for the composite, a high filler loading (> 50 wt%) is necessary for conventional micro sized spherical or flake-like fillers. Such high loading usually results in problems of poor processablity/flowability and high cost etc., causing limited practical applications for IC encapsulation. To pursue a fundamental

improvement in the thermal conductivity of polymer composite, novel nanofillers with ultrahigh thermal conductivity and a high aspect ratio have attracted numerous attentions. For example, thermal conductivities higher than 3000 W/mK were observed in carbon nanotubes and graphene, twice of that for graphite. Moreover, the high aspect ratio of fillers allows the formation of the thermal percolating network at a lower filler loading. Chen et al. reported that the thermal percolation of 2D graphite nanoflake suspension occurs at a very low loading of 0.07-0.2 vol%.[267] The thermal conductivities are significantly enhanced for the composites of carbon nanotube/epoxy and graphite nanoplatelet/epoxy.[262, 268, 269] Balandin et al. prepared multilayer graphene-epoxy nanocomposite, which achieved a high enhancement of thermal conductivity by 2,300% at a filler loading of 10 vol%.[6] A similar result was reported by Jeon et al.[270] These researches demonstrate that the high aspect ratio filler enables high the thermal conductivity at a low filler loadings, which maintains the processablity of the polymer composite.

Hexagonal boron nitride (h-BN) nanosheet is a promising filler for formulating high performance encapsulant material.[271-276] Single layer h-BN is an analogy of graphene with a high theoretical thermal conductivity approaching 1,700–2,000 W/mK.[277] Among the typical 2D materials, the thermal conductivity of single layer hBN is only inferior to that of graphene because of the isotope impurity scattering; [3, 278, 279] but it is much higher than those of MoS_2 and other transition metal dichalcogenides.[280, 281] Moreover, the h-BN has a large electrical bandgap (~ 5.5 eV) and a small dielectric constant (3.9), which are highly advantageous over metallic fillers and carbon nanomaterials when the electrical resistivity and dielectric constant of

composite are concerned. However, the application of h-BN nanosheet has been less explored, due to the challenge of the large-scale preparation. In this study, we used a liquid exfoliation method to prepare h-BN nanosheet in large quantity, and formulated its epoxy composites whose thermal conductivities are remarkably higher than that of bulk h-BN based control samples. The high thermal conductivities of h-BN nanosheet/epoxy composite successfully reduce the thermal interface resistance when it was used as thermally conductive adhesives between Si and Cu substrate. Moreover, we carried out detailed characterizations on additional materials properties of the h-BN nanosheets/epoxy nanocomposite, including flowability, coefficient of thermal expansion (CTE), glass transition temperature, moisture absorption, etc. and discussed its potential application as underfill or thermal interface materials in electronic packaging.

Experimental

Sample preparation

The preparation of h-BN nanosheets follows the method reported in our previous work.[282] The starting h-BN powders were supplied by Momentive. The suspension of h-BN powder (NX-1, 1 μm) in NMP was ball-milled for 48 hours. The milled samples were sonicated for 5 hour to further exfoliate h-BN into nanosheets. The exfoliated BN nanosheets were collected by filtration, washed repeatedly by ethanol and dried at 60 °C in an oven. The exfoliation of different sizes of h-BN powders, including 5, 7, 12 and 45 μm, were carried out using the same process.

BN nanosheet powder was dispersed in epoxy resin and acetone by sonication, and then acetone was removed by vacuum and mild heating. After that, the curing agent, hexahydro-4-methyl phthalic anhydride, and catalyst, 1-cyanoethyl-2-ethyl-4-

methylimidazole, were added and mixed by stirring and soncation. The sample was transferred to an aluminum pan and cured at 150 °C for 1 hour.

Characterizations

TEM images were obtained using JEOL TEM 100CX. The morphologies of the h-BN nanosheet and h-BN nanocomposite were obtained using SEM LEO 1530. The chemical composition of h-BN nanosheet was determined by XPS (Thermo K-Alpha). The linear coefficient of thermal expansion (CTE) was measured in a thermal mechanical analyzer (TMA Q400, TA instruments). Samples were heated in a nitrogen atmosphere at a ramping rate of 5 °C/min to 250 °C. The thermal diffusivities (α) of h-BN/epoxy nanocomposites were measured by the laser flash method using LFA 471 (Nanoflash, Netzsch). The thermal conductivity was calculated by $\kappa = \alpha C_p \rho$, in which ρ and C_p are the density and heat capacity of the composite. The C_p was measured using differential scanning calorimetry (DSC, Q-600 TA Instruments). All thermal measurements were carried out at room temperature. The thermal resistances of tri-layer Si-(h-BN nanocomposite)-Cu samples were measured in an in-house infrared thermal imaging setup.[283]

Results and discussion

The exfoliation of bulk h-BN into h-BN nanosheets was carried out in NMP upon the application of mechanical forces during ball milling and sonication. The starting bulk h-BN flake has a lateral size of ~ 0.8-1 μm and thickness of 100-300 nm. The ball milling and sonication provide a combination of various types mechanical forces, including compression, sheer, scission and vibration, which either peel off thin layer of h-BN from bulk flakes or break the flake into smaller pieces.[282] The NMP plays an important role

in this process by stabilizing the thin h-BN nanosheets, preventing them from re-agglomeration. The semi-transparent h-BN nanosheets can be clearly observed though the TEM characterizations (Figure 109a and b), indicating the small thickness. The lateral size of h-BN nanosheets is usually smaller than 300 nm. At the same time, we also noticed that thick h-BN flakes co-exist with the h-BN nanosheets (Figure 109c). The presence of thick h-BN flakes can assist the thermal transport in the composite because they are less subject to thermal conductivity degradation due to phonon−boundary scattering, and in the composite h-BN nanosheets can form thermal links that interconnect the thick h-BN flakes.[6]

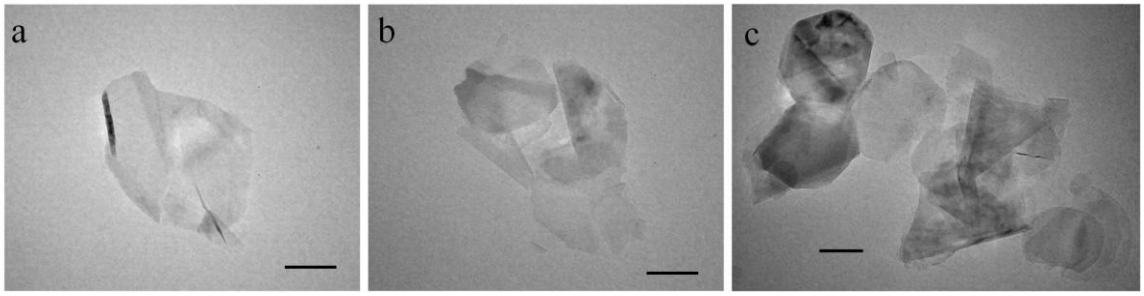

Figure 109. TEM images of h-BN naonsheets: (a), (b) single/few layer h-BN nanosheets and (c) thick h-BN sheets. All the scale bars are 100 nm. Reprinted with permission from [284]. Copyright 2014 Elsevier.

The chemical composition of h-BN nanosheets was analyzed by XPS in order to probe the possible impurities that were introduced during the exfoliations process. As shown in Figure 110, B, N, C and O are present in both h-BN control and h-BN nanosheets. The O and C exist in the form of boron oxide and boron carbon, which are typical impurities in h-BN powders. After the exfoliation, the atomic percentages of B and N, drops whereas the contents of C and O increases (Table 6), suggesting the additional impurities and NMP residual. These impurities can potentially degrade the thermal conductivity of h-BN nanosheets as phonon scattering centers.

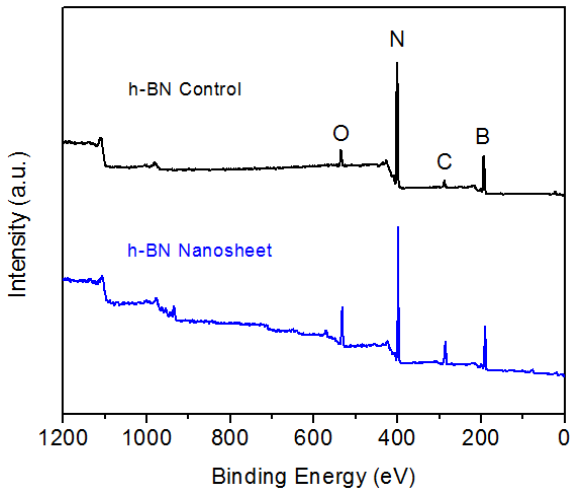

Figure 110. XPS survey spectra of h-BN control and nanosheets. Reprinted with permission from [284]. Copyright 2014 Elsevier.

Table 6. Chemical composition of h-BN control and h-BN nanosheets. Reprinted with permission from [284]. Copyright 2014 Elsevier.

Atomic Percentage (%)	B	N	C	O
h-BN control	44	44.9	5.9	5.2
h-BN nanosheet	35.8	38.1	16.0	10.1

The h-BN-nanosheet/expoxy composite was prepared using a solvent transfer method. In order to evaluate the interfacial interaction of h-BN nanosheet with epoxy resin, we firstly observed the fractured surface of 20 wt% h-BN nanosheet/epoxy composite using SEM, as shown in Figure 111. The large surface roughness of fractured surface indicates strong interfacial interaction between h-BN nanosheet and epoxy resin. As we did not carry out any surface modification of h-BN surfaces, the interaction between h-BN and epoxy resin are pure Van der Waals force. The surface energy of h-BN (cubic phase) films was found to be ~ 40 mJ/m^2,[285] which closely matches that of epoxy resin.[286] As a result, the epoxy resin well wets the h-BN nanosheets, forming strong interfaces.

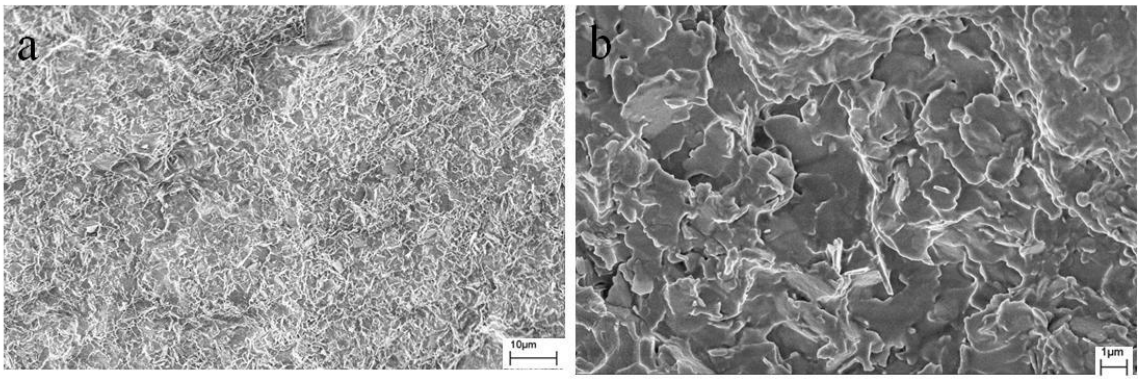

Figure 111. The SEM images of the fractured surface of 20 wt% h-BN nanosheet/epoxy composite at (a) high and (c) low magnification. Reprinted with permission from [284]. Copyright 2014 Elsevier.

The thermal conductivity of h-BN/epoxy composite was measured by the laser flash method. The neat epoxy has a thermal conductivity of 0.15 W/mK. The addition of h-BN leads to the increase of thermal conductivity. The thermal enhancement factor (TEF) is defined as

$$\frac{\kappa_{composite}-\kappa_{epoxy}}{\kappa_{epoxy}}\times 100\%,$$

in which the κ refers to the thermal conductivity. As shownFigure 112, the exfoliated h-BN nanosheet is more effective in increasing the thermal conductivity of composite comparing with the h-BN control. At a loading of 5 wt%, the TEF is 113% for h-BN nanosheets, while is only 28% for h-BN control. The high aspect ratio of h-BN-nanosheets is one of most critical factor for the impressive TEF. Moreover, the exfoliation of h-BN into single layers also leads to a several-fold improvement of thermal conductivity. Increasing the filler loadings further increases the TEF and consistently the h-BN nanosheet has better performance than h-BN control. On the other hand, we noticed that the effect of using h-BN nanosheets becomes less obvious. For example, the TEF of 30 wt% h-BN nanosheet/epoxy is 316 %, which is only slightly higher than the 247%

control. This is mainly because that the smaller lateral size of h-BN nanosheets brings in more filler-filer and filler-epoxy interfaces. The thermal boundary resistance, which is found to 7.6 × 10^{-8} m^2K/W,[266] takes a dominant role in determining the thermal conductivity at high filler loadings, overriding the effect of high aspect ratio of fillers. Consequently, the thermal conductivity of h-BN control based composite slowly approaches that of h-BN-nanosheets at high filler loadings.

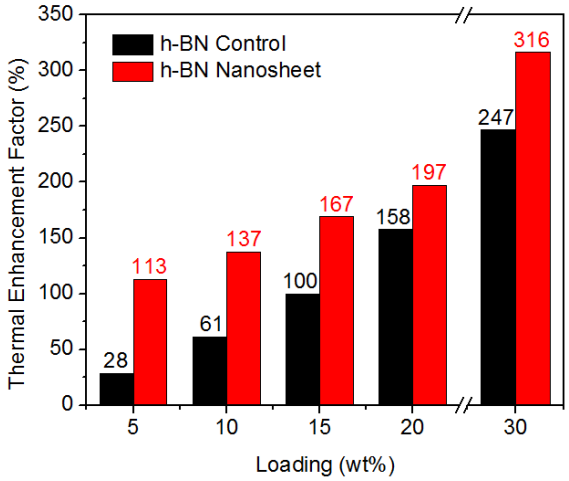

Figure 112. Thermal enhancement factors of h-BN nanosheet based composites and h-BN control based nanocomposites. Reprinted with permission from [284]. Copyright 2014 Elsevier.

The smaller lateral size of h-BN nanosheets hinders further improvement of thermal conductivity for the composite. To overcome this limitation, we explored the use of larger starting h-BN flakes whose lateral sizes are 5, 7, 12, and 45 μm. However, it is found that the larger size of starting h-BN does not necessarily lead to the larger size of h-BN nanosheets. During the exfoliation process, the large BN flakes firstly break into small pieces that are easier to be exfoliated into nanosheets. Therefore, the dimension of h-BN nanosheet is weakly dependent on the size of starting h-BN flakes. Moreover, when large h-BN flakes were used, the yield of exfoliation is much lower. The fact that the exfoliation of h-BN is more difficult than that of graphite could be attributed to the high

chemical resistance and intercalation resistance of h-BN,[287] and becomes one of the major hurdles for developing high performance h-BN nanocomposite.

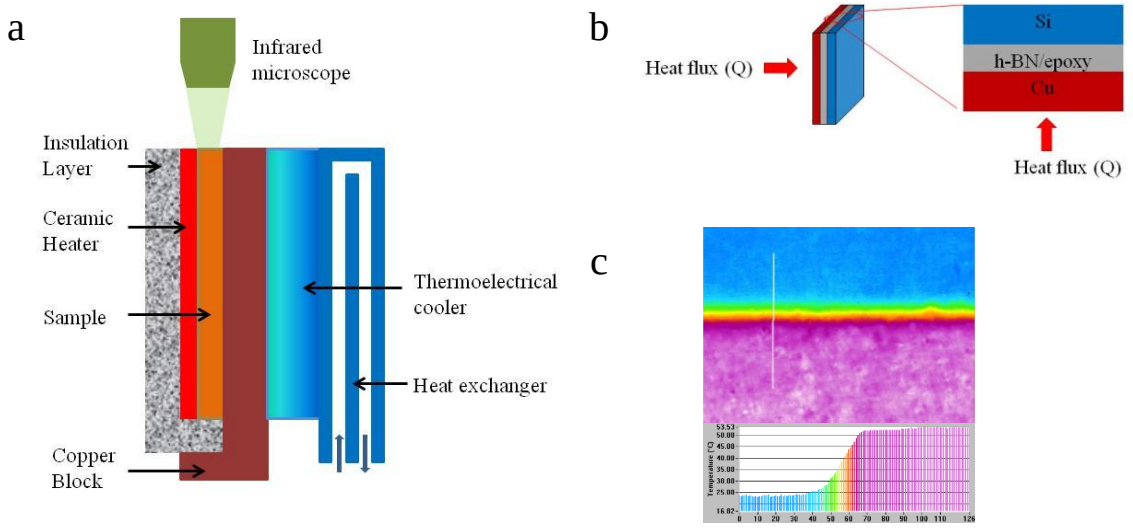

Figure 113. Schematics of (a) IR thermal imaging test fixture and (b) tri-layer sandwiched Si-nanocomposite-Cu sample configuration. (c) Rrepresentative thermal image and temperature profile. Reprinted with permission from [284]. Copyright 2014 Elsevier.

Table 7. Thermal resistance of Si-composite-Cu tri-layer structure. Reprinted with permission from [284]. Copyright 2014 Elsevier.

Sample	Power (W/cm^2)	Temperature Drop (°C)	Thermal resistance (cm^2K/W)
Neat epoxy	15.4	65.8	4.27
5 wt% h-BN nanosheet	15.7	29.4	1.87
10 wt% h-BN nanosheet	15.7	26.9	1.63
20 wt% h-BN nanosheet	15.7	21.3	1.26
30 wt% h-BN nanosheet	19.7	18.9	0.96

The performance of h-BN nanocomposite for reducing the thermal interface resistance was evaluated by using an infrared thermal imaging method. The infrared thermal imaging setup consists of an insulation layer, a ceramic heater, a copper block, a thermoelectrical cooler and a heat exchanger, as shown in Figure 113a. The sample is

mounted between the heater and copper block with the help of thermal grease. The heat flux from the ceramic heater transports across the sample to the cooler, producing a temperature gradient that is captured by an IR microscope at the edge of sample. A typical sample configuration for measurement is tri-layer sandwiched Si-nanocomposite-Cu (Figure 113b), where the heat flux transports from Cu to Si substrate. The thickness of h-BN/epoxy composite layer is controlled to be ~ 70 μm by adding ~ 0.5 wt% 70 μm glass beads as spacers. Figure 113c shows a typical thermal image and temperature profile across the interface. The drop of temperature occurs mainly at the h-BN/epoxy nanocomposite layer due to its much lower thermal conductivity than those of Cu (398 W/mK) and Si (~ 149 W/mK). The thermal resistance between the Cu and Si substrate can be calculated by:

$$R = \frac{T_{hot} - T_{cold}}{Q}$$

where R is the thermal resistance, T_{hot} and T_{cold} are the averaged temperature of Cu and Si surfaces respectively, and Q is the heat flux supplied to the sample per unit area controlled by the power applied to the heater. The thermal resistances of various materials were measurement using this configuration and summarized in Table 7. The neat epoxy has a high thermal resistance of 4.27 cm^2K/W, and the addition of 5 wt% h-BN nanosheet dramatically reduces the thermal resistance to 1.87 cm^2K/W. Further increase of h-BN nanosheet loading continuously reduces the thermal resistance. At 30 wt%, the thermal resistance is 0.96 cm^2K/W.

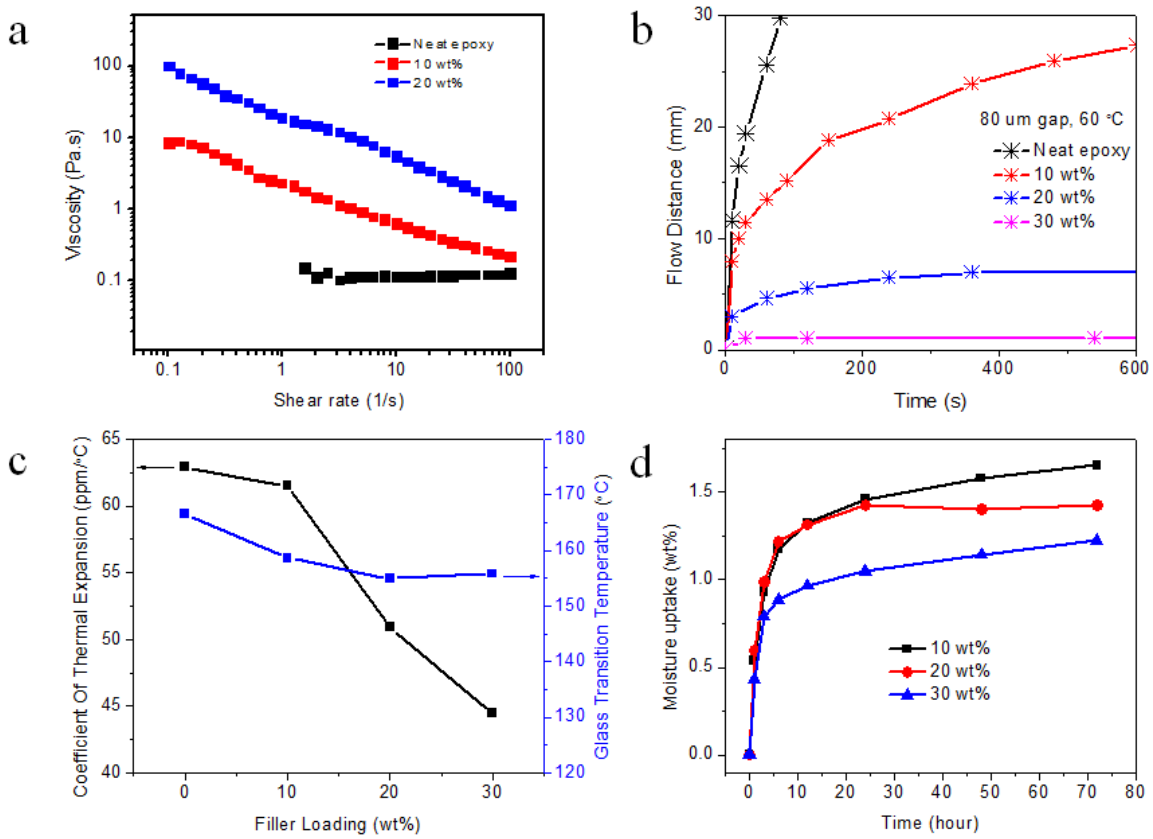

Figure 114. (a) The viscosity and (b) flow test of neat epoxy and h-BN nanosheet/epoxy uncured composites; (c) the CTE and Tg and (d) moisture adsorption of h-BN nanosheet/epoxy cured composites. Reprinted with permission from [284]. Copyright 2014 Elsevier.

In addition to the thermal conductivity, the viscosity of uncured h-BN-epoxy composite is an important property with regard to the processability for its application as underfill or adhesive. Low viscosity is highly desirable for the uncured nanocomposite to easily spread out on the bonding surface and flow into small gaps between IC chips and bonding substrate. The room temperature viscosity of the neat epoxy resin as low as 0.18 Pa·s. When h-BN nanosheets are added, the viscosity of composite dramatically increases due to the high surface area of nanofillers, as shown in Figure 114a. Moreover, shear thinning is observed for h-BN nanosheet/epoxy composites, which could be probably attributed to the shear alignment of h-BN nanosheet at high shear rate. The results in

Figure 114a suggest that 10 wt % nanocomposite can be used as the capillary-flow underfill with acceptable flowability, whereas the 20 wt% nanocomposite is more suitable for higher pressure to be applied such as stencil printing etc. We further investigated the flowability of epoxy and nanocomposites for its application as capillary flow underfill. These experiments were carried out for 80 μm gaps at 60 °C. The neat epoxy can easily flow 30 mm within 80 s. The 10 wt% nanocomposite flowed 27 mm at 600 s. The flowability dropped rapidly at higher loadings. The 20 wt% nanocomposite flowed only 7 mm and the flow of 30 wt% nanocomposite was very small (1 mm for 10 mins).

The CTE and Tg of h-BN nanosheets/epoxy composite were measured by TMA and shown in Figure 114c. The CTE of nanocomposites decreases with the loading of h-BN nanosheets reaching 45 ppm/K at 30 wt% loading, due to the negative in plane CTE of h-BN nanosheets. The Tg of nanocomposites slightly drops from 167 °C for neat epoxy to 159, 155, and 156 °C for 10 %, 20%, and 30 wt% loadings respectively. The drop of Tg is due to the large free volume at the filler-epoxy interfaces, especially for nanosized fillers and has been observed in other nanocomposite systems.[288] We tested the moisture absorption of h-BN nanosheet/epoxy composites under 85 C and 85 % relative humidity condition (Figure 114d). The nanocomposites gain weight rapidly during the first 6 hours and reached saturated values of 1.7, 1.4, and 1.2 wt% after 100 hours for 10 %, 20%, and 30 wt% loadings respectively. The nanocomposites with higher filler loadings have lower moisture adsorption because that the inorganic h-BN fillers does not absorb any moisture. The moisture adsorption normalized to the epoxy resin is ~ 1.7-1.8 wt% for all three loadings, indicating that the filler-epoxy interface does not

increase the moisture absorption. These characterizations suggest that the h-BN nanosheet is suitable for electronic packaging applications.

Conclusions

We prepared h-BN nanosheet using a liquid exfoliation method and its epoxy nanocomposite, and demonstrated enhanced thermal conductivity compared with the micron-sized h-BN flake-based control samples, which could be attributed to the high thermal conductivity and aspect ratio of the nanosheet. However, it is found that thermal enhancement effect of h-BN nanosheet becomes less obvious when the filler loading increases as a result of the small lateral size of the nanosheet (a larger amount of filler-filler and filler epoxy interface) and relatively high thermal boundary resistance. Nevertheless, the infrared thermal imaging measurement revealed much reduced thermal interface resistance in trilayer Cu-nanocomposite-Si samples. In addition to the high thermal conductivity, the h-BN nanosheet/epoxy nanocomposite possesses acceptable flowability, high Tg, reduced CTE and low moisture absorption, rendering its promising applications for electronic encapsulation.

APPENDIX D

MAGNETIC ALIGNMENT OF HEXAGONAL BORON NITRIDE PLATELETS IN POLYMER MATRIX: TOWARD HIGH PERFORMANCE ANISOTROPIC POLYMER COMPOSITES FOR ELECTRONIC ENCAPSULATION

Introduction

The rapid development of new generation electronics, fine-pitch integrated circuits (ICs) and three-dimensional (3D) integration set stringent requirements for packaging materials to ensure the long lifetime of electronic devices.[256, 258, 259] High thermal conductivity, electrical insulating and low CTE polymer composites are in great need as encapsulants for ICs to provide environmental protection, facilitate the heat dissipation and relieve the thermal stress. Conventional underfill materials, containing polymers and silica fillers, are widely used in current electronics but cannot meet these requirements due to its poor thermal conductivity of lower than 0.5 W/mK that results from the low intrinsic thermal conductivity of silica fillers (1.4 W/mK). Thermal interface materials (TIMs), another important example of polymer composite, are filled with high thermal conductivity ceramic or metallic fillers and have thermal conductivity of 1-5 W/mK. However, to reach high thermal conductivity, extremely high filler loading are required (>50 vol%), resulting in the loss of processiblity and degradation of mechanical properties.[257, 271, 289] So far, the lack of high performance materials for IC encapsulation has been one of major bottlenecks for next-generation electronics.

The unsatisfactory performance of known polymer composites in electronic packaging is largely due to the slowly developed filler technology. With the excellent mechanical and adhesive properties of polymers, fillers are added to introduce desired properties for target applications: silica is used to lower down the CTE for underfills because of its low CTE of 0.5 ppm/K;[288, 290] high thermal conductivity ceramics are used in TIMs to improve the thermal conductivity;[271, 274, 289, 291, 292] and metallic fillers (silver, copper etc.) are used in electrical conductive adhesives (ECAs) to boost the electrical conductivity.[258, 293] In addition to the intrinsic properties of fillers, the performances of composites are also affected by filler geometries,[6, 272] orientations[274] and interfacial properties,[288, 290, 294] which are being actively researched recently. Among these factors, the filler alignment is less explored because of technical difficulties in controlling the filler alignment. Several approaches were used to prepare polymer composites with aligned fillers. Pre-aligned fillers, e.g. carbon nanotube arrays, were used to prepare the polymer composites with enhanced performance in alignment direction.[294-297] Shear alignment is another approach in which fillers are aligned by shear force during the flow or stretch of polymers.[274, 298-302] Moreover, the gravitational force can lead to horizontal alignment of high aspect ratio fillers.[5, 303] However, these methods only produce composite materials with pre-defined geometry and filler alignment direction, and therefore have limited applications. It is highly desirable to develop new methods for effective filler alignment after the application of composite and with flexible control over the alignment direction.

Magnetic alignment is very attractive in this regard due to the remote control of filler alignment and possibility of orienting filler at arbitrary directions.[304, 305] A

variety of structures can be achieved under optimized conditions.[305-311] In this work, we explored the magnetic alignment of hexagonal boron nitride (hBN) platelets in epoxy composites and the resulting materials properties. hBN platelets is an outstanding filler to demonstrate the impact of filler alignment not only because of its non-spherical shape but also the anisotropic properties. As seen in Figure 115, hBN platelets have excellent in-plane properties including high thermal conductivity of ~ 600 W/mK and low CTE of -2.7 ppm/K. However, the inferior out-of-plane properties, low thermal conductivity of 30 ppm/K and large CTE of 38 ppm/K, cause poor performance for conventional hBN-based composites in which the fillers are randomly oriented (Figure 115).[271] Therefore, controlling the orientation of hBN in polymer matrix is critically important for optimizing the performance of its composites.

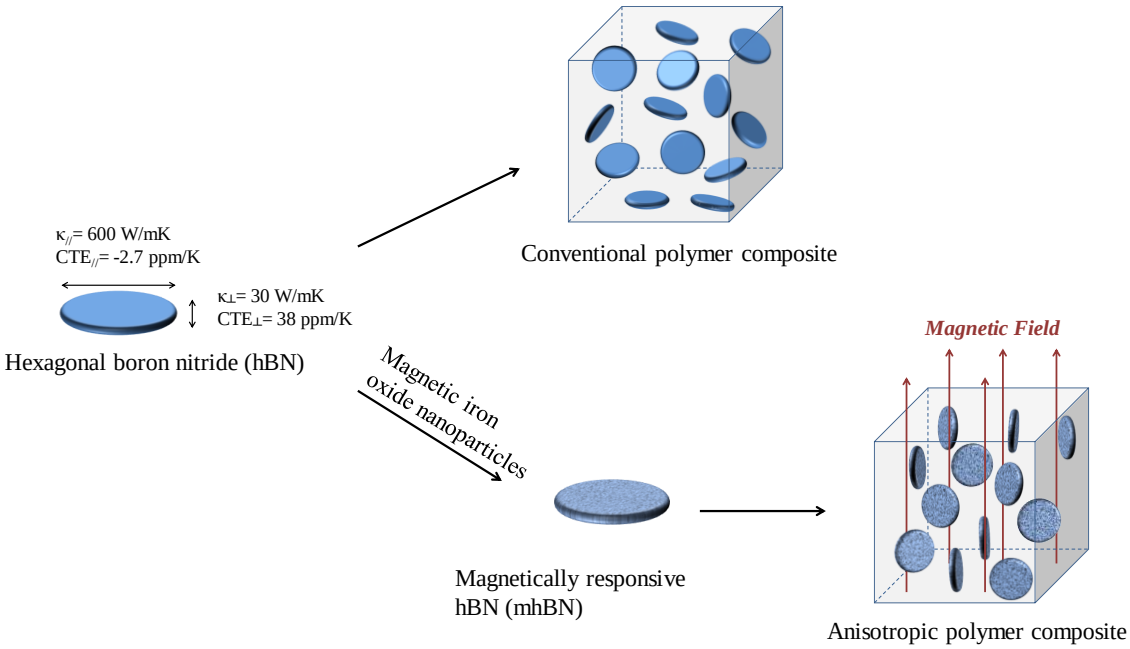

Figure 115. Anisotropic properties of hBN platelets and schematics of conventional polymer composite in which hBN platelets are randomly oriented; schematic illustration of the preparation of magnetically responsive hBN and its alignment hBN under an external magnetic field for anisotropic polymer composite. Reprinted with permission from [266].Copyright 2013 American Chemical Society.

Magnetic alignment requires the filler to respond to the external magnetic field magnetic. Although hBN is not an intrinsically magnetic material, magnetically responsive hBN (mhBN) can be prepared from commercial hBN by surface modification using superparamagnetic iron oxide nanoparticles. The attachment of iron oxide nanoparticles to hBN surface is through the electrostatic interaction between the positively charged iron oxide nanoparticles and negatively charged hBN platelets. The mhBN platelets can orient themselves along the direction of external magnetic field to minimize the magnetic energy.[305] The size of hBN platelet affects the strength of magnetic field required for efficient alignment. Using an optimized size reported by Erb et al, the mhBN platelet can be easily aligned using a rare-earth magnet.[305] As a result, the mhBN-epoxy composites inherit the anisotropic properties from the mhBN fillers. This process has been schematically illustrated in Figure 115.

Experimental Section

Materials

Hexagonal boron nitride (AC6041) was provided by Momentive, which has an averaged particle size of 5 μm and BET surface area of 6.77 m^2/g. The magnetic iron oxide nanoparticles solution (3.9 vol%) were supplied by Ferrotec (EMG 605) with the saturation magnetization of 22 mT and initial magnetic susceptibility of 3.02. The epoxy resin are the mixture of diglycidyl ether of bispenol A and 3,4-epoxy cyclohexylmethyl-3,4-epoxy cyclohexyl carboxylate. Hexahydro-4-methyl phthalic anhydride and 1-cyanoethyl-2-ethyl-4-methylimidazole were used as curing agent and catalyst respectively. Other chemical were used as received.

Magnetic modification of hBN

In a typical process, 4 g hBN powder was dispersed in water by gentle stir and sonication. 400 μL ferrofluid was then added and mixed by stir. The suspension was incubated overnight to allow the bonding between hBN and iron oxide nanoparticles. After that, mhBN powder was separated from the suspension by centrifuge at 2000 rpm for 30 min, and was dried at 60 °C in vacuum.

Preparation of aligned mhBN-epoxy composites

mhBN powder was mixed with epoxy resin by 5 min sonication. A small amount of acetone was added in this process to help the dispersion of BN, and was then removed by vacuum at elevated temperatures. After that, the curing agent and catalyst was added and mixed by stir. The composite was transferred to a Teflon mold and placed in between two parallel arranged rare-earth magnets. The strength of magnetic field is 400 mT measured by a Gaussmeter (Lakesure, model 410-SCT). The curing of epoxy was carried out by placing the whole fixture in an oven, including both Teflon mold and the magnet, so that the magnetic field was applied throughout the curing process. The curing profile was 100 °C for 12 hours and 150 °C for 1 hour.

Characterizations

XRD analysis of mhBN and mhBN-epoxy composites was carried out with an X'Pert PRO Alpha-1 system using Cu Kα radiation (45 kV and 40 mA). The zeta potential of iron oxide nanoparticles was measured using Malvern Zetasizer Nano ZS. TEM was carried out using the JEOL TEM 100CX. SEM (LEO 1530 and 1550) was used to characterize the morphology of mhBN-epoxy composite surfaces using an accelerating voltage of 4 kV; samples were sputter coated with a thin layer of gold for better imaging.

The energy dispersive spectroscopy was measured on uncoated mhBN powders using SEM 1530 equipped with an EDS detector. In order to observe the orientation of mhBN in the composite, the cracked composite surface was exposed to oxygen reaction ion etching (RIE) to etch away the outer epoxy layer. The Young's modulus of neat epoxy and epoxy composite were measured by TriboIndenter (TI 900, Hysitron) using a 10 μm cono-spherical probe. TMA (Q-400 TA instrument) was used to measure the CTE of composites. The thermal diffusivity (α) of mhBN-epoxy composites was measured by the laser flash method using a LFA 471 (Netzsch). The thermal conductivity was calculated by $\kappa = \alpha C_p \rho$, in which ρ and C_p are the density and heat capacity of mhBN-epoxy composite. The C_p was measured using DSC (Q-600 TA instrument). All thermal measurements were carried out at room temperature. The complex viscosity of uncured hBN-epoxy composites were measured using discovery hybrid rheometer-2 (HR2, TA instrument).

Results and Discussion

Magnetic modification of hBN

To prepare mhBN, hBN platelets were dispersed in water and a solution of iron oxide nanoparticle was then added. Iron oxide nanoparticles are coated by cationic surfactants and have a zeta potential of 30 mV, indicating the positive surface charge. The dispersed hBN have negative surface charges and thus a strong electrostatic interaction with iron oxide nanoparticles.[305, 312] After being added to the hBN suspension, these magnetic nanoparticles are quickly attached onto the hBN surface. Consequently, the mhBN can respond to the external magnetic field as shown in Figure 116a. It is found that such electrostatic force is very strong that the magnetic response of

mhBN is maintained after continuous sonication of the mhBN suspension. The presence of iron oxide particles is confirmed by the XRD pattern of mhBN (Figure 116b), in which feature peaks from both hBN and iron oxide are observed. The TEM characterization reveals that the size of iron oxide nanoparticles ranges from ~ 10 to ~ 25 nm (Figure 116c), and confirms the successful attachment of iron oxide nanoparticles to the surface of hBN platelets (Figure 116d). Further, the energy dispersive spectroscopy (EDS) analysis of mhBN reveals the presence of 0.32 at% iron (Figure 117). Moreover, the elemental mapping by EDS shows a uniform distribution of iron oxide and no large agglomerate of nanoparticles is observed.

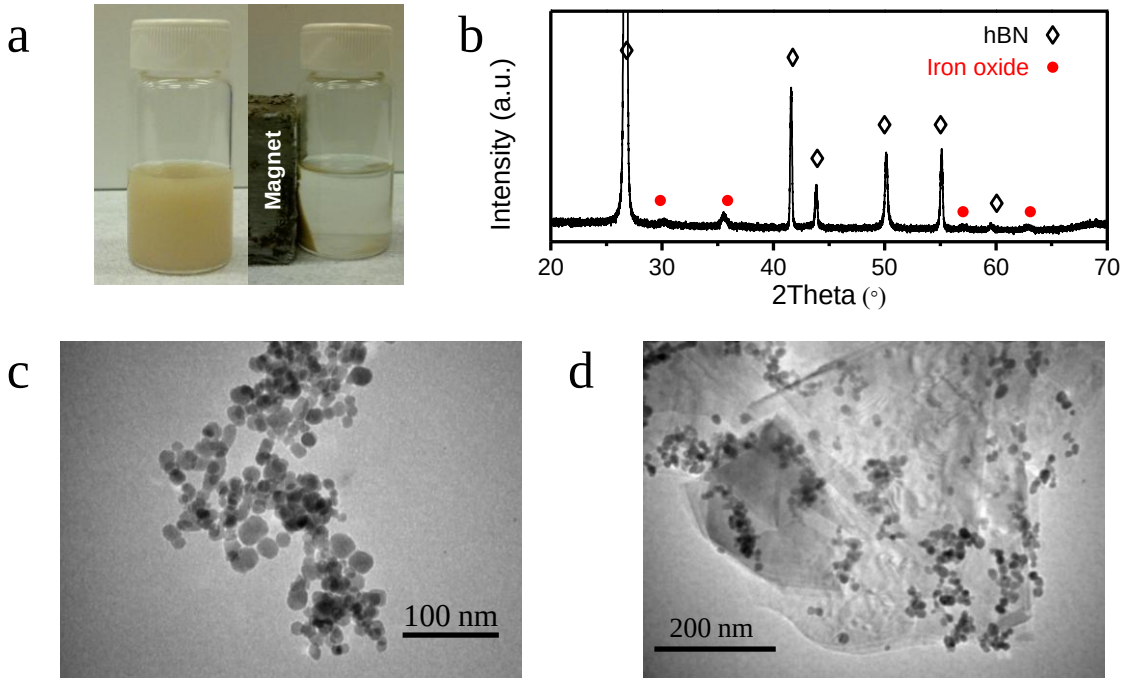

Figure 116. (a) Images of mBN dispersion in acetone and its response to external magnetic field when a magnet is placed near the dispersion. (b)XRD pattern of mBN; the black labels refer to peaks from hBN and the red labels refer peaks from iron oxide nanoparticles. TEM images of (c) iron oxide nanoparticles and (d) mhBN. Reprinted with permission from [266].Copyright 2013 American Chemical Society.

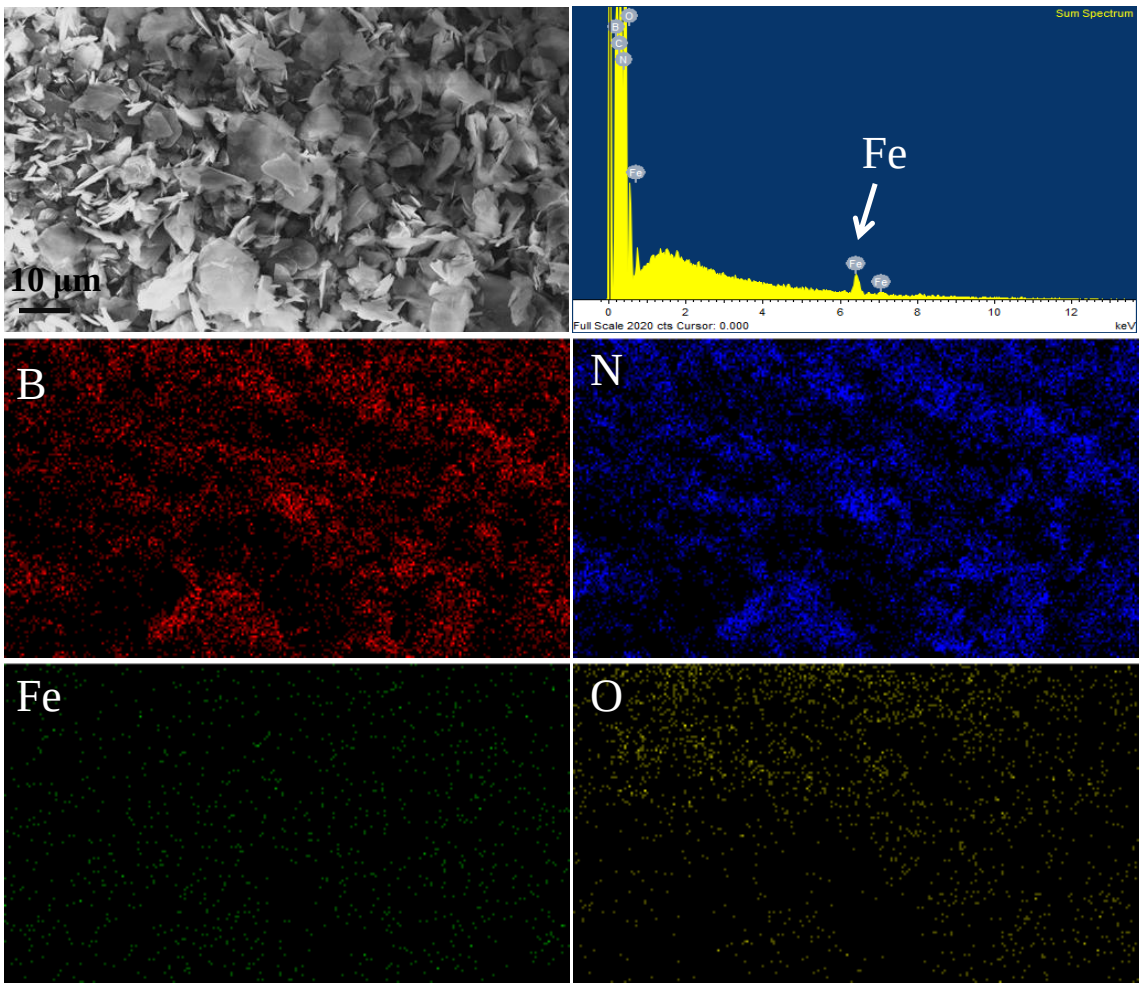

Figure 117. SEM image of hmBN, and the EDS and elemental mapping collected from the same location. Reprinted with permission from [266].Copyright 2013 American Chemical Society.

The optimization of mhBN-epoxy composite preparation

The mhBN-epoxy composites were prepared using a solvent transfer method as described in the experimental section. During the curing of epoxy resin, an external magnetic field was applied by placing the mold between two magnets (Figure 118), which guides the orientation of mhBN platelets in the composites. The amount of iron oxide nanoparticles on mhBN surface is an important factor affecting the magnetic alignment. We changed the loading of iron oxide nanoparticles on hBN from 0.5, 1, to 2 wt%. The 2 wt% is found to be maximum loading, which achieves the highest

performance enhancement in terms of thermal conductivity (Figure 119). At 2 wt%, the magnetic susceptibility of mhBN is calculated to be 0.17 using the method developed by Erb et al.[305, 313] Moreover, the curing profile of composite was optimized to allow the efficient alignment of mhBN before the fully curing of epoxy resin. The typical curing profile of mhBN-epoxy consists of two steps: a pre-cure at lower temperature for 12 hour, and a fully cure at 150 °C for 1 hour. The pre-cure step used temperatures higher than room temperature in order to lower down the viscosity of the resin for efficient filler alignment. However, if the temperature is too high, immediate curing of polymer resins occurs that the mhBN does not have enough time for fully alignment. We tried different pre-curing temperature, including 60, 100 and 150 °C (no pre-cure cure). It is clear from Figure 120 that 100 °C is an optimal temperature among the conditions tested which gave rise to highest thermal conductivity for the composite. It is also found that at temperatures around or higher than 120 °C the curing of epoxy resin is obvious within 30 min. Therefore, we chose 100 °C as the optimized pre-cure temperature.

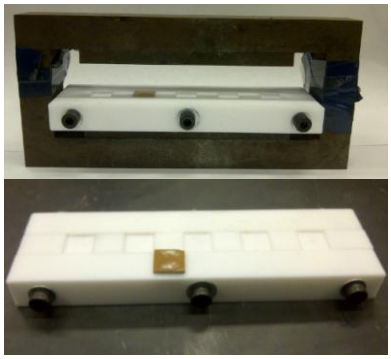

Figure 118. The magnet and Teflon mold used to cure mhBN-epoxy composites. The cured mhBN-epoxy can be easily peeled out of the mode after curing.

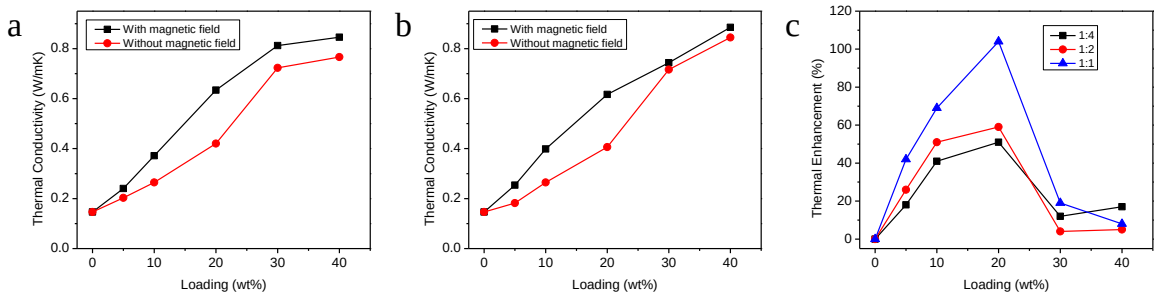

Figure 119. Thermal conductivities of VmhBN-epoxy and RmhBN-epoxy when different ratios of iron oxide nanoparticles and hBN were used: (a) 1:4 and (b) 1:2 (volume of iron oxide solution/100 uL to weight of hBN/g, corresponding to the 0.5 and 1 wt% of iron oxide nanoparticles) ; (c) comparison of thermal enhancement (1:1 ratio corresponds to 2 wt% of iron oxide nanoparticles).

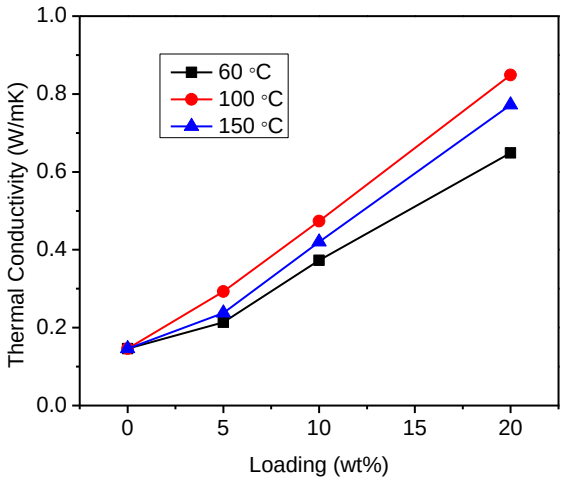

Figure 120. The effect of curing profile on the thermal conductivities of VmhBN-epoxy.

Characterizations of mhBN-epoxy composites

The alignment mhBN in composites

Vertical aligned mhBN-epoxy composites (VmhBN-epoxy) were prepared by applying a vertical magnetic field, and randomly oriented mhBN-epoxy composites (RmhBN-epoxy) were produced as control samples when no magnetic field was used. The SEM images of cracked surface of VmhBN-epoxy are shown in Figure 121. The large roughness of the cracked surface of VmhBN-epoxy compared to that of neat epoxy indicates strong interfacial interactions between mhBN and epoxy resin. However, the

orientation of mhBN platelets could not be visualized from SEM images due to the poor contrast between mhBN and epoxy resin which are both electrically insulating. Therefore, oxygen reactive ion etching (RIE) was carried out to selectively remove the outer layer of epoxy resin, resulting in exposed the mhBN platelets. Figure 122a and b show the SEM images of cracked cross-section of 20 wt% mhBN-epoxy composites after RIE treatment. It is clear that in VmhBN-epoxy, the mhBN platelets are aligned along the direction of magnetic field so that the normal of platelets are perpendicular to the magnetic field direction and within the horizontal plane of the composite. In two representative cases, the aligned mhBN platelets are projected in the cross-section view as 1D vertical rods and 2D plates, which are indicated by red and orange arrows respectively. In contrast, in RmhBN-epoxy, the mhBN platelets are randomly orientated. One of most obvious indications is the existence of horizontally oriented platelets that are projected as 1D horizontal rods (indicated by blue arrows). To further prove the vertical alignment, the top-view SEM images of RIE-treated VmhBN-epoxy (Figure 122c) and RmhBN-epoxy (Figure 122d) were also collected. As expected, the mhBN platelets mostly show as 1D rods in VmhBN, whereas plate-shape mhBN can be found in RmhBN. The observed SEM morphology is very close to the schematic drawings in the insets and clearly proves the effective magnetic alignment of mhBN in epoxy composites. Moreover, the magnetic alignment is with high uniformity as the SEM morphology of VmhBN-epoxy does not show any noticeable variation across the sample.

The XRD analysis of mhBN-epoxy composites in Figure 123 provides additional support for the magnetic alignment of mhBN. The hBN peaks in RmhBN-epoxy show similar intensities to those of mhBN powder, whereas dramatically changed peak

intensities are observed in VmhBN-epoxy, suggesting the change of mhBN platelets orientations in the composite. Using the epoxy peak at ~ 17 ° as a reference, the hBN (002) peak becomes six times weaker, the (004) peak disappears, and (100) peak becomes more than four times stronger in VmhBN-epoxy than those in RmhBN-epoxy. These changes in the XRD pattern of VmhBN-epoxy can be explained by the reduced amount of horizontally oriented mhBN and larger amount of vertically oriented mhBN, as schematically illustrated in Figure 123.

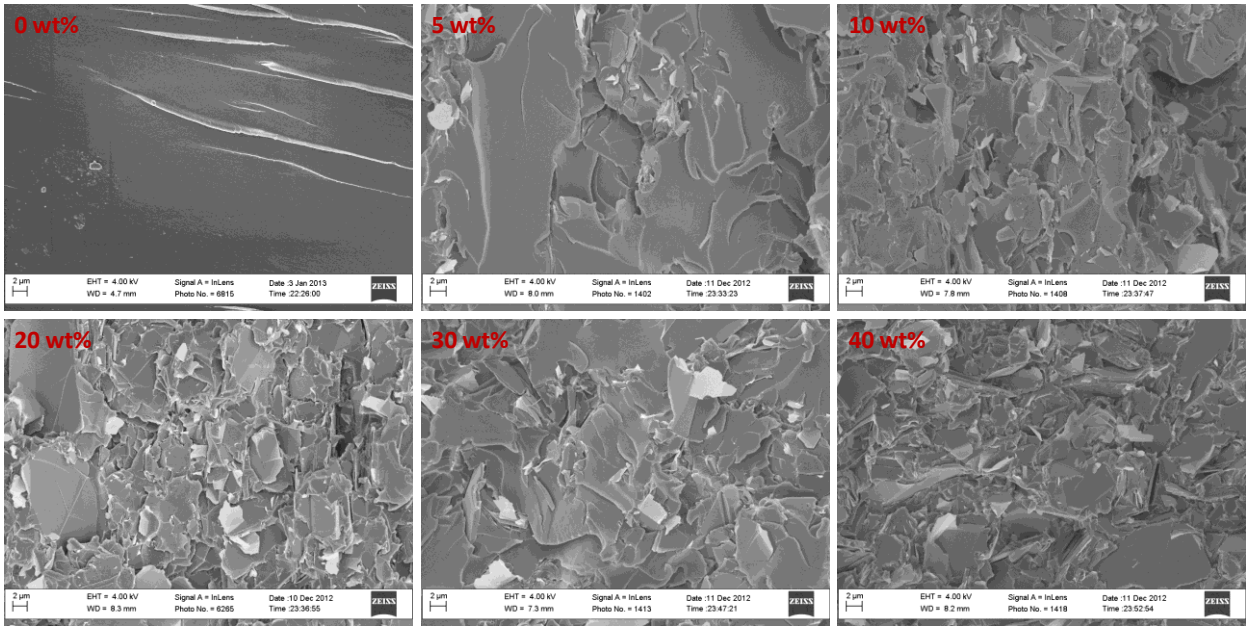

Figure 121. SEM images of the cracked surfaces of neat epoxy and VhmBN-epoxy composites.

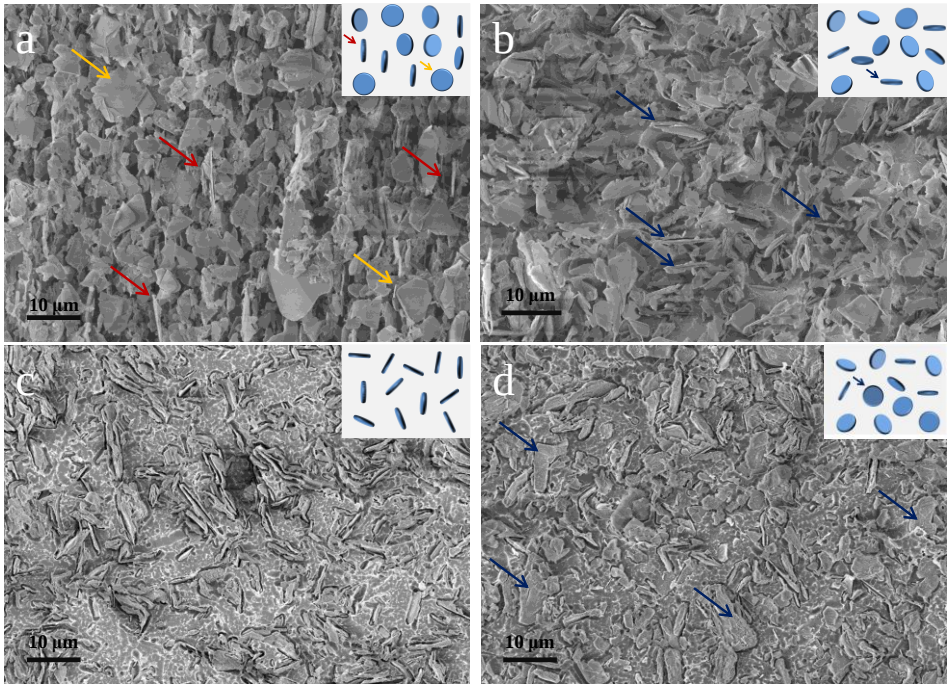

Figure 122. SEM cross-section images of RIE-treated 20 wt% (a) VmhBN-epoxy and (b) RmhBN-epoxy composites; Arrows point to the representative orientations: red and orange arrows indicate vertical alignment while blue arrows indicate horizontal alignment. Top-view images of RIE-treated 20 wt% (c) VmhBN-epoxy and (d) RmhBN-epoxy composites. Insets in these images schematically show the oriented fillers. Reprinted with permission from [266].Copyright 2013 American Chemical Society.

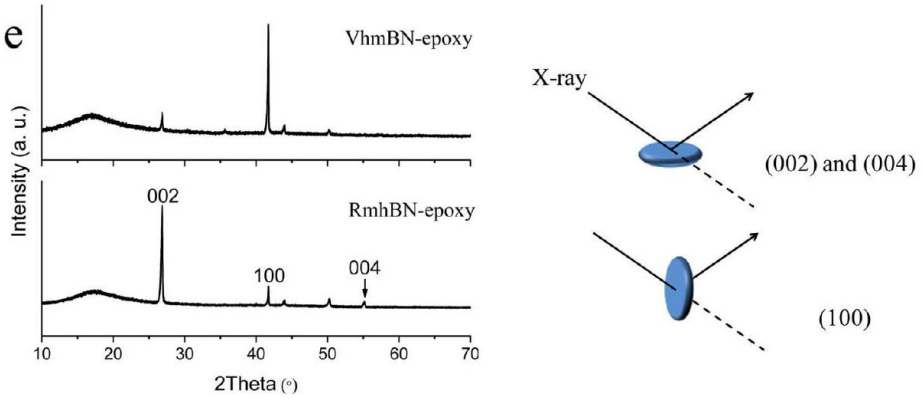

Figure 123. XRD patterns of VhmBN-epoxy and RhmBN-epoxy composites and the illustration of filler alignment effect on XRD pattern: the horizontally oriented mhBN is responsive for hBN (002) and (004) peaks and some vertically oriented mhBN are related to the (100) peak. Reprinted with permission from [266].Copyright 2013 American Chemical Society.

Thermoechanical properties

The alignment of mhBN in its epoxy composite greatly impacts its CTEs due to aforementioned anisotropic properties of hBN. The linear CTEs of mhBN-epoxy composites were measured along their z direction. As shown in Figure 124, the CTEs of RmhBN-epoxy at different loadings are in between 60-66 ppm/°C, close to the value for neat epoxy. In sharp contrast, VmhBN-epoxy shows a dramatic CTE reduction initially with the increase of filler loading, being as low as 28.7 ppm/°C at 20 wt%. However, further increase of filler loading above 20 wt% leads to larger CTEs than that of 20 wt% mhBN-epoxy. The less reduction of CTE at higher filler loading is because the alignment of mhBN requires low viscosity to allow the free rotation of mhBN platelets in epoxy resin. As the loading of mhBN increases above 20 wt%, the viscosity of mhBN-epoxy increases significantly (Figure 125) that inhibits the filler alignment. Indeed, the examination of SEM cross-section images of 30 and 40 wt% VmhBN-epoxy reveals significant amount of unaligned mhBN platelets (Figure 126), which do not appear in VmhBN-epoxy composites at lower loadings.

To better understand the CTE reduction effect by filler alignment, the following analytical models are used to predict the CTE of VmhBN-epoxy considering the anisotropic properties of hBN:

- Rule of mixture

$$\alpha_c = f\alpha_f + (1-f)\alpha_m$$

where α_c , α_f and α_m are the CTE of the composite, filler and matrix, respectively; f is the volume fraction of the filler. In our calculation, α_f =-2.7 ppm/°C (in-plane CTE of hBN) and α_m=60.6 ppm/°C; f is calculated from the loading of mhBN in the composite using the density values of 2.1 and 1.2 g/cm^3 for mhBN and epoxy resin, respectively.

– Turner Model[314]

$$\alpha_c = \frac{fK_f\alpha_f + (1-f)K_m\alpha_m}{fK_f + (1-f)K_m}$$

where K_f and K_m are the bulk modulus of the filler and matrix. In the calculation, the K_f =450 GPa and K_m =2.4 Gpa.

– Schapery Model[315]

The Schapery model gives an upper limit (α_c^u) and a lower limit α_c^l for the CTE of composite:

$$\alpha_c^u = \alpha_m + \frac{K_f}{K_c^l}\frac{(K_m - K_c^l)(\alpha_f - \alpha_m)}{K_m - K_f}$$

$$\alpha_c^l = \alpha_m + \frac{K_f}{K_c^u}\frac{(K_m - K_c^u)(\alpha_f - \alpha_m)}{K_m - K_f}$$

K_c^u and K_c^l are calculated from model using the H-S equation:

$$K_c^u = K_f + \frac{1-f}{\frac{1}{K_m - K_f} + \frac{3f}{3K_f + 4G_f}}$$

$$K_c^l = K_m + \frac{f}{\frac{1}{K_f - K_m} + \frac{3(1-f)}{3K_m + 4G_m}}$$

where G_f and G_m are the shear modulus of the filler and matrix. In the calculation, G_f =112 Gpa and G_m = 0.9 Gpa.

The results calculated from these models are compared with the experimental values in Figure 124. The simple rule of mixture assumes a uniform stress distribution in the composite and only account for the effect of the CTEs of filler and matrix. However,

it fails to explain low CTE values, suggesting that the negative in-plane CTE of hBN is not the sole reason for the dramatic CTE reduction. Turner model assumes a homogeneous strain in the composite and gives an overestimated CTE reduction, indicating the critical role of high in-plane modulus of hBN for CTE reduction.[314] The Schapery model considers both normal and shear stresses between fillers and matrix and gives the upper and lower limits for CTEs.[315] The experimental CTEs of VmhBN-epoxy composites lie within the Schapery limits, showing that the negative in-plane CTE, high bulk modulus and shear modulus of hBN all contribute to the CTE reduction of composites. These results also suggest that the large out-of-plane CTE and low bulk modulus cause the insignificant CTE reduction in RmhBN-epoxy and other hBN-epoxy composites.

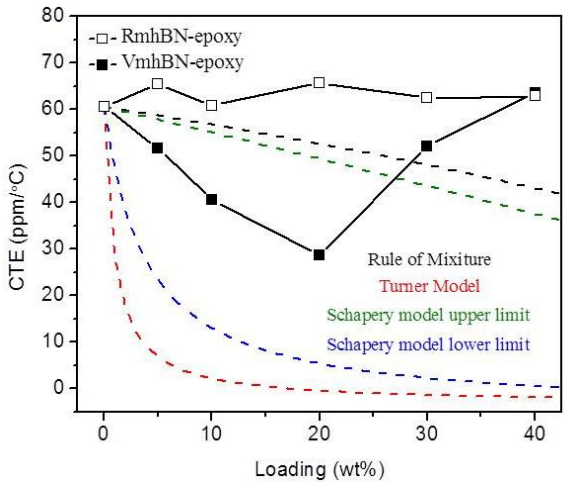

Figure 124. Measured CTEs of VmhBN-epoxy and RmhBN-epoxy and the predicted CTEs by analytical models considering the anisotropic properties of hBN. Reprinted with permission from [266].Copyright 2013 American Chemical Society.

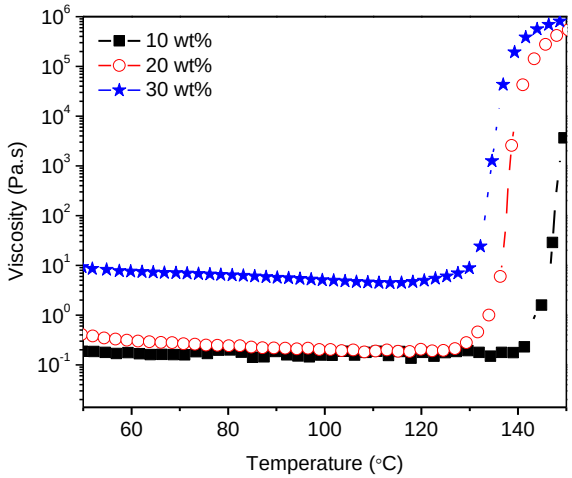

Figure 125. Rheology measurement of uncured hmBN-epoxy with different loadings.

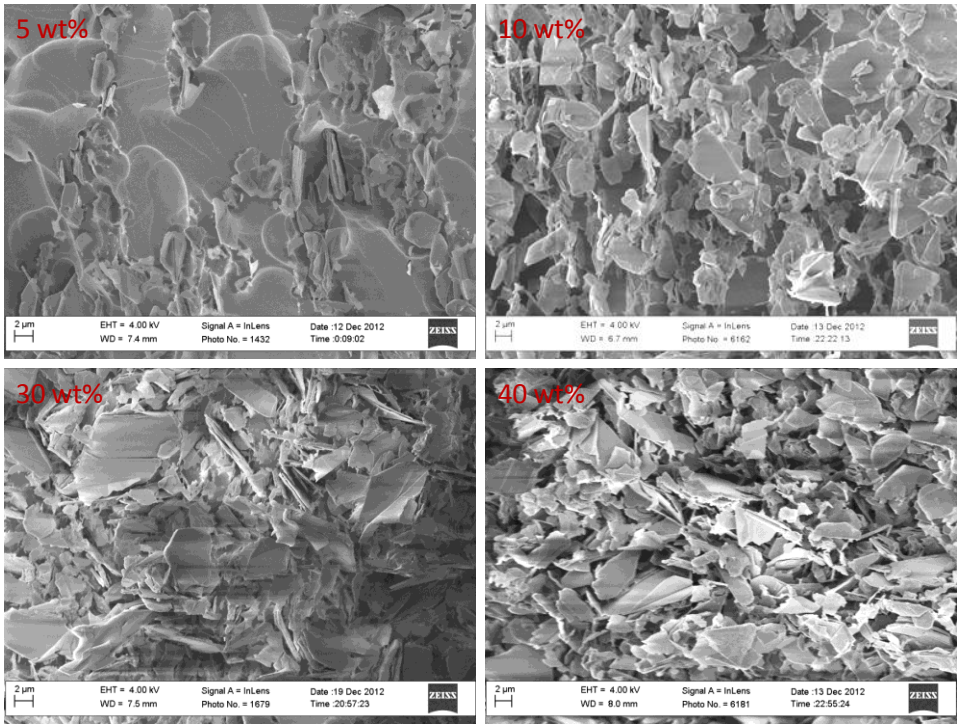

Figure 126. SEM cross-section images of RIE-treated VmhBN-epoxy of different loadings.

Thermal Conductivity

The thermal conductivity of mhBN-epoxy composites is greatly enhanced by filler alignment. Figure 127 shows the z-direction thermal conductivities of VmhBN-epoxy and RmhBN-epoxy, and the corresponding thermal enhancement. Here the thermal enhancement is defined as the percentage of thermal conductivity improvement by

magnetic alignment of mhBN: $(\kappa_{VmhBN-epoxy} - \kappa_{RmhBN-epoxy})/\kappa_{RmhBN-epoxy}$ (κ refers to thermal conductivity). It is found that the thermal enhancement increases initially with the filler loading, reaching 104% at 20 wt%, and drops rapidly to 19 and 8% at 30 and 40 wt% respectively. The drop of thermal enhancement at high filler loadings is due to the same reason in the discussion of CTEs, that is, the increased viscosity hinders the alignment of mhBN during curing. Remarkably, at the optimal filler loading of 20 wt%, the thermal conductivity of VmhBN-epoxy is 0.85 W/mK, which is 5.7 times of measured value for neat epoxy (0.15 W/mK) and twice of that for conventional silica-filled underfills. Table 8 compares the thermal conductivity enhancement of VmhBN-epoxy with reported hBN-polymer composite. It is evident that thermal conductivity enhancement of VmhBN-epoxy (5.7 times) represents one of the highest for 20 wt% filler loading. Table 8 also tells that the filler alignment is the major reason for the exciting result because the RmhBN-epoxy shows 2.8 times enhancement of thermal conductivity, which is comparable to 1.5-3 times from similar works.

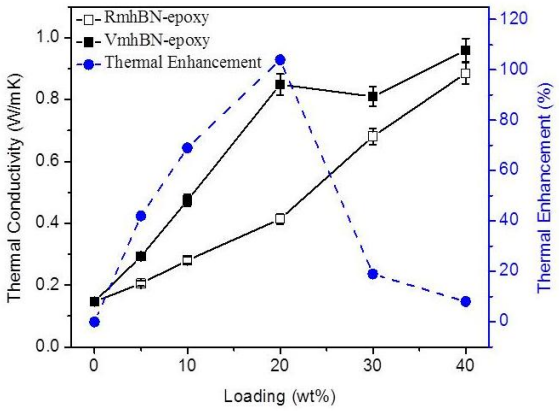

Figure 127. Thermal conductivities of VmhBN-epoxy and RmhBN-epoxy composites and corresponding thermal enhancement. Reprinted with permission from [266].Copyright 2013 American Chemical Society.

Table 8. Thermal conductivity enhancement ($\kappa_{composite}/\kappa_{resin}$) of various BN-polymer composites. Reprinted with permission from [266].Copyright 2013 American Chemical Society.

Materials	Filler size (μm)	Loading (wt%)	Thermal conductivity enhancement
hBN-epoxy[271]	12	20	~ 3
	60-100	20	~ 5.6
hBN-polyimide[291]	1 and 0.07	20	~ 1.5
hBN-photosensitive polyimide[292]	0.07	20	~ 1.5
hBN-polyimide[294]	0.7	~ 40	~ 6.8
hBN-epoxy (this work)	5 um	20	5.7 (VmhBN-epoxy) 2.8 (RmhBN-epoxy)

Effective medium approximation of thermal properties for mhBN-epoxy composites

We used a modified effective medium approximation (EMA) to analyze our experimental data.[316] This model takes into account the thermal conductivity of filler and matrix, filler geometry and orientation, and thermal boundary resistance (TBR), and could give important insights into the fundamental parameters governing the thermal transport in mhBN-epoxy composites.

Basic Framework

For particulate inclusion in polymer matrix, the effective thermal conductivity of composite K_{11}^*, K_{22}^* (in-plane direction) and K_{33}^* (z-direction) can be expressed as

$$K_{11}^* = K_{22}^* = K_m \frac{2 + f[\beta_{11}(1-L_{11})(1+\langle\cos^2\theta\rangle) + \beta_{33}(1-L_{33})(1-\langle\cos^2\theta\rangle)]}{2 - f[\beta_{11}L_{11}(1+\langle\cos^2\theta\rangle) + \beta_{33}L_{33}(1-\langle\cos^2\theta\rangle)]},$$

$$K_{33}^{*} = K_m \frac{1 + f[\beta_{11}(1-L_{11})(1-\langle\cos^2\theta\rangle) + \beta_{33}(1-L_{33})\langle\cos^2\theta\rangle]}{1 - f[\beta_{11}L_{11}(1-\langle\cos^2\theta\rangle) + \beta_{33}L_{33}\langle\cos^2\theta\rangle]},$$

with

$$\beta_{ii} = \frac{K_{ii}^{c} - K_m}{K_m + L_{ii}(K_{ii}^{c} - K_m)},$$

$$\langle\cos^2\theta\rangle = \frac{\int \rho(\theta)\cos^2\theta\sin\theta d\theta}{\int \rho(\theta)\sin\theta d\theta}.$$

Here θ is the angle between the composite axis X_3 and local ellipsoidal particle symmetric axis $X_3^{'}$, which is the normal of mhBN platelets in this case. $\rho(\theta)$ is a distribution function describing the orientation of ellipsoidal particles. K_{ii}^{c} is the equivalent thermal conductivity along the $X_{ii}^{'}$ symmetric axis of the ellipsoidal composite unit cell

$$K_{ii}^{c} = \frac{K_p}{1 + \frac{\gamma L_{ii} K_p}{K_m}},$$

where K_p and K_m are the thermal conductivities of ellipsoidal particles and the matrix; L_{ii} is a geometrical factor dependent on the shape of ellipsoidal particles. For platelets,

$L_{11} = L_{22} = \frac{p^2}{2(p^2-1)} + \frac{p}{2(1-p^2)^{3/2}}\cos^{-1} p, L_{33} = 1 - 2L_{11}$, where $p = a_3/a_1$ is the aspect ratio of ellipsoidal particles (for platelets, $a_1 = a_2 > a_3$, thus $p < 1$).

$\gamma = (1+2p)\alpha$, when $p < 1$.

Here α is a dimensionless parameter describing the interfacial properties between ellipsoidal particles and matrix, defined as

$$\alpha = \frac{R_{BD} K_m}{a_3},$$

where the thermal boundary resistance (TBR) $R_{BD} = \lim_{\delta, K_s \to 0} (\frac{\delta}{K_s})$, assuming interface layer with a thickness of δ and thermal conductivity of K_s.

Extraction of TBR

For randomly oriented platelets, $\langle \cos^2 \theta \rangle = 1/3$, the equation for K_{33}^* could be reduced to:

$$K_{33}^* = K_m \frac{3 + f[2\beta_{11}(1 - L_{11}) + \beta_{33}(1 - L_{33})]}{3 - f[2\beta_{11}L_{11} + \beta_{33}L_{33}]}$$

For the extraction of TBR, the theoretical in-plane thermal conductivity of hBN and the measured thermal conductivity of neat epoxy resin are input as known parameter:

K_p = 600 W/mK, K_m =0.15 W/mK,

The average diameter of hBN platelets is 5 μm, which is obtained from the material vendor. The thickness is measured from SEM images, which shows a broad distribution from 100 to 400 nm. As the aspect ratio (p) of hBN plays an important in EMA calculation, several thicknesses are input and calculated individually: p =300 nm/5μm =0.06, p =250 nm/5μm=0.05, p =200 nm/5μm=0.04.

Therefore, TBR is the only unknown in the calculation of K_{33}^*. The data fitting results for p =0.05 are show in Figure 128 as an example and the full results are listed in Table 9.

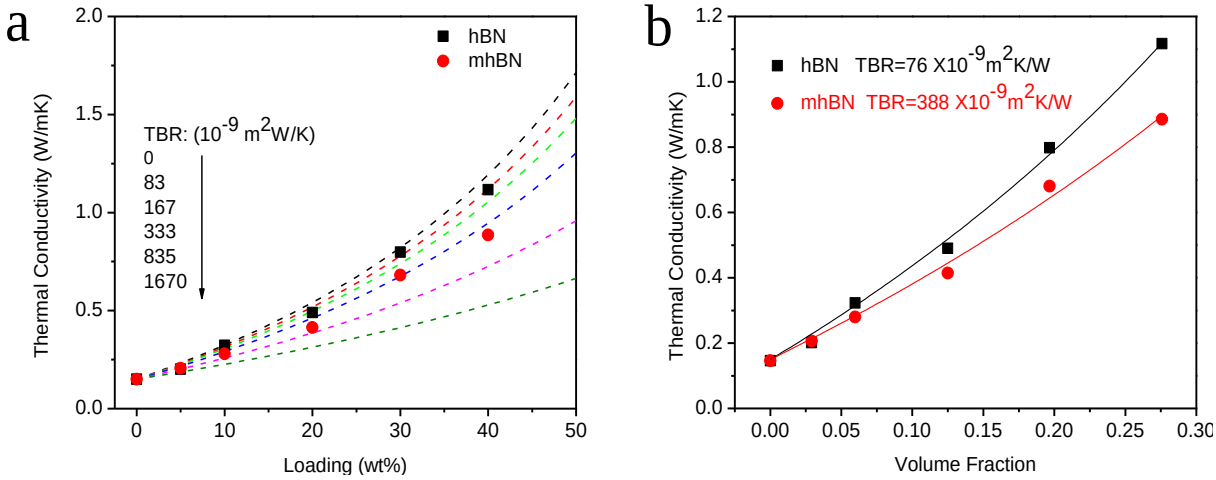

Figure 128. (a) Measured thermal conductivity of hBN-epoxy and mhBN-epoxy composites cured without an external magnetic field (dots); the predicted thermal conductivity (colored dash lines) from effective medium approximation (EMA) with the consideration of thermal boundary resistance (TBR). (b) Data fitting to extract the TBR of randomly oriented mhBN-epoxy composites assuming p =0.05.

Table 9. Calculated TBRs using different aspect ratios.

P	hBN-epoxy (10^{-9} m^{2}K/W)	mhBN-epoxy (10^{-9} m^{2}K/W)
0.06	negligible	218
0.05	83	424
0.04	280	613

Prediction of thermal enhancement

In the laser flash measurement, the thermal conductivity along the X_3 is measured. Therefore, the equation for K_{33}^* was used for thermal conductivity calculation.

For vertical aligned fillers $\langle \cos^2\theta \rangle$=0, other parameters are input as follows:

K_p = 600 W/mK, K_m =0.15 W/mK, p =0.05, TBR=388×10^{-9} m^{2}K/W.

Similarly, $\langle \cos^2\theta \rangle$=1 is used for composites with horizontally aligned fillers with other parameters the sample.

The thermal enhancement is calculated by

$$\frac{K_{33}^{*}(VmhBN-epoxy)-K_{33}^{*}(RmhBN-epoxy)}{K_{33}^{*}(RmhBN-epoxy)}\times 100\%$$

,

and the results are shown in Figure 129.

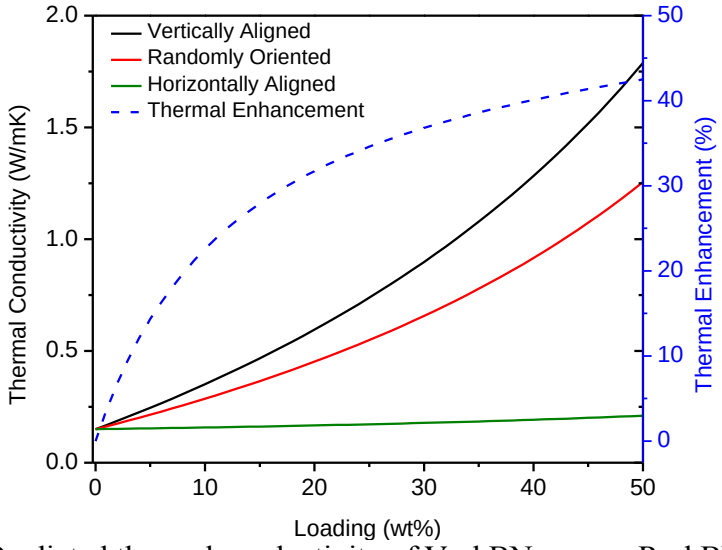

Figure 129. Predicted thermal conductivity of VmhBN-epoxy, RmhBN-epoxy and horizontally aligned mhBN-epoxy composites by EMA and the thermal enhancement between VmhBN-epoxy and RmhBN-epoxy.

Extraction of TBR for vertically aligned mhBN-epoxy

For vertically aligned platelets, $\langle \cos^2\theta \rangle$=0, the equation for K_{33}^{*} could be reduced to:

$$K_{33}^{*}=K_m\frac{1+f[\beta_{11}(1-L_{11})]}{1-f[\beta_{11}L_{11}]}$$

where K_p = 600 W/mK, K_m=0.15 W/mK . We used p=0.04 in the calculation in order to get physically meaningful result. The data points for fitting are measured thermal conductivities of neat epoxy, 5, 10, 20 wt% VmhBN-epoxy composites. The fitting result is shown in Figure 130. It is found that the TBR is as low as 8.3×10^{-9} m^2K/W.

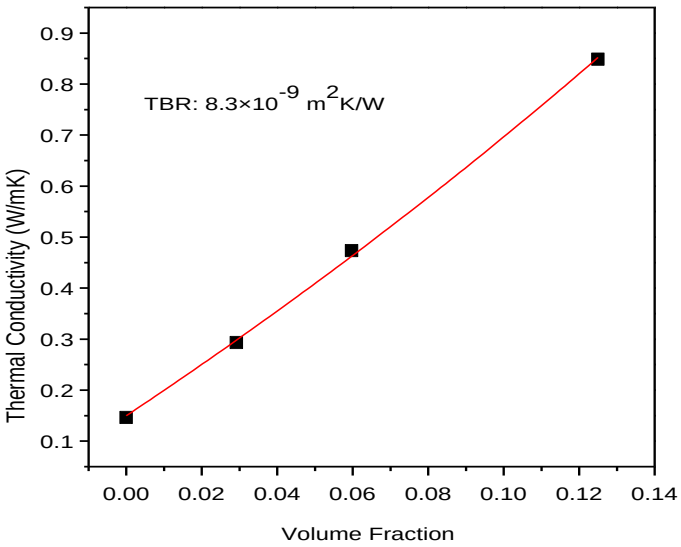

Figure 130. Data fitting to extract the TBR of vertically aligned mhBN-epoxy composites

Discussions on EMA results

First, we study a possible adverse effect of adding iron oxide nanoparticles on hBN surface in terms of TBR change. It is well accepted that TBR is a major factor determining the overall thermal conductivity of composite materials. We have experimentally observed that the thermal conductivities of RmhBN-epoxy composites are lower than those of hBN-epoxy composite (Figure 128a), which is an indication of TBR change. The actual TBR for each composite is extracted by fitting the measured thermal conductivity to EMA equations (Figure 128b and Table 9). When assuming a filler aspect ratio of 0.05, the TBR for hBN-epoxy is found to be 76×10^{-9} m^2K/W, which increases over four times to 388×10^{-9} m^2K/W for RmhBN-epoxy. Although the result of dramatically increased TBR is qualitative, it tells clearly that the additional iron oxide nanoparticles in mhBN, with a relatively low thermal conductivity of ~ 6 W/mK,[317] hinders the thermal transport across the hBN-epoxy interface probably by reducing the contact area between the hBN-hBN and hBN-epoxy.

Despite of the large TBR, a high thermal conductivity is still achieved by magnetic alignment. The significance of controlling the filler aligned is shown in Figure 129. VmhBN-epoxy theoretically gives higher thermal conductivity than RmhBN-epoxy, while the horizontally aligned composites have much suppressed thermal conductivities. The theoretical thermal enhancement increases with filler loading, which is consistent with the experimental data. This trend can be explained by the increasing contribution of thermal transport through hBN fillers at higher loadings. Moreover, it is interesting to note that the predicted thermal enhancement is lower than that observed in our experiments. For example, at 20 wt%, the predicted thermal enhancement is only ~ 32 %, compared to the experimental value of 104 %. This disparity could attribute to the complexity of real systems such as the variation of mhBN size, shape and thickness. Specifically, there are several aspects that lead the EMA calculation to underestimate thermal conductivities for VmhBN-epoxy and overestimate those for RmhBN-epoxy. First, a uniform TBR are simply assumed in EMA calculation. However, in the case of VmhBN-epoxy, the TBR for the hBN edges-epoxy interface could be much smaller than that for hBN basal plane-epoxy interface. Such anisotropic TBR has been found in materials with similar atomic structure to hBN, such as graphite and carbon nanotubes.[318-321] Tentative fitting of the thermal conductivities of VmhBN-epoxy to EMA equation indeed shows a one order of magnitude smaller TBR (Figure 130). Second, the assumed isotropic thermal conductivity for hBN (600 W/mK) overestimates the thermal conductivity of RmhBN-epoxy as the out-of-plane thermal conductivity of hBN is considerably smaller (30 W/mK). Third, the gravity force tends to horizontally orientate the mhBN platelets and lowers the thermal conductivities. Thus a complete

random orientation assumed in modeling overestimates the thermal conductivity for RmhBN-epoxy.

Other material properties

The mechanical and dielectric properties of polymer composite are also important for electronic packaging applications. As shown in Figure 131, the Young's modulus of neat epoxy and 20 wt% RmhBN-epoxy are 2.70 and 3.45 GPa respectively. A clear anisotropicity is observed for 20 wt% VmhBN-epoxy with a higher z-direction modulus of 4.55 GPa and a lower x-y direction modulus of 3.52 GPa, which results from the magnetic alignment and high in-plane modulus of hBN. Moreover, dielectric constant and dielectric loss tangent of 20 wt% VmhBN-epoxy only shows slight increase from those of neat epoxy (Figure 132). This result could be attributed to the low dielectric constant and high electric resistivity of hBN fillers, and is highly desirable for underfill applications.

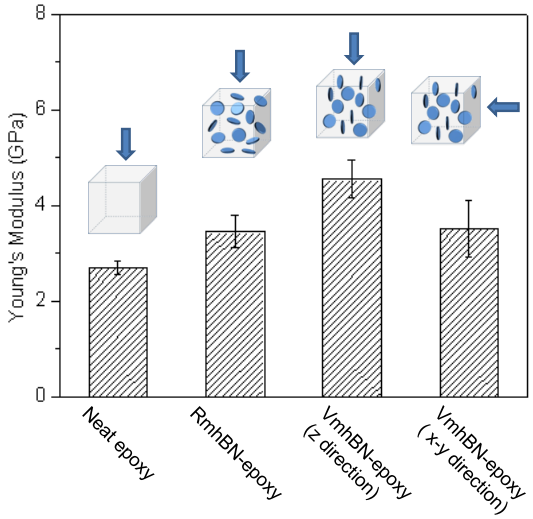

Figure 131. Young's modulus of neat epoxy, 20 wt% RmhBN-epoxy and VmhBN-epoxy along z direction and in x-y direction (arrows indicate the measurement direction). Reprinted with permission from [266].Copyright 2013 American Chemical Society.

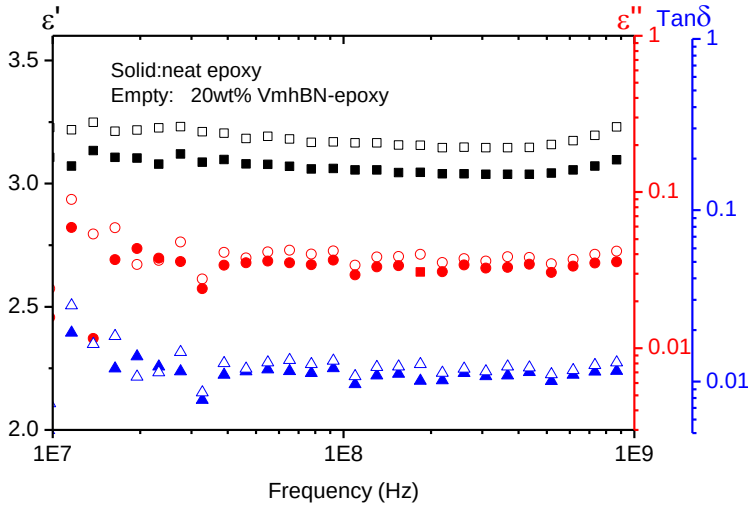

Figure 132. Dielectric properties of neat epoxy and 20 wt% VmhBN-epoxy.

Finite-element analysis of VmhBN-epoxy as an anisotropic underfill

The VmhBN-epoxy is a promising material for electronic encapsulation where low CTE and high thermal conductivity are required to meet the increasingly stringent device reliability and thermal management needs. We used finite-element analysis (FEA) to investigate the application of VmhBN-epoxy as an underfill from a thermomechanical point of view. The underfill is an encapsulation material widely used to improve the reliability of solder interconnects. Figure 133a shows a schematic of a flipped IC assembled on an organic substrate with solder bumps that are encapsulated with an underfill. The details of FEA are depicted in next section. To compare the performance of VmhBN-epoxy and RmhBN-epoxy, a three-dimensional half-symmetric generalized plane deformation (GPD) model of the assembly was created, and the model was simulated to be thermally cycled between 0 and 100 °C. It is known that the corner solder joints experience the highest thermo-mechanical stress/strains due to coefficient of CTE mismatch between silicon die and organic substrate. The fatigue life of corner solder joints can be determined using the accumulated plastic strain as damage metric in a

Coffin-Manson type relationship.[322] As seen in Figure 133b, the results from the simulation show that VmhBN-epoxy has a smaller accumulated plastic strain than RmhBN-epoxy, this is attributed to lower z-direction CTE of VmhBN-epoxy compared to RmhBN-epoxy. Thus, the predicted solder fatigue life is 2014 cycles for VmhBN-epoxy and 1769 cycles for RmhBN-epoxy. This value is beyond the typical industrial requirements for commercial packages.

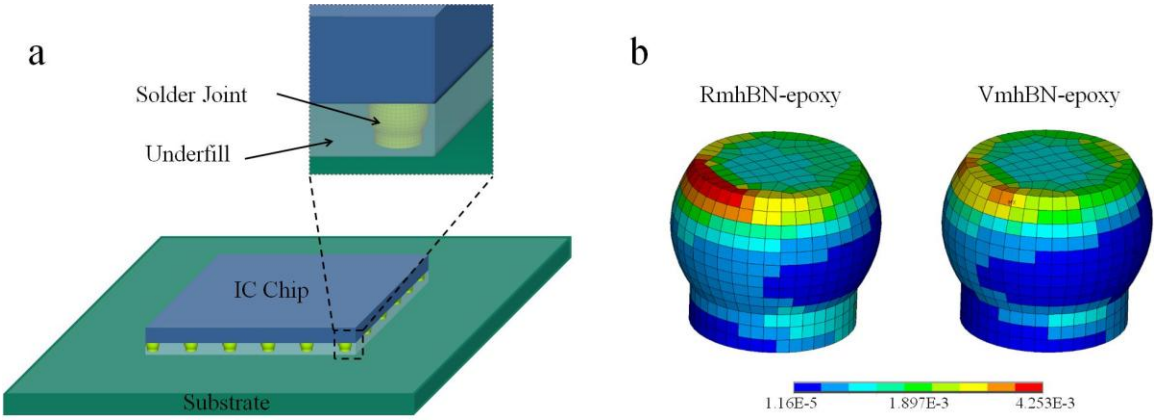

Figure 133. FEA of VmhBN-epoxy as a potential underfill in a flip-chip package. (a) Schematic illustration of the structure of flip-chip packaging used for FEA. The solder joint interconnections between the substrate and IC chip are encapsulated by underfill for reliability improvement. (b) The accumulated plastic stain of a peripheral solder joint when RmhBN-epoxy or VmhBN-epoxy is used as underfills. Reprinted with permission from [266].Copyright 2013 American Chemical Society.

Details of FEA

FEA was carried out using ANSYS. A global plane displacement 2.5D model was used as shown in Figure 134. All nodes were coupled in the normal direction in this face and the parallel face. The parameters and material properties used in the modeling are given in Table 10 and

Table 11. The model was cooled down from underfill curing temperature to room temperature. Then, the model was simulated to cycle between 0 ^{0}C and 100 ^{0}C. Stable plastic strain range was achieved after 3 cycles and it was used for calculating life based coffin-manson relationship, $N = (\frac{21.9}{\text{Accumulated plastic strain} \times 0.5})^{0.93}$, Where, N refers to solder lifetime in cycles. [322]

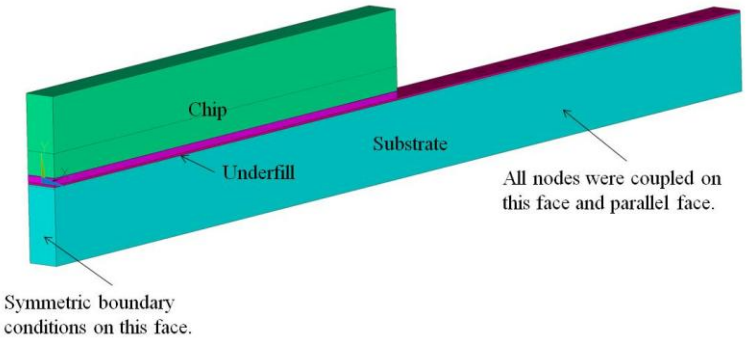

Figure 134. The boundary conditions for FEA.

Table 10. Model dimensions for FEA

Parameter	Value
Chip dimensions	10.24 x 10.24 mm
Substrate dimensions	20.48 x 20.48 mm
Die thickness	780 µm
Substrate thickness	780 µm
Solder Height	65 µm
Solder Diameter	~106 µm
Pitch	320 µm
Al pad diameter on chip	85 µm

Table 11. A list of material properties for FEA

Substrate:

Temperature (^{0}C)	30	95	125	150	270
E_{xx} (Gpa)	22.4	20.68	19.3	17.92	16
E_{zz} (Gpa)	22.4	20.68	19.3	17.92	16
E_{yy} (Gpa)	1.6	1.2	1.0	0.6	0.45
V_{xz}	0.02	0.02	0.02	0.02	0.02
$V_{xy} = V_{yz}$	0.143	0.143	0.143	0.143	0.143
G_{xy} G_{yz} G_{xz} (GPa)	4.782	4.882	4.511	4.42	4.3
CTE_x CTE_z (ppm)	16	16	16	12	12
CTE_y (ppm)	23	23	23	150	150

Silicon Chip

Young's Modulus (GPa)	129.85
Poisson ratio	0.27
CTE (ppm/K)	2.56

`

Tin-silver solder

Temperature (^{0}C)	-25	25	60	100	150	227
E_x (MPa)	58881	49229	42472	34750	25097	10232
v_{xy}	0.4	0.4	0.4	0.4	0.4	0.4
CTE (ppm/^{0}C)	24	24	24	24	24	24

Aluminum (Chip pad)

Young's Modulus (GPa)	68.0
Poisson ratio	0.33
CTE (ppm/K)	24

Underfill

Underfill	Modulus (GPa)	CTE (ppm/°C)
VmhBN-epoxy	3.52 – in plane	65.7 – in plane
	4.55 – out of plane	28.7 – out of plane
RmhRN-epoxy	3.45	65.7

Conclusions

In summary, we modify the hBN with magnetic iron oxide nanoparticles and demonstrate controlled alignment of mhBN in epoxy composite by an external magnetic field. The resulting mhBN-epoxy composite inherited anisotropic properties from the hBN fillers. Remarkably, low CTE and high thermal conductivity along the alignment direction have been achieved at low filler loadings so that the excellent processiblity and mechanical and dielectric properties of epoxy resin can be maintained in these composites. To the best of our knowledge, this is the first exploration on the alignment of hBN in polymer composites and its impact to materials properties. The anisotropic polymer composite, which can be prepared using a fairly low-cost method, has very promising applications as underfills or TIMs for advanced microelectronics packaging.

APPENDIX E

AUTHOR'S PUBLICATION

Refereed Journal Publications

1. ***Lin, Z. Y.;*** Mcnamara, A.; Liu, Y.; Moon, K. S.; Wong, C. P., Exfoliated Hexagonal Boron Nitride-based Polymer Nanocomposite with Enhanced Thermal Conductivity for Electronic Encapsulation, *Compos. Sci. Technol.***2013**, 90, 123-128

2. ***Lin, Z. Y.;*** Liu, Y.; Raghavan S.; Moon, K. S.; Sitaraman, S.; Wong, C. P, Magnetic alignment of hexagonal boron nitride platelets in polymer matrix: toward high performance anisotropic polymer composites for electronic encapsulation. *ACS Appl. Mater. Interfaces* **2013,** 5, 7633-7640

3. ***Lin, Z. Y.;*** Li, Z.; Moon, K. S.; Fang, Y. N.; Yao, Y. G.; Li, L.Y.; Wong, C. P., Robust vertically aligned carbon nanotube-carbon fiber paper hybrid as versatile electrodes for supercapacitors and capacitive deionization. *Carbon* **2013** 63,547-553

4. ***Lin, Z. Y.***; Waller, G.; Liu, Y.; Liu, M.; Wong, C. P., Simple preparation of nanoporous few-layer nitrogen-doped graphene for use as an efficient electrocatalyst for oxygen reduction and oxygen evolution reactions. *Carbon,* **2013** 53, 130–136

5. ***Lin, Z. Y.***; Waller, G.; Liu, Y.; Liu, M.; Wong, C. P., 3D Nitrogen-doped graphene prepared by pyrolysis of graphene oxide with polypyrrole for electrocatalysis of oxygen reduction reaction. *Nano Energy **2013,*** 2, 241–248

6. ***Lin, Z. Y.;*** Le, T.R.; Song, J.; Yao, Y.G.; Li, Z; Moon, K.S.; Tentzeris, M.; Wong, C.P., Preparation of Water-based Carbon Nanotube Inks and Application in the Inkjet Printing of Carbon Nanotube Gas Sensors, *J. Electron. Packag.* **2013,** 135(1), 011001-011005

7. ***Lin, Z. Y.***; Waller, G.; Liu, Y.; Liu, M.; Wong, C. P., Facile Synthesis of Nitrogen-doped Graphene via Pyrolysis of Graphene Oxide and Urea and its Electrocatalytic Activity toward Oxygen Reduction Reaction. *Adv. Energ. Mater.* **2012**, 2, 884-888.

8. ***Lin, Z. Y.***; Song, M. K.; Ding, Y.; Liu, Y.; Liu, M. L.; Wong, C. P., Facile preparation of nitrogen-doped graphene as a metal-free catalyst for oxygen reduction reaction. *Phys. Chem. Chem. Phys.* **2012**, 14, 3381-3387.

9. ***Lin, Z. Y.;*** Liu, Y.; Yao, Y. G.; Hildreth, O. J.; Li, Z.; Moon, K.; Wong, C. P., Superior Capacitance of Functionalized Graphene. *J Phys. Chem. C* **2011**, 115, 7120-7125.

10. ***Lin, Z. Y.;*** Yao, Y.; Li, Z.; Liu, Y.; Li, Z.; Wong, C.P., Solvent-Assisted Thermal Reduction of Graphite Oxide. *J. Phys. Chem. C* **2010,** 114, 14819-14825.

11. ***Lin, Z. Y.;*** Liu, Y.; Wong, C. P., Facile Fabrication of Superhydrophobic Octadecylamine-Functionalized Graphite Oxide Film. *Langmuir* **2010,** 26, 16110-16114.

12. Liu, Y.; ***Lin, Z. Y.;*** Zhao, X. Y.; Tuan, C. C.; Moon, K. S.; Yoo, S. H.; Choi, J.; Wong, C. P., High Refractive Index and Transparent Nanocomposites as Encapsulant for High Brightness LED Packaging", *IEEE Trans. Compon. Packag. Manuf. Technol.*, **2014**. accepted

13. Zhang, X. D.; ***Lin, Z. Y.;*** Chen, B.; Zhang, W.; Sharma, S.; Gu, W. T..; Deng, Y. L., Solid-state flexible polyaniline/silver cellulose nanofibrils aerogel supercapacitors. *J. Power Sources,* **2014,** 246, 283-289

14. Zhang, X. D.; ***Lin, Z. Y.;*** Chen, B.; Sharma, S.; Wong, C. P.; Zhang, W.; Deng, Y. L., *J. Mater. Chem. A* **2013**, 1, 5835-5839.

15. Liu, Y.; ***Lin, Z. Y.;*** Moon, K. S.; Wong, C. P., Superhydrophobic Nanocomposites Coating for Reliability Improvement of Microelectronics", *IEEE Trans. Compon. Packag. Manuf. Technol.*, **2013**. 3, 1079-1083.

16. Liu, Y.; ***Lin, Z. Y.;*** Lin, W.; Moon, K. S.; Wong, C. P., Reversible Superhydrophobic-Superhydrophilic Transition of ZnO Nanorod/Epoxy Composite Films. *ACS Appl. Mater. Interfaces* **2012**, 4, (8), 3959-3964.

17. Yao, Y.; ***Lin, Z.Y***.; Li, Z.; Song, X.; Moon, K.-S.; Wong, C.P., Large-scale production of two-dimensional nanosheets. *J. Mater. Chem.* **2012**, 22, 13494-13499.

18. Yang, P.H.; Ding, Y.; ***Lin, Z. Y.;*** Chen, Z. W.; Li, Y. Z.; Qiang, P. F.; Ebrahimi, M.; Mai, W. J.; Wong, C. P.; Wang, Z. L., Low-Cost High-Performance Solid-State Asymmetric Supercapacitors Based on MnO2 Nanowires and Fe2O3 Nanotubes, *Nano Lett.*, **2014,** 14, 731-726

19. Yang, P.H.; Li, Y.; ***Lin, Z. Y.;*** Ding, Y.; Yue, S.; Wong, C. P.; Cai, X.; Tan, S.; Mai, W. J., Worm-like amorphous MnO 2 nanowires grown on textiles for high-performance flexible supercapacitors, *J. Mater. Chem. A.***2014**, 2, 595-599.

20. Gao. Y.; Li. Z.; **Lin, Z. Y.;** Zhu, L.J.; Tannenbaum, A.; Bouix, S.; Wong, C. P.; Automated dispersion and orientation analysis for carbon nanotube reinforced polymer composites. *Nanotechnology*, **2012**, 23, 435706

21. Liu, Y; Lin, W.; ***Lin, Z. Y.;*** Xiu, Y. H.; Wong, C.P. A combined etching process toward robust superhydrophobic SiC surfaces, *Nanotechnology*, **2012**, 23, 255703

22. Liu, Y.; Das, A.; Xu, S.; ***Lin, Z. Y.;*** Xu, C.; Wang, Z. L.; Rohatgi, A.; Wong, C. P., Hybridizing ZnO Nanowires with Micropyramid Silicon Wafers as Superhydrophobic High-Efficiency Solar Cells. *Adv. Energy. Mater.* **2012**, 2, 47-51.

23. Yao, Y. G.; Li, Z.; ***Lin, Z. Y.;*** Moon, K. S.; Agar, J.; Wong, C. P., Controlled Growth of Multilayer, Few-Layer, and Single-Layer Graphene on Metal Substrates. *J. Phys Chem. C* **2011**, 115, 5232-5238.

24. Li, Z.; Yao, Y. G.; ***Lin, Z. Y.;*** Moon, K. S.; Lin, W.; Wong, C. P., "Ultrafast, dry microwave synthesis of graphene sheets." *J. Mater. Chem.* **2010,** 20, 4781-4783.

25. Yang, P.H.; Xiao, X.; Li, Y.Z; Ding, Y.; Qiang, P.F.; Tan, X. H.; Mai, W. J.; ***Lin, Z. Y.;*** Wu, W. Z.; Li, T. Q.; Jin, H.Y.,; Liu, P. Y.; Zhou, J.; Wong, C. P.; Wang, Z. L., "Hydrogenated ZnO Core–Shell Nanocables for Flexible Supercapacitors and Self-Powered Systems" *ACS Nano,* **2013,** 7, 2617–2626.

CONFERENCE PROCEEDINGS

26. ***Lin, Z. Y.;*** Li, Z.; Moon, K. S.; Wong, C. P., Capacitive Deionization of Water Coolant Using Hybrid Carbon Electrodes for High Power Electronic Applications. *2014 IEEE 64th Electronic Components and Technology Conference (ECTC)* 2014, accepted

27. ***Lin, Z. Y.;*** Liu, Y.; Moon, K.S; Wong, C. P., Novel Surface Modification of Nanosilica for Low Stress Underfill. *2013 IEEE 63rd Electronic Components and Technology Conference (ECTC)* 2013, 773-777.

28. ***Lin, Z. Y.;*** Liu, Y.; Moon, K.S; Wong, C. P., Enhanced Thermal Transport of Hexagonal Boron Nitride Filled Polymer Composite by Magnetic Field-assisted Alignment. *2013 IEEE 63rd Electronic Components and Technology Conference (ECTC)* 2013, 1692-1696.

29. ***Lin, Z. Y.;*** Yao, Y.G.; Mcnamara, A.; Moon, K.S; Wong, C. P., Single/Few-Layer Boron Nitride-Based Nanocomposites for High Thermal Conductivity Underfills. *2012 IEEE 62nd Electronic Components and Technology Conference (ECTC)* 2012, 1437-1441.

30. ***Lin, Z. Y.;*** Lau, S. Y.; Moon, K.S; Wong, C. P., Polyhedral Oligomeric Silsesquioxanes (POSS)-Filled Underfill with Excellent High Temperature Performance. 2012 IEEE 62nd Electronic Components and Technology *Conference (ECTC)* 2012, 1599-1604.

31. ***Lin, Z. Y.;*** Liu, Y.; Li, Z.; Wong, C. P., Novel Preparation of Functiona lized Graphene Oxide for Large Scale, Low cost, and Self-cleaning Coatings of Electronic Devices. *2011 IEEE 61st Electronic Components and Technology Conference (ECTC)* 2011, 358-362.

32. ***Lin, Z. Y.;*** Liu, Y.; Yao, Y. G.; Hildreth, O. J.; Li, Z.; Moon, K.; Agar, J. C.; Wong, C. P., Surface Engineering of Graphene for High Performance Supercapacitors. *2011 IEEE 61st Electronic Components and Technology Conference (ECTC)* 2011, 236-241.

33. ***Lin, Z. Y.;*** Moon, K. S.; Wong, C. P., Nanocomposite for Low Stress Underfill. *2011 IEEE 61st Electronic Components and Technology Conference (ECTC)* 2011, 2045-2049.

34. Tuan C. C.; ***Lin, Z. Y.;*** Liu, Y.; Moon, K.S; Yoo, S.H.; Jang, M. G.; Wong, C. P., Ultra-high Refractive Index LED Encapsulant, *2014 IEEE 64th Electronic Components and Technology Conference (ECTC)* 2014 accepted.

35. Tuan C. C.; ***Lin, Z. Y.;*** Liu, Y.; Moon, K.S; Wong, C. P., Self-Patterning, Pre-Applied Underfilling Technology for Stack-Die Packaging, *2014 IEEE 64th Electronic Components and Technology Conference (ECTC)* 2014 accepted.

36. Le, T. R; ***Lin, Z. Y.;*** Wong, C. P.; Tentzeris, M., Enhanced-Performance Wireless Conformal "Smart Skins" Utilizing Inkjet-Printed Carbon-Nanostructures. *2014 IEEE 64th Electronic Components and Technology Conference (ECTC)* 2014 accepted.

37. Liu, Y.; ***Lin, Z. Y.;*** Moon, K. S.; Wong, C. P., Novel ZnO Nanowires/Silicon Hierarchical Structures for Superhydrophobic, Low Reflection, and High Efficiency Solar Cells. *2011 IEEE 61st Electronic Components and Technology Conference (ECTC)* 2011, 2114-2118.

38. Le, T. R; Lakafosis, V.; ***Lin, Z. Y.;*** Wong, C. P.; Tentzeris, M., Inkjet-Printed Graphene-Based Wireless Gas Sensor Modules. *2012 IEEE 62nd Electronic Components and Technology Conference (ECTC)* 2012, 1003-1008.

39. Liu, Y.; ***Lin, Z. Y.;*** Moon, K.S; Wong, C. P., Robust, Novel, and Low Cost Superhydrophobic Nanocomposites Coating for Reliability Improvement of Microelectronics. *2012 IEEE 62nd Electronic Components and Technology Conference (ECTC)* 2012, 2135- 2139.

40. Liu, Y.; ***Lin, Z. Y.;*** Zhao, X.Y.; Yoo, S.H.; Moon, K.S; Wong, C. P., ZnO Quantum Dots-Filled Encapsulant for LED Packaging. *2012 IEEE 62nd Electronic Components and Technology Conference (ECTC)* 2012, 2140-2144.

41. Liu, Y.; ***Lin, Z. Y.;*** Moon, K.S; Yoo, S.H.; Wong, C. P., High Refractive Index and Transparency Nanocomposites as Encapsulant for High Brightness LED packaging, *2013 IEEE 63rd Electronic Components and Technology Conference (ECTC)* 2013, 553-556.

42. Le, T.R.; Lakafosis, V.; Thai, T.; ***Lin, Z. Y.;*** Tentzeris, M., Inkjet printing of graphene thin films for wireless sensing applications, *2012 International Conference on Electromagnetics in Advanced Applications (ICEAA),* 2012, 954 – 957

43. Le, T. R; ***Lin, Z. Y.;*** Fang, Y. N.; Wong, C. P.; Tentzeris, M., Novel Enhancement Techniques for Ultra-High-Performance Conformal Wireless Sensors. *2013 IEEE 63rd Electronic Components and Technology Conference (ECTC)* 2013, 1640-1643.

REFERENCES

[1] K. S. Novoselov, A. K. Geim, S. V. Morozov, D. Jiang, Y. Zhang, S. V. Dubonos, I. V. Grigorieva, and A. A. Firsov, "Electric field effect in atomically thin carbon films" Science, vol. 306, pp. 666-669, 2004.

[2] K. I. Bolotin, K. J. Sikes, Z. Jiang, M. Klima, G. Fudenberg, J. Hone, P. Kim, and H. L. Stormer, "Ultrahigh electron mobility in suspended graphene" Solid State Commun, vol. 146, pp. 351-355, 2008.

[3] A. A. Balandin, S. Ghosh, W. Z. Bao, I. Calizo, D. Teweldebrhan, F. Miao, and C. N. Lau, "Superior thermal conductivity of single-layer graphene" Nano Lett, vol. 8, pp. 902-907, 2008.

[4] Z. L. Gao, Y. Zhang, Y. F. Fu, M. M. F. Yuen, and J. Liu, "Thermal chemical vapor deposition grown graphene heat spreader for thermal management of hot spots" Carbon, vol. 61, pp. 342-348, 2013.

[5] Q. Z. Liang, X. X. Yao, W. Wang, Y. Liu, and C. P. Wong, "A Three-Dimensional Vertically Aligned Functionalized Multilayer Graphene Architecture: An Approach for Graphene-Based Thermal Interfacial Materials" ACS Nano, vol. 5, pp. 2392-2401, 2011.

[6] K. M. F. Shahil and A. A. Balandin, "Graphene−Multilayer Graphene Nanocomposites as Highly Efficient Thermal Interface Materials" Nano Lett, vol. 12, pp. 861–867, 2012.

[7] R. R. Nair, P. Blake, A. N. Grigorenko, K. S. Novoselov, T. J. Booth, T. Stauber, N. M. R. Peres, and A. K. Geim, "Fine structure constant defines visual transparency of graphene" Science, vol. 320, pp. 1308-1308, 2008.

[8] S. Bae, H. Kim, Y. Lee, X. F. Xu, J. S. Park, Y. Zheng, J. Balakrishnan, T. Lei, H. R. Kim, Y. I. Song, Y. J. Kim, K. S. Kim, B. Ozyilmaz, J. H. Ahn, B. H. Hong, and S. Iijima, "Roll-to-roll production of 30-inch graphene films for transparent electrodes" Nat Nanotechnol, vol. 5, pp. 574-578, 2010.

[9] C. Lee, X. D. Wei, J. W. Kysar, and J. Hone, "Measurement of the elastic properties and intrinsic strength of monolayer graphene" Science, vol. 321, pp. 385-388, 2008.

[10] C. Berger, Z. M. Song, T. B. Li, X. B. Li, A. Y. Ogbazghi, R. Feng, Z. T. Dai, A. N. Marchenkov, E. H. Conrad, P. N. First, and W. A. de Heer, "Ultrathin epitaxial graphite: 2D electron gas properties and a route toward graphene-based nanoelectronics" J Phys Chem B, vol. 108, pp. 19912-19916, 2004.

[11] C. Virojanadara, M. Syvajarvi, R. Yakimova, L. I. Johansson, A. A. Zakharov, and T. Balasubramanian, "Homogeneous large-area graphene layer growth on 6H-SiC(0001)" Phys Rev B, vol. 78, pp. 245403, 2008.

[12] Y. M. Lin, C. Dimitrakopoulos, K. A. Jenkins, D. B. Farmer, H. Y. Chiu, A. Grill, and P. Avouris, "100-GHz Transistors from Wafer-Scale Epitaxial Graphene" Science, vol. 327, pp. 662-662, 2010.

[13] J. D. Caldwell, T. J. Anderson, J. C. Culbertson, G. G. Jernigan, K. D. Hobart, F. J. Kub, M. J. Tadjer, J. L. Tedesco, J. K. Hite, M. A. Mastro, R. L. Myers-Ward, C. R. Eddy, P. M. Campbell, and D. K. Gaskill, "Technique for the Dry Transfer of Epitaxial Graphene onto Arbitrary Substrates" ACS Nano, vol. 4, pp. 1108-1114, 2010.

[14] D. S. Lee, C. Riedl, B. Krauss, K. von Klitzing, U. Starke, and J. H. Smet, "Raman Spectra of Epitaxial Graphene on SiC and of Epitaxial Graphene Transferred to SiO2" Nano Lett, vol. 8, pp. 4320-4325, 2008.

[15] S. Unarunotai, Y. Murata, C. E. Chialvo, H. S. Kim, S. MacLaren, N. Mason, I. Petrov, and J. A. Rogers, "Transfer of graphene layers grown on SiC wafers to other substrates and their integration into field effect transistors" Appl Phys Lett, vol. 95, 2009.

[16] R. S. Edwards and K. S. Coleman, "Graphene Film Growth on Polycrystalline Metals" Accounts Chem Res, vol. 46, pp. 23-30, 2013.

[17] Z. Yan, J. Lin, Z. W. Peng, Z. Z. Sun, Y. Zhu, L. Li, C. S. Xiang, E. L. Samuel, C. Kittrell, and J. M. Tour, "Toward the Synthesis of Wafer-Scale Single-Crystal Graphene on Copper Foils" ACS Nano, vol. 6, pp. 9110-9117, 2012.

[18] H. L. Zhou, W. J. Yu, L. X. Liu, R. Cheng, Y. Chen, X. Q. Huang, Y. Liu, Y. Wang, Y. Huang, and X. F. Duan, "Chemical vapour deposition growth of large single crystals of monolayer and bilayer graphene" Nat Commun, vol. 4, 2013.

[19] Y. G. Yao, Z. Li, Z. Y. Lin, K. S. Moon, J. Agar, and C. P. Wong, "Controlled Growth of Multilayer, Few-Layer, and Single-Layer Graphene on Metal Substrates" J Phys Chem C, vol. 115, pp. 5232-5238, 2011.

[20] G. D. Ruan, Z. Z. Sun, Z. W. Peng, and J. M. Tour, "Growth of Graphene from Food, Insects, and Waste" ACS Nano, vol. 5, pp. 7601-7607, 2011.

[21] R. S. Weatherup, B. C. Bayer, R. Blume, C. Ducati, C. Baehtz, R. Schlogl, and S. Hofmann, "In Situ Characterization of Alloy Catalysts for Low-Temperature Graphene Growth" Nano Lett, vol. 11, pp. 4154-4160, 2011.

[22] A. Dato, V. Radmilovic, Z. Lee, J. Phillips, and M. Frenklach, "Substrate-free gas-phase synthesis of graphene sheets" Nano Lett, vol. 8, pp. 2012-2016, 2008.

[23] J. Kim, M. Ishihara, Y. Koga, K. Tsugawa, M. Hasegawa, and S. Iijima, "Low-temperature synthesis of large-area graphene-based transparent conductive films using surface wave plasma chemical vapor deposition" Appl Phys Lett, vol. 98, 2011.

[24] L. T. Qu, Y. Liu, J. B. Baek, and L. M. Dai, "Nitrogen-Doped Graphene as Efficient Metal-Free Electrocatalyst for Oxygen Reduction in Fuel Cells" ACS Nano, vol. 4, pp. 1321-1326, 2010.

[25] D. C. Wei, Y. Q. Liu, Y. Wang, H. L. Zhang, L. P. Huang, and G. Yu, "Synthesis of N-Doped Graphene by Chemical Vapor Deposition and Its Electrical Properties" Nano Lett, vol. 9, pp. 1752-1758, 2009.

[26] H. Wang, Y. Zhou, D. Wu, L. Liao, S. L. Zhao, H. L. Peng, and Z. F. Liu, "Synthesis of Boron-Doped Graphene Monolayers Using the Sole Solid Feedstock by Chemical Vapor Deposition" Small, vol. 9, pp. 1316-1320, 2013.

[27] J. Y. Chen, Y. G. Wen, Y. L. Guo, B. Wu, L. P. Huang, Y. Z. Xue, D. C. Geng, D. Wang, G. Yu, and Y. Q. Liu, "Oxygen-Aided Synthesis of Polycrystalline Graphene on Silicon Dioxide Substrates" J Am Chem Soc, vol. 133, pp. 17548-17551, 2011.

[28] M. H. Rummeli, A. Bachmatiuk, A. Scott, F. Borrnert, J. H. Warner, V. Hoffman, J. H. Lin, G. Cuniberti, and B. Buchner, "Direct Low-Temperature Nanographene CVD Synthesis over a Dielectric Insulator" ACS Nano, vol. 4, pp. 4206-4210, 2010.

[29] J. N. Coleman, "Liquid Exfoliation of Defect-Free Graphene" Accounts Chem Res, vol. 46, pp. 14-22, 2013.

[30] W. S. Hummers and R. E. Offeman, "Preparation of Graphitic Oxide" J Am Chem Soc, vol. 80, pp. 1339-1339, 1958.

[31] B. C. Brodie, "On the Atomic Weight of Graphite" Philosophical Transactions of the Royal Society of London, vol. 149, pp. 249-259, 1859.

[32] L. Staudenmaier, "Verfahren zur Darstellung der Graphitsäure" Berichte der deutschen chemischen Gesellschaft, vol. 31, pp. 1481-1487, 1898.

[33] D. C. Marcano, D. V. Kosynkin, J. M. Berlin, A. Sinitskii, Z. Z. Sun, A. Slesarev, L. B. Alemany, W. Lu, and J. M. Tour, "Improved Synthesis of Graphene Oxide" ACS Nano, vol. 4, pp. 4806-4814, 2010.

[34] J. Chen, B. W. Yao, C. Li, and G. Q. Shi, "An improved Hummers method for eco-friendly synthesis of graphene oxide" Carbon, vol. 64, pp. 225-229, 2013.

[35] P. L. Chiu, D. D. T. Mastrogiovanni, D. G. Wei, C. Louis, M. Jeong, G. Yu, P. Saad, C. R. Flach, R. Mendelsohn, E. Garfunkel, and H. X. He, "Microwave- and

Nitronium Ion-Enabled Rapid and Direct Production of Highly Conductive Low-Oxygen Graphene" J Am Chem Soc, vol. 134, pp. 5850-5856, 2012.

[36] A. Lerf, H. Y. He, M. Forster, and J. Klinowski, "Structure of graphite oxide revisited" J Phys Chem B, vol. 102, pp. 4477-4482, 1998.

[37] S. Stankovich, D. A. Dikin, R. D. Piner, K. A. Kohlhaas, A. Kleinhammes, Y. Jia, Y. Wu, S. T. Nguyen, and R. S. Ruoff, "Synthesis of graphene-based nanosheets via chemical reduction of exfoliated graphite oxide" Carbon, vol. 45, pp. 1558-1565, 2007.

[38] M. J. Fernandez-Merino, L. Guardia, J. I. Paredes, S. Villar-Rodil, P. Solis-Fernandez, A. Martinez-Alonso, and J. M. D. Tascon, "Vitamin C Is an Ideal Substitute for Hydrazine in the Reduction of Graphene Oxide Suspensions" J Phys Chem C, vol. 114, pp. 6426-6432, 2010.

[39] H. J. Shin, K. K. Kim, A. Benayad, S. M. Yoon, H. K. Park, I. S. Jung, M. H. Jin, H. K. Jeong, J. M. Kim, J. Y. Choi, and Y. H. Lee, "Efficient Reduction of Graphite Oxide by Sodium Borohydride and Its Effect on Electrical Conductance" Advanced Functional Materials, vol. 19, pp. 1987-1992, 2009.

[40] G. X. Wang, J. Yang, J. Park, X. L. Gou, B. Wang, H. Liu, and J. Yao, "Facile synthesis and characterization of graphene nanosheets" J Phys Chem C, vol. 112, pp. 8192-8195, 2008.

[41] S. F. Pei, J. P. Zhao, J. H. Du, W. C. Ren, and H. M. Cheng, "Direct reduction of graphene oxide films into highly conductive and flexible graphene films by hydrohalic acids" Carbon, vol. 48, pp. 4466-4474, 2010.

[42] C. G. Hu, X. Q. Zhai, L. L. Liu, Y. Zhao, L. Jiang, and L. T. Qu, "Spontaneous Reduction and Assembly of Graphene oxide into Three-Dimensional Graphene Network on Arbitrary Conductive Substrates" Sci Rep-Uk, vol. 3, 2013.

[43] M. J. McAllister, J. L. Li, D. H. Adamson, H. C. Schniepp, A. A. Abdala, J. Liu, M. Herrera-Alonso, D. L. Milius, R. Car, R. K. Prud'homme, and I. A. Aksay, "Single sheet functionalized graphene by oxidation and thermal expansion of graphite" Chemistry of Materials, vol. 19, pp. 4396-4404, 2007.

[44] H. C. Schniepp, J. L. Li, M. J. McAllister, H. Sai, M. Herrera-Alonso, D. H. Adamson, R. K. Prud'homme, R. Car, D. A. Saville, and I. A. Aksay, "Functionalized single graphene sheets derived from splitting graphite oxide" J Phys Chem B, vol. 110, pp. 8535-8539, 2006.

[45] W. Scholz and H. P. Boehm, "Die thermische Zersetzung von Graphitoxyd" Naturwissenschaften, vol. 51, pp. 160-160, 1964.

[46] Y. W. Zhu, S. Murali, M. D. Stoller, A. Velamakanni, R. D. Piner, and R. S. Ruoff, "Microwave assisted exfoliation and reduction of graphite oxide for ultracapacitors" Carbon, vol. 48, pp. 2118-2122, 2010.

[47] Z. Li, Y. G. Yao, Z. Y. Lin, K. S. Moon, W. Lin, and C. P. Wong, "Ultrafast, dry microwave synthesis of graphene sheets" J Mater Chem, vol. 20, pp. 4781-4783, 2010.

[48] Z. Y. Lin, Y. G. Yao, Z. Li, Y. Liu, Z. Li, and C. P. Wong, "Solvent-Assisted Thermal Reduction of Graphite Oxide" J Phys Chem C, vol. 114, pp. 14819-14825, 2010.

[49] S. Dubin, S. Gilje, K. Wang, V. C. Tung, K. Cha, A. S. Hall, J. Farrar, R. Varshneya, Y. Yang, and R. B. Kaner, "A One-Step, Solvothermal Reduction Method for Producing Reduced Graphene Oxide Dispersions in Organic Solvents" ACS Nano, vol. 4, pp. 3845-3852, 2010.

[50] H. P. Viet, V. C. Tran, S. H. Hur, E. Oh, E. J. Kim, E. W. Shin, and J. S. Chung, "Chemical functionalization of graphene sheets by solvothermal reduction of a graphene oxide suspension in N-methyl-2-pyrrolidone" J Mater Chem, vol. 21, pp. 3371-3377, 2011.

[51] D. A. Sokolov, K. R. Shepperd, and T. M. Orlando, "Formation of Graphene Features from Direct Laser-Induced Reduction of Graphite Oxide" J Phys Chem Lett, vol. 1, pp. 2633-2636, 2010.

[52] V. Abdelsayed, S. Moussa, H. M. Hassan, H. S. Aluri, M. M. Collinson, and M. S. El-Shall, "Photothermal Deoxygenation of Graphite Oxide with Laser Excitation in Solution and Graphene-Aided Increase in Water Temperature" J Phys Chem Lett, vol. 1, pp. 2804-2809, 2010.

[53] Y. Y. Shao, J. Wang, M. Engelhard, C. M. Wang, and Y. H. Lin, "Facile and controllable electrochemical reduction of graphene oxide and its applications" J Mater Chem, vol. 20, pp. 743-748, 2010.

[54] Z. J. Wang, X. Z. Zhou, J. Zhang, F. Boey, and H. Zhang, "Direct Electrochemical Reduction of Single-Layer Graphene Oxide and Subsequent Functionalization with Glucose Oxidase" J Phys Chem C, vol. 113, pp. 14071-14075, 2009.

[55] W. Gao, L. B. Alemany, L. J. Ci, and P. M. Ajayan, "New insights into the structure and reduction of graphite oxide" Nat Chem, vol. 1, pp. 403-408, 2009.

[56] S. Some, Y. Kim, Y. Yoon, H. Yoo, S. Lee, Y. Park, and H. Lee, "High-Quality Reduced Graphene Oxide by a Dual-Function Chemical Reduction and Healing Process" Sci Rep-Uk, vol. 3, 2013.

[57] V. Lopez, R. S. Sundaram, C. Gomez-Navarro, D. Olea, M. Burghard, J. Gomez-Herrero, F. Zamora, and K. Kern, "Chemical Vapor Deposition Repair of Graphene Oxide: A Route to Highly Conductive Graphene Monolayers" Adv Mater, vol. 21, pp. 4683-4686, 2009.

[58] B. Y. Dai, L. Fu, L. Liao, N. Liu, K. Yan, Y. S. Chen, and Z. F. Liu, "High-Quality Single-Layer Graphene via Reparative Reduction of Graphene Oxide" Nano Res, vol. 4, pp. 434-439, 2011.

[59] J. M. Cai, P. Ruffieux, R. Jaafar, M. Bieri, T. Braun, S. Blankenburg, M. Muoth, A. P. Seitsonen, M. Saleh, X. L. Feng, K. Mullen, and R. Fasel, "Atomically precise bottom-up fabrication of graphene nanoribbons" Nature, vol. 466, pp. 470-473, 2010.

[60] A. Narita, X. L. Feng, Y. Hernandez, S. A. Jensen, M. Bonn, H. F. Yang, I. A. Verzhbitskiy, C. Casiraghi, M. R. Hansen, A. H. R. Koch, G. Fytas, O. Ivasenko, B. Li, K. S. Mali, T. Balandina, S. Mahesh, S. De Feyter, and K. Mullen, "Synthesis of structurally well-defined and liquid-phase-processable graphene nanoribbons" Nat Chem, vol. 6, pp. 126-132, 2014.

[61] D. V. Kosynkin, A. L. Higginbotham, A. Sinitskii, J. R. Lomeda, A. Dimiev, B. K. Price, and J. M. Tour, "Longitudinal unzipping of carbon nanotubes to form graphene nanoribbons" Nature, vol. 458, pp. 872-U5, 2009.

[62] L. Y. Jiao, L. Zhang, X. R. Wang, G. Diankov, and H. J. Dai, "Narrow graphene nanoribbons from carbon nanotubes" Nature, vol. 458, pp. 877-880, 2009.

[63] P. K. Ang, S. A. Wang, Q. L. Bao, J. T. L. Thong, and K. P. Loh, "High-Throughput Synthesis of Graphene by Intercalation - Exfoliation of Graphite Oxide and Study of Ionic Screening in Graphene Transistor" ACS Nano, vol. 3, pp. 3587-3594, 2009.

[64] L. M. Viculis, J. J. Mack, O. M. Mayer, H. T. Hahn, and R. B. Kaner, "Intercalation and exfoliation routes to graphite nanoplatelets" J Mater Chem, vol. 15, pp. 974-978, 2005.

[65] X. M. Geng, Y. F. Guo, D. F. Li, W. W. Li, C. Zhu, X. F. Wei, M. L. Chen, S. Gao, S. Q. Qiu, Y. P. Gong, L. Q. Wu, M. S. Long, M. T. Sun, G. B. Pan, and L. W. Liu, "Interlayer catalytic exfoliation realizing scalable production of large-size pristine few-layer graphene" Sci Rep-Uk, vol. 3, 2013.

[66] A. Yoshida, Y. Hishiyama, and M. Inagaki, "Exfoliated Graphite from Various Intercalation Compounds" Carbon, vol. 29, pp. 1227-1231, 1991.

[67] J. W. Bai, X. Zhong, S. Jiang, Y. Huang, and X. F. Duan, "Graphene nanomesh" Nat Nanotechnol, vol. 5, pp. 190-194, 2010.

[68] Y. W. Zhu, S. Murali, M. D. Stoller, K. J. Ganesh, W. W. Cai, P. J. Ferreira, A. Pirkle, R. M. Wallace, K. A. Cychosz, M. Thommes, D. Su, E. A. Stach, and R. S. Ruoff, "Carbon-Based Supercapacitors Produced by Activation of Graphene" Science, vol. 332, pp. 1537-1541, 2011.

[69] T. Ramanathan, A. A. Abdala, S. Stankovich, D. A. Dikin, M. Herrera-Alonso, R. D. Piner, D. H. Adamson, H. C. Schniepp, X. Chen, R. S. Ruoff, S. T. Nguyen, I. A. Aksay, R. K. Prud'homme, and L. C. Brinson, "Functionalized graphene sheets for polymer nanocomposites" Nat Nanotechnol, vol. 3, pp. 327-331, 2008.

[70] X. B. Fan, W. C. Peng, Y. Li, X. Y. Li, S. L. Wang, G. L. Zhang, and F. B. Zhang, "Deoxygenation of Exfoliated Graphite Oxide under Alkaline Conditions: A Green Route to Graphene Preparation" Adv Mater, vol. 20, pp. 4490-4493, 2008.

[71] Y. Zhou, Q. L. Bao, L. A. L. Tang, Y. L. Zhong, and K. P. Loh, "Hydrothermal Dehydration for the "Green" Reduction of Exfoliated Graphene Oxide to Graphene and Demonstration of Tunable Optical Limiting Properties" Chemistry of Materials, vol. 21, pp. 2950-2956, 2009.

[72] Y. W. Zhu, M. D. Stoller, W. W. Cai, A. Velamakanni, R. D. Piner, D. Chen, and R. S. Ruoff, "Exfoliation of Graphite Oxide in Propylene Carbonate and Thermal Reduction of the Resulting Graphene Oxide Platelets" ACS Nano, vol. 4, pp. 1227-1233, 2010.

[73] G. X. Wang, B. Wang, J. Park, J. Yang, X. P. Shen, and J. Yao, "Synthesis of enhanced hydrophilic and hydrophobic graphene oxide nanosheets by a solvothermal method" Carbon, vol. 47, pp. 68-72, 2009.

[74] J. F. Che, L. Shen, Y, and Y. H. and Xiao, "A New Approach to Fabricate Graphene Nanosheets in Organic Medium: Conbination of Reduction and Dispesion " J Mater Chem, vol. 20, pp. 1722-1727, 2010.

[75] J. A. Yan, L. D. Xian, and M. Y. Chou, "Structural and Electronic Properties of Oxidized Graphene" Physical Review Letters, vol. 103, 2009.

[76] I. Jung, D. A. Dikin, R. D. Piner, and R. S. Ruoff, "Tunable Electrical Conductivity of Individual Graphene Oxide Sheets Reduced at "Low" Temperatures" Nano Lett, vol. 8, pp. 4283-4287, 2008.

[77] H. L. Wang, H. S. Casalongue, Y. Y. Liang, and H. J. Dai, "Ni(OH)(2) Nanoplates Grown on Graphene as Advanced Electrochemical Pseudocapacitor Materials" J Am Chem Soc, vol. 132, pp. 7472-7477, 2010.

[78] G. Goncalves, P. A. A. P. Marques, C. M. Granadeiro, H. I. S. Nogueira, M. K. Singh, and J. Gracio, "Surface Modification of Graphene Nanosheets with Gold Nanoparticles: The Role of Oxygen Moieties at Graphene Surface on Gold Nucleation and Growth" Chemistry of Materials, vol. 21, pp. 4796-4802, 2009.

[79] K. Jasuja and V. Berry, "Implantation and Growth of Dendritic Gold Nanostructures on Graphene Derivatives: Electrical Property Tailoring and Raman Enhancement" ACS Nano, vol. 3, pp. 2358-2366, 2009.

[80] J. I. Paredes, S. Villar-Rodil, A. Martinez-Alonso, and J. M. D. Tascon, "Graphene oxide dispersions in organic solvents" Langmuir, vol. 24, pp. 10560-10564, 2008.

[81] S. Park, J. H. An, I. W. Jung, R. D. Piner, S. J. An, X. S. Li, A. Velamakanni, and R. S. Ruoff, "Colloidal Suspensions of Highly Reduced Graphene Oxide in a Wide Variety of Organic Solvents" Nano Lett, vol. 9, pp. 1593-1597, 2009.

[82] T. Szabo, O. Berkesi, P. Forgo, K. Josepovits, Y. Sanakis, D. Petridis, and I. Dekany, "Evolution of surface functional groups in a series of progressively oxidized graphite oxides" Chemistry of Materials, vol. 18, pp. 2740-2749, 2006.

[83] B. J. Clark, T. Frost, and M. A. Russell, UV spectroscopy: techniques, instrumentation, data handling/ UV Spectrometry Group; Chapman&Hall: London, vol. 4, 1997.

[84] D. Li, M. B. Muller, S. Gilje, R. B. Kaner, and G. G. Wallace, "Processable aqueous dispersions of graphene nanosheets" Nat Nanotechnol, vol. 3, pp. 101-105, 2008.

[85] F. Tuinstra and J. L. Koenig, "Raman Spectrum of Graphite" J Chem Phys, vol. 53, pp. 1126-&, 1970.

[86] M. A. Pimenta, G. Dresselhaus, M. S. Dresselhaus, L. G. Cancado, A. Jorio, and R. Saito, "Studying disorder in graphite-based systems by Raman spectroscopy" Phys Chem Chem Phys, vol. 9, pp. 1276-1291, 2007.

[87] A. C. Ferrari and J. Robertson, "Raman spectroscopy of amorphous, nanostructured, diamond-like carbon, and nanodiamond" Philos Trans Roy Soc A, vol. 362, pp. 2477-2512, 2004.

[88] H. A. Becerril, J. Mao, Z. Liu, R. M. Stoltenberg, Z. Bao, and Y. Chen, "Evaluation of solution-processed reduced graphene oxide films as transparent conductors" ACS Nano, vol. 2, pp. 463-470, 2008.

[89] I. Jung, D. A. Field, N. J. Clark, Y. W. Zhu, D. X. Yang, R. D. Piner, S. Stankovich, D. A. Dikin, H. Geisler, C. A. Ventrice, and R. S. Ruoff, "Reduction Kinetics of Graphene Oxide Determined by Electrical Transport Measurements and Temperature Programmed Desorption" J Phys Chem C, vol. 113, pp. 18480-18486, 2009.

[90] D. Yang, A. Velamakanni, G. Bozoklu, S. Park, M. Stoller, R. D. Piner, S. Stankovich, I. Jung, D. A. Field, C. A. Ventrice, and R. S. Ruoff, "Chemical analysis of graphene oxide films after heat and chemical treatments by X-ray

photoelectron and Micro-Raman spectroscopy" Carbon, vol. 47, pp. 145-152, 2009.

[91] S. R. Wang, Y. Zhang, N. Abidi, and L. Cabrales, "Wettability and Surface Free Energy of Graphene Films" Langmuir, vol. 25, pp. 11078-11081, 2009.

[92] J. A. Riddick, W. B. Bunger, and T. K. Sakano, Organic SolVents: Physical Properties and Methods of Purification; John Wiley & Sons: New York, , vol., 1986.

[93] J. T. Paci, T. Belytschko, and G. C. Schatz, "Computational studies of the structure, behavior upon heating, and mechanical properties of graphite oxide" J Phys Chem C, vol. 111, pp. 18099-18111, 2007.

[94] S. Kim, S. Zhou, Y. K. Hu, M. Acik, Y. J. Chabal, C. Berger, W. de Heer, A. Bongiorno, and E. Riedo, "Room-temperature metastability of multilayer graphene oxide films" Nat Mater, vol. 11, pp. 544-549, 2012.

[95] J. L. Li, K. N. Kudin, M. J. McAllister, R. K. Prud'homme, I. A. Aksay, and R. Car, "Oxygen-driven unzipping of graphitic materials" Physical Review Letters, vol. 96, pp. -, 2006.

[96] R. Larciprete, S. Fabris, T. Sun, P. Lacovig, A. Baraldi, and S. Lizzit, "Dual Path Mechanism in the Thermal Reduction of Graphene Oxide" J Am Chem Soc, vol. 133, pp. 17315-17321, 2011.

[97] H. Liu, B. Kang, and J. Y. Lee, "Hidden Role of a Hydroxyl Group in Mediating the Oxygen Line Defect on a Graphene Surface" J Phys Chem C, vol. 117, pp. 17832-17838, 2013.

[98] R. Kotz and M. Carlen, "Principles and applications of electrochemical capacitors" Electrochim Acta, vol. 45, pp. 2483-2498, 2000.

[99] H. M. Jeong, J. W. Lee, W. H. Shin, Y. J. Choi, H. J. Shin, J. K. Kang, and J. W. Choi, "Nitrogen-Doped Graphene for High-Performance Ultracapacitors and the Importance of Nitrogen-Doped Sites at Basal Planes" Nano Lett, vol. 11, pp. 2472-2477, 2011.

[100] C. G. Liu, Z. N. Yu, D. Neff, A. Zhamu, and B. Z. Jang, "Graphene-Based Supercapacitor with an Ultrahigh Energy Density" Nano Lett, vol. 10, pp. 4863-4868, 2010.

[101] E. Frackowiak and F. Beguin, "Carbon materials for the electrochemical storage of energy in capacitors" Carbon, vol. 39, pp. 937-950, 2001.

[102] Z. Lin, Y. Yao, Z. Li, Y. Liu, Z. Li, and C.-P. Wong, "Solvent-Assisted Thermal Reduction of Graphite Oxide" The Journal of Physical Chemistry C, vol. 114, pp. 14819-14825, 2010.

[103] H. L. Wang, J. T. Robinson, X. L. Li, and H. J. Dai, "Solvothermal Reduction of Chemically Exfoliated Graphene Sheets" J Am Chem Soc, vol. 131, pp. 9910-9911, 2009.

[104] M. D. Stoller, S. J. Park, Y. W. Zhu, J. H. An, and R. S. Ruoff, "Graphene-Based Ultracapacitors" Nano Lett, vol. 8, pp. 3498-3502, 2008.

[105] M. Acik, C. Mattevi, C. Gong, G. Lee, K. Cho, M. Chhowalla, and Y. J. Chabal, "The Role of Intercalated Water in Multilayered Graphene Oxide" ACS Nano, vol. 4, pp. 5861-5868, 2010.

[106] A. Bagri, R. Grantab, N. V. Medhekar, and V. B. Shenoy, "Stability and Formation Mechanisms of Carbonyl- and Hydroxyl-Decorated Holes in Graphene Oxide" J Phys Chem C, vol. 114, pp. 12053-12061, 2010.

[107] C. Gomez-Navarro, J. C. Meyer, R. S. Sundaram, A. Chuvilin, S. Kurasch, M. Burghard, K. Kern, and U. Kaiser, "Atomic Structure of Reduced Graphene Oxide" Nano Lett, vol. 10, pp. 1144-1148, 2010.

[108] K. Erickson, R. Erni, Z. Lee, N. Alem, W. Gannett, and A. Zettl, "Determination of the Local Chemical Structure of Graphene Oxide and Reduced Graphene Oxide" Adv Mater, vol. 22, pp. 4467-4472, 2010.

[109] J. P. Randin and E. Yeager, "Differential Capacitance Study of Stress/Annealed Pyrolytic Graphite Electrodes" J Electrochem Soc, vol. 118, pp. 711-714, 1971.

[110] Z. Y. Lin, Y. Liu, Y. G. Yao, O. J. Hildreth, Z. Li, K. Moon, and C. P. Wong, "Superior Capacitance of Functionalized Graphene" J Phys Chem C, vol. 115, pp. 7120-7125, 2011.

[111] Y. Chen, X. O. Zhang, D. C. Zhang, P. Yu, and Y. W. Ma, "High performance supercapacitors based on reduced graphene oxide in aqueous and ionic liquid electrolytes" Carbon, vol. 49, pp. 573-580, 2011.

[112] K. Zhang, L. L. Zhang, X. S. Zhao, and J. Wu, "Graphene/Polyaniline Nanofiber Composites as Supercapacitor Electrodes" Chemistry of Materials, vol. 22, pp. 1392-1401, 2010.

[113] J. J. Xu, K. Wang, S. Z. Zu, B. H. Han, and Z. X. Wei, "Hierarchical Nanocomposites of Polyaniline Nanowire Arrays on Graphene Oxide Sheets with Synergistic Effect for Energy Storage" ACS Nano, vol. 4, pp. 5019-5026, 2010.

[114] S. Chen, J. W. Zhu, X. D. Wu, Q. F. Han, and X. Wang, "Graphene Oxide-MnO2 Nanocomposites for Supercapacitors" ACS Nano, vol. 4, pp. 2822-2830, 2010.

[115] M. J. Bleda-Martinez, J. A. Macia-Agullo, D. Lozano-Castello, E. Morallon, D. Cazorla-Amoros, and A. Linares-Solano, "Role of surface chemistry on electric

double layer capacitance of carbon materials" Carbon, vol. 43, pp. 2677-2684, 2005.

[116] Z. Y. Lin, H. B. Chu, Y. H. Shen, L. Wei, H. C. Liu, and Y. Li, "Rational preparation of faceted platinum nanocrystals supported on carbon nanotubes with remarkably enhanced catalytic performance" Chem Commun, vol., pp. 7167-7169, 2009.

[117] V. R. Stamenkovic, B. Fowler, B. S. Mun, G. F. Wang, P. N. Ross, C. A. Lucas, and N. M. Markovic, "Improved oxygen reduction activity on Pt3Ni(111) via increased surface site availability" Science, vol. 315, pp. 493-497, 2007.

[118] S. Mukerjee, "Particle-Size and Structural Effects in Platinum Electrocatalysis" J Appl Electrochem, vol. 20, pp. 537-548, 1990.

[119] B. James, J. Kalinoski, and K. Baum. in DOE-EERE Fuel Cell Technologies Program—2009 DOE Hydrogen Program Review

[120] R. J. Brodd and M. Winter, "What are batteries, fuel cells, and supercapacitors?" Chem Rev, vol. 104, pp. 4245-4269, 2004.

[121] M. Lefevre, E. Proietti, F. Jaouen, and J. P. Dodelet, "Iron-Based Catalysts with Improved Oxygen Reduction Activity in Polymer Electrolyte Fuel Cells" Science, vol. 324, pp. 71-74, 2009.

[122] F. Y. Cheng, Y. Su, J. Liang, Z. L. Tao, and J. Chen, "MnO(2)-Based Nanostructures as Catalysts for Electrochemical Oxygen Reduction in Alkaline Media" Chemistry of Materials, vol. 22, pp. 898-905, 2010.

[123] K. P. Gong, F. Du, Z. H. Xia, M. Durstock, and L. M. Dai, "Nitrogen-Doped Carbon Nanotube Arrays with High Electrocatalytic Activity for Oxygen Reduction" Science, vol. 323, pp. 760-764, 2009.

[124] R. L. Liu, D. Q. Wu, X. L. Feng, and K. Mullen, "Nitrogen-Doped Ordered Mesoporous Graphitic Arrays with High Electrocatalytic Activity for Oxygen Reduction" Angew Chem Int Edit, vol. 49, pp. 2565-2569, 2010.

[125] S. Maldonado and K. J. Stevenson, "Influence of nitrogen doping on oxygen reduction electrocatalysis at carbon nanofiber electrodes" J Phys Chem B, vol. 109, pp. 4707-4716, 2005.

[126] Z. Y. Lin, G. H. Waller, Y. Liu, M. L. Liu, and C. P. Wong, "3D Nitrogen-doped graphene prepared by pyrolysis of graphene oxide with polypyrrole for electrocatalysis of oxygen reduction reaction" Nano Energy, vol. 2, pp. 241-248, 2013.

[127] H. Niwa, K. Horiba, Y. Harada, M. Oshima, T. Ikeda, K. Terakura, J. Ozaki, and S. Miyata, "X-ray absorption analysis of nitrogen contribution to oxygen

reduction reaction in carbon alloy cathode catalysts for polymer electrolyte fuel cells" J Power Sources, vol. 187, pp. 93-97, 2009.

[128] L. F. Lai, J. R. Potts, D. Zhan, L. Wang, C. K. Poh, C. H. Tang, H. Gong, Z. X. Shen, L. Y. Jianyi, and R. S. Ruoff, "Exploration of the active center structure of nitrogen-doped graphene-based catalysts for oxygen reduction reaction" Energ Environ Sci, vol. 5, pp. 7936-7942, 2012.

[129] K. R. Lee, K. U. Lee, J. W. Lee, B. T. Ahn, and S. I. Woo, "Electrochemical oxygen reduction on nitrogen doped graphene sheets in acid media" Electrochem Commun, vol. 12, pp. 1052-1055, 2010.

[130] T. Ikeda, M. Boero, S. F. Huang, K. Terakura, M. Oshima, and J. Ozaki, "Carbon alloy catalysts: Active sites for oxygen reduction reaction" J Phys Chem C, vol. 112, pp. 14706-14709, 2008.

[131] L. P. Zhang and Z. H. Xia, "Mechanisms of Oxygen Reduction Reaction on Nitrogen-Doped Graphene for Fuel Cells" J Phys Chem C, vol. 115, pp. 11170-11176, 2011.

[132] S. Ni, Z. Y. Li, and J. L. Yang, "Oxygen molecule dissociation on carbon nanostructures with different types of nitrogen doping" Nanoscale, vol. 4, pp. 1184-1189, 2012.

[133] H. Kim, K. Lee, S. I. Woo, and Y. Jung, "On the mechanism of enhanced oxygen reduction reaction in nitrogen-doped graphene nanoribbons" Phys Chem Chem Phys, vol. 13, pp. 17505-17510, 2011.

[134] C. H. Zhang, L. Fu, N. Liu, M. H. Liu, Y. Y. Wang, and Z. F. Liu, "Synthesis of Nitrogen-Doped Graphene Using Embedded Carbon and Nitrogen Sources" Adv Mater, vol. 23, pp. 1020-1024, 2011.

[135] D. H. Deng, X. L. Pan, L. A. Yu, Y. Cui, Y. P. Jiang, J. Qi, W. X. Li, Q. A. Fu, X. C. Ma, Q. K. Xue, G. Q. Sun, and X. H. Bao, "Toward N-Doped Graphene via Solvothermal Synthesis" Chemistry of Materials, vol. 23, pp. 1188-1193, 2011.

[136] X. R. Wang, X. L. Li, L. Zhang, Y. Yoon, P. K. Weber, H. L. Wang, J. Guo, and H. J. Dai, "N-Doping of Graphene Through Electrothermal Reactions with Ammonia" Science, vol. 324, pp. 768-771, 2009.

[137] L. S. Panchokarla, K. S. Subrahmanyam, S. K. Saha, A. Govindaraj, H. R. Krishnamurthy, U. V. Waghmare, and C. N. R. Rao, "Synthesis, Structure, and Properties of Boron- and Nitrogen-Doped Graphene" Adv Mater, vol. 21, pp. 4726-4730, 2009.

[138] Y. Wang, Y. Y. Shao, D. W. Matson, J. H. Li, and Y. H. Lin, "Nitrogen-Doped Graphene and Its Application in Electrochemical Biosensing" ACS Nano, vol. 4, pp. 1790-1798, 2010.

[139] N. Liu, L. Fu, B. Y. Dai, K. Yan, X. Liu, R. Q. Zhao, Y. F. Zhang, and Z. F. Liu, "Universal Segregation Growth Approach to Wafer-Size Graphene from Non-Noble Metals" Nano Lett, vol. 11, pp. 297-303, 2011.

[140] K. S. Novoselov, V. I. Fal'ko, L. Colombo, P. R. Gellert, M. G. Schwab, and K. Kim, "A roadmap for graphene" Nature, vol. 490, pp. 192-200, 2012.

[141] K. N. Kudin, B. Ozbas, H. C. Schniepp, R. K. Prud'homme, I. A. Aksay, and R. Car, "Raman spectra of graphite oxide and functionalized graphene sheets" Nano Lett, vol. 8, pp. 36-41, 2008.

[142] X. L. Li, H. L. Wang, J. T. Robinson, H. Sanchez, G. Diankov, and H. J. Dai, "Simultaneous Nitrogen Doping and Reduction of Graphene Oxide" J Am Chem Soc, vol. 131, pp. 15939-15944, 2009.

[143] A. Das, S. Pisana, B. Chakraborty, S. Piscanec, S. K. Saha, U. V. Waghmare, K. S. Novoselov, H. R. Krishnamurthy, A. K. Geim, A. C. Ferrari, and A. K. Sood, "Monitoring dopants by Raman scattering in an electrochemically top-gated graphene transistor" Nat Nanotechnol, vol. 3, pp. 210-215, 2008.

[144] J. Yan, Y. Zhang, P. Kim, and A. Pinczuk, "Electric Field Effect Tuning of Electron-Phonon Coupling in Graphene" Physical Review Letters, vol. 98, pp. 166802, 2007.

[145] A. C. Ferrari, J. C. Meyer, V. Scardaci, C. Casiraghi, M. Lazzeri, F. Mauri, S. Piscanec, D. Jiang, K. S. Novoselov, S. Roth, and A. K. Geim, "Raman spectrum of graphene and graphene layers" Phys Rev Lett, vol. 97, 2006.

[146] Q. Su, S. P. Pang, V. Alijani, C. Li, X. L. Feng, and K. Mullen, "Composites of Graphene with Large Aromatic Molecules" Adv Mater, vol. 21, pp. 3191-3195, 2009.

[147] M. C. Hsiao, S. H. Liao, M. Y. Yen, P. I. Liu, N. W. Pu, C. A. Wang, and C. C. M. Ma, "Preparation of Covalently Functionalized Graphene Using Residual Oxygen-Containing Functional Groups" Acs Appl Mater Inter, vol. 2, pp. 3092-3099, 2010.

[148] H. S. Kang and S. Jeong, "Nitrogen doping and chirality of carbon nanotubes" Phys Rev B, vol. 70, 2004.

[149] E. Cruz-Silva, F. Lopez-Urias, E. Munoz-Sandoval, B. G. Sumpter, H. Terrones, J. C. Charlier, V. Meunier, and M. Terrones, "Electronic Transport and Mechanical Properties of Phosphorus- and Phosphorus-Nitrogen-Doped Carbon Nanotubes" ACS Nano, vol. 3, pp. 1913-1921, 2009.

[150] P. A. Schaber, J. Colson, S. Higgins, D. Thielen, B. Anspach, and J. Brauer, "Thermal decomposition (pyrolysis) of urea in an open reaction vessel" Thermochim Acta, vol. 424, pp. 131-142, 2004.

[151] Z. Lin, G. Waller, Y. Liu, M. Liu, and C.-P. Wong, "Facile Synthesis of Nitrogen-Doped Graphene via Pyrolysis of Graphene Oxide and Urea, and its Electrocatalytic Activity toward the Oxygen-Reduction Reaction" Advanced Energy Materials, vol. 2, pp. 884-888, 2012.

[152] J. R. Pels, F. Kapteijn, J. A. Moulijn, Q. Zhu, and K. M. Thomas, "Evolution of Nitrogen Functionalities in Carbonaceous Materials during Pyrolysis" Carbon, vol. 33, pp. 1641-1653, 1995.

[153] M. Seredych, D. Hulicova-Jurcakova, G. Q. Lu, and T. J. Bandosz, "Surface functional groups of carbons and the effects of their chemical character, density and accessibility to ions on electrochemical performance" Carbon, vol. 46, pp. 1475-1488, 2008.

[154] Z. Y. Lin, M. K. Song, Y. Ding, Y. Liu, M. L. Liu, and C. P. Wong, "Facile preparation of nitrogen-doped graphene as a metal-free catalyst for oxygen reduction reaction" Phys Chem Chem Phys, vol. 14, pp. 3381-3387, 2012.

[155] F. Dong, L. W. Wu, Y. J. Sun, M. Fu, Z. B. Wu, and S. C. Lee, "Efficient synthesis of polymeric g-C(3)N(4) layered materials as novel efficient visible light driven photocatalysts" J Mater Chem, vol. 21, pp. 15171-15174, 2011.

[156] L. Costa and G. Camino, "Thermal Behavior of Melamine" Journal of Thermal Analysis, vol. 34, pp. 423-429, 1988.

[157] Z. Y. Lin, Y. Liu, and C. P. Wong, "Facile Fabrication of Superhydrophobic Octadecylamine-Functionalized Graphite Oxide Film" Langmuir, vol. 26, pp. 16110-16114, 2010.

[158] J. D. Wuest and A. Rochefort, "Strong adsorption of aminotriazines on graphene" Chem Commun, vol. 46, pp. 2923-2925, 2010.

[159] Z. H. Sheng, L. Shao, J. J. Chen, W. J. Bao, F. B. Wang, and X. H. Xia, "Catalyst-Free Synthesis of Nitrogen-Doped Graphene via Thermal Annealing Graphite Oxide with Melamine and Its Excellent Electrocatalysis" ACS Nano, vol. 5, pp. 4350-4358, 2011.

[160] Y. Q. Liu, D. C. Wei, Y. Wang, H. L. Zhang, L. P. Huang, and G. Yu, "Synthesis of N-Doped Graphene by Chemical Vapor Deposition and Its Electrical Properties" Nano Lett, vol. 9, pp. 1752-1758, 2009.

[161] D. Marton, K. J. Boyd, A. H. Albayati, S. S. Todorov, and J. W. Rabalais, "Carbon Nitride Deposited Using Energetic Species - a 2-Phase System" Physical Review Letters, vol. 73, pp. 118-121, 1994.

[162] A. Ganguly, S. Sharma, P. Papakonstantinou, and J. Hamilton, "Probing the Thermal Deoxygenation of Graphene Oxide Using High-Resolution In Situ X-ray-Based Spectroscopies" J Phys Chem C, vol. 115, pp. 17009-17019, 2011.

[163] X. F. Li, J. Zhang, L. H. Shen, Y. M. Ma, W. W. Lei, Q. L. Cui, and G. T. Zou, "Preparation and characterization of graphitic carbon nitride through pyrolysis of melamine" Appl Phys a-Mater, vol. 94, pp. 387-392, 2009.

[164] H. Bai, C. Li, X. L. Wang, and G. Q. Shi, "On the Gelation of Graphene Oxide" J Phys Chem C, vol. 115, pp. 5545-5551, 2011.

[165] H. Bai, K. X. Sheng, P. F. Zhang, C. Li, and G. Q. Shi, "Graphene oxide/conducting polymer composite hydrogels" J Mater Chem, vol. 21, pp. 18653-18658, 2011.

[166] Z. Y. Lin, G. Waller, Y. Liu, M. L. Liu, and C. P. Wong, "Facile Synthesis of Nitrogen-Doped Graphene via Pyrolysis of Graphene Oxide and Urea, and its Electrocatalytic Activity toward the Oxygen-Reduction Reaction" Advanced Energy Materials, vol. 2, pp. 884-888, 2012.

[167] K. S. W. Sing, "Reporting Physisorption Data for Gas Solid Systems - with Special Reference to the Determination of Surface-Area and Porosity" Pure Appl Chem, vol. 54, pp. 2201-2218, 1982.

[168] Z. Y. Lin, G. H. Waller, Y. Liu, M. L. Liu, and C. P. Wong, "Simple preparation of nanoporous few-layer nitrogen-doped graphene for use as an efficient electrocatalyst for oxygen reduction and oxygen evolution reactions" Carbon, vol. 53, pp. 130-136, 2013.

[169] R. J. J. Jansen and H. Vanbekkum, "Xps of Nitrogen-Containing Functional-Groups on Activated Carbon" Carbon, vol. 33, pp. 1021-1027, 1995.

[170] S. Biniak, G. Szymanski, J. Siedlewski, and A. Swiatkowski, "The characterization of activated carbons with oxygen and nitrogen surface groups" Carbon, vol. 35, pp. 1799-1810, 1997.

[171] E. M. Scherr, A. G. Macdiarmid, S. K. Manohar, J. G. Masters, Y. Sun, X. Tang, M. A. Druy, P. J. Glatkowski, V. B. Cajipe, J. E. Fischer, K. R. Cromack, M. E. Jozefowicz, J. M. Ginder, R. P. Mccall, and A. J. Epstein, "Polyaniline - Oriented Films and Fibers" Synthetic Met, vol. 41, pp. 735-738, 1991.

[172] C. H. Chen, "Thermal and morphological studies of chemically prepared emeraldine-base-form polyaniline powder" J Appl Polym Sci, vol. 89, pp. 2142-2148, 2003.

[173] M. Trchova, J. Stejskal, and J. Prokes, "Infrared spectroscopic study of solid-state protonation and oxidation of polyaniline" Synthetic Met, vol. 101, pp. 840-841, 1999.

[174] A. L. M. Reddy, A. Srivastava, S. R. Gowda, H. Gullapalli, M. Dubey, and P. M. Ajayan, "Synthesis Of Nitrogen-Doped Graphene Films For Lithium Battery Application" ACS Nano, vol. 4, pp. 6337-6342, 2010.

[175] X. F. Li, D. S. Geng, Y. Zhang, X. B. Meng, R. Y. Li, and X. L. Sun, "Superior cycle stability of nitrogen-doped graphene nanosheets as anodes for lithium ion batteries" Electrochem Commun, vol. 13, pp. 822-825, 2011.

[176] C. C. Ma, X. H. Shao, and D. P. Cao, "Nitrogen-doped graphene nanosheets as anode materials for lithium ion batteries: a first-principles study" J Mater Chem, vol. 22, pp. 8911-8915, 2012.

[177] H. B. Wang, C. J. Zhang, Z. H. Liu, L. Wang, P. X. Han, H. X. Xu, K. J. Zhang, S. M. Dong, J. H. Yao, and G. L. Cui, "Nitrogen-doped graphene nanosheets with excellent lithium storage properties" J Mater Chem, vol. 21, pp. 5430-5434, 2011.

[178] D. H. Deng, L. Yu, X. L. Pan, S. Wang, X. Q. Chen, P. Hu, L. X. Sun, and X. H. Bao, "Size effect of graphene on electrocatalytic activation of oxygen" Chem Commun, vol. 47, pp. 10016-10018, 2011.

[179] G. Y. Chen, S. R. Bare, and T. E. Mallouk, "Development of supported bifunctional electrocatalysts for unitized regenerative fuel cells" J Electrochem Soc, vol. 149, pp. A1092-A1099, 2002.

[180] V. Neburchilov, H. J. Wang, J. J. Martin, and W. Qu, "A review on air cathodes for zinc-air fuel cells" J Power Sources, vol. 195, pp. 1271-1291, 2010.

[181] D. S. Geng, Y. Chen, Y. G. Chen, Y. L. Li, R. Y. Li, X. L. Sun, S. Y. Ye, and S. Knights, "High oxygen-reduction activity and durability of nitrogen-doped graphene" Energ Environ Sci, vol. 4, pp. 760-764, 2011.

[182] I. Y. Jeon, D. S. Yu, S. Y. Bae, H. J. Choi, D. W. Chang, L. M. Dai, and J. B. Baek, "Formation of Large-Area Nitrogen-Doped Graphene Film Prepared from Simple Solution Casting of Edge-Selectively Functionalized Graphite and Its Electrocatalytic Activity" Chemistry of Materials, vol. 23, pp. 3987-3992, 2011.

[183] T. L. Sun, L. Feng, X. F. Gao, and L. Jiang, "Bioinspired surfaces with special wettability" Accounts Chem Res, vol. 38, pp. 644-652, 2005.

[184] N. A. Patankar, "Mimicking the lotus effect: Influence of double roughness structures and slender pillars" Langmuir, vol. 20, pp. 8209-8213, 2004.

[185] M. L. Ma and R. M. Hill, "Superhydrophobic surfaces" Curr Opin Colloid In, vol. 11, pp. 193-202, 2006.

[186] C. R. Crick and I. P. Parkin, "Preparation and Characterisation of Super-Hydrophobic Surfaces" Chem-Eur J, vol. 16, pp. 3568-3588, 2010.

[187] Y. Liu, Y. H. Xiu, D. W. Hess, and C. P. Wong, "Silicon Surface Structure-Controlled Oleophobicity" Langmuir, vol. 26, pp. 8908-8913, 2010.

[188] Y. Xiu, L. Zhu, D. W. Hess, and C. P. Wong, "Hierarchical silicon etched structures for controlled hydrophobicity/superhydrophobicity" Nano Lett, vol. 7, pp. 3388-3393, 2007.

[189] Y. H. Xiu, L. B. Zhu, D. W. Hess, and C. P. Wong, "Biomimetic creation of hierarchical surface structures by combining colloidal self-assembly and Au sputter deposition" Langmuir, vol. 22, pp. 9676-9681, 2006.

[190] Y. H. Xiu, D. W. Hess, and C. R. Wong, "UV and thermally stable superhydrophobic coatings from sol-gel processing" J Colloid Interf Sci, vol. 326, pp. 465-470, 2008.

[191] C. H. Choi, U. Ulmanella, J. Kim, C. M. Ho, and C. J. Kim, "Effective slip and friction reduction in nanograted superhydrophobic microchannels" Phys Fluids, vol. 18, 2006.

[192] S. T. Wang, L. Feng, and L. Jiang, "One-step solution-immersion process for the fabrication of stable bionic superhydrophobic surfaces" Adv Mater, vol. 18, pp. 767-770, 2006.

[193] L. B. Zhu, Y. H. Xiu, J. W. Xu, P. A. Tamirisa, D. W. Hess, and C. P. Wong, "Superhydrophobicity on two-tier rough surfaces fabricated by controlled growth of aligned carbon nanotube arrays coated with fluorocarbon" Langmuir, vol. 21, pp. 11208-11212, 2005.

[194] T. Sun, G. J. Wang, H. Liu, L. Feng, L. Jiang, and D. B. Zhu, "Control over the wettability of an aligned carbon nanotube film" J Am Chem Soc, vol. 125, pp. 14996-14997, 2003.

[195] L. Zhang and D. E. Resasco, "Single-Walled Carbon Nanotube Pillars: A Superhydrophobic Surface" Langmuir, vol. 25, pp. 4792-4798, 2009.

[196] K. K. S. Lau, J. Bico, K. B. K. Teo, M. Chhowalla, G. A. J. Amaratunga, W. I. Milne, G. H. McKinley, and K. K. Gleason, "Superhydrophobic carbon nanotube forests" Nano Lett, vol. 3, pp. 1701-1705, 2003.

[197] Z. J. Han, B. Tay, C. M. Tan, M. Shakerzadeh, and K. Ostrikov, "Electrowetting Control of Cassie-to-Wenzel Transitions in Superhydrophobic Carbon Nanotube-Based Nanocomposites" ACS Nano, vol. 3, pp. 3031-3036, 2009.

[198] O. Leenaerts, B. Partoens, and F. M. Peeters, "Water on graphene: Hydrophobicity and dipole moment using density functional theory" Phys Rev B, vol. 79, 2009.

[199] Z. Zong, C. L. Chen, M. R. Dokmeci, and K. T. Wan, "Direct measurement of graphene adhesion on silicon surface by intercalation of nanoparticles" J Appl Phys, vol. 107, 2010.

[200] Y. J. Shin, Y. Y. Wang, H. Huang, G. Kalon, A. T. S. Wee, Z. X. Shen, C. S. Bhatia, and H. Yang, "Surface-Energy Engineering of Graphene" Langmuir, vol. 26, pp. 3798-3802, 2010.

[201] J. Rafiee, M. A. Rafiee, Z. Z. Yu, and N. Koratkar, "Superhydrophobic to Superhydrophilic Wetting Control in Graphene Films" Adv Mater, vol. 22, pp. 2151-2154, 2010.

[202] A. B. Bourlinos, D. Gournis, D. Petridis, T. Szabo, A. Szeri, and I. Dekany, "Graphite oxide: Chemical reduction to graphite and surface modification with primary aliphatic amines and amino acids" Langmuir, vol. 19, pp. 6050-6055, 2003.

[203] Y. Matsuo, T. Miyabe, T. Fukutsuka, and Y. Sugie, "Preparation and characterization of alkylamine-intercalated graphite oxides" Carbon, vol. 45, pp. 1005-1012, 2007.

[204] O. C. Compton, D. A. Dikin, K. W. Putz, L. C. Brinson, and S. T. Nguyen, "Electrically Conductive "Alkylated" Graphene Paper via Chemical Reduction of Amine-Functionalized Graphene Oxide Paper" Adv Mater, vol. 22, pp. 892-896, 2010.

[205] H. T. Ham, C. M. Koo, S. O. Kim, Y. S. Choi, and I. J. Chung, "Chemical modification of carbon nanotubes and preparation of polystyrene/carbon nanotubes composites" Macromol Res, vol. 12, pp. 384-390, 2004.

[206] E. V. Basiuk, M. Monroy-Pelaez, I. Puente-Lee, and V. A. Basiuk, "Direct solvent-free amination of closed-cap carbon nanotubes: A link to fullerene chemistry" Nano Lett, vol. 4, pp. 863-866, 2004.

[207] Z. Y. Lin, Y. Liu, Z. Li, and C. P. Wong, "Novel Preparation of Functionalized Graphene Oxide for Large Scale, Low cost, and Self-cleaning Coatings of Electronic Devices" 2011 IEEE 61st Electronic Components and Technology Conference (ECTC), vol., pp. 358-362, 2011.

[208] S. A. Trammell, D. S. Seferos, M. Moore, D. A. Lowy, G. C. Bazan, J. G. Kushmerick, and N. Lebedev, "Rapid proton-coupled electron-transfer of hydroquinone through phenylenevinylene bridges" Langmuir, vol. 23, pp. 942-948, 2007.

[209] S. Cattarin, L. Doubova, G. Mengoli, and G. Zotti, "Electrosynthesis and Properties of Ring-Substituted Polyanilines" Electrochim Acta, vol. 33, pp. 1077-1084, 1988.

[210] M. E. Vaschetto and B. A. Retamal, "Substituents effect on the electronic properties of aniline and oligoanilines" J Phys Chem A, vol. 101, pp. 6945-6950, 1997.

[211] X. Y. Fan, R. Nouchi, L. C. Yin, and K. Tanigaki, "Effects of electron-transfer chemical modification on the electrical characteristics of graphene" Nanotechnology, vol. 21, 2010.

[212] Z. H. Sheng, H. L. Gao, W. J. Bao, F. B. Wang, and X. H. Xia, "Synthesis of boron doped graphene for oxygen reduction reaction in fuel cells" J Mater Chem, vol. 22, pp. 390-395, 2012.

[213] C. Z. Zhang, N. Mahmood, H. Yin, F. Liu, and Y. L. Hou, "Synthesis of Phosphorus-Doped Graphene and its Multifunctional Applications for Oxygen Reduction Reaction and Lithium Ion Batteries" Adv Mater, vol. 25, pp. 4932-4937, 2013.

[214] J. E. Park, Y. J. Jang, Y. J. Kim, M. S. Song, S. Yoon, D. H. Kim, and S. J. Kim, "Sulfur-doped graphene as a potential alternative metal-free electrocatalyst and Pt-catalyst supporting material for oxygen reduction reaction" Phys Chem Chem Phys, vol. 16, pp. 103-109, 2014.

[215] J. Liang, Y. Jiao, M. Jaroniec, and S. Z. Qiao, "Sulfur and Nitrogen Dual-Doped Mesoporous Graphene Electrocatalyst for Oxygen Reduction with Synergistically Enhanced Performance" Angew Chem Int Edit, vol. 51, pp. 11496-11500, 2012.

[216] C. H. Choi, M. W. Chung, H. C. Kwon, S. H. Park, and S. I. Woo, "B, N- and P, N-doped graphene as highly active catalysts for oxygen reduction reactions in acidic media" J Mater Chem A, vol. 1, pp. 3694-3699, 2013.

[217] T. Z. Huang, S. Mao, H. H. Pu, Z. H. Wen, X. L. Huang, S. Q. Ci, and J. H. Chen, "Nitrogen-doped graphene-vanadium carbide hybrids as a high-performance oxygen reduction reaction electrocatalyst support in alkaline media" J Mater Chem A, vol. 1, pp. 13404-13410, 2013.

[218] L. Jia, D. H. Wang, Y. X. Huang, A. W. Xu, and H. Q. Yu, "Highly Durable N-Doped Graphene/CdS Nanocomposites with Enhanced Photocatalytic Hydrogen Evolution from Water under Visible Light Irradiation" J Phys Chem C, vol. 115, pp. 11466-11473, 2011.

[219] B. P. Vinayan, R. Nagar, N. Rajalakshmi, and S. Ramaprabhu, "Novel Platinum-Cobalt Alloy Nanoparticles Dispersed on Nitrogen-Doped Graphene as a Cathode Electrocatalyst for PEMFC Applications" Advanced Functional Materials, vol. 22, pp. 3519-3526, 2012.

[220] V. Chandra, S. U. Yu, S. H. Kim, Y. S. Yoon, D. Y. Kim, A. H. Kwon, M. Meyyappan, and K. S. Kim, "Highly selective CO2 capture on N-doped carbon produced by chemical activation of polypyrrole functionalized graphene sheets" Chem Commun, vol. 48, pp. 735-737, 2012.

[221] X. H. Li and M. Antonietti, "Polycondensation of Boron- and Nitrogen-Codoped Holey Graphene Monoliths from Molecules: Carbocatalysts for Selective Oxidation" Angew Chem Int Edit, vol. 52, pp. 4572-4576, 2013.

[222] W. Lu, L. T. Qu, K. Henry, and L. M. Dai, "High performance electrochemical capacitors from aligned carbon nanotube electrodes and ionic liquid electrolytes" J Power Sources, vol. 189, pp. 1270-1277, 2009.

[223] M. G. Hahm, A. L. M. Reddy, D. P. Cole, M. Rivera, J. A. Vento, J. Nam, H. Y. Jung, Y. L. Kim, N. T. Narayanan, D. P. Hashim, C. Galande, Y. J. Jung, M. Bundy, S. Karna, P. M. Ajayan, and R. Vajtai, "Carbon Nanotube-Nanocup Hybrid Structures for High Power Supercapacitor Applications" Nano Lett, vol. 12, pp. 5616-5621, 2012.

[224] B. Kim, H. Chung, and W. Kim, "High-performance supercapacitors based on vertically aligned carbon nanotubes and nonaqueous electrolytes" Nanotechnology, vol. 23, 2012.

[225] P. Lv, P. Zhang, F. Li, Y. Li, Y. Y. Feng, and W. Feng, "Vertically aligned carbon nanotubes grown on carbon fabric with high rate capability for super-capacitors" Synthetic Met, vol. 162, pp. 1090-1096, 2012.

[226] S. Dorfler, M. Hagen, H. Althues, J. Tubke, S. Kaskel, and M. J. Hoffmann, "High capacity vertical aligned carbon nanotube/sulfur composite cathodes for lithium-sulfur batteries" Chem Commun, vol. 48, pp. 4097-4099, 2012.

[227] K. Evanoff, J. Khan, A. A. Balandin, A. Magasinski, W. J. Ready, T. F. Fuller, and G. Yushin, "Towards Ultrathick Battery Electrodes: Aligned Carbon Nanotube - Enabled Architecture" Adv Mater, vol. 24, pp. 533-537, 2012.

[228] W. Lu, A. Goering, L. T. Qu, and L. M. Dai, "Lithium-ion batteries based on vertically-aligned carbon nanotube electrodes and ionic liquid electrolytes" Phys Chem Chem Phys, vol. 14, pp. 12099-12104, 2012.

[229] P. G. He and L. M. Dai, "Aligned carbon nanotube-DNA electrochemical sensors" Chem Commun, vol., pp. 348-349, 2004.

[230] M. Penza, R. Rossi, M. Alvisi, and E. Serra, "Metal-modified and vertically aligned carbon nanotube sensors array for landfill gas monitoring applications" Nanotechnology, vol. 21, pp. 105501-14, 2010.

[231] S. Talapatra, S. Kar, S. K. Pal, R. Vajtai, L. Ci, P. Victor, M. M. Shaijumon, S. Kaur, O. Nalamasu, and P. M. Ajayan, "Direct growth of aligned carbon nanotubes on bulk metals" Nat Nanotechnol, vol. 1, pp. 112-116, 2006.

[232] Y. Zhu, L. Li, C. G. Zhang, G. Casillas, Z. Z. Sun, Z. Yan, G. D. Ruan, Z. W. Peng, A. R. O. Raji, C. Kittrell, R. H. Hauge, and J. M. Tour, "A seamless three-

dimensional carbon nanotube graphene hybrid material" Nat Commun, vol. 3, 2012.

[233] L. B. Zhu, Y. Y. Sun, D. W. Hess, and C. P. Wong, "Well-aligned open-ended carbon nanotube architectures: An approach for device assembly" Nano Lett, vol. 6, pp. 243-247, 2006.

[234] W. Lin, Y. H. Xiu, H. J. Jiang, R. W. Zhang, O. Hildreth, K. S. Moon, and C. P. Wong, "Self-assembled monolayer-assisted chemical transfer of in situ functionalized carbon nanotubes" J Am Chem Soc, vol. 130, pp. 9636-9637, 2008.

[235] W. Lin, R. W. Zhang, K. S. Moon, and C. P. Wong, "Molecular phonon couplers at carbon nanotube/substrate interface to enhance interfacial thermal transport" Carbon, vol. 48, pp. 107-113, 2010.

[236] C. L. Pint, Y. Q. Xu, S. Moghazy, T. Cherukuri, N. T. Alvarez, E. H. Haroz, S. Mahzooni, S. K. Doorn, J. Kono, M. Pasquali, and R. H. Hauge, "Dry Contact Transfer Printing of Aligned Carbon Nanotube Patterns and Characterization of Their Optical Properties for Diameter Distribution and Alignment" ACS Nano, vol. 4, pp. 1131-1145, 2010.

[237] L. T. Qu, R. A. Vaia, and L. M. Dai, "Multilevel, Multicomponent Microarchitectures of Vertically-Aligned Carbon Nanotubes for Diverse Applications" ACS Nano, vol. 5, pp. 994-1002, 2011.

[238] A. C. Allen, E. Sunden, A. Cannon, S. Graham, and W. King, "Nanomaterial transfer using hot embossing for flexible electronic devices" Appl Phys Lett, vol. 88, 2006.

[239] H. J. Jiang, L. B. Zhu, K. S. Moon, and C. P. Wong, "Low temperature carbon nanotube film transfer via conductive polymer composites" Nanotechnology, vol. 18, pp. 125203-6, 2007.

[240] Y. W. Zhu, X. D. Lim, M. C. Sim, C. T. Lim, and C. H. Sow, "Versatile transfer of aligned carbon nanotubes with polydimethylsiloxane as the intermediate" Nanotechnology, vol. 19, pp. 325304-10, 2008.

[241] Z. Y. Lin, Z. Li, K. S. Moon, Y. N. Fang, Y. G. Yao, L. Y. Li, and C. P. Wong, "Robust vertically aligned carbon nanotube-carbon fiber paper hybrid as versatile electrodes for supercapacitors and capacitive deionization" Carbon, vol. 63, pp. 547-553, 2013.

[242] W. Primak, "C-Axis Electrical Conductivity of Graphite" Phys Rev, vol. 103, pp. 544-546, 1956.

[243] D. Z. Tsang and M. S. Dresselhaus, "C-Axis Electrical-Conductivity of Kish Graphite" Carbon, vol. 14, pp. 43-46, 1976.

[244] L. B. Zhu, J. W. Xu, Y. H. Xiu, Y. Y. Sun, D. W. Hess, and C. P. Wong, "Electrowetting of aligned carbon nanotube films" J Phys Chem B, vol. 110, pp. 15945-15950, 2006.

[245] D. R. Kauffman and A. Star, "Carbon nanotube gas and vapor sensors" Angew Chem Int Edit, vol. 47, pp. 6550-6570, 2008.

[246] Q. F. Pengfei, O. Vermesh, M. Grecu, A. Javey, O. Wang, H. J. Dai, S. Peng, and K. J. Cho, "Toward large arrays of multiplex functionalized carbon nanotube sensors for highly sensitive and selective molecular detection" Nano Lett, vol. 3, pp. 347-351, 2003.

[247] P. Calvert, "Inkjet printing for materials and devices" Chemistry of Materials, vol. 13, pp. 3299-3305, 2001.

[248] J. Jang, J. Ha, and J. Cho, "Fabrication of water-dispersible polyaniline-poly(4-styrenesulfonate) nanoparticles for inkjet-printed chemical-sensor applications" Adv Mater, vol. 19, pp. 1772-1775, 2007.

[249] L. Yang, D. Staiculescu, R. Zhang, C. P. Wong, and M. M. Tentzeris, "A Novel "Green" Fully-integrated Ultrasensitive RFID-enabled Gas Sensor Utilizing Inkjet-printed Antennas and Carbon Nanotubes" 2009 IEEE Antennas and Propagation Society International Symposium and Usnc/Ursi National Radio Science Meeting, Vols 1-6, vol., pp. 804-807, 2009.

[250] H. Lee, G. Shaker, K. Naishadham, X. J. Song, M. McKinley, B. Wagner, and M. Tentzeris, "Carbon-Nanotube Loaded Antenna-Based Ammonia Gas Sensor" Ieee T Microw Theory, vol. 59, pp. 2665-2673, 2011.

[251] J. Liu, A. G. Rinzler, H. J. Dai, J. H. Hafner, R. K. Bradley, P. J. Boul, A. Lu, T. Iverson, K. Shelimov, C. B. Huffman, F. Rodriguez-Macias, Y. S. Shon, T. R. Lee, D. T. Colbert, and R. E. Smalley, "Fullerene pipes" Science, vol. 280, pp. 1253-1256, 1998.

[252] Z. Y. Lin, T. Le, X. J. Song, Y. G. Yao, Z. Li, K. S. Moon, M. M. Tentzeris, and C. P. Wong, "Preparation of Water-Based Carbon Nanotube Inks and Application in the Inkjet Printing of Carbon Nanotube Gas Sensors" J Electron Packaging, vol. 135, 2013.

[253] P. C. P. Watts, N. Mureau, Z. N. Tang, Y. Miyajima, J. D. Carey, and S. R. P. Silva, "The importance of oxygen-containing defects on carbon nanotubes for the detection of polar and non-polar vapours through hydrogen bond formation" Nanotechnology, vol. 18, 2007.

[254] H. Chang, J. D. Lee, S. M. Lee, and Y. H. Lee, "Adsorption of NH3 and NO2 molecules on carbon nanotubes" Appl Phys Lett, vol. 79, pp. 3863-3865, 2001.

[255] L. Valentini, F. Mercuri, I. Armentano, C. Cantalini, S. Picozzi, L. Lozzi, S. Santucci, A. Sgamellotti, and J. M. Kenny, "Role of defects on the gas sensing properties of carbon nanotubes thin films: experiment and theory" Chem Phys Lett, vol. 387, pp. 356-361, 2004.

[256] S. V. Garimella, A. S. Fleischer, J. Y. Murthy, A. Keshavarzi, R. Prasher, C. Patel, S. H. Bhavnani, R. Venkatasubramanian, R. Mahajan, Y. Joshi, B. Sammakia, B. A. Myers, L. Chorosinski, M. Baelmans, P. Sathyamurthy, and P. E. Raad, "Thermal Challenges in Next-Generation Electronic Systems" Ieee T Compon Pack T, vol. 31, pp. 801-815, 2008.

[257] R. Prasher, "Thermal interface materials: Historical perspective, status, and future directions" Proceedings of the IEEE, vol. 94, pp. 1571-1586, 2006.

[258] D. Lu and C. P. Wong. (2009). *Materials for Advanced Packaging*.

[259] C. P. Wong, K. S. Moon, and Y. Li, Eds., *Nano-Bio-Electronic, Photonic and MEMS Packaging* (Thermally conductive nanocomposites. Springer, 2010, p.^pp. Pages.

[260] A. Bjorneklett, L. Halbo, and H. Kristiansen, "Thermal-Conductivity of Epoxy Adhesives Filled with Silver Particles" Int J Adhes Adhes, vol. 12, pp. 99-104, 1992.

[261] D. Kumlutas, I. H. Tavman, and M. T. Coban, "Thermal conductivity of particle filled polyethylene composite materials" Compos Sci Technol, vol. 63, pp. 113-117, 2003.

[262] Q. Z. Liang, K. S. Moon, H. J. Jiang, and C. P. Wong, "Thermal Conductivity Enhancement of Epoxy Composites by Interfacial Covalent Bonding for Underfill and Thermal Interfacial Materials in Cu/Low-K Application" Ieee T Comp Pack Man, vol. 2, pp. 1571-1579, 2012.

[263] Y. X. Zhang, X. Y. Hu, J. H. Zhao, K. Sheng, W. R. Cannon, X. H. Wang, and L. Fursin, "Rheology and Thermal Conductivity of Diamond Powder-Filled Liquid Epoxy Encapsulants for Electronic Packaging" Ieee T Compon Pack T, vol. 32, pp. 716-723, 2009.

[264] A. P. Yu, P. Ramesh, M. E. Itkis, E. Bekyarova, and R. C. Haddon, "Graphite nanoplatelet-epoxy composite thermal interface materials" J Phys Chem C, vol. 111, pp. 7565-7569, 2007.

[265] K. C. Yung and H. Liem, "Enhanced thermal conductivity of boron nitride epoxy-matrix composite through multi-modal particle size mixing" J Appl Polym Sci, vol. 106, pp. 3587-3591, 2007.

[266] Z. Y. Lin, Y. Liu, S. Raghavan, K. S. Moon, S. K. Sitaraman, and C. P. Wong, "Magnetic Alignment of Hexagonal Boron Nitride Platelets in Polymer Matrix:

Toward High Performance Anisotropic Polymer Composites for Electronic Encapsulation" Acs Appl Mater Inter, vol. 5, pp. 7633-7640, 2013.

[267] R. T. Zheng, J. W. Gao, J. J. Wang, S. P. Feng, H. Ohtani, J. B. Wang, and G. Chen, "Thermal Percolation in Stable Graphite Suspensions" Nano Lett, vol. 12, pp. 188-192, 2012.

[268] A. P. Yu, P. Ramesh, X. B. Sun, E. Bekyarova, M. E. Itkis, and R. C. Haddon, "Enhanced Thermal Conductivity in a Hybrid Graphite Nanoplatelet - Carbon Nanotube Filler for Epoxy Composites" Adv Mater, vol. 20, pp. 4740-4, 2008.

[269] M. J. Biercuk, M. C. Llaguno, M. Radosavljevic, J. K. Hyun, A. T. Johnson, and J. E. Fischer, "Carbon nanotube composites for thermal management" Appl Phys Lett, vol. 80, pp. 2767-2769, 2002.

[270] S. H. Song, K. H. Park, B. H. Kim, Y. W. Choi, G. H. Jun, D. J. Lee, B. S. Kong, K. W. Paik, and S. Jeon, "Enhanced Thermal Conductivity of EpoxyGraphene Composites by Using Non-Oxidized Graphene Flakes with Non-Covalent Functionalization" Adv Mater, vol. 25, pp. 732-737, 2013.

[271] Q. Z. Liang, Y. H. Xiu, W. Lin, K. S. Moon, and C. P. Wong, "Epoxy/h-BN Composites for Thermally Conductive Underfill Material" 2009 IEEE 59th Electronic Components and Technology Conference, Vols 1-4, vol., pp. 437-440, 2009.

[272] Z. Y. Lin, Y. G. Yao, A. Mcnamara, K. S. Moon, and C. P. Wong, "Single/few-layer Boron Nitride-based Nanocomposites for High Thermal Conductivity Underfills" 2012 IEEE 62nd Electronic Components and Technology Conference (ECTC), vol., pp. 1437-1441, 2012.

[273] C. Y. Zhi, Y. Bando, C. C. Tang, H. Kuwahara, and D. Golberg, "Large-Scale Fabrication of Boron Nitride Nanosheets and Their Utilization in Polymeric Composites with Improved Thermal and Mechanical Properties" Adv Mater, vol. 21, pp. 2889-93, 2009.

[274] W. L. Song, P. Wang, L. Cao, A. Anderson, M. J. Meziani, A. J. Farr, and Y. P. Sun, "Polymer/Boron Nitride Nanocomposite Materials for Superior Thermal Transport Performance" Angew Chem Int Edit, vol. 51, pp. 6498-6501, 2012.

[275] U. Khan, P. May, A. O'Neill, A. P. Bell, E. Boussac, A. Martin, J. Semple, and J. N. Coleman, "Polymer reinforcement using liquid-exfoliated boron nitride nanosheets" Nanoscale, vol. 5, pp. 581-587, 2013.

[276] X. B. Wang, A. Pakdel, J. Zhang, Q. H. Weng, T. Y. Zhai, C. Y. Zhi, D. Golberg, and Y. Bando, "Large-surface-area BN nanosheets and their utilization in polymeric composites with improved thermal and dielectric properties" Nanoscale Res Lett, vol. 7, pp. 662, 2012.

[277] O. Y. Tao, Y. P. Chen, Y. E. Xie, K. K. Yang, Z. G. Bao, and J. X. Zhong, "Thermal transport in hexagonal boron nitride nanoribbons" Nanotechnology, vol. 21, 2010.

[278] I. Jo, M. T. Pettes, J. Kim, K. Watanabe, T. Taniguchi, Z. Yao, and L. Shi, "Thermal Conductivity and Phonon Transport in Suspended Few-Layer Hexagonal Boron Nitride" Nano Lett, vol. 13, pp. 550-554, 2013.

[279] J. H. Seol, A. L. Moore, L. Shi, I. Jo, and Z. Yao, "Thermal Conductivity Measurement of Graphene Exfoliated on Silicon Dioxide" J Heat Trans-T Asme, vol. 133, pp. 022403, 2011.

[280] C. Muratore, V. Varshney, J. J. Gengler, J. J. Hu, J. E. Bultman, T. M. Smith, P. J. Shamberger, B. Qiu, X. Ruan, A. K. Roy, and A. A. Voevodin, "Cross-plane thermal properties of transition metal dichalcogenides" Appl Phys Lett, vol. 102, pp. 081604, 2013.

[281] S. Sahoo, A. P. S. Gaur, M. Ahmadi, M. J. F. Guinel, and R. S. Katiyar, "Temperature-Dependent Raman Studies and Thermal Conductivity of Few-Layer MoS2" J Phys Chem C, vol. 117, pp. 9042-9047, 2013.

[282] Y. G. Yao, Z. Y. Lin, Z. Li, X. J. Song, K. S. Moon, and C. P. Wong, "Large-scale production of two-dimensional nanosheets" J Mater Chem, vol. 22, pp. 13494-13499, 2012.

[283] A. McNamara, V. Sahu, Y. Joshi, and Z. Zhang, "Infrared Imaging Microscope as an Effective Tool for Measuring Thermal Resistance of Emerging Interface Materials" ASME Conference Proceedings, vol. 2011, pp. T30026-T30026-6, 2011.

[284] Z. Lin, A. McNamara, Y. Liu, K.-s. Moon, and C.-P. Wong, "Exfoliated hexagonal boron nitride-based polymer nanocomposite with enhanced thermal conductivity for electronic encapsulation" Compos Sci Technol, vol. 90, pp. 123-128, 2014.

[285] A. Spiesser, Y. M. Chong, K. M. Leung, G. Abel, G. G. Ross, M. J. Walzak, R. Jacklin, W. M. Lau, W. J. Zhang, and I. Bello, "Surface free energy of cubic boron nitride films deposited on nanodiamond" J Phys Chem C, vol. 111, pp. 12768-12772, 2007.

[286] S. J. Luo and C. P. Wong, "Effect of UV/ozone treatment on surface tension and adhesion in electronic packaging" Ieee T Compon Pack T, vol. 24, pp. 43-49, 2001.

[287] B. Q. Dai and G. L. Zhang, "A DFT study of hBN compared with graphite in forming alkali metal intercalation compounds" Mater Chem Phys, vol. 78, pp. 304-307, 2003.

[288] Y. Y. Sun, Z. Q. Zhang, and C. P. Wong, "Study and characterization on the nanocomposite underfill for flip chip applications" Ieee T Compon Pack T, vol. 29, pp. 190-197, 2006.

[289] C. P. Wong and R. S. Bollampally, "Thermal conductivity, elastic modulus, and coefficient of thermal expansion of polymer composites filled with ceramic particles for electronic packaging" J Appl Polym Sci, vol. 74, pp. 3396-3403, 1999.

[290] Y. Y. Sun, Z. Q. Zhang, and C. P. Wong, "Study on mono-dispersed nano-size silica by surface modification for underfill applications" J Colloid Interf Sci, vol. 292, pp. 436-444, 2005.

[291] T. L. Li and S. L. C. Hsu, "Enhanced Thermal Conductivity of Polyimide Films via a Hybrid of Micro- and Nano-Sized Boron Nitride" J Phys Chem B, vol. 114, pp. 6825-6829, 2010.

[292] T. L. Li and S. L. C. Hsu, "Preparation and Properties of Thermally Conductive Photosensitive Polyimide/Boron Nitride Nanocomposites" J Appl Polym Sci, vol. 121, pp. 916-922, 2011.

[293] R. W. Zhang, W. Lin, K. S. Moon, and C. P. Wong, "Fast Preparation of Printable Highly Conductive Polymer Nanocomposites by Thermal Decomposition of Silver Carboxylate and Sintering of Silver Nanoparticles" Acs Appl Mater Inter, vol. 2, pp. 2637-2645, 2010.

[294] K. Sato, H. Horibe, T. Shirai, Y. Hotta, H. Nakano, H. Nagai, K. Mitsuishi, and K. Watari, "Thermally conductive composite films of hexagonal boron nitride and polyimide with affinity-enhanced interfaces" J Mater Chem, vol. 20, pp. 2749-2752, 2010.

[295] L. Li, Z. B. Yang, H. J. Gao, H. Zhang, J. Ren, X. M. Sun, T. Chen, H. C. Kia, and H. S. Peng, "Vertically Aligned and Penetrated Carbon Nanotube/Polymer Composite Film and Promising Electronic Applications" Adv Mater, vol. 23, pp. 3730-3735, 2011.

[296] W. Lin, K. S. Moon, and C. P. Wong, "A Combined Process of In Situ Functionalization and Microwave Treatment to Achieve Ultrasmall Thermal Expansion of Aligned Carbon Nanotube-Polymer Nanocomposites: Toward Applications as Thermal Interface Materials" Adv Mater, vol. 21, pp. 2421-2424, 2009.

[297] C. Wei, L. M. Dai, A. Roy, and T. B. Tolle, "Multifunctional chemical vapor sensors of aligned carbon nanotube and polymer composites" J Am Chem Soc, vol. 128, pp. 1412-1413, 2006.

[298] L. J. Lanticse, Y. Tanabe, K. Matsui, Y. Kaburagi, K. Suda, M. Hoteida, M. Endo, and E. Yasuda, "Shear-induced preferential alignment of carbon nanotubes

resulted in anisotropic electrical conductivity of polymer composites" Carbon, vol. 44, pp. 3078-3086, 2006.

[299] T. Terao, C. Y. Zhi, Y. Bando, M. Mitome, C. C. Tang, and D. Golberg, "Alignment of Boron Nitride Nanotubes in Polymeric Composite Films for Thermal Conductivity Improvement" J Phys Chem C, vol. 114, pp. 4340-4344, 2010.

[300] C. A. Cooper, D. Ravich, D. Lips, J. Mayer, and H. D. Wagner, "Distribution and alignment of carbon nanotubes and nanofibrils in a polymer matrix" Compos Sci Technol, vol. 62, pp. 1105-1112, 2002.

[301] L. Jin, C. Bower, and O. Zhou, "Alignment of carbon nanotubes in a polymer matrix by mechanical stretching" Appl Phys Lett, vol. 73, pp. 1197-1199, 1998.

[302] R. Haggenmueller, H. H. Gommans, A. G. Rinzler, J. E. Fischer, and K. I. Winey, "Aligned single-wall carbon nanotubes in composites by melt processing methods" Chem Phys Lett, vol. 330, pp. 219-225, 2000.

[303] N. Yousefi, M. M. Gudarzi, Q. B. Zheng, S. H. Aboutalebi, F. Sharif, and J. K. Kim, "Self-alignment and high electrical conductivity of ultralarge graphene oxide-polyurethane nanocomposites" J Mater Chem, vol. 22, pp. 12709-12717, 2012.

[304] M. A. Correa-Duarte, M. Grzelczak, V. Salgueirino-Maceira, M. Giersig, L. M. Liz-Marzan, M. Farle, K. Sierazdki, and R. Diaz, "Alignment of carbon nanotubes under low magnetic fields through attachment of magnetic nanoparticles" J Phys Chem B, vol. 109, pp. 19060-19063, 2005.

[305] R. M. Erb, R. Libanori, N. Rothfuchs, and A. R. Studart, "Composites Reinforced in Three Dimensions by Using Low Magnetic Fields" Science, vol. 335, pp. 199-204, 2012.

[306] C. Goubault, P. Jop, M. Fermigier, J. Baudry, E. Bertrand, and J. Bibette, "Flexible magnetic filaments as micromechanical sensors" Physical Review Letters, vol. 91, 2003.

[307] H. Singh, P. E. Laibinis, and T. A. Hatton, "Synthesis of flexible magnetic nanowires of permanently linked core-shell magnetic beads tethered to a glass surface patterned by microcontact printing" Nano Lett, vol. 5, pp. 2149-2154, 2005.

[308] J. P. Ge, Y. X. Hu, and Y. D. Yin, "Highly tunable superparamagnetic colloidal photonic crystals" Angew Chem Int Edit, vol. 46, pp. 7428-7431, 2007.

[309] D. Lee, R. E. Cohen, and M. F. Rubner, "Heterostructured magnetic nanotubes" Langmuir, vol. 23, pp. 123-129, 2007.

[310] J. Fresnais, J. F. Berret, B. Frka-Petesic, O. Sandre, and R. Perzynski, "Electrostatic Co-Assembly of Iron Oxide Nanoparticles and Polymers: Towards the Generation of Highly Persistent Superparamagnetic Nanorods" Adv Mater, vol. 20, pp. 3877-3881, 2008.

[311] M. Yan, J. Fresnais, S. Sekar, J. P. Chapel, and J. F. Berret, "Magnetic Nanowires Generated via the Waterborne Desalting Transition Pathway" Acs Appl Mater Inter, vol. 3, pp. 1049-1054, 2011.

[312] M. J. Crimp, D. A. Oppermann, and K. Krehbiel, "Suspension properties of hexagonal BN powders: effect of pH and oxygen content" J Mater Sci, vol. 34, pp. 2621-2625, 1999.

[313] R. M. Erb, H. S. Son, B. Samanta, V. M. Rotello, and B. B. Yellen, "Magnetic assembly of colloidal superstructures with multipole symmetry" Nature, vol. 457, pp. 999-1002, 2009.

[314] P. S. Turner, "Thermal-Expansion Stresses in Reinforced Plastics" J Res Nat Bur Stand, vol. 37, pp. 239-250, 1946.

[315] R. A. Schapery, "Thermal Expansion Coefficients of Composite Materials Based on Energy Principles" J Compos Mater, vol. 2, pp. 380-&, 1968.

[316] C. W. Nan, R. Birringer, D. R. Clarke, and H. Gleiter, "Effective thermal conductivity of particulate composites with interfacial thermal resistance" J Appl Phys, vol. 81, pp. 6692-6699, 1997.

[317] G. A. Slack, "Thermal Conductivity of Mgo, Al2o3, Mgal2o4, and Fe3o4 Crystals from 3 Degrees to 300 Degrees K" Phys Rev, vol. 126, pp. 427-&, 1962.

[318] J. Hirotani, T. Ikuta, T. Nishiyama, and K. Takahashi, "Thermal boundary resistance between the end of an individual carbon nanotube and a Au surface" Nanotechnology, vol. 22, 2011.

[319] R. Prasher, "Thermal boundary resistance and thermal conductivity of multiwalled carbon nanotubes" Phys Rev B, vol. 77, 2008.

[320] J. C. Duda, P. E. Hopkins, T. E. Beechem, J. L. Smoyer, and P. M. Norris, "Inelastic phonon interactions at solid-graphite interfaces" Superlattice Microst, vol. 47, pp. 550-555, 2010.

[321] A. J. Schmidt, K. C. Collins, A. J. Minnich, and G. Chen, "Thermal conductance and phonon transmissivity of metal-graphite interfaces" J Appl Phys, vol. 107, 2010.

[322] J. H. L. Pang, B. S. Xiong, and T. H. Low, "Low cycle fatigue models for lead-free solders" Thin Solid Films, vol. 462, pp. 408-412, 2004.